Rubber-ice friction : a multi-scale and multi-physical approach

Sylvain Hemette

N° d'ordre MNT : 2019LYSEC17

THÈSE de DOCTORAT de L'UNIVERSITÉ de LYON
opéré au sein de
l'École Centrale de Lyon

École doctorale n°162:
Mécanique - Energétique - Génie civil - Acoustique (MEGA)

Laboratoire:
Laboratoire de Tribologie et Dynamique des Systèmes (LTDS)

Soutenue publiquement le 17 Juin 2019, par :
Sylvain HEMETTE

Pour obtenir le grade de
Docteur en Mécanique

Rubber-Ice Friction
A Multi-Scale and Multi-Physical Approach

Devant le jury composé de :

A. CHATEAUMINOIS	DR CNRS	Laboratoire de Sciences et Ingènierie de la Matiére Molle	Rapporteur
J. DENAPE	Professeur	Laboratoire Génie de Production	Rapporteur
J-Y. CAVAILLE	Professeur Émerite	ELyTMax, CNRS	Président
M. RUTLAND	Professeur	KTH	Examinateur
J. CAYER-BARRIOZ	DR CNRS	LTDS	Directeur de Thèse
D. MAZUYER	Professeur	LTDS	Directeur de Thèse
K. KURIHARA	Professeur	NiCHe	Directeur de Thèse

Contents

List of Figures

List of Tables

Nomenclature

α_{dry} The partitioning coefficient between surface and lubricant viscous contributions to the friction

α_T The shift coefficient of the WLF theory associated to the temperature T

$\chi_{pixel\ contact}$ A threshold that judges whether the pixel is part of the contact in the function $f_{pixel\ contact}$

δ The loss angle in rad

ϵ The instantaneous deformation

ϵ_0 The amplitude of deformation

η The viscosity in N.m^{-2}.s^{-1}

w The adhesion work of two materials in J.m^{-2}

γ_{ice} The surface energy of the ice in J.m^{-2}

$\lambda_{typical}$ The periodical average distance of material stress in mm

μ The friction coefficient

$\mu_{surface}$ The surface contribution to the friction

$\mu_{viscous}$ The lubricant viscous contribution to the friction

ν The Poisson coefficient

ν_{ice} The Poisson coefficient of the ice

ω The stress pulsation of a material in rad.s^{-1}

ϕ The phase shift between two response signals in rad

ρ_{ice} The density of the ice in kg.m^{-3}

σ The instantaneous shear stress in MPa

σ_0 The amplitude of the shear stress in MPa

θ The static contact angle of a sessile drop of water on slider material in rad

a The semi major axis of the elliptical contact which is also the radius of the circular contact in mm

A_0 The equivalent material constant used in JKR theory in mm^3.N^{-1}

a_{equiv} The equivalent contact radius calculated via the Gaussian curvature from the major and minor semi axis of the elliptical contact

b The semi minor axis of the elliptical contact in mm

b_1 The viscosity of the leaf spring of the SFA-RSM upper unit in N.m^{-1}.s^{-1}

b_3 The viscosity of the leaf spring of the SFA-RSM lower unit in N.m^{-1}.s^{-1}

$B_{x,y}$ The level of blue at the position $\{x, y\}$ in an image

C_1 A coefficient of the WLF transform

C_2 A coefficient of the WLF transform in K

c_{ice} The specific heat of the ice in kJ.kg^{-1}.K^{-1}
C_{in} The constant of displacement-voltage conversion of the piezo-tube in the SFA-RSM in V.m^{-1}
C_{out} The constant of displacement-voltage conversion of the capacitance probe in the SFA-RSM in V.m^{-1}
δ_{heat} The heat partitioning factor
d_{ice} The asperity diameter of the ice surface in m
D_{sample} The rubber sample diameter corresponding to the semi-minor sample radius R_b in mm
d_{slider} The asperity diameter on the slider surface in m
E The Young modulus in MPa
E_{ice} The Young modulus of the ice in MPa
E^* The equivalent elasticity modulus of two solids in MPa
$\widetilde{E}$ The effective Young modulus in MPa
f The stress frequency of a material in Hz
F_0 The adhesion force in N
F_a The adhesion loss force due to the combined adhesion of the rubber and the track in N
F_c The force of cohesion loss caused by rubber wear in N
$f_{guessed}$ The guessed resonance frequency during a Resonance Shear Measurement in Hz
F_h The loss force caused by the hysteresis of the bulk rubber viscoelastic deformation in N
$f_{pixel\ contact}$ The function that judges whether the pixel is part of the contact
f_{ref} The stress frequency at which is known the master curve in Hz
F_v The viscous loss force due to the lubricant within the contact in N
F_y The tangential friction force in N
F_z The applied normal force in N
G The shear modulus in MPa
g The gravitational acceleration in m.s^{-2}
$\underline{G}$ The complex shear modulus in MPa
$\underline{g}$ The complex model modeling the rubber viscoelastic properties in N.m^{-1}
G_{ice} The shear modulus of the ice in MPa
G' The elastic shear modulus in MPa
g' The elastic stiffness in N.m^{-1}
G'' The dissipative shear modulus in MPa
g'' The dissipative stiffness in N.m^{-1}
G^* The absolute value of the complex shear modulus $\underline{G}$ in MPa
$G^*_{plateau}$ The rubber plateau rigidity in MPa
$G_{x,y}$ The level of green at the position $\{x, y\}$ in an image
H_{ice} The hardness of the ice in MPa

h_{ice} The enthalpy of fusion of the ice in kJ.kg^{-1}
$I_{average}$ The average image used in phantom imaging algorithm
$I_{phantom}$ The phantom image
$I_{phantom\ homogeneized}$ The phantom image with homogenized light
$I_{phantom\ normalized}$ The normalized phantom image
$I_{x,y\ compared}$ The compared image between unloaded and loaded images for JKR experiments
$I_{x,y\ normalized}$ The normalized post-treated compared image for JKR experiments
j The complex unit ($j^2 = -1$)
k_1 The rigidity of the leaf spring of the SFA-RSM upper unit in N.m^{-1}
k_3 The rigidity of the leaf spring of the SFA-RSM lower unit in N.m^{-1}
k_{ice} The thermal conductivity of the ice in W.m^{-1}.K^{-1}
k_{slider} The thermal conductivity of the slider in W.m^{-1}.K^{-1}
m_{1_1} The mass of SFA-RSM upper unit in kg
m_{1_2} The mass of the piezo-tube 'tip' in SFA-RSM in kg
m_2 The mass of SFA-RSM lower unit in kg
P_{atm} The atmospheric pressure in MPa
P_e The Peclet number
$\overline{q}_{heat}$ The average flux in W.m^{-2}
R The equivalent radius of two solids in mm
R_a The rubber sample semi-major sample radius in mm
R_b The rubber sample semi-minor sample radius in mm
R_{ice} The radius of the ice disc for SFA experiments in mm
R' Reduced radius of curvature in mm.
$R_{rubber\ disc}$ The radius of the silica disc were is located the rubber sample for SFA experiments in mm
$R_{x,y}$ The level of red at the position $\{x, y\}$ in an image
S_a The contact area in m^2
S_e A function for elliptical source of heat
S_q The surface root mean squared roughness in m
T The temperature in K
t The time coordinate in s
T_0 The temperature far from the contact and corresponding to the environment temperature in K
$\tan\delta$ The dissipative factor
T_c The temperature within the contact in K
T_{disc} The rubber disc bulk temperature during SFA experiments in K
T_g The temperature of glassy transition in K
T_{ice} The rubber disc bulk temperature during SFA experiments in K
T_m The melting temperature in K

T_{ref}	The reference temperature at which is known the master curve in K
T_{slider}	The temperature within the contact on the slider surface in K
T_{track}	The temperature within the contact on the track surface in K
U_{in}	The input voltage amplitude applied on the piezo-tube of the SFA-RSM in V
U_{out}	The output voltage amplitude measured with the capacitance probe of the SFA-RSM in V
V_g	The sliding velocity in mm.s^{-1}
$Y_{x,y}$	The grey scale of the pixel analyzed at the position $\{x, y\}$

Introduction

Even though driving on ice can be seen as a challenging fun experience on an automotive dedicated track, a specific training is necessary to be able to safely control the trajectory, brake, turn, *etc*. Another way to remain safe on an icy road is to use studded tires. In many countries, the use of studded tires is tightly restricted to specific winter conditions. In France, for example, the use of studded tires is restricted to touring cars to the period from November to March according to the 'Arrêté du 18 juillet 1985'. In Japan, the use of studded tires has even been prohibited and considered as a criminal offense since winter 1991-1992 to prevent from the environmental pollution caused by road wear dust. As a result, tire manufacturers are interested in developing specific tires for arctic conditions that guarantee high driving performance on snow or ice.

The pioneering work of Tabor [1] on ice friction enlightened the role of adhesion. Nevertheless, the hypothesis of a surface modification was also considered. Further and later works showed that the tribological behavior of rubber-ice contacts results from intricated mechanisms such as adhesion on ice, viscoelastic dissipation within the rubber, ice creep and melting, *etc*. In order to better understand the contact between rubber and ice, an experimental strategy was proposed based on a multiscale investigation of the rubber-ice contact.

Intrinsically multidisciplinary, this approach was based on a collaboration between industry and academy in the framework of the international laboratory (LIA) ElyTLab via the support of the CNRS through a BDI grant:

- Nihon Michelin Tire (日本ミシュランタイヤ), one of the world leaders in tire manufacturing;
- Laboratoire de Tribologie et Dynamique des Sytèmes (LTDS), Ecole Centrale de Lyon, CNRS UMR5513, which is a world expert in the understanding of contact phenomena;
- The Kurihara Laboratory in Tohoku University, which brings its expertise in the analysis of surface interactions at the microscale.

More specifically, this work aims at understanding the mechanisms responsible for dissipation in rubber-ice contact, for rubber representative of real tire material.

The first chapter of this thesis presents a state of the art on the tire, rubber material and ice and their tribological interactions when in contact. First, the structure and the

composition of the tire, as well as its kinematics during the braking phases, were introduced leading to a description of the microstructure and mechanical properties of rubber and ice. Contact mechanics theories, Hertzian for non-adhesive materials and variations for adhesive materials, were also described before a review of the tribological behavior of rubber and ice was exposed. Finally, the goals and the experimental strategy of this thesis were presented.

The second chapter analyzed the influence of the rubber composition on the contact mechanics of the rubber-ice interface using a dedicated Surface Force Apparatus. The viscoelastic properties of the thin interfacial rubber layer were also identified. Parameters such as the presence of carbon blacks and oils were investigated.

Sliding of the rubber-ice contact was introduced in the third chapter. A dedicated tribometer was developed allowing one to simultaneously measure the contact forces and visualize the ice-rubber interface for controlled contact kinematics and cold environment. The effect of sliding velocity and temperature was investigated. The mechanical properties of the rubber were also varied.

The fourth chapter presents a discussion on the friction mechanisms of rubber-ice contact. Viscoelasticity and thermal effects competed in the range of experimental conditions investigated and the transition between these different regimes of friction was analyzed.

Chapter 1

State of the Art

The friction of tires on icy roads involves two complex materials with specific tribological interactions: rubber and ice. The tire is a composite material whose matrix is composed of several types of rubbers. These different materials fulfill multiple functions which govern the driving performance. The rubber ensures the contact with the road through the treads. The rubber itself is a composite material made of vulcanized elastomers, plasticizers, oils and fillers such as silica and carbon black particles. It is then possible to design rubbers resistant to the environment and, with controlled viscoelastic properties. The ice is a complex polycrystalline material composed of H_2O molecules. On Earth, ice is subjected to environmental conditions close to that leading to melting. The presence of an unstable surface layer so called 'premelting' layer or 'quasi' liquid layer is still under debate.

The contact between rubber and ice depends on adhesion and on their respective mechanical properties. This is well described using contact mechanics theories such as the Hertz theory or the Johnson-Kendall-Roberts theory.

Sliding over a rubber dissipates energy. This energy dissipation arises from interfacial adhesion loss caused by the creation and breaking of molecular bonds, and from bulk energy loss due to the deformation of the rubber by its counter face. Other forms of dissipation are the cohesion loss due to the rubber wear and viscous loss due to the presence of a lubricant, such as water. Friction on ice involves adhesion, creep and heating, likely to cause melting of the ice surface. Friction between ice and rubber is less documented.

Nevertheless, the influence of the temperature-frequency dependence, of the ice surface evolution was identified. In this context, the goal of this thesis is to contribute to the understanding of ice-rubber friction mechanisms and a multiscale experimental strategy was proposed.

1.1. The Tire

Tires are essential elements of vehicles ensuring the only contacts with the road. Several functions are provided by the tire: transmit the efforts to the ground, secure the driver by ensuring control of his car in all circumstances whether during turning or acceleration-braking phases, ensure driving comfort by reducing noises and damping shocks, minimize energy consumption and be recyclable.

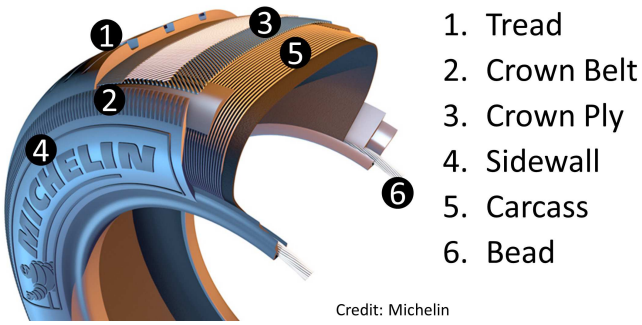

Figure 1.1.: The structure of a modern tire. The tire is made of a multitude of materials as elastomers, carbon black, silica, steel organized in several function-structure [2].

Several main elements give the tire its structure [2, 3]:

- The carcass is a mix of textile or metal cables surrounded by rubber. It absorbs the air pressure stress, shocks and weight.
- The tread is a thick layer of rubber. It comes in contact with the road and can be carved to evacuate water.
- The crown belt is composed of textile cables. It limits the deformation of the carcass at high velocity.
- The crown ply is composed of metal cables. It links the tread to the carcass and increases the tread resistance.
- The bead is composed of reinforced steel wires and low flexibility rubber. It keeps the tire on the wheel.
- The sidewall is composed of rubber. It links the tread to the bead and protects the carcass.

According to the second and the third laws of Newton, the acceleration and deceleration of a vehicle arise from the force exercised by the tire on the road - and by the road on the tire - through the tire-road contact. The efforts are transmitted within a limited contact area, slightly larger than that of a smartphone - approximately 100x150 mm^2. Therefore, ensuring a high friction within the contact ensures the transmission of efforts

and the control of the vehicle. High friction can be reached by controlling the surface of the road and the design of the tire tread. These two aspects interested us here:

- Icy roads are hardly controllable. But understanding ice properties may allow to design adapted tire treads.
- Tire tread properties that are the only parameters that can be designed by tire manufacturers.

In order to ensure maximum safety, all modern cars are equipped of the so called ABS - i.e Anti Blockier System - which prevents the wheel from locking during the braking phase to dissipate kinetic energy in the brake rather than in the tire-road contact. Therefore even during braking, the wheel does not stop rotating and the tire is never in a complete sliding state.

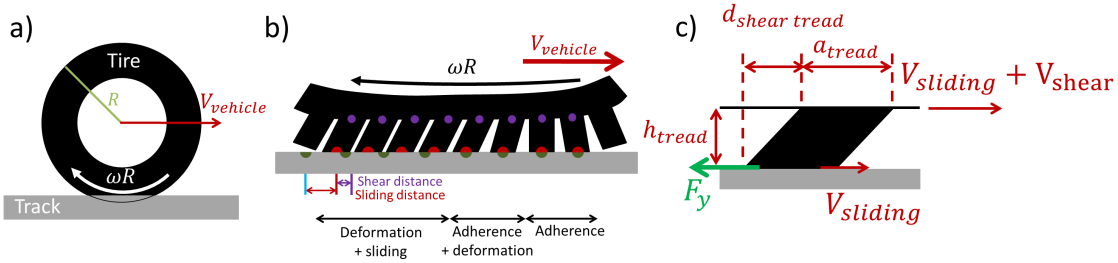

Figure 1.2.: Schematic of the tire during the braking phase. Figure (a) shows the different velocities of the tire and its deformation at the contact point. The vehicle is moved at the translation velocity $V_{vehicle}$ and the tire rotates at the angular velocity ω_{wheel} with a linear velocity $\omega_{wheel} R_{wheel}$ when the tread comes in contact with the track. Figure (b) presents the behavior of tread sculptures during the braking phase with ABS. The treads initially come in contact with the track, then shear and finally slide until they leave the contact. Figure (c) shows the shear of one tread block of a size a_{tread} and height h_{tread} on a distance $d_{tread\ shear}$. The shear is caused by the difference in velocity - between that of the wheel and that of the vehicle - within the contact.

During the rotation of the wheel, tread blocks follow different phases due to the deformation of the tire at the contact point:

1. Tread blocks come in contact with the track;
2. Blocks are compressed;
3. Blocks shear;
4. Blocks slide on the track;
5. Blocks leave the track.

These different phases imply that tire tread and its composing rubber undergo deformation and sliding on the track at several velocities.

1.2. The Elastomer

Elastomers come from two different origins. The first one is the transformation of 'natural' latex harvested in Heveas (rubber tree) plantations. The second one is the synthesis of elastomers resulting from several chemical reactions - polymerization, polycondensation and copolymerization - of monomers to obtain larger molecules with properties similar to those of the latex. To improve the properties of the rubber - such as mechanical properties, UV resistance, aging or oxidation resistance - multiple additives are added. These additives can be grouped in five categories [3]:

- Fillers such as silica or carbon black which improve mechanical properties. They decrease the production cost of tires by decreasing the proportion of elastomers used. They also have some anti-UV and anti-aging properties.
- Plasticizers which facilitate the mixing of the mixture. They increase the mobility of the polymer chains thus decrease the glass temperature transition of the polymer.
- Vulcanization agents - such as sulfur - that form reticulated bonds between elastomer molecules during heating. Therefore it gives its mechanical properties to the mixture.
- Protective agents that avoid the degradation of tire properties due to the environmental aggression such as UV, oxidizing or aging.
- Various additives that can improve fire resistance, facilitate mixing or help to obtain structures in tires such as a honeycomb structure.

The term elastomer, which is derived from 'elastic polymer', is often used interchangeably with the term rubber, although the latter is preferred when referring to vulcanisates [4]. From now on, the term 'rubber' will be used to describe the final mixture.

As a composite material, rubber has a complex behavior depending on its compounds. The complex structure of the reticulated elastomer matrix provides the viscoelastic properties. Fillers bring heterogeneity of elasticity as well as non-linearity. In addition, the characterization of these mechanical properties also depends on:

- The type of the applied stress, such as shear or normal stress;
- The scale of the applied stress;
- The frequency of the applied stress.

1.2.1. Viscoelasticity

Elastomers are viscoelastic materials. This property is driven by the freedom of movement of the elastomer molecules due to the thermal motion. The vulcanization process tends to decrease this freedom but the global structure of the rubber remains viscoelastic. Therefore the behavior of the reticulated rubber is directly related to the possibilities of movement of the polymer chains linked by bonds and entanglements. From this structure, different behaviors can be observed as function of the frequency and amplitude of the elongation of the rubber. For example, viscoelasticity implies hysteresis during loading and unloading cycle [3].

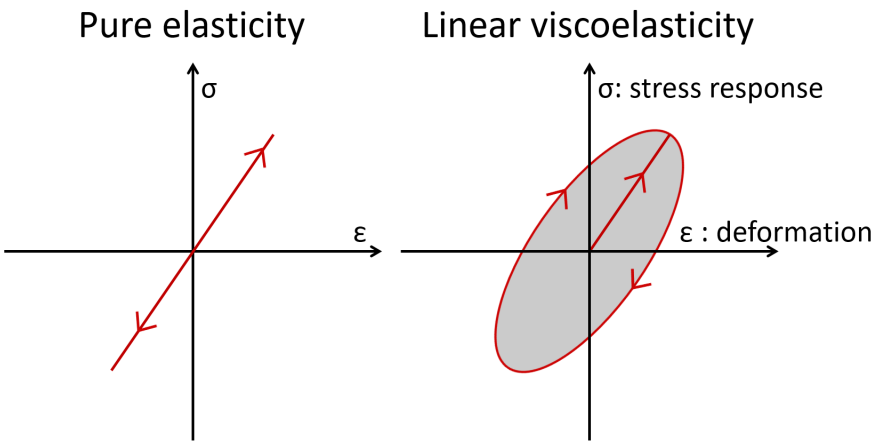

Figure 1.3.: Illustration of the shear response σ to an imposed deformation ϵ in the purely elastic case and the viscoelastic case. An hysteresis exists in the viscoelastic case, which causes energy dissipation.

Viscoelastic representation Shear and elasticity modulus - i.e G and E - of viscoelastic materials can be represented by a complex expression of the form:

$$\underline{G} = G' + jG'' \tag{1.1}$$

where G' is the elastic shear modulus (elastic energy storage), G'' the dissipative shear modulus (viscous energy loss) and j is the complex unit ($j^2 = -1$).

From this definition, the modulus G^* and the dissipative factor $\tan\delta$ can be introduced:

$$G^* = \sqrt{G'^2 + G''^2} \qquad \text{and} \qquad \tan\delta = \frac{G''}{G'}$$

where δ is the loss angle of G^* in the complex domain.

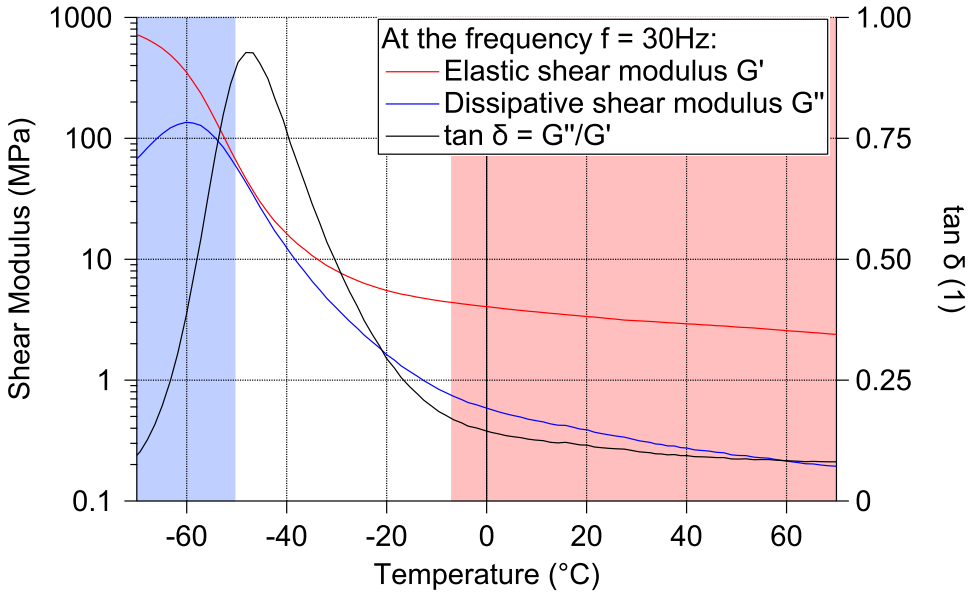

Figure 1.4.: Example of evolution of shear properties of a rubber as a function of the temperature at 30 Hz. The blue area - at low temperature - highlights the glassy state of the rubber, the red area - at high temperature - highlights the rubbery state. The T_g value is estimated as the temperature at which $\tan\delta$ is maximum. (Data from Michelin)

Glassy transition The mechanical properties of amorphous materials, such as rubbers, are characterized by one parameter - the glass temperature transition T_g - given as the limit of the α type transition between two different states: the glassy and the rubbery states. The glassy state, observed at low temperature, is characterized by a high Young modulus and a brittle behavior. For temperature higher than T_g, the elastomer molecules can move and the rubber becomes rubbery. The rubbery state is characterized by a lower Young modulus than in the glassy state, between two or three magnitude order lower. The glass transition temperature T_g is dependent on the stress frequency applied to the rubber and on the operating conditions. Therefore, measurements of the different mechanical properties of the rubber are given for one stress frequency value - as shown in figure 1.4.

Temperature-frequency equivalence The increase of the stress frequency increases the temperature of the glass transition T_g. The WLF equation - an acronym for William,

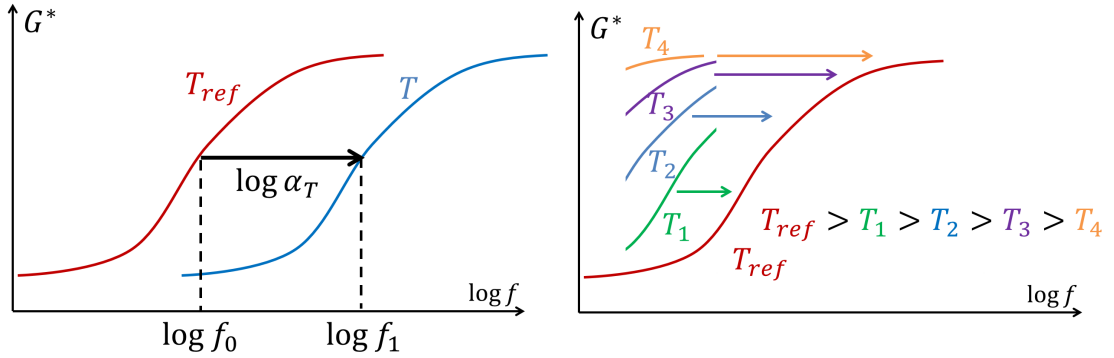

(a) Illustration of the frequency-temperature dependence shift formulated by the WLF equation. The temperatures T_{ref} and T are in the range between T_g, the glass transition temperature, and $T_g + 100\ K$.

(b) Illustration of the building of a master curve from multiple measurements performed at several temperatures over a limited frequency range.

Figure 1.5.: Illustrations of the WLF theory.

Landel and Ferry - gives a description of this phenomenon of frequency-temperature equivalence of rubber properties [5] - as illustrated in figure 1.5a.

$$\log \alpha_T = -\frac{C_1(T - T_{ref})}{C_2 + T - T_{ref}} \tag{1.2}$$

where $\alpha_T = f_{ref}/f_T$ is the factor of frequency shift, f_T is the stress frequency at the temperature T, f_{ref} is the stress frequency at the temperature T_{ref}, T_{ref} is the reference temperature of the rubber properties, T is the target temperature and C_1 and C_2 are two coefficients depending on the material. The validity of this expression is usually given for a temperature range from T_g to T_g+100 K. The two coefficients C_1 and C_2 are usually set to:

$$C_1 = 8.86 \qquad C_2 = 101.5\ \mathrm{K}$$

These values can also be obtained by building a master-curve - as shown in figure 1.5b, by measuring the properties of the material for different temperature in a limited range of stress frequency.

The physical interpretation of this frequency-temperature equivalence is based on the theory of the specific volume. From Doolittle free-space equation [6] for viscosity and assuming a linear evolution of the free volume as a function of the temperature:

$$\ln \eta(T) = \ln A_{Doolittle} + B_{Doolittle}\frac{v_{ref}(T_{ref})}{v_f(T)} \qquad V = \frac{v_f(T)}{v_{ref}(T_{ref})} = V_{ref} + \alpha_V(T - T_{ref})$$

where η is the viscosity, v_{ref} is the occupied molecular volume of reference, $v_f = v - v_{ref}$ is the free volume, v is the molecular specific volume, T is the target temperature, T_{ref} is the reference temperature, α_V is the thermal expansion coefficient above and below the glass transition temperature T_g, V is the fraction of free volume at T, V_{ref} is the fraction of free volume at T_g and $A_{Doolittle}$ and $B_{Doolittle}$ are two constants. Therefore the following relationship was obtained:

$$\ln \eta(T) - \ln \eta(T_{ref}) = B_{Doolittle}\left(\frac{1}{V} - \frac{1}{V_{ref}}\right) = -\frac{B_{Doolittle}}{V_{ref}} \frac{T - T_{ref}}{V_{ref}/\alpha_V + T - T_{ref}}$$

$$\log \alpha_T = \ln 10 \ln \frac{\eta(T)}{\eta(T_{ref})} = -\frac{C_1(T - T_{ref})}{C_2 + T - T_{ref}}$$

$$\text{with} \quad C_1 = \frac{\ln 10 B_{Doolittle}}{V_{ref}} \quad \text{and} \quad C_2 = \frac{V_{ref}}{\alpha_V}$$

Another way to obtain a similar relationship is to use the Arrhenius law that is applied to type β material transition. The use of this relationship is limited to the temperature of the glass transition T_g and the temperature above.

$$\log(\alpha_T) = \frac{\delta H_a}{R_{Boltzmann}}\left(\frac{1}{T} - \frac{1}{T_{ref}}\right)$$

with $R_{Boltzmann}$ is the ideal gas constant and δH_a is the activation energy.

Rheological models Rheological models are used to describe the viscous and elastic behavior of rubbers. These models consist in a combination of springs, dampers or Coulomb pad. The complex phenomena are mainly modeled using two basic elements:

- Hookian solids which are able to restitute entirely the absorbed strained energy. The stress response is modeled by a spring with the equation: $\sigma(t) = G\epsilon(t)$.
- Newtonian liquids that dissipate all the absorbed deformation energy, usually in the form of heat. The stress response is modeled by a damper with the equation: $\sigma(t) = \eta\frac{d\epsilon}{dt}(t)$. A phase shift of $\pi/2$ is then induced.

When rubbers are stressed periodically - on the form of $\epsilon(t) = \epsilon_0 \sin(\omega t)$ - complex numbers can be used to give a relationship between the stress response and the strain displacement. The applied deformation ϵ and the stress response σ become respectively:

$$\underline{\epsilon} = \epsilon_0(\omega)e^{j\omega t} \qquad \underline{\sigma} = \sigma_0(\omega)e^{j\omega t + j\phi(\omega)}$$

where ϵ_0 is the amplitude of deformation, σ_0 is the amplitude of the stress response, $\omega = 2\pi f$ is the pulsation, f is the strain deformation frequency, t is the instantaneous time, ϕ is the phase shift between ϵ and σ. The relationship for the models presented in figure 1.6 are the following:

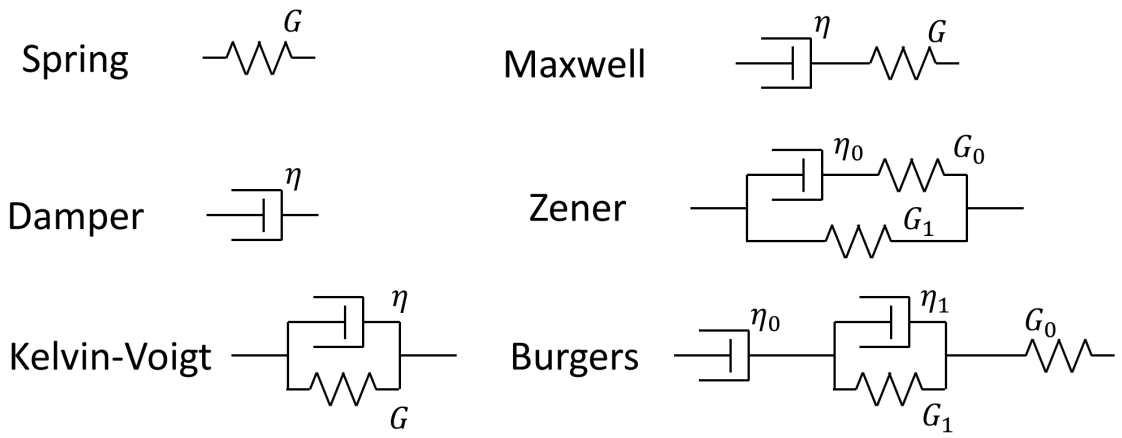

Figure 1.6.: Basic rheological models used to model viscoelastic behaviors.

- Spring:

$$\frac{\underline{\underline{\sigma}}}{\underline{\epsilon}}(\omega) = G$$

- Damper:

$$\frac{\underline{\underline{\sigma}}}{\underline{\epsilon}}(\omega) = j\omega\eta$$

- Kelvin-Voigt:

$$\frac{\underline{\underline{\sigma}}}{\underline{\epsilon}}(\omega) = G + j\omega\eta$$

- Maxwell:

$$\frac{\underline{\underline{\sigma}}}{\underline{\epsilon}}(\omega) = \frac{j\omega\eta G}{G + j\omega\eta}$$

- Zener:

$$\frac{\underline{\underline{\sigma}}}{\underline{\epsilon}}(\omega) = G_1 + \frac{j\omega\eta_0 G_0}{G_0 + j\omega\eta_0}$$

- Burgers:

$$\frac{\underline{\underline{\sigma}}}{\underline{\epsilon}}(\omega) = \frac{(jw)^2\eta_0\eta_1 G_0 + jw\eta_0 G_1}{(jw)^2\eta_0\eta_1 + (jw)[G_0\eta_0 + G_0\eta_1 + G_1\eta_1] + G_0 G_1}$$

The addition of elements in series or in parallel makes possible to model a more and more complex behavior. A generalization through the generalized Maxwell model - also called Prony series - can be achieved through the addition of a multitude of Maxwell model elements - as many as required - in parallel to a Zener model element. This usually allows to introduce different relaxation times into a rubber model.

1.2.2. Influence of fillers

During the rubber blending process, heterogeneities such as that due to filler aggregates appear. Petitet in his PhD manuscript [7] estimated the size of average aggregates with the Kendall approach [8, 9] composing the energy of cohesion of the aggregates to the energy necessary to break them:

$$D_{aggregate} = 0.064 \left(\frac{E'_{grain} d_{grain}^{5/2}}{W_{grain}(1-\nu_{grain}^2)} \right)^{\frac{2}{3}} \qquad E'_{aggregate} = 17.1 \phi_{filler}^4 \left(\frac{{E'_{grain}}^2 W_{grain}}{d_{grain}/} \right)^{\frac{1}{3}}$$

where $D_{aggregate}$ is the aggregate diameter, $E'_{aggregate}$ is the Young modulus of the aggregate, E'_{grain} is the Young modulus of a filler grain, ν_{grain} is the Poisson coefficient of the grain, W_{grain} is the surface energy of the grain, d_{grain} is the diameter of the grain and ϕ_{filler} is the volume fraction of the filler.
The numerical application gives:

$$D_{aggregate} \approx 130 \text{ nm} \qquad E'_{aggregate} \approx 500 \text{ MPa}$$

with $E'_{grain} = 33$ GPa for graphite, $\nu = 0.25$, $W \approx 0.7$ J.m^{-2}, $d = 20$ nm and $\phi_{filler} = 0.3$ (equal to the threshold of percolation).

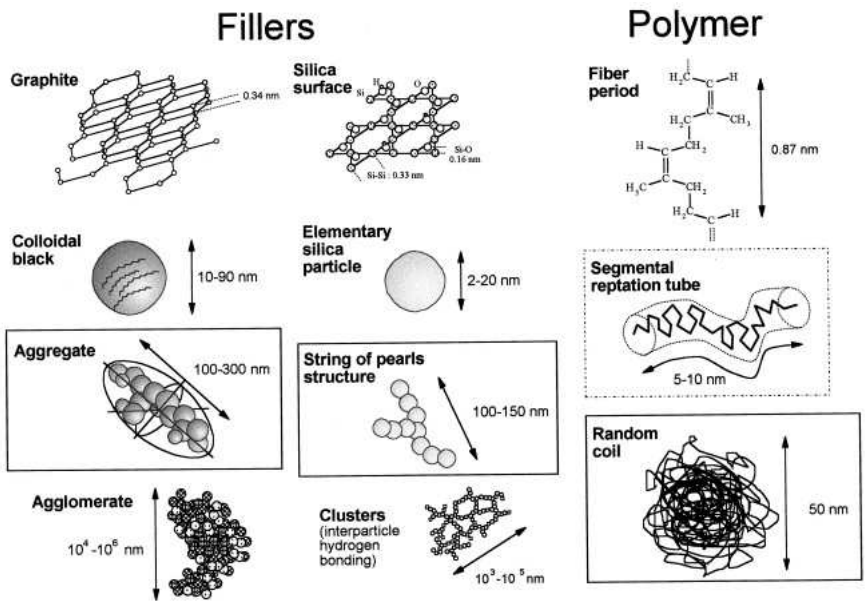

Figure 1.7.: Schematic and scale of the different structures observed within rubbers [10].

The estimate of the diameter of aggregates is consistent with the size of aggregates indicated in figure 1.7. The estimated Young modulus of aggregates is higher than the order of magnitude obtained for elastomers ($E'_{aggregate} \approx 500$ MPa $> E'_{elastomer\ matrix} \approx 3$ MPa). It highlights a real difference of mechanical properties between the two compounds. In his PhD manuscript, Petitet [7] also pointed out the presence of agglomerates of aggregates within the rubber - figure 1.8. The diameter of these agglomerates is about 70 μm, typically in the range indicated in figure 1.7.

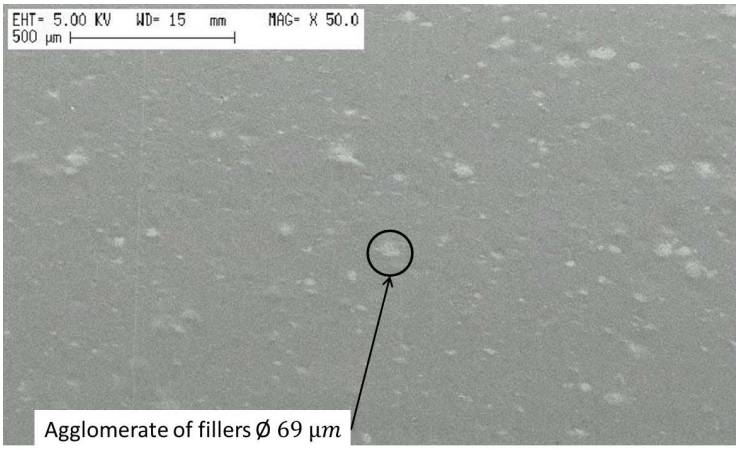

Figure 1.8.: SEM image of the cross section of a rubber reinforced with fillers measured by Petitet [7]. The light grey color area corresponds to agglomerates of filler aggregates.

The shear modulus of the mixture elastomer-fillers can be modeled via the equation of Guth-Gold which gives the expression [4, 11]:

$$G'_{mixture} = G'_{matrice}(1 + 2.5\phi_{filler} + 14.1\phi^2_{filler})$$

where $G'_{mixture}$ is the shear modulus of the mixture, $G'_{matrice}$ is the shear modulus of the matrix of elastomer and ϕ_{filler} is the volume fraction of fillers. This equation is based on the Einstein equation which gives the expression of the viscosity of a fluid containing rigid spheres [12].

Payne effect The Payne effect is a non-linearity of the shear modulus behavior linked to the inclusion of fillers within the elastomer matrix as highlighted in Figure1.9. For small deformations of the rubber, elastomers included in carbon black network do not participate to the deformation of the rubber. The resistance to the deformation of the rubber is then increased and driven by the fillers. For higher deformations - higher than

1 or 10% - the fillers network is broken and occluded elastomers are released and can participate to the deformation [13].

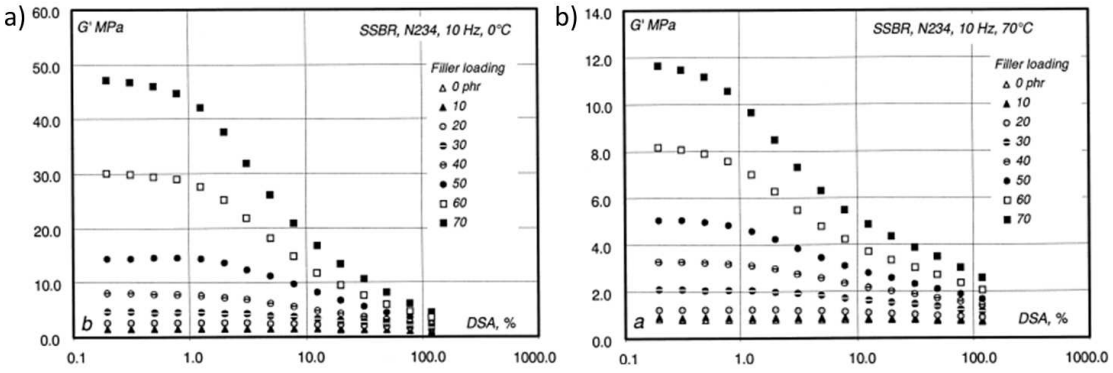

Figure 1.9.: Strain dependence of G' as a function of filler addition in parts per hundred of rubber (phr) and of the double strain amplitude at 0°C in (a) and 70°C in (b) at 10 Hz for styrene-butadienne rubber compounds with different concentrations of carbon black N234 (VULCAN®7H from Cabot) [13]. The effect of the filler concentration on the rubber rigidity modulus for low deformation is clearly visible for the two temperatures.

Carbon black hysteresis Carbon black particles of agglomerates within rubbers increase hysteresis by dissipating energy during the elongation of the material. This dissipation of energy results from the breaking of the high number of bonds between the carbon black network and the elastomer matrix - during shearing - until the filler particles are detached from the bulk material [11].

Mullins effect If consecutive stress cycles are applied to a rubber, independently of the rate of deformation, a variation in the deformation path is observed and is associated to a damage of the rubber. This remaining deformation - up to 10% - depends on the rate of stress deformation and the temperature of the rubber. The rubber can recover partially its initial state by steaming or after a long resting time. Several interpretations linked to the elastomer-filler interaction exist. The first one is the amplification of the damage due to the presence of fillers within the elastomer matrix. The second one is the existence of occlusions of rubber within aggregates of fillers that cause dissipation by relative movement or delamination of the two materials. In a context where materials are continuously stressed thousands of thousands of times, this phenomenon must be taken in account to characterize the mechanical properties of the rubber [3].

1.3. The Ice

Ice is the name given to the solid phase of water molecules H_2O. The presence of ice is a common phenomenon usually observed in northern countries where negative Celsius temperatures can be reached. This phenomenon is often considered problematic because ice can make driving or walking difficult.

1.3.1. Water freezing

The ice-water system has miscellaneous 'anomalies' that do not appear for a 'more common' material. The first one is the well-known density variation during the phase change of the ice-water system - as shown in figure 1.10a. If you put a water-filled bottle inside a freezer, after few hours you will observe a deformation or breakage of the container due to the volume expansion of the ice. Water itself is to some extent 'abnormal' because it has a maximum density at almost 4°C as shown in figure 1.10b.

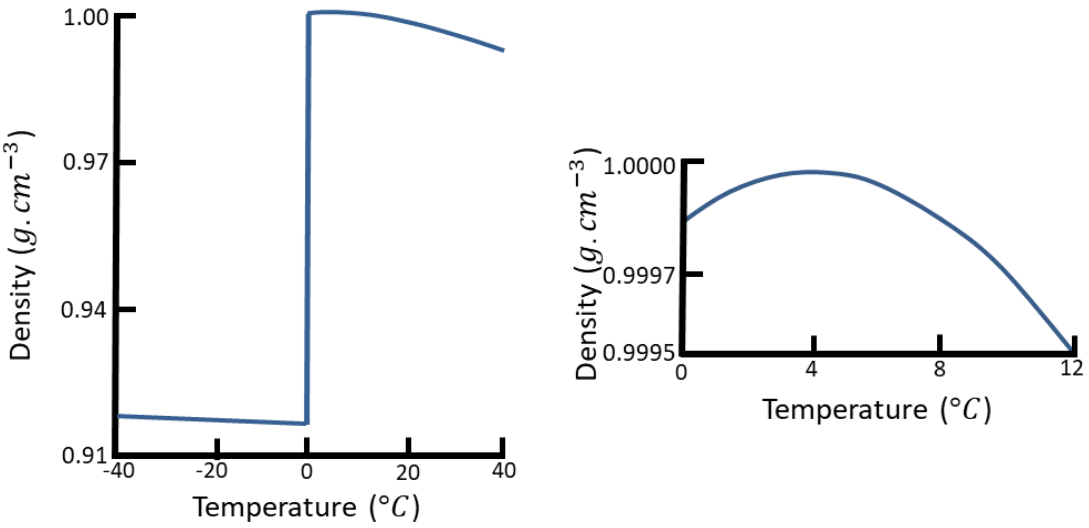

(a) Density of ice and water at atmospheric pressure.

(b) Water density at atmospheric pressure.

Figure 1.10.: Evolution of density of ice and water as a function of the temperature [14]. The influence of the phase change on the density can be observed at 0°C. Water presents a maximum of density at almost 4°C.

1.3.2. Cristallization and Nucleation

Ice is usually a polycrystalline material consisting of multiple small crystals whose 'random' orientation is caused by environmental conditions such as temperature, pressure or nucleation seeds. Crystals are defined as those parts of ice with a high degree of order and constitute the structural unit of macrometric ice.

Crystallization phenomenon results from two phenomena of nucleation, homogeneous and heterogeneous nucleation [15].

Homogeneous nucleation refers to the freezing without a seed such as in pure water case. To initiate the freezing process, a certain amount of super-cooled water (cooled below the usual freezing point of 0°C) is mandatory. As freezing requires the creation of a new solid-liquid interface in the water, it can be energetically favorable for the H_2O to have a large amount of super-cooled water. Once a more favorable energy condition is reached, the growth of ice crystals can begin.

The most common nucleation phenomenon is heterogeneous nucleation which starts from a foreign particle in liquid H_2O. The crystalline seeds formed around the particles are 'large' and have a different structure from the usual structure of ice. Then from this seed is formed a more common structure: the hexagonal ice Ih.

1.3.3. The different forms of ice

Ice has several types of solid phase. The most commonly observed ice is the Ih phase which refers to ice with an hexagonal structure. The cubic ice Ic and disordered ice Isd can be observed in high clouds. At least sixteen other phases also exist - numbered from two to seventeen with roman numerals - with various structures and temperature-pressure conditions of emergence - as shown in figure 1.11. This large number of ice phases is due to the possible arrangements for the crystalline structure when the H_2O molecules are crushed under high pressure [16]. Many of those phases are metastable outside of the pressure-temperature range where they are formed. This metastability is explained by the difficulty of rearrangement of the structure of the H_2O molecules due to the lack of thermal energy at low temperatures [17].

According to the phase diagram in figure 1.11, the most common ice phase on Earth is the Ih phase. The temperature on Earth is rarely lower than -100°C - that is the frontier of temperature of the Ih phase existence - the lowest temperature ever measured on Earth was -89.2°C in 1983 at the base of Vostok in Antarctica. The Ih phase is also stable up to 30 MPa which is difficult to reach at the 'surface' of the Earth outside of a laboratory. One example of extreme pressure condition for the 'natural' ice is the glacier Lambert in Antarctica - the largest glacier on Earth - that have a thickness of 2.5 km. A simple

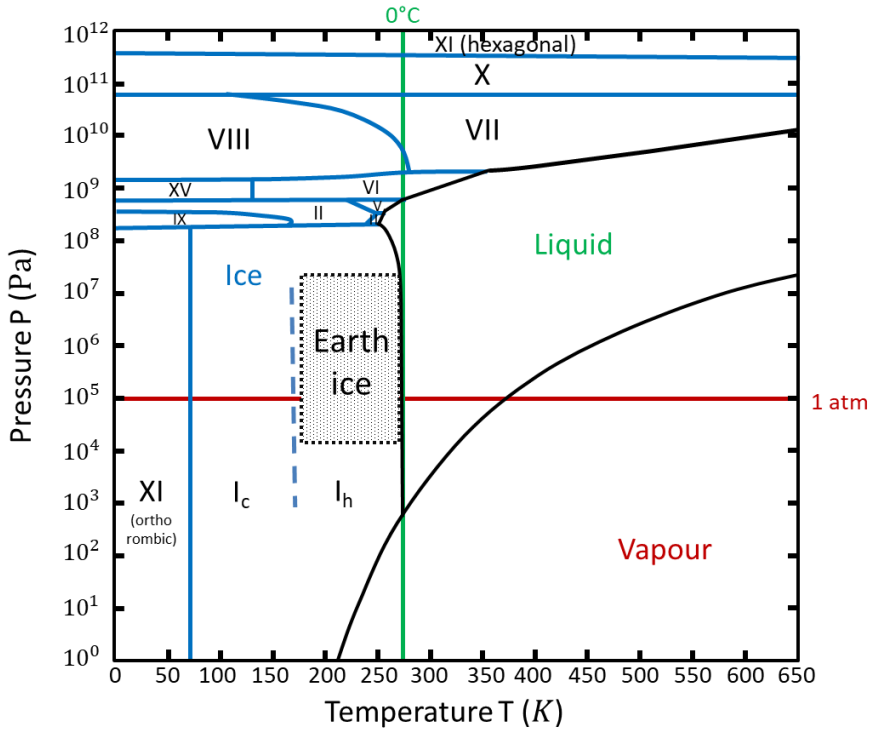

Figure 1.11.: Phase diagram of H_2O [16]. The vapour, liquid and solid phases are indicated as a function of pressure and temperature. The different solid phases are indicated with a roman numeral. The state of the ice on Earth is limited by the temperature and pressure attainable. The lowest temperature reached was -89.2°C at Vostok and the highest being the melting point at 0°C. The highest pressure is probably 24.6 MPa at the foot of the Lambert glacier - the thickest glacier in the world - and the lowest is 30 kPa at the summit of Mount Everest - the highest mountain in the world. Therefore in Earth atmospheric conditions, Ih ice phase is the most prominent.

estimation of the pressure at the bottom of the glacier gives the value:

$$P = \rho_{ice} h_{glacier} g + P_{atm} = 22.9 \text{ MPa}$$

where $h_{glacier}$ is the glacier thickness, g is the gravitational acceleration, $\rho_{ice} = 912 \text{ kg.m}^{-3}$ is the density of the glacier and $P_{atm} \approx 0.1$ MPa is the atmospheric pressure.

1.3.4. Structure of ice Ih

The structure of ice is composed of assembly of water molecules H_2O. Each molecule of H_2O is surrounded by four others in a tetrahedric arrangement via covalent hydrogen bonds. This arrangement presented in figure 1.12 - so called 'Ice rule' or Bernal-Fowler rule [18] - minimizes its energy when:

- Each of the H-nuclei of the molecule is facing the O-nuclei of two other molecules;
- And the O-nuclei faces a H-nuclei from two other molecules.

This non compact structure is responsible for the decrease of the H_2O density during its solidification.

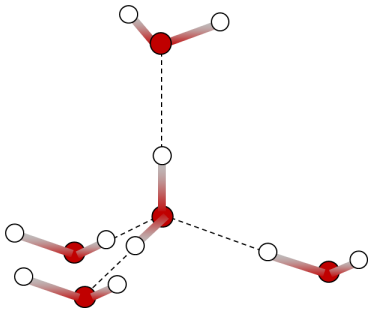

Figure 1.12.: Elementary tetrahedric unit of an ice crystal following the 'Ice rule' or the so-called Bernal-Fowler rule [16].

Crystals of ice are composed of layers with a basic mesh composed of three-dimensional hexagons. The faces of these three dimensional hexagons are deformed hexagons - referred to as 'chair-form' hexamers, 'boat-form' hexamers and 'envelope-form' - illustrated in figure 1.13. The figure 1.13 presents idealy ordered hydrogen bonds.

In reality, there is movement of H-nuclei in a random way which could be associated to tunneling effect [19]. Even with this movement, H_2O molecules continue to obey the 'Ice rule' which limits the arrangement of H_2O molecules to six possible orientations. Failure to respect this 'ice rule' will result in a defect, and therefore a weakness within the structure of the ice [20].

In the global structure of the ice - as ideally shown in figure 1.14 - the H_2O molecules have a staggered arrangement in the 'chair-form' hexamers plane and these layers can be stacked along the C-axis. According to these constraints, there is no long-range order in orientations of the molecules [17].

1.3.5. Quasi-liquid layer

One of the most common admitted properties of the ice is to be slippery whereas other solid materials present usually a high friction coefficient. This apparent contradiction

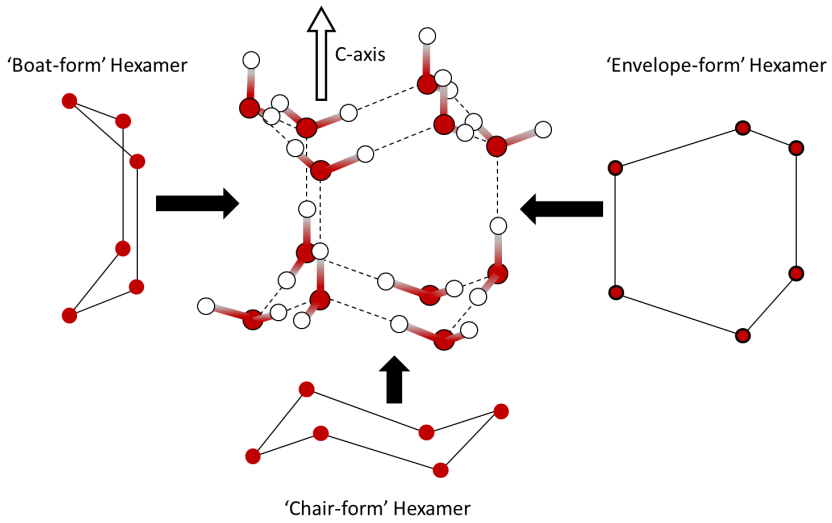

Figure 1.13.: Ordered hexagonal structure of ice respecting the 'ice rule'. The 'boat-form', the 'chair-form' and the 'envelope-form' are highlighted on the sides of the structure. The C-axis - which is normal to the average plan of the 'chair-form' hexamer - is given by the white arrow direction [16].

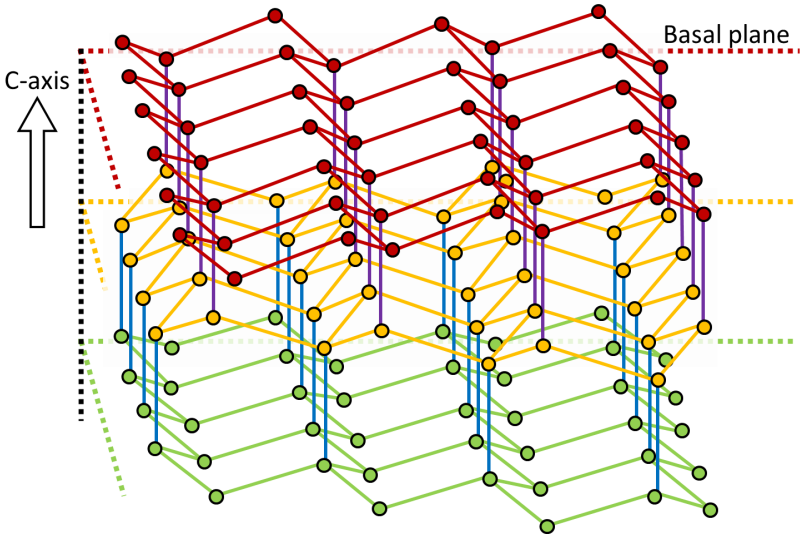

Figure 1.14.: Long range ideally ordered monocrystal of ice. The staggered structure is highlighted in the plan of the 'chair-form' hexamers. Ice hexameric cells are stagered along the C-axis [16].

is caused by a bias due to the temperature of observation which is often 'almost' the melting point of the ice. This behavior of liquid-like films on the surface of solids at temperatures below the melting point is so-called 'liquid-like surface layer' or 'quasi-liquid layer' [15].
Several mechanisms may cause the existence of this quasi-liquid layer [21, 22]:

- The existence of a phenomenon of incomplete integration, at the surface, of H_2O molecule into the crystalline structure of ice. So the H_2O molecules are disordered and have a liquid-like behavior;
- A thermodynamic consideration of the ice-air interface: this interface is more expensive in energy than a ice-liquid-air interface which minimizes the free energy of the surface;
- The persistence of a melted layer over a finite temperature range after freezing below the normal melting point.

In the case of a 'quasi-liquid layer' with a vapor-liquid-solid interface, a thermodynamic model of the quasi-liquid layer considering the minimization of the total free energy can be expressed [21]. It considers the change in free energy of Gibbs per unit of area because of the formation of a liquid layer of thickness d_l:

$$\Delta G_m = \rho_l \Delta\mu_l d_l + \Delta_{qll}\gamma f(d_l)$$

where:

- $\Delta\mu_l$ is the chemical potential of the bulk liquid

$$\Delta\mu_l = h_{ice}\frac{T_m - T}{T_m}$$

- $\Delta\gamma_{qll}$ is a difference in surface energy between two interface types: a solid-liquid-vapor interfaces ($\gamma_{lv} + \gamma_{sl}$) and a solid-vapor interface (γ_{sv})

$$\Delta\gamma_{qll} = \gamma_{lv} + \gamma_{sl} - \gamma_{sv}$$

- $f(d)$ is a function of d that varies between 0 and 1. It can be derived empirically from van der Waals interactions

$$f(d_l) = \frac{d_l^2}{d_l^2 + d_0^2}$$

where h_{ice} is the latent heat, T_m is the melting temperature, d_0 is a 'typical' molecular distance, ρ_l is the density of the liquid phase and T is the temperature of the ice.
Minimization of the Gibbs free energy gives the result:

$$d_l = \left(\frac{-2d_0^2\Delta\gamma_{qll}}{\rho_l h_{ice}}\frac{T_m}{T_m - T}\right)^{1/3}$$

This model is currently disputed due to evidence of $\Delta\gamma < 0$ which implies that no liquid layer exists with this model. An explanation is that the interface is not truly liquid and thus that this approach is not valid.

This failure highlights the difficulty of defining a meaning for the quasi-liquid layer which also depends of the studied properties [15]:

- X-ray diffraction shows effects of the surface layer down to -10°C;
- Proton scattering - which probes the open structure of crystals - shows effect down to -60°C;
- Optical ellipsometry shows difference of refraction index down to -5°C;
- Nuclear Magnetic Resonance - which is sensitive to the location and the motion of protons on a single layer - shows measurable effect down to -100°C.

It is therefore important to remain careful and to follow the principle of parsimony when talking about a 'quasi-liquid' layer effect on ice surfaces.

1.3.6. Ice in nature

In nature, ice can present many forms such as:

- Snow, resulting from the H_2O in the atmosphere. This snow then falls to the ground and it consolidates with the gravity in the form of ice as time goes by;
- Ice at the surface of lakes, rivers and seas;
- Permafrost in cold regions where the H_2O in ground becomes frozen;
- Antediluvian ice in solar system where many planets, moons, comets and other astronomical objects are formed partially or entirely of antediluvian ice. The ice of these celestial bodies can be subject to extreme phenomena - not present on Earth - such as cryovolcanism or very high pressure melting.

1.3.6.a . Ice growing in lakes and rivers

'Natural' ice on lake and rivers is made of three layers [17]. First, ice forms at the surface for two reasons related to the properties of density of the ice and the water. The maximum density of the water occurs at almost 4°C - as shown in figure 1.10b. Thus, during the global cooling of a lake, the water goes down with the increasing density. Once most of the water is at a temperature of 4°C, the water at a lower temperature remains at the surface due to the decrease in density. This layer of 'top' water is therefore the first to become ice. During this solidification step, the density of ice decreases considerably - as shown in figure 1.10b - and the ice stays at the surface. This primary layer grows until it covers the entire surface. A secondary layer then grows downward from the previous one along the direction of the existent temperature gradient. A 'superimposed layer' may appear on the top of the primary layer by flooding from any sources. Several types of primary and secondary ice can grow in various ways according to the environmental conditions [23]:

- In the case of still water, platelets nucleate and float at the surface with the C-axis vertical - a and b axis are randomly oriented in the platelet plane. The secondary ice naturally forms from this primary layer with an approximately vertical C-axis;
- In the case of a large gradient of temperature at the surface, many crystals are nucleated. Platelets and needles form. The secondary ice grows from the primary ice with the C-axis in the horizontal plane;
- In the case of an agitated surface - by wind or flow - platelets and needles are formed and remain in suspension. This ice is named 'frazil ice' and the grain orientations are random. The secondary ice grows as in the case of a large temperature gradient;
- In the case of nucleation from snow fall, the grains are small and have a random orientation. The secondary ice grows in the same way as the case of a large temperature gradient.

Water in natural conditions - in lakes or rivers - differs from the distilled water which can be used in laboratories by the presence of multiple 'impurities' that can be dissolved (gases, solid particles, salts *etc*). These impurities can affect the optical properties of the ice as well as the melting point or the surface state. The mechanical properties are maintained as they are primarily determined by the polycrystalline structure.

1.3.7. Properties

Ice has several temperature-dependent properties such as density, specific heat, thermal conductivity and enthalpy. From handbooks it is possible to make a linear approximation of these properties - as shown in figure 1.15 - as a function of the temperature difference $T - T_m$ in K [24]:

- Melting temperature

$$T_m = 273.15 \text{ K } at \text{ } 101325 \text{ Pa } (1 \text{ atmosphere})$$

- The density in kg.m^{-3}

$$\rho_{ice} = 917.00 - 0.13\,(T - T_m)$$

- The specific heat in kJ.kg^{-1}.K^{-1}

$$c_{ice} = 2.120 + 0.008\,(T - T_m)$$

- The thermal conductivity in W.m^{-1}.K^{-1}

$$k_{ice} = 2.210 - 0.012\,(T - T_m)$$

- The ice enthalpy of fusion in kJ.kg^{-1}

$$h_{ice} = -332.40 + c_{ice}(T)\,(T - T_m)$$

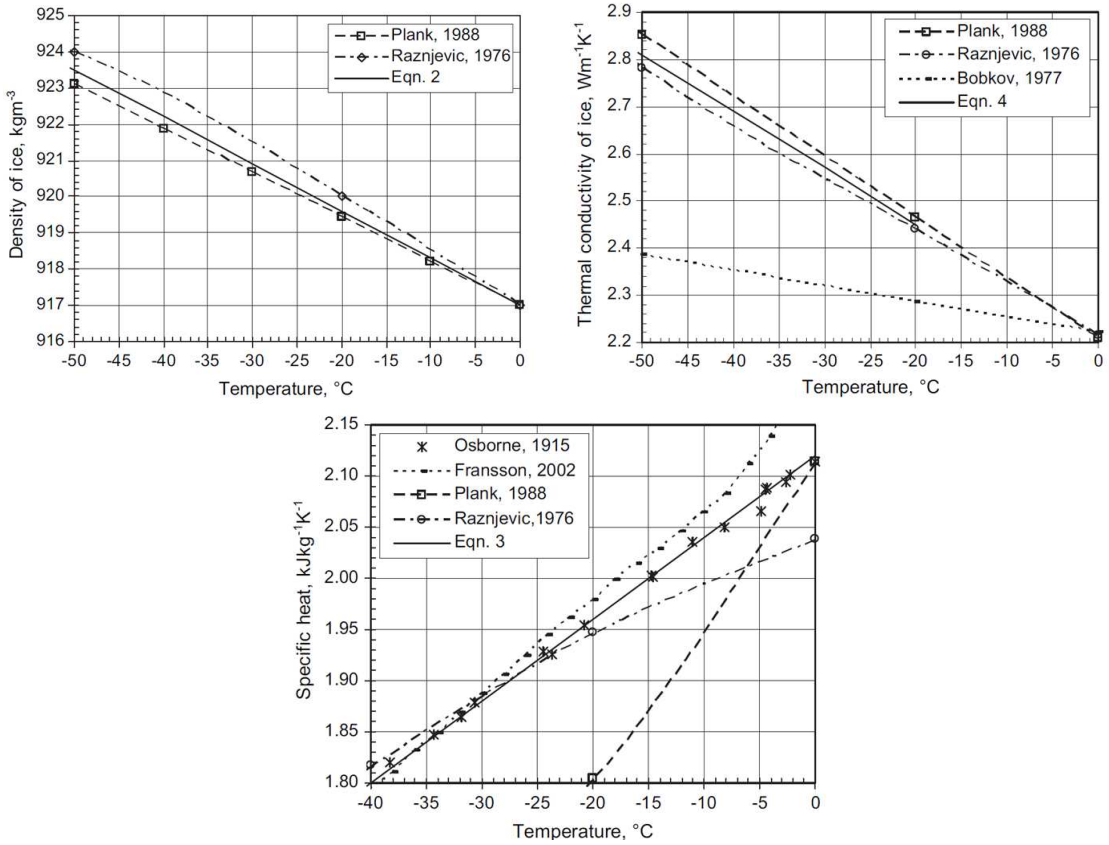

Figure 1.15.: Evolution of density, thermal conductivity and specific heat of ice for a temperature range from -50 to 0°C. Linear approximation is performed on data from multiple handbooks [24].

1.3.7.a . Mechanical properties

Ice - like other solids - behaves differently depending on the magnitude of the stress applied and the time scale. Over short time scales, the ice behaves like a solid and is elastic. On long time scales, ice behaves more like a fluid, it can flow and creep. A good example of this phenomenon is the movement of glaciers in mountains. For high stress application, ice presents brittle failure behavior.

Deformation mechanisms can be significantly different between a polycrystalline or mono-crystal structure. Polycrystalline structure exhibits anisotropy of mechanical

properties due to the preferential growth of ice during formation - such as lake and river ice. Additional anisotropy is induced by ice fracture. These cracks appear preferentially parallel to the direction of compression and perpendicular to the direction of traction [15]. Mechanical properties of polycrystaline ice - measured by Gammon *et al* [25] - are listed:

- Young modulus at -5°C
$$E_{ice} = 9.5 \text{ GPa}$$
- Shear modulus at -5°C
$$G_{ice} = 3.5 \text{ GPa}$$
- Poisson coefficient at -5°C
$$\nu_{ice} \approx 1/3$$

1.3.7.b . Optic

Ice exhibits a variation of optical properties as a function of the wavelength of the light. Ice absorbs infrared and ultraviolet but is almost transparent for radio-microwave and visible light. In the case of visible light, a property of birefringence [17] also appears.

Visible light For visible light and near ultraviolet light, ice is a transparent material with birefringence properties. This property of birefringence is a consequence of the orientation of the hexagonal structure of the ice. If light travels along the C-axis, therefore the electric field direction E is perpendicular to the C-axis and all polarizations are equivalent. Such perpendicular electric fields E are so called 'ordinary'. Electric field E parallel to the C-axis are so called 'extraordinary' and have a larger refractive index. The refractive index of ice can be given as a function of the wavelength of the light - as shown in Table.1.1.

Infrared In the near infrared region, the effect of the basic lattice and the molecular vibrational modes of H_2O ice causes light absorption. This property is often used to detect the presence of ice in an environment.

In the microwave region, H_2O molecule motions occur in phase with the electric field E, this phenomenon is used in the heating process of the microwave oven.

1.4. Contact Mechanics

When two elastic solids are brought into contact, the contact between them is not limited to a merely mathematical point, but to a finite part of their surfaces. These two

Wavelength (nm)	n^O	n^E
405	1.3185	1.3200
436	1.3161	1.3176
492	1.3128	1.3143
546	1.3105	1.3119
589	1.3091	1.3105
624	1.3082	1.3096
691	1.3067	1.3081

Table 1.1.: Indexes of ordinary and extraordinary refraction n^O and n^E measured by Ehringhaus (1917) [17] at -3.6°C with an accuracy of ± 0.0001. A decrease in the refraction index is observed with the increase of the wavelength in the infrared range.

elastic solids in contact create a new interface whose area depends, among others, on the mechanical properties of the solids. Theories of contact mechanics were developed to quantify the stress distribution, the contact area and the adhesion.

1.4.1. Theory of non adhesive contact

In 1880, Hertz studied Newton's optical interference fringes in the interval between two glass lenses. He was concerned about the possible influence of elastic deformation of the lens surfaces due to the contact pressure between them. He developed a contact theory for elastic solids [26, 27] - during his Christmas vacation at the age of twenty-three - a theory that has never been contradicted until now [28].

The theory of Hertz is based on several hypotheses:

- Surfaces are smooth, continuous and non-conforming;
- The strains are small;
- Each solid can be considered as an elastic half-space;
- Surfaces are frictionless and non-adhesive.

For the case of circular contact such as for sphere-sphere, sphere-plan or a cylinder-cylinder solids, the pressure distribution is as follows:

$$p = p_0 \left(1 - \left(\frac{r}{a}\right)^2\right)^{1/2}$$

where p is the contact pressure at the radial position r, a is the radius of the circular contact and p_0 is the maximum of pressure within the contact at $r = 0$.

The main results of Hertz's theory are:

$$a = \left(\frac{3F_z R}{4E^*}\right)^{1/3} \qquad \delta_{def} = \frac{a^2}{R} = \left(\frac{9F_z^2}{16RE^{*2}}\right)^{1/3} \qquad p_0 = \frac{3F_z}{2\pi a^2} = \left(\frac{6F_z E^{*2}}{\pi^3 R^2}\right)^{1/3}$$

with:

$$R = \frac{R_1 R_2}{R_1 + R_2} \qquad \text{and} \qquad \frac{1}{E^*} = \frac{1-\nu_1^2}{E_1} + \frac{1-\nu_2^2}{E_2}$$

where a is the radius of the contact, δ_{def} is the total mutual deformation depth of the two solids, p_0 is the maximum pressure at $r = 0$, F_z is the applied load, R is the equivalent radius of the two solids and E^* is the equivalent elasticity modulus of the two solids.

1.4.2. Theory of adhesive contact

Hertz's theory works perfectly well for elastic solids with a negligible adhesion force between them such as in the case of a steel ball in contact with a glass track. But for other types of material such as rubber, the effect of the force of attraction is not negligible and must be taken in account. Several theories - which are variations of the Hertz contact theory - were developed such as the JKR theory or the DMT theory - as shown in figure 1.16.

1.4.2.a . Bradley

In 1932, Bradley [30] developed an adhesion model for two rigid and perfectly smooth solids. He considers that each molecule of each surface is attracted to each other via van der Waals forces.

The resulting attractive force is described as follows:

$$F_0 = 2\pi w R$$

where w is the adhesion work of the two materials and R is the equivalent radius of the two solids.

1.4.2.b . Johnson, Kendall and Roberts (JKR)

In 1971, Johnson, Kendall and Roberts [31] presented an adhesive contact model for materials with large elasticity and adhesion. This adhesion is characterized by the presence of a 'neck' at the edge of the contact.

In addition to the hypothesis of the Hertz theory, it is considered that the adhesion energy is strong, the radius of contact is large and the materials are soft. Two types of mechanisms are considered [32]:

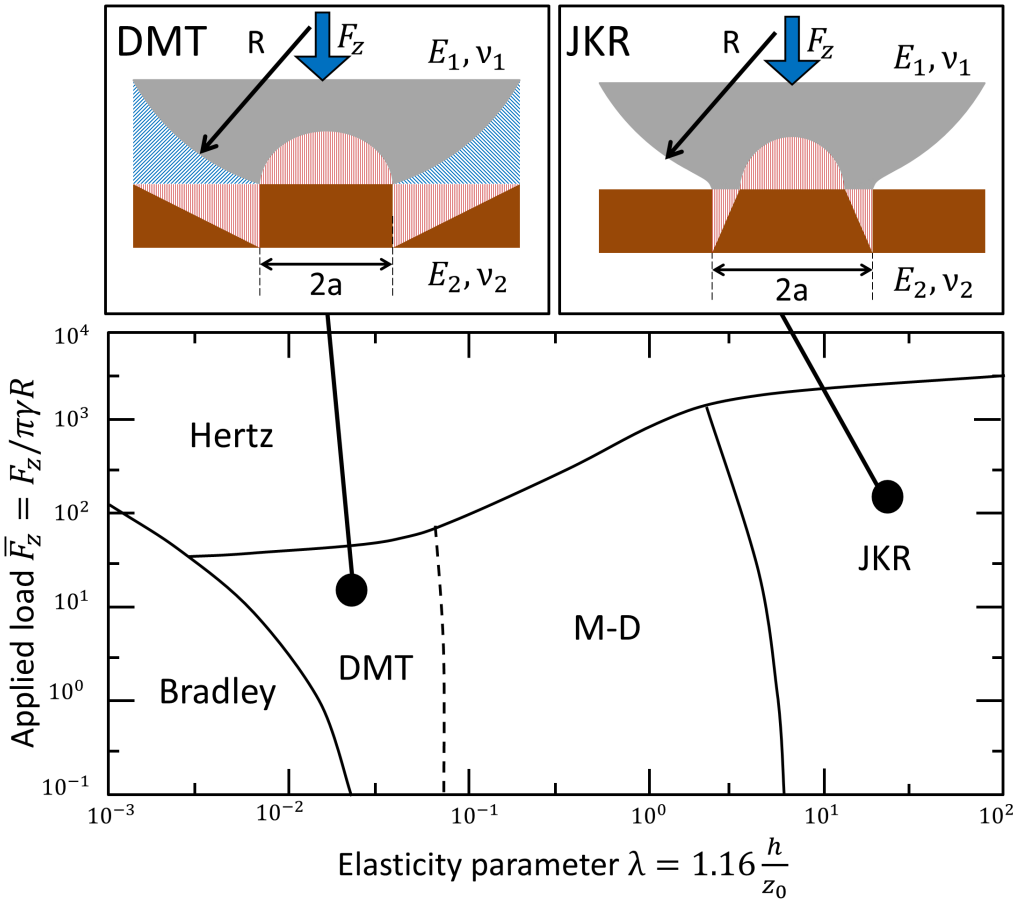

Figure 1.16.: Map of the validity domains of the different theories of contact mechanics given by Johnson and Greenwood [29] according to the elasticity parameter $\lambda_{elasticity}$ and the dimensionless load $\overline{F}_z$. The stress distribution within the contact is represented for the DMT theory and the JKR theory. The elasticity parameter λ is given as a function of z_0, the equilibrium separation between two atoms, and h_{neck}, the height of the 'neck' around the contact zone.

- A compressive stress on the form of a Hertzian pressure:

$$p = p_0 \left(1 - (r/a)^2\right)^{1/2}$$

- An homogeneous normal displacement caused by adhesion and pressure becomes:

$$p = p_0 \left(1 - (r/a)^2\right)^{-1/2}$$

Outside the contact, the intensity of the adhesion force is null. Once the two solids are in contact, a mechanical equilibrium is established between the compressive stress due to the elastic deformation of the solids and the adhesion force occurring within the contact area. Thus, this model gives an important compression stress at the center of the contact and a strong traction stress near the edge of the contact - as shown in figure 1.16.

The main results of the JKR theory are:

$$a^3 = A_0 \left(F_z + 2F_0 + 2\sqrt{F_0(F_z + F_0)} \right) \tag{1.3}$$

$$p_m = \frac{1}{\pi} \sqrt[3]{\frac{16}{9} \left(\frac{E^*}{R} \right)^2 \frac{(F_z + F_0)^3}{\left(F_z + 2F_0 + 2\sqrt{F_0(F_z + F_0)} \right)^2}}$$

with:

$$F_0 = \frac{3}{2}\pi w R \qquad \text{and} \qquad A_0 = \frac{3}{4}\frac{R}{E^*}$$

where a is the radius of the contact, δ_{def} is the mutual deformation of the two solids, p_m is the average contact pressure, F_0 is the adhesion force, A_0 a material constant, w is the adhesion work of the two materials, F_z is the applied load, R is the equivalent radius of the two solids and E^* is the equivalent elasticity modulus of the two solids.

1.4.2.c . Derjaguin, Muller and Toporov (DMT)

An alternative model was developed by Derjaguin, Muller and Toporov [33, 34]. They considered a variation of the Hertz contact theory in which there is an effect of the attraction force outside of the contact but a negligible one within the contact - as illustrated in figure 1.16. In addition to the hypotheses of the Hertz theory, it is considered that the adhesion energy is weak, radii are small and the materials are rigid.

The main results of the DMT theory are:

$$a^3 = A_0 \left(F_z + F_0 \right)$$

$$p_m = \frac{1}{\pi} \sqrt[3]{\frac{16}{9} \left(\frac{E^*}{R} \right)^2 (F_z + F_0)}$$

with:

$$F_0 = 2\pi\gamma R \qquad \text{and} \qquad A_0 = \frac{3}{4}\frac{R}{E^*}$$

where a is the radius of the contact, δ_{def} is the mutual deformation of the two solids, p_m is the average contact pressure within the contact, F_0 is the adhesion force, A_0 is a

material constant, w is the adhesion work of the two materials, F_z is the applied load, R is the equivalent radius of the two solids and E^* is the equivalent elasticity modulus of the two solids.

1.4.2.d . Tabor parameter and Maugis-Dugdale: transition between JKR and DMT

In 1976, Tabor [35] showed that the apparent contradiction between the JKR and DMT theories was solved by considering that they are two 'extreme' cases of the same theory of elasticity-adhesion. He presented a dimensionless parameter related to z_0, the equilibrium separation between two atoms, and h, the height of the 'neck' around the contact zone:

$$\frac{h}{z_o} \approx \left(\frac{R\gamma^2}{E^{*2} z_0^3} \right)$$

where γ is the adhesion work of the two materials, R is the equivalent radius of the two solids and E^* is the equivalent elasticity modulus of the two solids.

Therefore, according to the Tabor parameter, different domains of validity of contact mechanics theories can be highlighted - as shown in figure 1.16:

- JKR theory applies for large radius and soft materials when $\frac{h}{z_o} \to \infty$;
- DMT theory applies for small radius and rigid materials when $\frac{h}{z_o} \to 0$;
- Bradley model applies for rigid materials when $\frac{h}{z_o} \approx 0$.

In 1991, Maugis proposed [36] a new model based on the idea of Tabor's parameter to complete the transition between JKR and DMT. In this model, surface traction is divided into two contributions:

- A compressive stress on the form of Hertzian pressure
- A Dugdale distribution of adhesive stress described as:

$$p = \begin{cases} -\frac{\sigma_0}{\pi} \cos^{-1}\left(\frac{2a^2}{c_{adh}^2 - r^2} - 1 \right) & \text{for} \quad r \leq a \\ -\sigma_0 & \text{for} \quad a \leq r \leq c_{adh} \end{cases}$$

where σ_0 is the adhesive stress magnitude, a is the contact radius and c_{adh} is the radius of the influence of the adhesive stress σ_0.

In addition, he also proposed a parameter of elasticity $\lambda_{elasticity}$ equivalent to the parameter of Tabor:

$$\lambda_{elasticity} = \sigma_0 \left(\frac{9R}{2\pi\gamma E^{*2}} \right)^{1/3} \approx 1.16 \frac{h}{z_o}$$

where γ is the adhesion work of the two materials, R is the equivalent radius of the two

solids and E^* is the equivalent elasticity modulus of the two solids.

A result of this theory is given via the generalized equations of Carpick, Ogletree and Salmeron (COS) [37] which estimates the contact area with an error of 1%:

$$a = a_0 \left(\frac{\alpha_{elasticity} + \sqrt{1 + F_z/F_0}}{1 + \alpha_{elasticity}} \right)^{2/3}$$

with:

$$\lambda_{elasticity} = -0.924 \ln \left(1 - 1.02 \alpha_{elasticity}\right)$$

where F_z is the applied load, F_0 is the adhesive force, a_0 is the contact area when $F_z = 0$ and $\alpha_{elasticity}$ is a parameter linked to Maugis parameter $\lambda_{elasticity}$.

1.5. Frictional properties of rubber

The earliest records of tribological experiments are associated to Leonardo da Vinci in the 15th century and were rediscovered by Guillaume Amontons in the 17th century. Their work has highlighted - in the case of a dry contact between two solids - a force threshold to be exceeded in order to move relatively the two solids.

The tribology of rubber has been extensively studied since the second half of the 20th century because of the massive use of elastomeric products for the personal automotive such as tires. Rubber friction differs from the metallic friction mainly in the contact mechanism with the surfaces.

The rubber friction resulting from tangential force F_y for the dry case is traditionally given as the contribution of three different mechanisms [38] - plus an additionnal contribution in the case of lubricated contact [39, 40]:

$$F_y = F_a + F_h + F_c + F_v$$

where:

- F_a is the adhesion loss force due to the combined adhesion of the rubber and the track;
- F_h is the loss force caused by the hysteresis of the bulk rubber viscoelastic deformation;
- F_c is the force of cohesion loss caused by rubber wear;
- F_v is the viscous loss force due to the lubricant within the contact.

The adhesion loss force F_a and the loss force caused by hysteresis F_h are illustrated in figure 1.17.

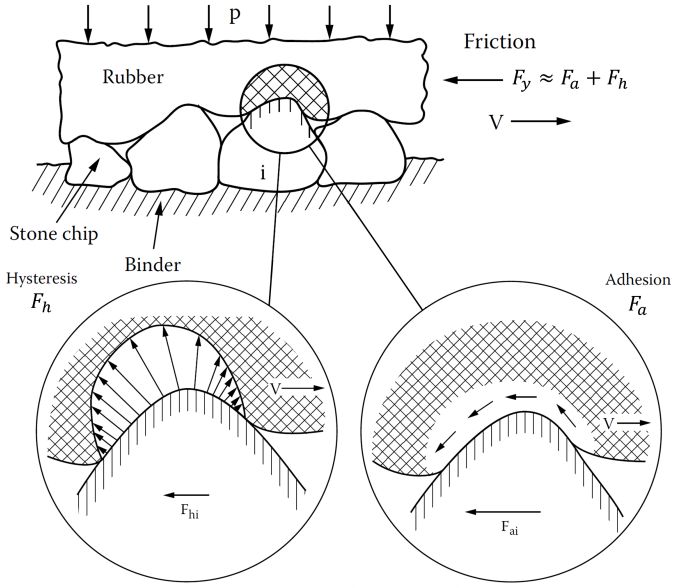

Figure 1.17.: Illustration of the adhesion force and hysteresis force for a rubber block sliding on a rough track given by Kummer [38] and Smith [41]. The van der Waals adhesion force develops a resultant force on the entire contact between the rubber and the track. The bulk deformation hysteresis causes a resultant force due the viscoelastic deformation of the surface by the asperities of the counter face - i.e here the stone chips.

It is important to remain cautious [40] about the definitions of F_a and F_h. The interfacial adhesion F_a may arise from an hysteretic contribution of microscopically rough surface according to the works of Yandell [42] and Golden [43]. There are also potential interactions between these two contributions according to the adhesion models reviewed by Schallamach [44].

The coefficient of friction μ is commonly used to give a non-dimension value of F_y under a constant normal force F_z. It is defined as the ratio between the resultant tangential force of friction F_y and the applied normal force F_z:

$$\mu = \frac{F_y}{F_z}$$

1.5.1. Hysteresis friction

The hysteresis friction is related to the local deformation of the rubber by the counter face and to the viscoelastic properties of the rubber. Several parameters influence the hysteresis friction which results in increasing the amount of stressed rubber:

- The number of asperities;
- The geometry of the asperities;
- The viscoelasticity of the rubber.

The number of asperities and the viscoelasticty of the rubber drive the hysteresis friction within certain limits. For example, a large number of large asperities can lead to high stress if the elasticity allows sufficient deformation of the rubber volume. However, if the asperities are too close [45] or the rubber too rigid, this can lead to a decrease in hysteresis friction.

This mechanism is clearly identified for bulk rubber [46]. It is also clearly suggested for rubber surfaces on smaller scales such as:

- Micro or nano stress arising from the topography of the track [41, 42, 43] (even the smoothest track presents asperities);
- Phenomenon of interlocking between the asperities of the rubber and the counter face [45, 47];
- Adhesion mechanisms [38, 41, 44, 48].

In 1963, Grosch [48] performed experiments with various sliding rubbers on smooth glass surfaces and rough silicon carbide paper surfaces for several temperatures and sliding velocities, that highlight this phenomenon of hysteresis due to asperities as well as the adhesion mechanism. He found that the friction curves of rubber sliding on a hard material are a part of a friction master-curve - just like other rubber properties such as shear modulus - that can be built thanks to the WLF theory. It implies that the friction arises from the viscoelastic properties of the rubber - as shown in figure 1.18.

The friction tests performed with a rubber having a 'single' relaxation time in figure 1.18 presents a master curve with a symmetrical friction peak - i.e the friction level has an axial symmetry compared to the velocity of the maximum peak - when sliding on a smooth surface. When the interface was dusted, the rubber-glass system had a constant friction. It suggests that these friction peaks were caused by the adhesion between the rubber and the glass surface.

The friction peak was quantitatively related to the frequency of the maximum of the dissipative modulus E'', as shown in the figure 1.19, with the following equation:

$$\lambda_{typical} = \frac{V_{\mu_{max}}}{f_{E''_{max}}} = V_{\mu_{max}} \tau_{max}$$

where $\lambda_{typical}$ is the periodical average distance of stress, $V_{\mu_{max}}$ is the velocity at which

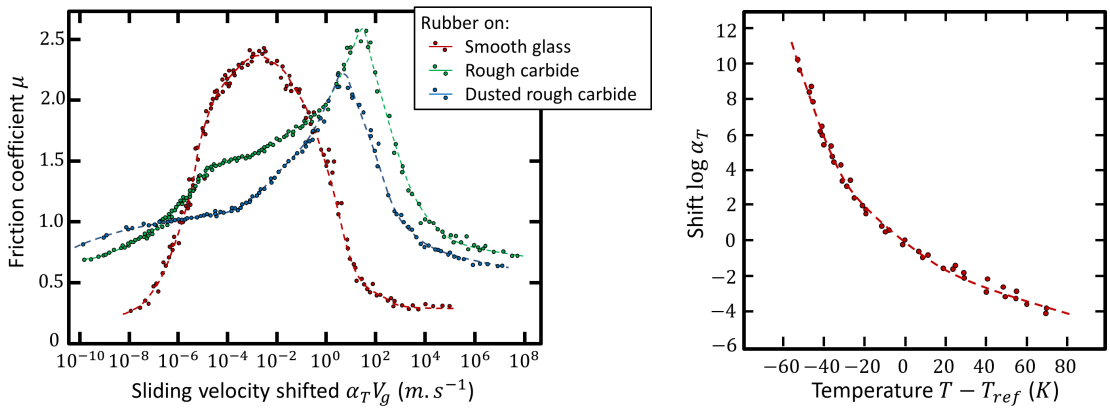

(a) In red, the friction curve of gum sliding on a smooth glass. In green, the friction curve of a rubber sliding on a clean and rough silicon carbide abrasive. In blue, the friction curve of a rubber sliding on a rough silicon carbide abrasive dusted with magnesium.

(b) Frequency shift as a function of temperature ($T_{ref} = 32°$C). The solid line represents the WLF equation.

Figure 1.18.: Composite friction curves of an acrylonitrile-butadiene rubber at -20°C (a) measured by Grosch [48]. The friction is measured as a function of the sliding velocity for several temperatures and shifted to a reference temperature in order to build a master friction curve. Differences appear between the different master-curves as a function of the surface state of the counter face. The figure (a) highlights that there are two different stress spectra of roughness of the counter face: one for the adhesion mechanism, the other one for the hysteresis mechanism. The figure (b) presents the evolution of the shifting coefficient $\log \alpha_T$ as a function of the temperature $T - T_{ref}$.

the maximum of friction is reached, $f_{E''_{max}}$ is the frequency of the maximum of the dissipative modulus and τ_{max} is the relaxation time for which the relaxation spectrum of the rubber is maximum.

Friction tests carried out with different rubbers on rough surface always have an asymmetric friction peak and generally present a higher friction peak. In the case of the clean rough track - as shown in figure 1.18a - friction curve has a secondary peak at slower sliding velocity. This maximum of the secondary peak on the rough surface is close to the frequency of the maximum of friction for the smooth surface - as shown in figure 1.18a. The secondary peak disappears when the rough track is dusted with magnesium powder (see the figure 1.18a). The distance is estimated at $\lambda_{typical} = 0.15$ mm for the peak of the figure 1.18a. This value closely agrees with the spacing of abrasive particles of the counter surface. The friction peak in the case of the dusted rough tracks,

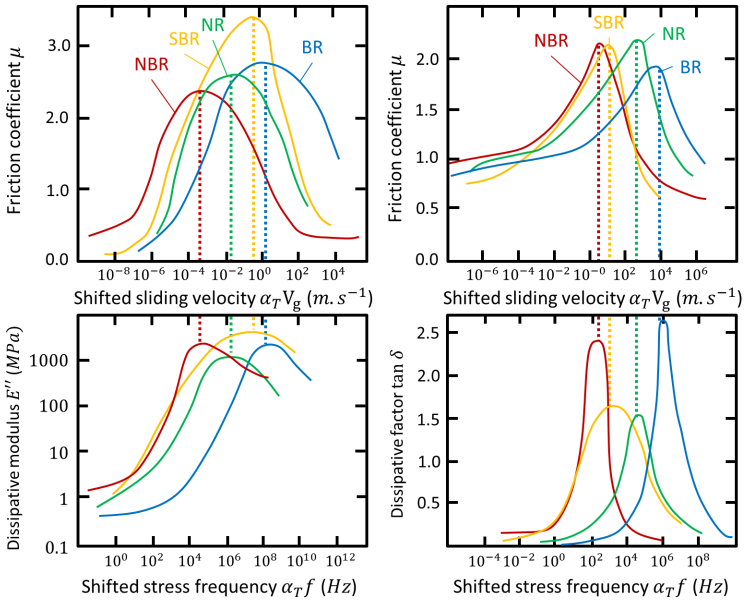

Figure 1.19.: Friction curves of different rubbers sliding on a smooth surface - on the left - and on a rough track - on the right - measured by Grosch [49]. The correspondence with the maximum of the dissipative modulus E'' - on the left - and the dissipative factor $\tan\delta$ - on the right - is evidenced by correlation of the maximum peaks.

is related to the maximum of the dissipative factor - as shown in the figure 1.19.

As the rubber used had only one relaxation peak, this experiment clearly shows two mechanisms of viscoelastic friction: adhesion and deformation losses (a.k.a hysteresis).

According to Grosch [49], friction on rough surfaces cannot be deduced solely from hysteretic losses due to the presence of small adhesion. The reason for this is that the indentation of asperities - which can cause a high local contact pressure - can lead to a large contact area and therefore a high tangential stress even if the adhesion is weak. This stress is compressive in front of the asperity and extensive behind [50], it leads to a high density of energy disspated in local heating and abrasion [49].

1.5.2. Adhesion friction

Roth *et al* [51] performed friction measurements between a smooth glass track and rough rubber with different apparent contact sizes for same sliding velocities. Two samples with a different contact size exhibit a decrease in the friction coefficient with an increase in the normal force. For the same applied normal force and the same material,

the largest size exhibits the largest friction coefficient. This experiment shows that for a rubber sliding on a hard counter material - such as glass - the friction coefficient depends on the contact area [41] in contradiction with the Coulomb's law for dry contacts. An explanation of these results is the presence of a significant adhesion force at least almost independent of the normal applied force, as it is evidenced by a mechanical test between a gum ball and glass plane, where the contact area was measured as a function of the load [40]. The adhesion may have several origins: capillary forces, van der Waals forces or electrostatics forces but all depend on the real contact area between the two materials. Therefore the value of the adhesion force is strongly dependent on the real contact area.

Several models were proposed to explain the rubber adhesion on a counter surface. All the models discussed below consider rubber elements that adhere to the track, then deform and detach once a critical force is reached. Thus, the rubber elements recover the stored energy in a form depending on the viscoelastic properties of the rubber.

1. The Savkoor model [47] considers a macroscopic energetic criterion for the breaking. The friction force is considered as equally arising from rubber asperities. Once bonds are created between rubber asperities and the track, asperities shear and compress until the stored energy is equal to the adhesion energy originated from van der Waals forces. Therefore, this model predicts the existence of a static friction phenomenon.
2. The Kummer model [38] considers the existence of an electrostatic attraction between the rubber and the counter face. This surface is supposed to carry electric charges that interact with rubber charges. The rubber charges can either exist independently or be created due to the existence of the counter face charges. The resulting electrostatic interaction leads to the deformation of the rubber during sliding. Thus the energy is dissipated through viscoelastic losses in the volume of rubber stressed.
3. The Schallamach model [44] is based on the thermally activated forming and breaking of bonds - due to van der Waals forces. A newly formed bond causes adhesive force when this bond - and the rubber surrounding it - is deformed by the relative motion. The bond breaks after a certain average time, then after another average lag time, the rubber surface provides a new bond with the counter face. The process of making and breaking of these bonds costs energy. This model is limited to the 'rubbery' frequency-temperature regions of the rubber and fails to predict static friction.
   In 1971, Schallamach [52] performed a direct visual observation of the contact between a transparent rubber slider and a smooth surface. He observed 'waves of detachment' on the surface of the rubber that reflect the loss of contact between the two surfaces. The adhesion force is then only provided by the remaining

contact areas. These waves are contact instabilities attributed to tangential compressive stress.

1.5.3. Lubricated friction

When a lubricant is present - such as water - within the rubber-counter face contact, a viscous dissipation coefficient of friction appear depending on the thickness of the water-film separating the two surfaces. Several friction behaviors may exist and can be analyzed by the Stribeck curve [53] illustrated in figure 1.20:

1. The hydrodynamic lubrication where the lubricant completely separates the two surfaces;
2. The boundary lubrication where the lubricant has a limited effect and the effect of the surface is preponderant;
3. The mixed lubrication where both surfaces are partially separated by the lubricant and solid contacts are more or less present.

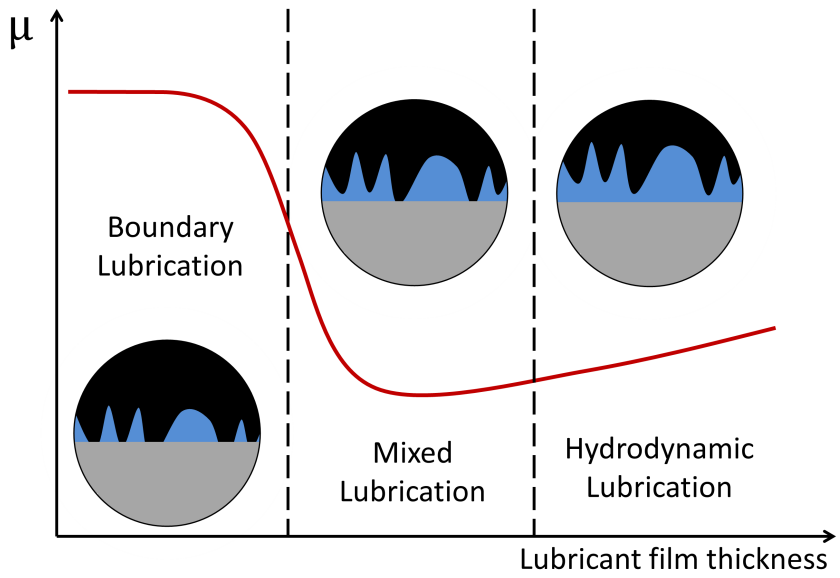

Figure 1.20.: Illustration of the curve of Stribeck with the different lubrication domains.

For this lubricated system, friction is traditionally written as:

$$\mu = \alpha_{dry}\mu_{surface} + (1 - \alpha_{dry})\mu_{viscous}$$

where μ is the friction coefficient, $\mu_{surface}$ is the friction coefficient for the two surfaces in contact, $\mu_{viscous}$ is the friction for a completely lubricated contact and α_{dry} is a partitioning coefficient function.

- $\alpha_{dry} \to 0$ is the full-film regime, where the load is totally borne by the lubricant;
- $\alpha_{dry} \to 1$ is the boundary regime, where the load is totally borne by the contacting asperities;
- $0 < \alpha_{dry} < 1$ is the mixed regime, where the load is partially borne by the contacting asperities and the viscous lubricant film.

Nevertheless, this simple approach is not sufficient to understand the friction response in lubricated contacts. Usually, a rubber sliding on a harder material deforms at multiple scales to follow the shape of the asperities of the counter face. This viscoelastic deformation is strongly associated with the friction. However, according to Persson *et al* [54], a rubber lubricated with water is not able to deform and to follow all scales of the asperities of the counter face, because of the presence of trapped water between the surface asperities and the rubber surface.

1.5.4. Effect of the fillers and oils on friction

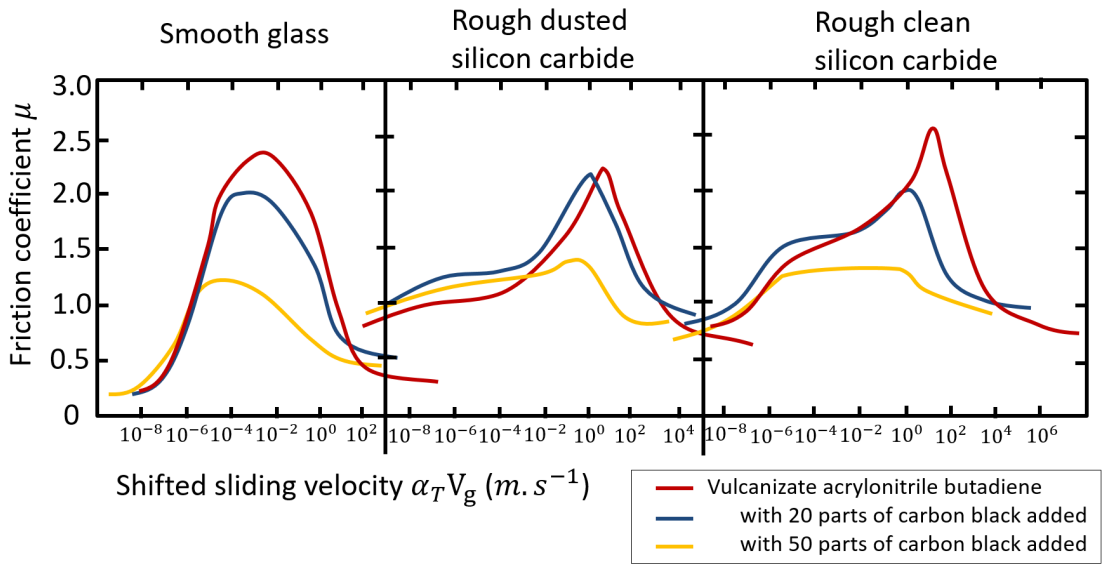

Figure 1.21.: Friction curve of rubbers sliding on a smooth and rough track measured by Grosch [49]. The addition of fillers to the rubber matrix decreases the level of friction when sliding on the smooth track. In the case of the rough track, the friction also decreases and a plateau appears on the master curve. The width of this plateau is dependent on the interval of frequency between the maximum of the dissipative modulus E'' and the loss factor $\tan\delta$.

According to Grosch [49], the addition of fillers - such as carbon black or silica - does not invalidate the WLF transform but affects the shape of the friction master-curve and reduces the maximum of friction as shown in figure 1.21. The addition of oils to rubber affects only the level of friction without changing the shape of the master curve, which implies that the glass transition temperature does not change.

1.6. Friction properties of ice

The interaction between ice and other materials have been extensively studied since Faraday's first experiments in 1859 [55] of sintering two blocks of ice below 0°C. This experiment highlighted the peculiarity of ice surface and gave rise to the so-called 'quasi-liquid' layer hypothesis.

1.6.1. Typical friction behavior

A typical ice friction behavior was exhibited by Tabor and Walker [56] - as shown in figure 1.22 - who performed friction experiments with a polycrystalline ice cone (170° in angle) sliding on granite and steel tracks. From these measurements, they showed different friction behaviors as a function of the material and the sliding velocity.

Sliding of the ice on granite exhibits a bell-shaped friction curve while sliding of ice on steel leads to the lowest friction with no velocity dependence despite a 'similar' counter face roughness. According to Tabor and Walker, this result could be due to an effect of the surface adhesion, lower for steel than for granite.

In addition, the increasing friction observed for granite at low sliding velocities - in segment AB of the figure 1.22 - was associated with ice creep. The drop of friction observed for granite - in segment CD of the figure 1.22 - correlates with frictional heating and melting.

1.6.1.a . Effect of the temperature and of the sliding velocity

Several observations were made during ice friction experiments for different parameters: temperature, sliding velocity, load and slider hardness.

The effect of environmental or contact temperature on friction has been repeatedly emphasized by measurements [57, 58, 59] and models [60, 61]. The general consensus is that the higher the temperature, the lower the friction. This effect is often linked to the case of high sliding velocities where frictional heating is expected within the contact and was effectively observed [62]. The sliding velocity dependence was clearly demonstrated by the experiments of Tabor and Walker with granite [56], but also in the case of PMMA, steel and many other materials [58, 63, 62, 60, 64]. This reduction in friction

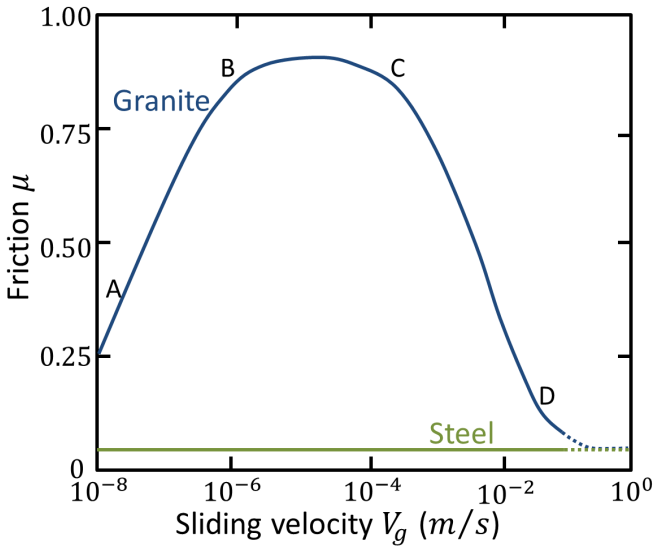

Figure 1.22.: Friction curve of ice on granite and steel as function of the sliding velocity measured by Tabor and Walker [56] at -11.7°C derived from fifty individual curves with ± 10 % scattering. The ice-steel contact exhibits a constant friction as a function of the sliding velocity while the granite presents a bell-shape curve friction.

is generally associated with the hypothesis of a 'quasi-liquid' layer and/or melting ice lubrication.

1.6.1.b . Adhesion on ice

Based on the nature of the crystalline H_2O bonds of ice demonstrated by Fowler and Bernal [65], Niven [66] suggested that the bonds between ice and slider material may be electrostatic. In this framework, below the ice surface, a force may be provided to gradually rearrange the upper crystalline ice layers. Several examples showed a correlation between the high polarization of the counter-material and the friction level against ice, the hydrophobic materials typically showing lower friction than more hydrophilic materials.

Maeno and Arakawa [64] suggested that adhesion between ice and slider is caused by ice sintering by extending Tabor adhesion theory [67] for metallic junction. They

wrote:

$$\mu = L_{sintering}\frac{\sigma}{p} \qquad \text{with} \qquad L_{sintering} = \left(1 + 2C\left(\frac{a}{R}\right)^{1-q_{sintering}} \frac{r_{asp}^{1-p_{sintering}}}{V_g}\right)^{2/q_{sintering}} \tag{1.4}$$

where σ is the shear strength, p is the compressive strength, $L_{sintering}$ is a constant called the sintering factor, C is a temperature-dependent parameter, $p_{sintering}$ and $q_{sintering}$ are constants specified by the physical working mechanisms of ice sintering, a is the radius of the contact area of one asperity, r_{asp} is the radius of the asperity itself and V_g is the sliding velocity.

The equation 1.4 shows that the factor of sintering clearly increases for lower sliding velocities. This mechanism was only proposed for sliding velocities slower than 0.01 m.s^{-1}. For higher velocities, the friction is no longer dominated by adhesive shear deformation but rather by a potential lubrication due to ice melting.

Makkonen [68] considered a dry slider-ice friction mechanism based on the surface energy γ due to the molecular attraction forces. The moving of the slider ice forces the conversion of bare ice surface - in front of the slider - into a slider-ice interface - within the contact - and then into a bare ice surface - to the exit of the contact. The suggested process - when $\gamma_{ice} > \gamma_{slider-ice}$ - is explained as follows:

1. The change of the bare ice to slider-ice surface releases energy in the form of heat which - hypothetically - does not affect the friction mechanism;
2. The change of slider-ice surface to bare ice costs kinetic energy.

The resulting friction equation given by Makkonen is as follows:

$$\mu = \frac{\gamma_{ice}}{H_{ice}}\left(\frac{1}{d_{ice}} + \frac{1}{d_{slider}}\right)\left(\frac{d_{ice}}{d_{slider}} + |\cos\theta|\right)$$

where γ_{ice} is the surface energy of the ice, d_{ice} is the asperity diameter of the ice, d_{slider} the asperity diameter of the slider, H_{ice} is the hardness of the softest material and θ is the static contact angle of a sessile drop of water on slider material. Different consequences of this model can be highlighted here:

- High hydrophilicity of the slider increases the friction;
- The higher the hardness, the lower the friction. This result was confirmed experimentally by Kietzig [69];
- The higher the surface energy of the ice, the higher the friction.

This model suggests that the friction of dry rubber-ice does not depend on the sliding velocity. It must be emphasized that this model does not explain the observation of the decrease of friction with the increase of temperature.

1.6.2. The mechanisms of dissipation in ice friction

1.6.2.a . The 'quasi-liquid' layer hypothesis

In 1959, Jellinek [57] studied the adhesion of ice to multiple materials such as polished stainless steel, polystyrene or polymethacrylate and highlighted two different adhesion behaviors depending on the applied stress: traction and shear as shown in figure 1.23.

The adhesion values between these two cases differ by an order of magnitude. These adhesions are independent of the cross-section and of the thickness of ice but depend on the temperature. This temperature dependence and the contradictory results between traction and shear can be explained by the hypothesis of the existence of an amorphous ice layer within the interface which has intermediate properties between ice and water and that has a Newtonian viscosity.

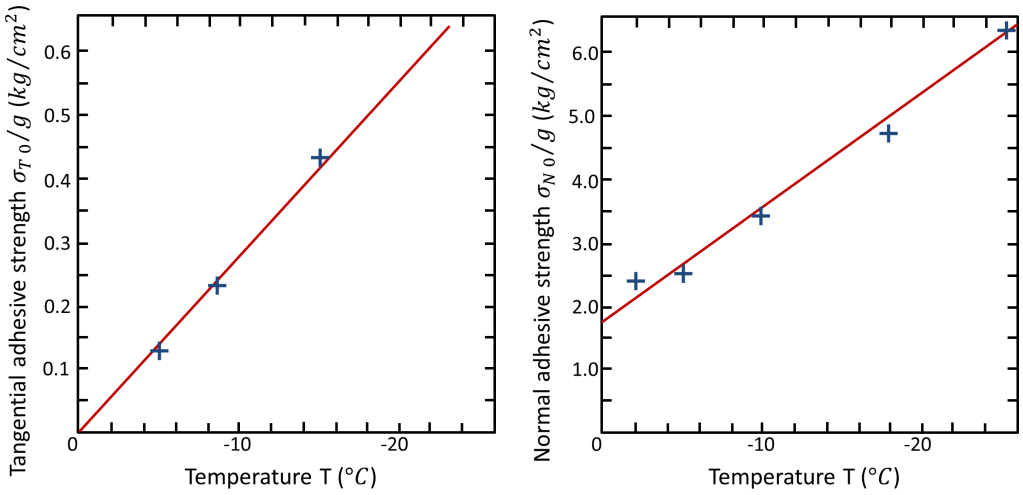

(a) Adhesive strength of polystyrene-ice obtained by shear.

(b) Adhesive strength of polystyrene-ice obtained by traction.

Figure 1.23.: Adhesive strength of ice-polystyrene as a function of the temperature [57]. Each point is the average of twelve measurements.

1.6.2.b . Ice creep hypothesis

The phenomenon of ice internal creep was observed by Tabor and Walker [56] for low sliding velocities on ice surface layer - at almost 0.2 mm under the ice surface. They suggested that for the low sliding velocity regime - where high friction can be expected between the ice and the slider - friction is determined by the force required to creep the thin layer of ice close to the surface. Because of this creep process, the ice surface

recrystallizes with an orientation parallel to the shear direction.

In 1976, Perez [70] carried out torsion strain deformation - with an inverted torsion pendulum - of monocrystalline ice at several temperatures, deformation frequencies and annealing treatments. He showed that strain deformation at high temperature - i.e within the temperature range of 50°C below the melting point - depends on the deformation frequency, temperature, plastic deformation rate and annealing treatment as follows:

- The lower the deformation frequency, the higher the deformation;
- The higher the temperature, the higher the deformation;
- The annealing - during 330 h at -1°C - of plastically deformed ice decreases its deformation.

These results were explained by the hypothesis of the glide of dislocations in the basal plane - confirmed by X-ray observations. If the H_2O molecules are correctly rotated - i.e in accordance to Bernal-Fowler rule - H_2O bonds are broken by this glide and new ones are formed.

1.6.2.c . Frictional heating and ice surface melting hypothesis

The hypothesis of melting of an ice layer has been suggested many times since the Faraday ice regelation experiment to explain the slippery behavior of ice. Two origins were identified to explain melting of the ice surface [66]:

- The pressure melting which is limited to the cases of very high pressure - as shown by the temperature-pressure diagram in figure 1.11;
- The frictional melting caused by temperature increase within the contact due to frictional heat dissipation.

In 1939, Bowden and Hughes [71] performed a sliding friction experiment between a ski and ice. They pointed out the extremely low contribution of the pressure melting to the observed friction drop. The decrease in friction was correlated with frictional heating caused by the sliding. They also observed that the friction was independent of the load, the apparent contact area and the sliding velocity over a certain range. The temperature dependence clearly demonstrated - the lower the temperature, the higher the friction.

The existence and influence of this melting layer resulting from frictional heating has been extensively studied and modeled over the last 50 years.

1.6.2.d . Slider thermal conductivity

Jones *et al* [59] studied the effect of the thermal conductivity and surface roughness of various sliders on pure ice at a temperature above the melting point of ice - at 2°C - by measuring friction force and melted ice amount. They showed that in a 'high'

temperature environment, a high thermal conduction through the slider provides a large amount of melted ice at the interface - frictional heating plays only a minor role in this case. As a result, the thicker the melted water, the lower the friction. It is explained by the melted ice covering the asperities of the slider, minimizing the contact between the ice and the slider. The effect of surface roughness on the friction was partially confirmed by Cho [72].

Kietzig *et al* [73] also studied the effect of the thermal conductivity of the slider on ice but in the case of negative Celsius temperature - from -1.5°C to -10°C. They observed that the lower the thermal conductivity, the lower the friction coefficient, and the potential influence of wettability and hardness of the material. The influence of the thermal conductivity is explained by the trapping of the frictional heat within the slider-ice contact, thus providing melted ice lubrication.

1.6.2.e . Effect of hydrophobicity

Kietzig *et al* [69] investigated the effect of surface texturing of a steel slider to vary the hydrophobicity without any change in hardness or thermal conductivity. They demonstrated that the higher the hydrophobicity, the lower the friction and the influence of the overall orientation of the scratches and grooves of the textured surface.

1.6.3. The ice friction models with melting

During ice sliding, melting of the ice surface is expected, especially if the ice temperature is 'close' to the melting temperature and the heat dissipated in the ice is significant. However, direct observation of the melted ice layer is not an easy task. To identify the presence and distribution of a layer of water, different models were proposed.

Oksanen [60] developed a model to calculate the friction between a non melting slider and ice. He considered that friction was only provided by the shear of a Newtonian water layer under all the contact area of the slider. The contact area is made of several small square contact asperities and the conduction occurs through these spots. Frictional heat energy goes to ice and is consumed to melt it and for heat conduction into the slider and the ice. Different consequences can be drawn from this model:

- Two different behaviors exist according to the temperature. When the temperature of the bulk material is 'far' below the melting temperature, the friction decreases linearly with sliding velocity. When it is 'close' to the melting temperature, the friction increases linearly with sliding velocity.
- For a bulk temperature 'far' below the melting temperature, a very thin self-balanced ice melted layer may exist for the following reasons:
    1. If the thickness of melted ice layer decreases, the frictional heat increases;
    2. Therefore, more ice melts and the thickness of lubricant increases;

3. Thus, the heat of friction decreases and the layer thickness decreases.

Hardness of the slider material also needs to be taken into account because it governs its ability to deform and thus to lead to large contact area: the harder, the lower the friction.

Pushkarev [61] developed a model to estimate the thickness of melting ice layer under a slider in a steady-state case. The heat flow caused by the friction heating is completely transmitted to the ice. The liquid thickness depends on the amount of melted ice, and therefore depends on the position under the slider.

Fowler and Bejan model [65] considered - in addition to the frictional melting - a contribution of pressure melting limited to some conditions. The effect of pressure here is limited to the contact between the slider and the asperities of the ice. These spots of contact between the slider and the ice asperities are small enough to allow very high pressure at the interface. The pressure melting at the asperities creates a layer of melted ice working as a lubricant.

Other works [74, 75] doubt the effect of a layer of melting ice as a lubricant.

Slotfeldt-Ellingsen and Torgersen [74] investigated the effect of water addition within a polyethylene-ice contact between 0 and -20°C in the form of a dilute solution of H_2SO_4 in water with a lower melting temperature than water alone. They showed that increasing the liquid content on the surface only reduces the friction - compared to a 'dry' case - by 10% to 30% maximum. For cases with large liquid content, the friction coefficient tends to increase. This result highlights that under these conditions, the water on the surface of the ice is a poor lubricant or that the friction mechanisms with water or melted ice are not well understood.

Strausky [75] performed a friction experiment between a PMMA slider and Coumarin-doped ice. The thickness of the liquid film was simultaneously measured by a spectroscopic method of fluorescence. The coefficient of friction of 0.03 - typically measured for hydrophobic plastic on ice - measured under -2°C ski conditions - was not correlated with the observation of a liquid layer thicker than 50 nm - which was the detection limit of the apparatus used. It suggests that very low friction coefficient can be achieved without surface melting or with a nanometric layer of lubricant.

Kozlov and Shugai [63] investigated the liquid layer regime of melting ice by frictional heating at a 'very' high sliding velocity up to 100 $m.s^{-1}$. They compared the expected friction calculated by the hydrodynamic theory to their results and showed a good correlation between the results up to 50 $m.s^{-1}$. For higher sliding velocity, a clear drop of friction - not modeled - appears and suggests a phenomenon of friction completely different from the viscous shearing of a liquid layer.

1.7. Rubber on ice friction

Rubber and ice are two materials with complex behaviors. Rubbers are a complex mixture of elastomers, fillers and oils. Their mechanical properties and their coefficient of friction are dependent on the temperature as well as on the frequency of applied stress. Ice exhibits remarkable properties such as the existence of a quasi-liquid surface layer that influences adhesion or melting that influences the friction.

Identifying some of these mechanisms in a rubber-ice contact is helpful in understanding how tire design can improve driving performance on ice.

1.7.1. Temperature-frequency dependence and bell-shaped curve

In 1972, Southern and Walker [76, 77] performed rubber-ice friction experiments down to -30°C for several types of gums for sliding velocities from 0.1 to 10 mm.s^{-1} in the same manner as Grosch [48]. They observed that the friction curve of the investigated rubbers obeys the WLF theory.

In the same year, Gnörich and Grosch [78] observed similar results at higher sliding velocity - presented in figure 1.24. In addition they observed that the friction levels between 0 and -5°C were impacted by the proximity of the melting point.

Later in 2008, Higgins *et al* [79] performed systematic rubber-ice friction experiments with a pin on disc tribometer as a function of temperature and velocity. For low velocities - lower than 0.2 m.s^{-1} - they highlighted a peak of friction around the glass transition temperature T_g of the tested rubber (-25°C). As the velocity increases, the friction peak disappears and does not reappear for higher velocity, in contradiction with what is expected from the frequency-temperature equivalence.

These results suggest that near the melting point, there is a change in the nature of the ice surface, such as a 'quasi-liquid' layer or melting. They also suggest that far from the melting point the friction mechanisms are more 'classic' because they depend mainly on the viscoelastic properties of the rubber. In addition, rubber-ice sliding produces a frictional heating that changes local temperature and brings it closer to the melting point.

1.7.2. Ice variability

Southern and Walker [77] and Roberts and Richardson [80] showed the existence of a large variation in friction for freshly prepared ice surfaces under the same conditions day-to-day. To obtain reproducible measurements, they conditioned the ice by repeated tests until the measurement became reproducible. They also observed that the friction measurements performed on fresh ice cannot form a master curve through the WLF transform. They suggested that for fresh ice, the friction does not arise from the viscoelastic properties but is related to the surface state of the ice.

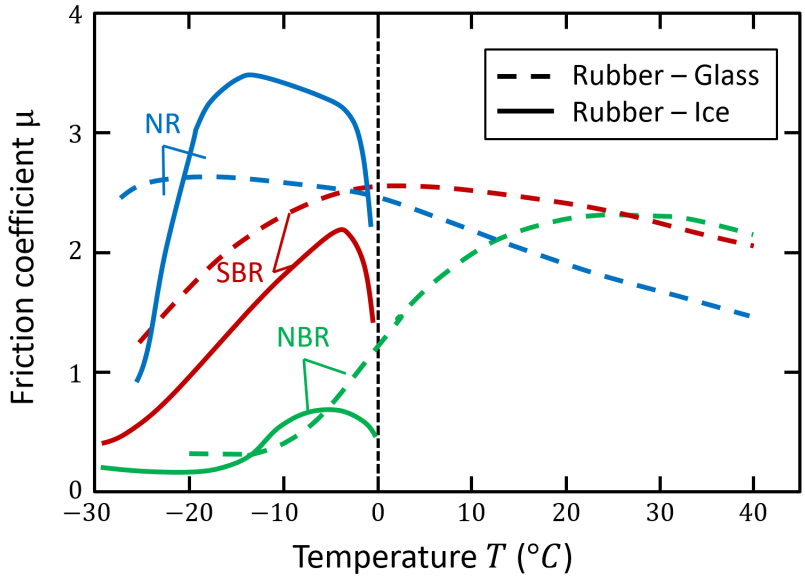

Figure 1.24.: Rubber-ice (solid curve) and rubber-glass (dotted curve) friction curves as function of the temperature measured by Gnörich and Grosch [78] at 50 mm.s^{-1}. The comparison of rubber friction curves on ice and glass clearly shows the effect of the melting point.

Roberts [40] also pointed out that aging of the ice changes the frictional response of rubber-ice sliding. He compared the friction response as a function of the temperature on a 2-weeks ice and a 10-month ice and found a clear difference, with the oldest ice leading to the lowest friction.

1.7.3. Effect of the rubber compounds

Two rubber additives were identified to have an influence on the friction:

- The oils and softeners (aka the plasticizers);
- The fillers such as carbon black and silica.

1.7.3.a . Oils and plasticizers

In 1988 Ahagon *et al* [81] systematically investigated multiple variations of rubber material properties such as $\tan\delta$, filler ratio and amount of oils. They observed that the usual parameters identified to increase friction on 'classic' surfaces can have opposite consequences on ice:

- The lower the maximum dissipative factor $\tan\delta$, the higher the friction on ice. In opposition with the wet road case where the lower the maximum $\tan\delta$, the lower

the friction;
- The lower the complex Young modulus E^*, the higher the friction;
- The amount of oil - such as a rubber softener - has a slight effect on friction. Increasing the amount of oil increases the friction until a maximum is reached. Thereafter, any increase in the amount of oil decreases the friction.
- The effect of surface temperature on friction is clearly highlighted. The lower the temperature, the higher the friction.

It appears that the main parameter driving the friction is the softness of the rubber through the Young modulus E^*. The solubility parameter of the plasticizer is considered to have a strong influence on the friction of the rubber. The closer the solubility value of the plasticizer to the solubility of the rubber matrix, the higher the friction. The higher the global solubility of the rubber, the higher the friction. This correlation with softener percentage was also emphasized by Venkatesh [82]. Grosch [49] and Southern and Walker [77] showed that oils affect the level of friction without contradiction with the WLF transform.

1.7.3.b . Fillers

Grosch [49] and Southern and Walker [77] also showed that fillers affect the level of the friction peak without contradiction with the WLF transform.

Kriston, Tuononen, Fülöp and Isitman [83, 84, 85] conducted optical investigations of ice surfaces before and after the sliding on filled rubbers. They observed the occurrence of scratches - as well as Klein-Paste and Sinha [86] - on the ice surface after sliding. The scratches, parallel to the sliding direction, were $12.5 \pm 6.9\ \mu m$ wide. This size was correlated with the apparent size of the agglomerates of fillers on the surface of the rubber. These surface agglomerates are similar - but smaller than - to those observed by Petitet [7] in figure 1.8.

Further investigations with several {soft/hard - smooth/rough} rubber couples were investigated at -10°C. Soft rubbers have a lower Young modulus than hard rubbers. Smooth rubbers have a lower density of agglomerates of filler on their surface than rough rubbers. Rough rubbers - with the highest number of asperities at the surface - present the highest friction regardless of their Young modulus. Soft rubbers - with the lowest Young modulus - have the highest friction. These results are explained by the fact that:

- The softer rubbers have a larger contact area;
- Additional forces arise from scratching and plowing due to surface fillers.

Due to the small contact areas - which are limited to the fillers - roughness carries higher pressure, hence higher frictional heating with a higher probability of melting ice. This is supported by the observation of several ice recrystallization structures associated to melting [83].

1.7.4. Effects of the tribological conditions

1.7.4.a . Applied pressure

Southern and Walker [77] and Venkatesh [82] studied the effect of pressure on the friction response and observed the typical decrease in friction with increasing applied pressure predicted by Schallamach theory as: $\mu \equiv \frac{1}{\sqrt{P}}$ with P the pressure. The pressure produces a scaling factor of the master curve.

1.7.4.b . Sliding velocity, temperature and frictional melting

For a high sliding velocity - faster than 450 mm.s^{-1} - Southern and Walker [77] identified a drastic decrease in friction. In this velocity range, the friction becomes independent of the use of fresh ice or (re)conditioned ice. This result is associated with a frictional melting phenomenon.

Roberts and Richardson [80] carried out a systematic measurement of friction on ice as a function of temperature - as shown in figure 1.25 - and showed a sharp drop in friction near the melting temperature. The frictional decrease as a function of temperature occurs for all sliding velocities performed on ice. However, close to the melting temperature:

- For 10 mm.s^{-1}, the friction level between ice and wet glass is similar;
- For 0.001 and 0.1 mm.s^{-1}, the friction level presents a large difference between ice and wet glass.

This result suggests that a lubrication effect is not sufficient to explain the friction drop observed on ice as it was suggested by Slotfeldt-Ellingsen and Torgersen [74].

Typically, an increase in the temperature always leads to a decrease in friction [78, 77, 80, 81, 82]. This phenomenon is also generally related to friction heating due to the sliding velocity.

In 2008, Higgins *et al* [79] observed refreezing ice structure after sliding at 2.1 m.s^{-1} at -5°C during a pin on disc measurement.

This result was in apparent contradiction with Klein-Paste and Sinha [86] observations that they performed via ice surface replicates after sliding at velocities of the order of 3 m.s^{-1} at -0.1°C with a British pendulum. They observed very low friction ($\mu = 0.08$) without refreezing structure at the surface of the ice after a single sliding pass.

The low friction observed by Klein-Paste and Sinha at high velocity slightly below the melting temperature is traditionnally associated with melting. However they did not observed it with replica, in the same way as Strausky [75]. If indeed there is no melting during the measurements performed by Klein-Paste and Sinha, the refreezing structure observed by Higgins *et al* may be explained by repeating the sliding on the same track.

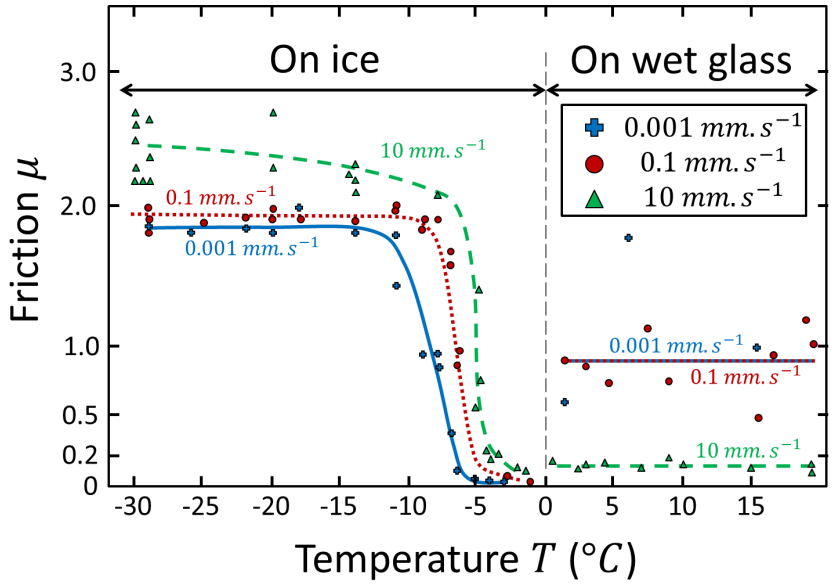

Figure 1.25.: Rubber-ice friction curve measured by Roberts [80] as a function of temperature. Rubber-wet glass friction curve is presented for temperature above 0°C. Friction were performed for three different sliding velocities: 0.001, 0.1 and 10 mm.s^{-1}.

1.7.5. The tire scale

At the tire scale, several other parameters need to be taken into account such as ABS usage, tire tread pattern size and the ice condition.

The effect of ABS was studied by Sokolovskij [87] in the case of tire performance on ice and snow. Two opposite results appear depending on the nature of the track:

- On ice, the use of ABS improves tire performance by increasing friction;
- On snow, the friction performance is decreased.

These results can be explained by the fact that, on ice, the ABS prevents sliding of the tire by preventing the locking of the rotation of the wheel. On snow, locking of the wheel causes it to push and thicken the snow in front of the wheel.

In 2015, Bhoopalam [88, 89] investigated the effect of several tire parameters on the resulting friction in a controlled laboratory environment as well as on outside roads. He observed that:

- The lower the inflation pressure, the higher the friction. It is associated with an increase of the contact area between the tire and the icy track.
- The lower the temperature, the higher the friction;
- The higher the applied load, the lower the friction;
- The state of the tread influences the friction. Two tires having the same material

and the same tread pattern but different surface state (buffed and not buffed) were compared. Bhoopalam showed that the buffed surface has the lowest friction.

On outside roads, tests showed only an influence of the surface of the tread. This difference between laboratory and outside road testing is associated with the lack of environmental control on outside roads, such as temperature, applied load and water composition.

Yamazaki [90] studied the effect of the number of sipes on the friction level and showed a slight effect. The larger the number of tread sipes in the rubber block, the higher the friction.

1.8. Goals and experimental strategy

Several interesting points arise from this bibliographic study. A synthetic representation of this analysis is shown in figure 1.26. The first one is the influence of the temperature on the friction intensity.

- Ice presents variation of its surfaces properties such as adhesion [57] and the appearance of a 'quasi' liquid layer or of a melted ice layer with viscous properties;
- Rubber presents a well known friction dependence on the temperature with a large variation of mechanical properties such as elasticity modulus or loss factor - as shown in figure 1.4.

The second one is the influence of the sliding velocity of the solids which is closely related to the temperature increase within the contact.

- High sliding velocity on ice leads to a local heating induced by friction and therefore to an increase in temperature, which consequences were explained before. In addition, if the temperature rises up to the melting temperature of the ice, a decrease of surface adhesion as well as a layer of water can be expected on the surface of the ice. This layer is generally supposed to act as a lubricant and decrease friction but some studies tend to indicate that this is not that obvious and that this effect might be limited [40, 74, 75, 86].
- The friction of the rubber is strongly influenced by the frequency of stress imposed by the surface of the counter face, therefore by its topography and the sliding velocity. The frequency parameter is also related to temperature, via temperature-frequency equivalence, which has been intensively studied by Grosch [48].

The third one is the influence of the composition of the rubber materials on the intensity of the friction on the ice as well as the conditions for which the properties of the ice may outweigh the effect of the rubber. This last point is especially important - as well as the sculptures - since it is one of the few parameters that can be engineered by tire manufacturers.

The fourth one is the difference in friction on ice between a 'small' block of rubber and a tire. The friction for 'small' blocks is the highest friction [78, 80] compared to the

case of tires [88, 89].

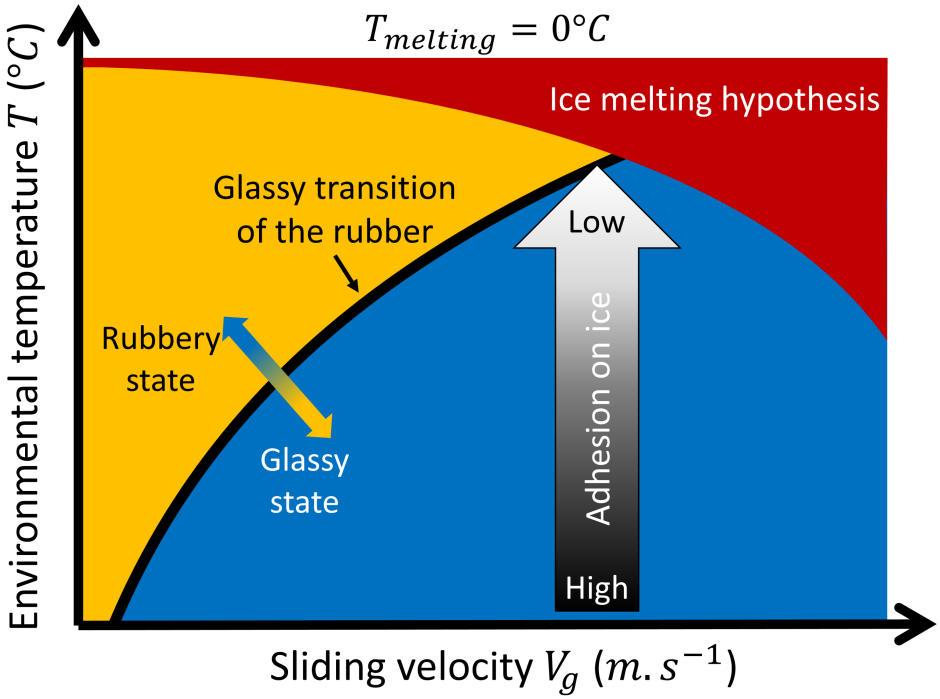

Figure 1.26.: Representation of the expected mechanisms during rubber-ice friction. In red the temperature limit of liquid-solid transition of the ice is represented. In blue the hypothesis of ice melting due to frictional heating is represented. In black the limit between the glass and rubbery state of the rubber is represented. With the black and white arrow is represented the decrease of the adhesion on ice.

In this framework, the goal of this PhD thesis is to contribute to the understanding of the physical mechanisms that are involved in rubber-ice friction. To do so, several parameters were investigated, such as:

- The rubber material and its composition, in terms of matrix, plasticizers, oils and fillers;
- The environmental temperature - i.e the ice, rubber and air - and the relative sliding velocity of the slider and the track;
- The contact scale: from few contact spots of few micrometers to the tire scale of several centimeters, including contact size of few millimeters.

Rubber type	Compounds		
"Pure"	SBR Vulcanized	-	-
"No Filler"	SBR Vulcanized	Plasticizer Anti-oxidizing oil Anti-aging oil	-
"Tire"	SBR Vulcanized	Plasticizer Anti-oxidizing oil Anti-aging oil	Carbon black Silica

Table 1.2.: Summary of the vulcanized Styrene-Butadiene Rubber (SBR) combination investigated. The name associated to each combination is indicated in the left column.

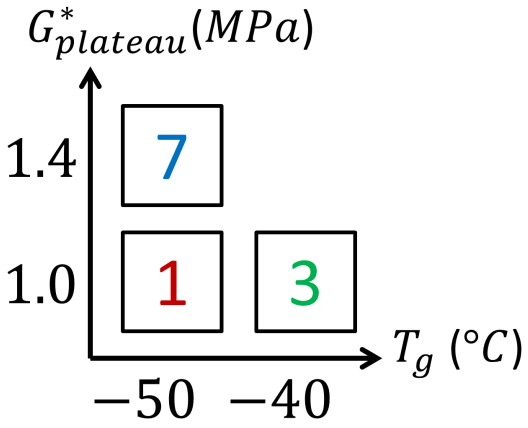

Figure 1.27.: Summary of the mechanical properties of the investigated 'tire' rubbers, two different glass transition temperatures T_g and two high temperature shear modulus plateau $G^*_{plateau}$. These rubber properties correspond to Dynamic Mechanical Analysis performed at 23°C for a stress frequency of 10 Hz and a strain deformation of 10%.

The rubber variations are summarized in Table.1.2, where the different combinations of components investigated and the associated names are presented. These rubber components are:

- The Styrene-Butadiene Rubber matrix (SBR);
- The plasticizers. They are used to control the mechanical properties of the rubber;
- The anti-aging and anti-oxidant oils. They protect the rubber against environmental aggressions.
- Fillers such as carbon black and silica.

In addition to the different combinations of components, several variations of mechanical properties for 'tire' rubbers such as the shear modulus of elasticity and the loss factor were investigated. The mechanical properties of the 'tire' rubbers - noted tire 1, tire 3 and tire 7 - are presented in detail in the annex A and reported in figure 1.27.

Both ice and rubber are sensitive to temperature variation - e.g the initial environmental temperature as well as the increasing temperature inside the contact due to frictional heating caused by the relative sliding of the two solids. Therefore, a large range of temperature - from -15°C to -2°C - and of sliding velocity - from 50 μm.s^{-1} to 1 m.s^{-1} - was investigated.

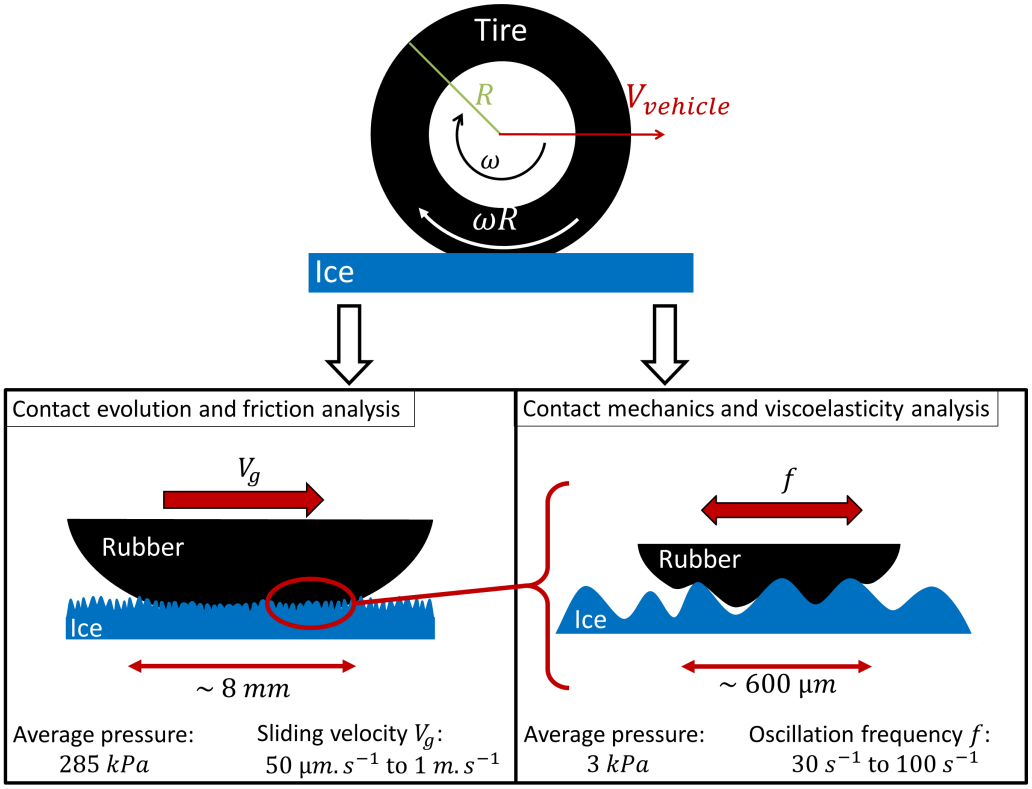

Figure 1.28.: Representation of the two experimental approaches considered from the real case of the tire on top. On the left, the study of the rubber ice-friction and contact behavior during sliding for similar conditions to real case but with a smaller contact size. On the right, the study of the rubber-ice interface.

Some interaction mechanisms between rubber and ice may appear with different intensity at different scales. Therefore, two approaches were realized - as illustrated in

figure 1.28 - which both vary in terms of contact area, ice kinematics. The first one was the study of the rubber-ice interface through the use of a thin layer of rubber having a contact size of approximately a few hundreds of μm. The second one was the analysis of the rubber sliding on ice with contact size of approximately few mm.

Chapter 2

Contact mechanics and viscoelasticity of the rubber-ice interface

---

This chapter presents an investigation of the rubber-ice interface, for contact size of few hundred μm and applied load of few mN, in terms of contact mechanics and viscoelasticity.

The Surface Force Apparatus (SFA) used for this study is first described. The protocols associated to the preparation and characterization of the surfaces were detailed as well the protocols used for the different measurements.

The evolution of the rubber-ice contact size as a function of the applied load was measured for different variants of rubber composition, with or without plasticizers, with or without oils and with or without fillers such as carbon black. Quantification of the size of the contact was performed using a variant of the 'flood-fill' algorithm. The application of JKR theory allowed us to analyze the influence of the rubber composition on the modulus of elasticity and the adhesion work.

The evolution of the viscoelastic properties of the rubber-ice interface was measured as a function of the applied load for different rubber compositions, using Resonance Shear Measurement (RSM). A specific mechanical model was developed to account for the viscoelasticity of the thin rubber layer.

In order to study rubber-ice interactions at smaller scale, a Surface Force Apparatus (SFA) based system was used to investigate contact areas as small as few spots of contact. Through this apparatus, the contact mechanics as well as the viscoelastic properties of thin rubber films of few μm thick were investigated with applied loads in the order of mN range - for maximum average pressure of 3 kPa.

2.1. The SFA-RSM

2.1.1. The SFA original principle

The first SFA measurements were performed by Tabor in the late sixties [91]. He measured van der Waals surface forces - normal and retarded - between two mica sheets separated by 200 Å with a SFA FECO (Fringe of Equal Chromatic Order interferometer) similar to the one presented in the figure 2.1.

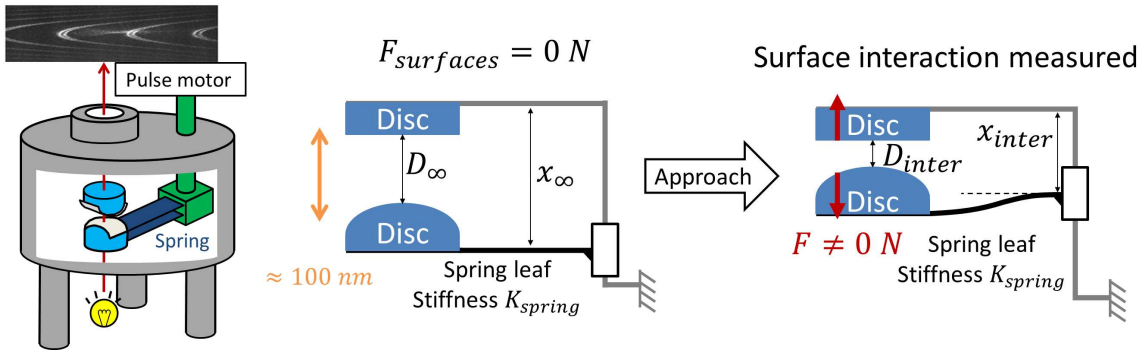

Figure 2.1.: The classical SFA FECO (Fringe of Equal Chromatic Order). For long separation distances, the measured forces are negligible. During the approach, the surfaces interact and deflect the spring. The interaction force of the two surfaces can be calculated based on the bending displacement of the spring and the stiffness value of the spring.

The original device was developed for the measurement of surface forces. The geometry of the two surfaces in contact were chosen to be mathematically equivalent to a sphere-plane ensemble. This choice makes it easier to measure the distance between the two surfaces, the measurement of the gap between two plates being more complex, because of the necessity to ensure surface parallelism. Therefore, sphere-plane or cylinder-cylinder ensembles are usually used. Surface forces are measured through the deflection of the spring when the two surfaces are brought towards each other. Thus, two distances are measured:

- The distance between the two surfaces D_{inter}. It is usually measured by interferometry - as in the figure 2.1 where a FECO interferometer is shown;

- The normal distance of the two surfaces x_{inter}. It is usually controlled with a pulse motor with a high displacement resolution of the order of 0.1 Å to 1 nm according to the technology used.

Therefore, measuring these distances gives the force according to the following equation:

$$F_{surface} = K_{spring} \left(\Delta x_{inter} - \Delta D_{inter} \right) \tag{2.1}$$

where $F_{surface}$ is the interaction force between the two surfaces, $\Delta x_{inter} = x_{inter} - x_{\infty}$ is the displacement controlled by the pulse motor, $\Delta D_{inter} = D_{inter} - D_{\infty}$ is the displacement of the two surfaces. The distance x_{inter} and x_{∞} are the approach distances controlled by the motor at the instant t and the distance at an infinite distance 'far' from any interaction - serving as a reference. The distance D_{inter} and D_{∞} are the distances between the two surfaces due to their interactions at the instant t and at an infinite distance for which no interactions occur - serving as a reference.

2.1.2. The low temperature SFA-RSM

The experimental setup used in this study is a mechanical oscillator developed by Dushkin and Kurihara [92] on the principle of a SFA. This mechanical oscillator was used to perform Resonance Shear Measurement (RSM).

The ability to control the local temperature of the ice and the rubber - down to -20°C - as well as the ice manufacturing protocol were developed by Lecadre *et al* [93]. The cooling function is performed with:

- A Peltier cell located under the ice holder;
- A cooling generator located outside of the SFA that cools the Peltier cell via an ethylene glycol-water flux.

This design only allows to cool down the ice locally. Consequently, there is a temperature gradient in the rubber-ice ensemble. Temperatures are monitored by means of platinum resistance probes:

- The first one is located within the ice;
- The second one within the silica disc holding a thin layer of rubber sample.

A gas flux was added in the chamber to dry the local atmosphere. The flow of Nitrogen gas initially used to minimize the humidity rate was replaced by a Helium gas flow which has a higher thermal conductivity - 152.0 mW.m^{-1}.K^{-1} for Helium versus 25.98 mW.m^{-1}.K^{-1} for Nitrogen. This change of gas flow made it possible to increase the gaseous conductivity between the different parts of the SFA - between the Peltier cell and the ice holder and between the ice surface and the rubber surface and to reach negative Celsius temperature in the rubber layer.

The complete SFA-RSM for low temperature is shown in figure 2.2.

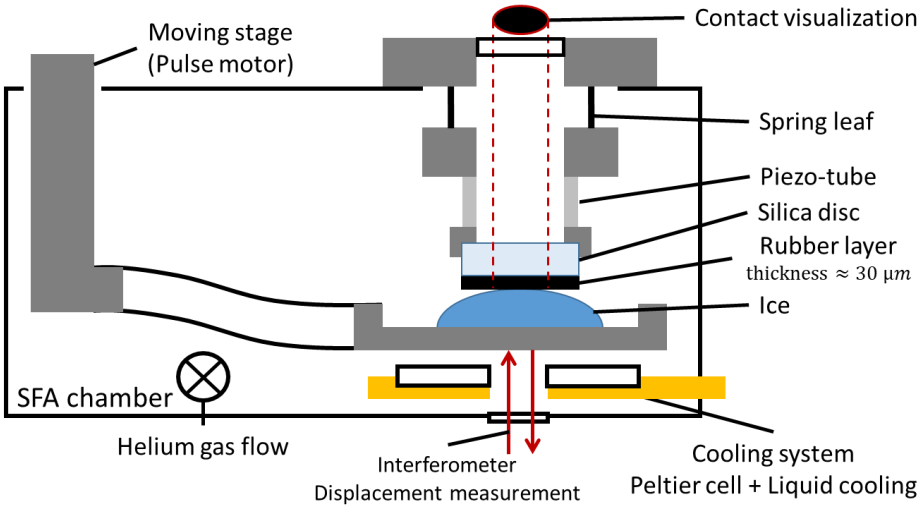

Figure 2.2.: Schematic of the mechanical oscillator - based on the SFA for low temperature applications - so called SFA-RSM. The vertical displacement of the lower unit is controlled by a pulse motor and the displacement of the ice holder is monitored by an interferometer. The cooling function is performed by a liquid cooling system and a Peltier cell. The contact area is measured through the thin rubber sample with a microscope located on top of the SFA.

2.1.2.a . Characterization of contact mechanics

The SFA-RSM allowed us to measure the contact area between ice and thin rubber films (10 to 60 μm thick). The applied load was controlled by the displacement of the pulse motor and the spring stiffness of the lower unit.

It is therefore possible to investigate the contact mechanics of few asperities at low temperature. From the contact area-normal force curves, parameters such as the adhesion work and the equivalent Young modulus were investigated in the framework of the JKR theory - explained in paragraph 1.4.2.b .

2.1.2.b . Characterization of rubber viscoelasticity

The RSM function was used in this study to perform shear measurements of rubber samples in contact with ice.

This function is based on a piezo-tube system, working as a motor, which imposes an horizontal displacement between the upper unit and the rubber sample disc. This displacement results in a non-equilibrium inside the oscillator - as shown in figure 2.3. In order to achieve a new state of equilibrium, the mechanical oscillator reacts by bending

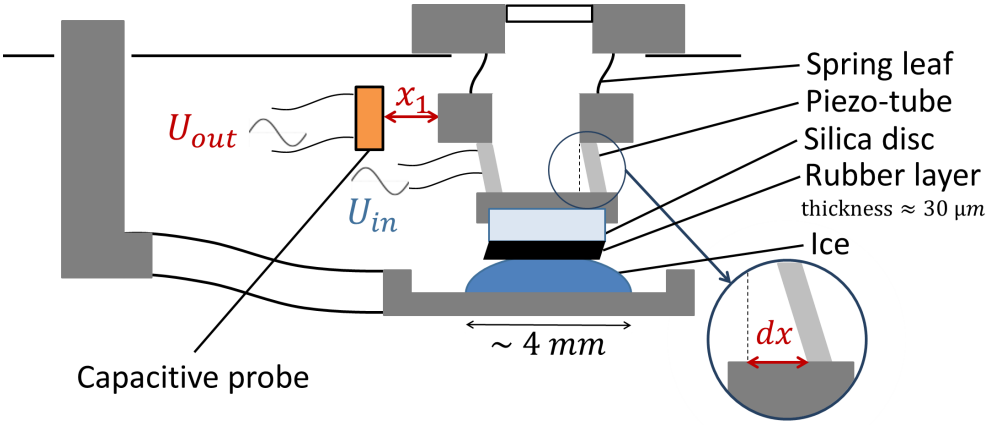

Figure 2.3.: Scheme of the SFA-RSM during a resonance shear measurement. The piezo-tube bends at the frequency of the applied voltage U_{in}. The capacitive probe measures the resultant oscillation and provides an output resonance signal U_{out}.

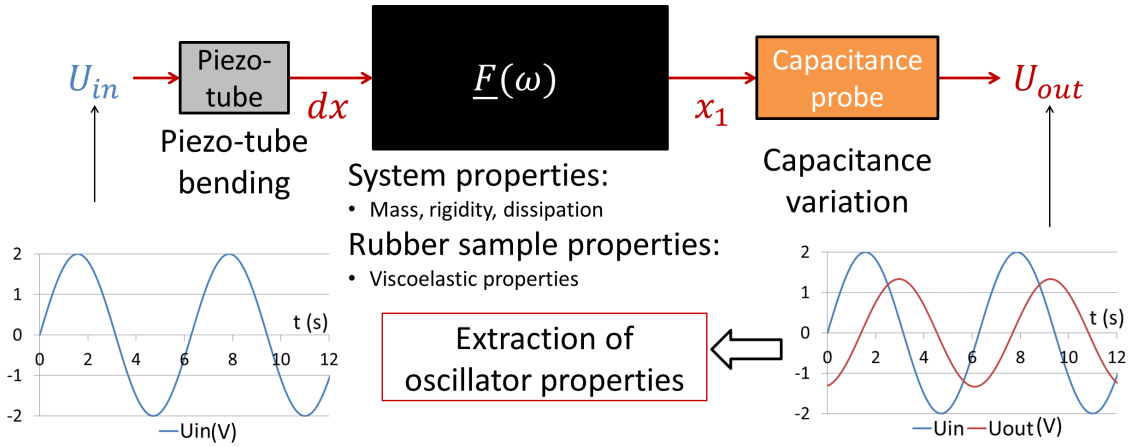

Figure 2.4.: Schematic of the Resonance Shear Measurement signal chain. An input harmonic voltage signal is applied on the piezo-tube which then bends at the same frequency. The oscillator reacts to the bending as a function of the mass, rigidity and dissipative properties of the system as well as viscoelastic properties of the rubber sample. The resulting displacement of the upper unit induces an output voltage via the capacitive probe.

the spring leafs of the upper unit and by shearing the rubber sample.

From these measurements, carried out at different frequencies around the resonance frequency of the system, an output signal is obtained depending on the mechanical prop-

erties of the oscillator as well as the viscoelastic response of the rubber in contact with ice for different loads - as shown in figure 2.4. A new mechanical model - detailed in section 2.3.2 - of the system was developed to extract the viscoelastic properties of the main layer of rubber from this output signal. Then, the shear properties of the rubber are obtained from the mechanical transfer function associated to the contact image and geometry of the sample.

2.1.3. Protocols

The protocol used to prepare a rubber-ice experiment contains two main steps: the preparation of the rubber and ice surfaces and the experimental procedure.

2.1.3.a . Surface preparation and characterization

The preparation of the ice and rubber as well as the characterization of the latter are described in the following.

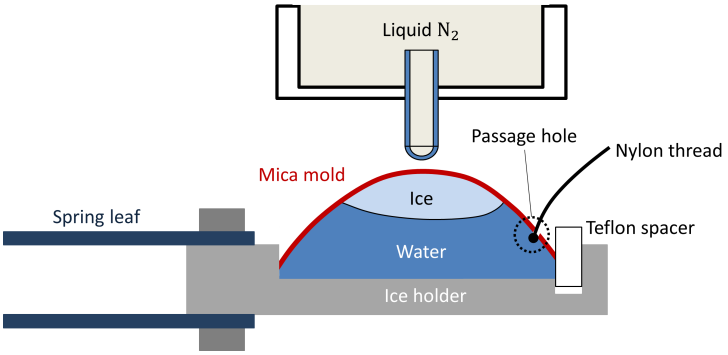

Figure 2.5.: Schematic of ice manufacturing in the SFA chamber. The distilled water was introduced under a mica sheet cleaved and bended. Cooling was performed by using liquid Nitrogen on top of the mold which produces a temperature gradient within the water.

The preparation of an atomically flat and transparent ice in the SFA chamber is presented in figure 2.5. The associated protocol is as follows:

1. The liquid cooling system was activated beforehand. The Peltier cell was kept off to avoid interference during the ice growing in step 6;
2. A mica sheet was prepared to serve as the mold for the ice surface. The mica sheet was first cleaved to obtain a thickness that allow to bend the sheet in the mold. The sheet was then cut with scissors to obtain a rectangle and was finally drilled on one of the sides;

3. A nylon thread is introduced in the previously drilled hole. This allowed the mold to be removed once ice manufacturing was completed;
4. A Teflon spacer was inserted into the ice holder and then the mica mold was placed. The bending of the mica sheet shaped a mold with a radius of approximately 7 mm;
5. The distilled water was introduced laterally under the mica mold with a pipette;
6. A container of liquid Nitrogen was placed on the top of the ice mold to cool down the water from top to bottom. It ensured an atomically flat ice surface by promoting the progression of the ice from the mold surface;
7. Once the ice was manufactured, an Helium gas flux was added and the Peltier cell was activated to its lowest temperature point.
8. Thereafter, the calibration measurements - detailed later in paragraph 2.1.3.e - were performed.
9. Then, the chamber was opened carefully and quickly to remove the Teflon spacer and the mica mold.

Several types of rubber were investigated with different compositions - detailed in table 2.1:

- The so-called 'pure' rubber composed of vulcanized Styrene-Butadiene rubber (SBR) only;
- The so-called 'tire' rubber which composition is equivalent to 'real' tire treads;
- The so-called 'no filler' rubber which is a 'tire' rubber without the presence of fillers such as silica or carbon black.

All these rubbers were prepared with the same protocol which ensures a clean and fresh rubber surface for measurements:

1. Rigid cleaved mica sheets - atomically flat - were prepared in Kurihara Laboratory as a rubber mold;
2. Rubber mixtures were prepared by Nihon Michelin. Then, they were pressed between two mica sheets to obtain a layer of 10 to 60 μm thick. This thickness allows one to observe the contact with ice through the rubber;
3. Prior to the experiment, the two mica sheets surrounding the rubber layer were cleaved until the sheets become thin enough to be bent;
4. Then, one of the mica sheets was separated from the rubber sample;
5. Next, the rubber layer on the mica sheet was glued with epoxy on a preheated silica disc at 140°C;
6. Subsequently, the rubber disc was attached to the upper unit of the SFA. The upper temperature probe was then set within the upper disc with the rubber.

Due to the composition and preparation of the rubber samples, their surface morphology might be different. Therefore, the rubber surface morphology was studied with a confocal microscope - as shown in figure 2.6 - and the average roughness of the rubber surface was estimated on five different surface locations.

	Material composition				
Sample name	SBR	Vulcanization	Plasticizer	Fillers	Anti-aging Anti-oxidant
'Pure' Rubber	X	X	-	-	-
'No filler' Rubber	X	X	X	-	X
'Tire' Rubber					
Tire 1 ($T_g = -50$°C, $G^* = 1.0$ MPa)	X	X	X	X	X
Tire 3 ($T_g = -40$°C, $G^* = 1.0$ MPa)	X	X	X	X	X
Tire 7 ($T_g = -50$°C, $G^* = 1.4$ MPa)	X	X	X	X	X

Table 2.1.: List of investigated samples with the SFA-RSM. Variations of compounds and mechanical properties are indicated for a temperature of 23°C, a stress frequency of 10 Hz and a shear strain deformation of 10%.

These observations show that the distribution of height asperities depends on the addition of compounds in the rubber. The asperities observed in the figure 2.6c seem correlated to the presence of agglomerates of fillers at the surface of the rubber sample. The average diameter of these asperities is approximately 10.9 ± 2.0 µm in figure 2.6c. This size corresponds to the expected size of agglomerates of fillers as shown in figure 1.7 as well as in the observations of Kriston, Tuononen, Fülöp and Isitman [83, 84, 85] described in paragraph 1.7.3.b .

Therefore, a strong effect of surface agglomerates is expected, such as an increase in the local stiffness as described by Petitet in section 1.2.2.

2.1.3.b . Existence of material transfer

A preliminary loading-unloading test was carried out with a set of rubber-silica disc. This test revealed the existence of a trace on the silica disc that is presented in figure 2.7.

Raman spectroscopy and X-Ray photoelectron spectroscopy (XPS) were performed to analyze the composition of the trace:

- X-Ray photoelectron spectroscopy confirmed the presence of large amount of Carbon, as well as some traces of Sulfur (a vulcanization agent) and Zinc (a catalyst agent).
- Raman spectroscopy confirmed the existence of $\mathrm{C-S}$, $\mathrm{C-H_2}$ and $\mathrm{C-H_3}$ bonds;

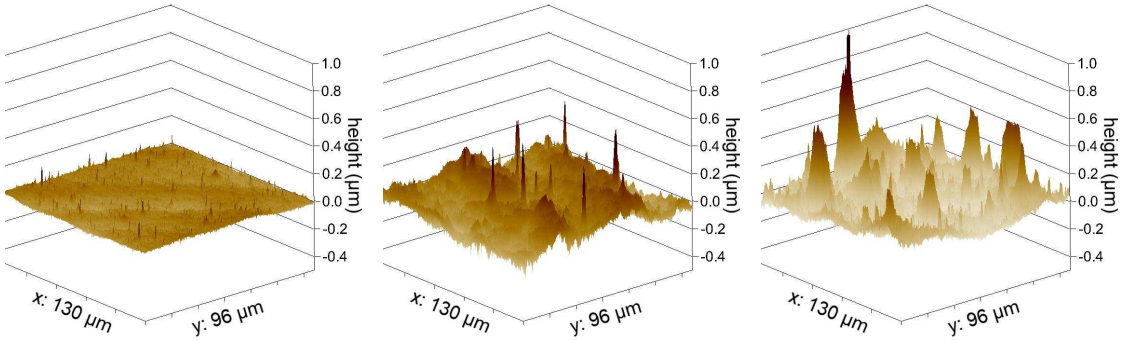

(a) 'Pure' rubber $S_q = 17 \pm 3\ nm.$

(b) 'No Filler' rubber $S_q = 59 \pm 13\ nm.$

(c) 'Tire' rubber $S_q = 123 \pm 77\ nm.$

Figure 2.6.: Confocal image of the rubber samples investigated. Associated average surface roughness S_q calculated on five positions, with their standard deviation.

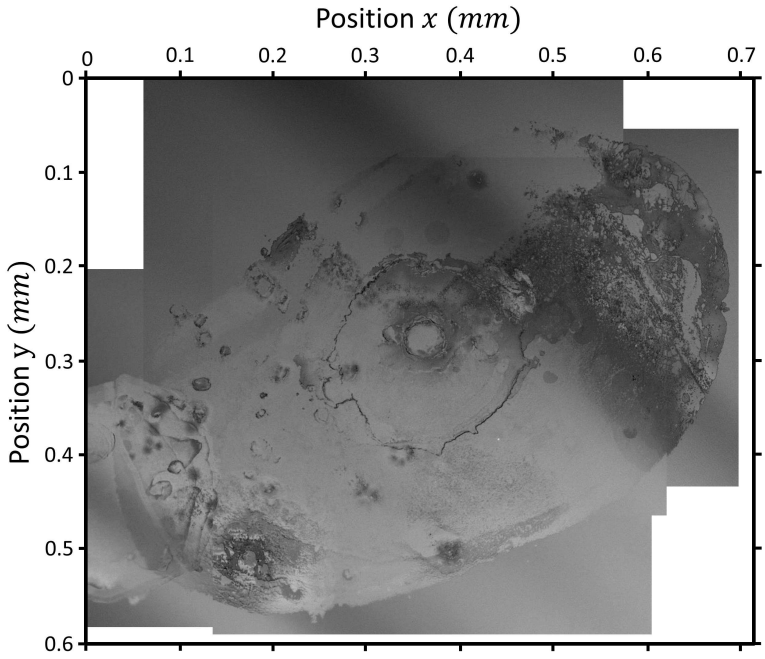

Figure 2.7.: Rebuilt image consisting of several confocal images of a transfer of material from rubber to a clean silica surface.

This result emphasized the existence of a transfer of material - such as oils - from the rubber to the silica disc. Therefore, it was decided to carry-out the rubber-ice measurements at first contact in order to avoid 'contamination' of the contact and therefore a

bias in the results. This implies changing position for each new measurement to ensure that the surfaces of rubber and ice were fresh and clean.

2.1.3.c . Existence of an ice 'bridge'

Preliminary low temperature resonance shear tests demonstrated the possibility of ice 'bridge' formation between the Peltier cell and the ice holder. This 'bridge' of ice thus increases the resonance frequency and therefore, introduces a bias in the measurements. The detection of the existence of an ice bridge during RSM is detailed later in paragraph 2.1.3.e .

2.1.3.d . Contact area versus load measurement - JKR

JKR measurements were performed with a continuous loading at 1 μm.s^{-1} - up to approximately 40 mN. Then, a continuous unloading - at the same velocity - was performed until the surfaces were detached. A video of the evolution of the contact was recorded during these two phases. After performing a measurement, the rubber and ice positions were changed to new fresh surfaces.

These measurements were performed for:

- a 'pure' tire rubber. The JKR test was made twice at the same rubber and ice location. These measurements are presented in paragraph 2.2.2;
- a 'tire' rubber 7. The JKR measurement was made only once after a RSM measurement on a same rubber and ice location. These results are presented in paragraph 2.2.3;

2.1.3.e . Resonance Shear Measurement - RSM

Resonance shear measurements were always carried out on a new rubber and fresh ice surfaces. They consist in frequency scans performed for several applied loads. However to obtain exploitable viscoelastic data, some pecular conditions - given by a preliminary calibration - must be respected. The duration time of the measurements for each position was approximately 2 hours.

Two calibration measurements were performed before the frequency scan at the different applied loads.

- The Solid Contact (SC), made for a set of silica disc without any rubber sample - {mica mold + ice} considered as a non sliding interface.
- The Air Separation (AS), made with a rubber layer on the silica disc in a free motion.

These two specific measurements are presented in figure 2.8 and give the two extreme cases of resonance peak occurrence (the upper and lower respectively). If a resonance

peak is detected above the SC peak or below the AS peak during measurements with the rubber samples, therefore it indicates a measurement bias.

For example, a typical bias that can be detected through this method is the appearance of an ice bridge - described earlier - which drastically increases the frequency of the resonance peak.

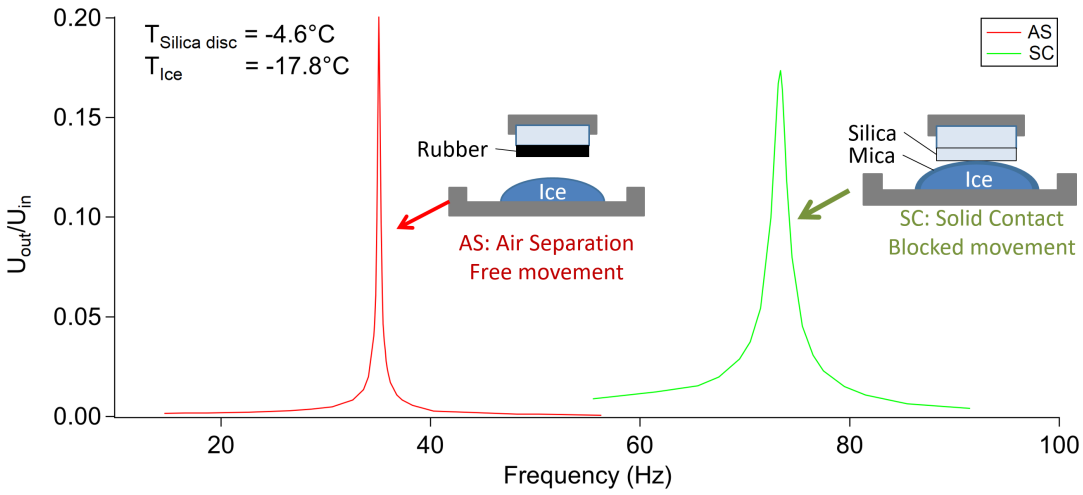

Figure 2.8.: Example of Air Separation (AS) and Solid Contact peaks. The lowest frequency peak - in red - represents the air separation case which corresponds to a free movement of the rubber surface. The highest frequency peak - in green - represents the solid contact which corresponds to a uniform displacement of the upper silica disc and the lower ice surface - covered with a mica sheet - together.

RSM were performed at several load values. During the loading, the steps used were separated by an exponential increment - in the form of $0.169 * 2^{n-1}$ with n the number of the sampling step - up to approximately 86 mN according to the following series:

Step:	0	1	2	3	4	5	6	7	8	9
Applied load (mN):	0	0.169	0.507	1.18	2.54	5.24	10.6	21.5	43.1	86.4

During the unloading, the steps used were separated by a linear decrement - on the form of $\frac{6-n}{6} F_{z\ max}$ - down to 0 mN according to the sequence below.

Step:	0	1	2	3	4	5	6	7	8	...
Applied load (mN):	86.4	72.0	57.6	43.2	28.8	14.4	0	-7.20	-14.4	...

For negative applied load, this step was divided by two until the rubber sample jump out. An image of the contact was taken at each step of applied load in order to get the

contact area evolution versus load.

A frequency scan was performed to get the peak resonance. The resonance peak frequency is initially unknown, however it should be flanked by the frequency of the SC and AS peaks. The frequency can also be guessed from the measurements performed during preceding steps.

Frequency sampling - centered on the guessed frequency of resonance $f_{guessed}$ - is as follows:

Step:	0	1	2	3	4	5	6	7	8	9	10	11
$f - f_{guessed}\,(Hz)$	-6	-4	-2	-2	-1	-1	-1	-0.5	-0.2	-0.2	-0.1	0

Step:	11	12	13	14	15	16	17	18	19	20	21	22
$f - f_{guessed}\,(Hz)$	0	0.1	0.2	0.2	0.5	1	1	1	2	2	4	6

2.2. Contact mechanics and surface characterization

JKR measurements were performed for 'pure' rubber and 'tire' rubber 7 during continuous loading at 1 μm.s^{-1} on fresh rubber and ice surfaces for the different positions investigated according to the protocol previously detailed (see paragraph 2.1.3.d).

These measurements allowed to investigate parameters such as the equivalent Young modulus and adhesion work via the JKR theory as well as to identify the preferential contact spots.

2.2.1. Contact area measurement

A large number of contact images was collected - examples are given in figure 2.9b and figure 2.9c. These contacts can have regular elliptical frontiers - as for the 'pure' rubber presented in figure 2.9b - which facilitates the measurement of the apparent contact area. But the contacts can also have more complex shapes and frontiers - such as the 'tire' rubber presented in figure 2.9c - which makes the extraction of the contact area a much more difficult exercise.

For that, an 'Explicit queue four-way flood-fill algorithm' was used. 'Flood-fill' algorithms are often used to detect and replace a group of connected pixels of the same color with a new color. In the case of our analysis, this algorithm was used to identify the pixels that can be considered as a part of the contact in black on figure 2.9.

The algorithm browses the matrix of pixels from an initial pixel, called the seed pixel and defined by the user, to build a new boolean matrix of contact/no-contact pixels. In order to take into account the variation of the light and the surface state condition of

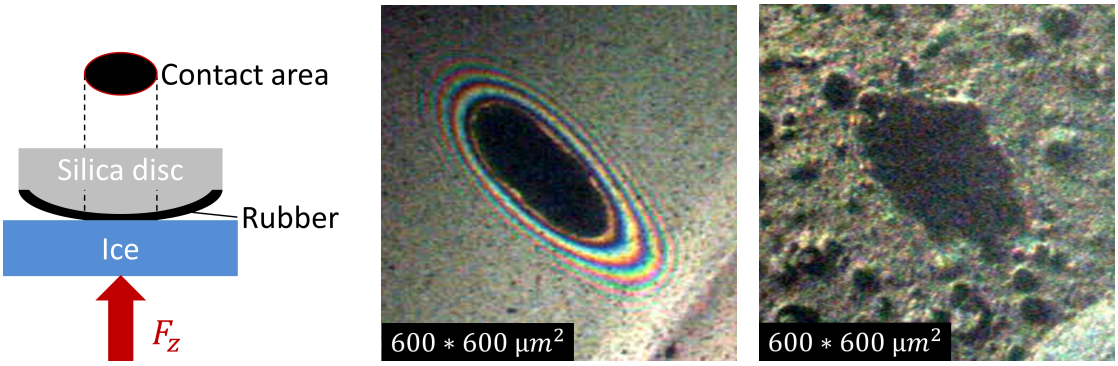

(a) Schematic of the JKR measurement.

(b) 'Pure' rubber-ice contact for a loading at 7.5 mN.

(c) 'Tire' rubber-ice contact loaded at 86 mN.

Figure 2.9.: The evolution of the contact area was monitored through the rubber layer and the silica disc as a function of the applied load F_z. The black area corresponds to the rubber-ice contact. Newton rings were observed for a rather smooth rubber (b), while an irregular contact was observed in the case of the 'tire' rubber (c).

the rubber, especially in the case of 'tire' rubbers, 'off-limit' areas were defined: this creates an artificial barrier over which no pixels were detected.

It is almost impossible to find a large group of pixels in the image having exactly the same RGB level. Therefore, to identify similar pixels, each of them was converted into a greyscale pixel and evaluated within a tolerance interval. If the grey level of the pixel is in the range of tolerance, it can be considered as a part of the contact area. Then the following criterion can be given to know whether a pixel at position (x,y) belongs to the contact or not:

$$N(x,y) = \begin{cases} 1, & \text{if } \chi_{sup} > Y_{x,y} - Y_{seed} > -\chi_{inf} \\ 0, & \text{otherwise} \end{cases}$$

with:

$$Y_{x,y} = 0.2126R_{x,y} + 0.7152G_{x,y} + 0.0722B_{x,y} \tag{2.2}$$

where $N(x,y)$ is the function that evaluates whether the pixel can be considered as a part of the contact, $Y_{x,y}$ is the grey scale of the pixel analyzed at the position $\{x,y\}$, Y_{seed} is the grey scale of the pixel seed, $R_{x,y}$ is the level of red, $G_{x,y}$ is the level of green, $B_{x,y}$ is the level of blue and χ_{sup} and χ_{inf} the superior and inferior tolerance values.

With this criterion only, a pixel that is not a part of the contact can be detected accidentally as a part of the contact. This false positive can cause uncontrolled spread of the

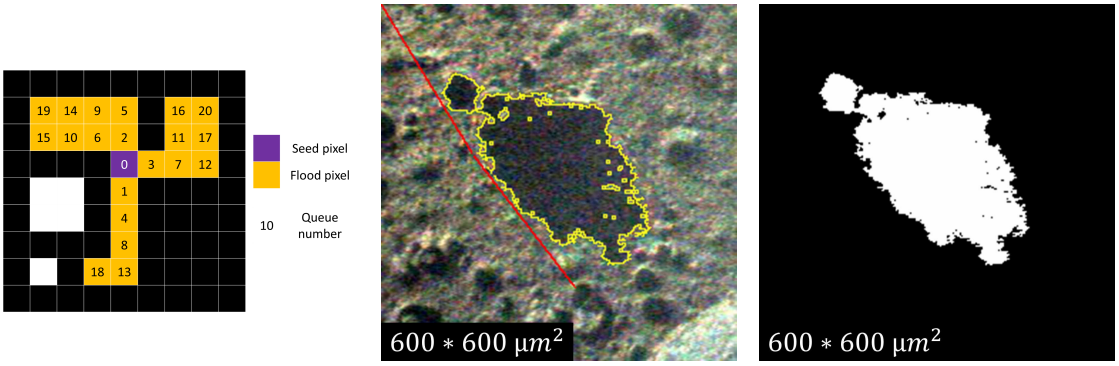

(a) Flood-fill algorithm schematic.

(b) Detected contact.

(c) Built boolean contact image.

Figure 2.10.: Application of the flood-fill algorithm. In figure (a), the example of an 'explicit queue four-way flood-fill' algorithm is presented. The seed pixel is highlighted in purple and the detected pixels are highlighted in yellow. The queue number is indicated in each pixel. The detected contact for a 'tire' rubber loaded at 86 mN is presented in figure (b) and (c). In figure (b), the detected edge of the contact is highlighted in yellow, and the 'off-limit' area is given by the red line. The extracted contact area is presented in figure (c).

detected contact area. For that reason, the surrounding eight pixels were also evaluated through a simili artificial neural network defined below.

$$f_{pixel\ contact}(x,y) = \begin{cases} 1, & \text{if } \sum_{i=0}^{1}\sum_{j=0}^{1} D(x,y,i,j) > \chi_{pixel\ contact} \text{ and } N(x,y) = 1 \\ 0, & \text{otherwise} \end{cases}$$

with:

$$D(x,y,i,j) = \sum_{x=0}^{1}\sum_{y=0}^{1} N(x-i, y-j)$$

where $f_{pixel\ contact}$ is the function that judges whether the pixels that surround a pixel belong to the contact at the position $\{x, y\}$, and the pixel itself, are part of the contact area and $\chi_{pixel\ contact}$ is a threshold.

Consequently, the algorithm is as follows:

floodFillBrowse (pixelSeed) {
1. Add to the queue the position of the pixelSeed
2. Loop on the queue until the end of the queue
    a) floodFill (x,y)

}
floodFill (x,y) {
1. If the pixel is a already detected as part of the contact → stop
2. If the pixel is off-limit → stop
3. If the pixel cannot be a contact $f_{pixel\ contact}(x, y) = 0$ → stop
4. If the pixel is a contact $f_{pixel\ contact}(x, y) = 1$:
    a) Add to the queue the pixel position {x,y-1}
    b) Add to the queue the pixel position {x,y+1}
    c) Add to the queue the pixel position {x-1,y}
    d) Add to the queue the pixel position {x+1,y}

}

2.2.2. 'Pure' rubber case: results and discussion

The evolution of the contact area as a function of the load was investigated for the 'pure' rubber during a continuous normal displacement at 1 μm.s^{-1}. The JKR measurements were performed at several positions with two iterations.

- The first iteration was performed on fresh surfaces of rubber and ice each time;
- The second iteration was performed on the same rubber and ice surfaces positions.

The results are presented in figure 2.11 and an image example is presented in figure 2.9b.

The figure 2.11a shows the variability of contact growth, position by position and between two iterations at the same position.

According to the contact mechanics theories, the variability of the evolution of the contact may arise from a variability of the modulus of elasticity and/or the adhesion work.

The JKR theory - explained in section 1.4.2.b - was used to fit the load/contact area evolution. However, it should be kept in mind that the rubber samples studied are thin films - between 10 and 60 μm thick - glued by epoxy on silica discs. This contradicts one of the main hypotheses of the JKR theory which is: 'Each solid can be considered as an elastic half-space'. Thus, the silica substrate - with a Young modulus of approximatively 70 GPa - should influence the measured value of the Young modulus of the rubber surface [32, 94].

The observed contact had an elliptical shape, which is explained by the difference between the curvature radius of the ice disc $R_{ice} = 7$ mm and the curvature radius of the rubber disc $R_{disc} = 20$ mm. According to Johnson and Greenwood [95], mildly

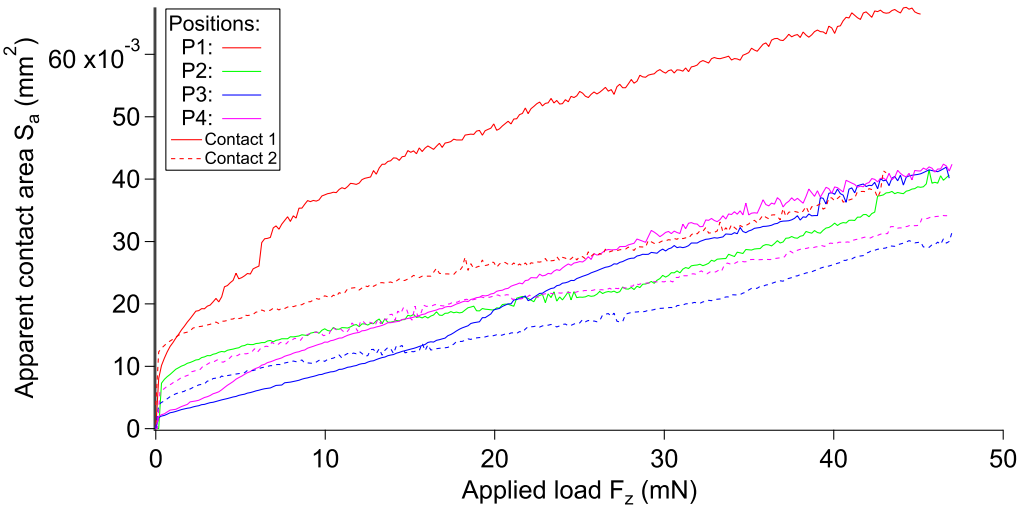

(a) Contact area measurements.

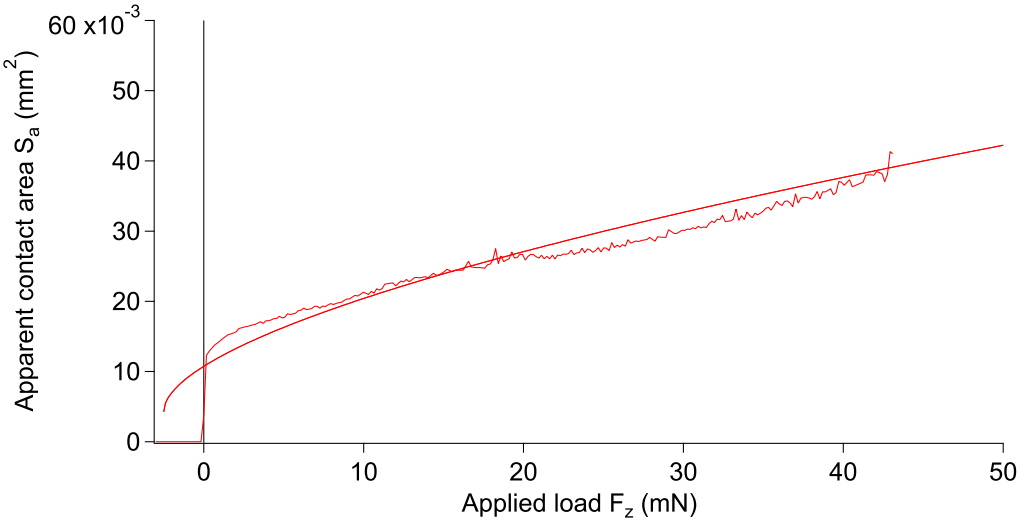

(b) JKR fit example for the second iteration at the position P1.

Figure 2.11.: Evolution of the contact area S_a for a 'pure' rubber as a function of the applied load F_z during loading. In figure (a) are presented the different JKR measurements. Each color represents a rubber-ice position. Continuous lines represent the first iterations on a fresh ice and broken lines represent the second iteration on the same position. In figure (b) is presented an example of fit with the JKR theory - detailed in paragraph 1.4.2.b . These measurements were performed with a rubber of a thickness of 44 μm during a continuous loading at 1 μm.s^{-1} (corresponding to almost 169 μN.s^{-1}).

elliptical contacts such as observed here ($R_{disc}/R_{ice} \approx 2.86 < 5$) can be approximated by circular contacts with approximation on the radius of contact and on the equivalent radius of the two solids.

The equivalent circular contact radius:

$$a_{equiv} = \sqrt{ab} \tag{2.3}$$

where a and b are the semi major and semi minor axes of the contact.

The equivalent radius of the two solids:

$$R = \sqrt{R_{ice}R_{disc}} \tag{2.4}$$

Therefore the JKR contact equation 1.3 can be rewritten on the form:

$$a_{equiv}^2 = ab = \left[A_0\left(F_z + 2F_0 + 2\sqrt{F_0(F_z + F_0)}\right)\right]^{2/3} \tag{2.5}$$

with the parameters A_0 and F_0:

$$A_0 = \frac{3}{4}\frac{R}{E^*} \qquad \text{and} \qquad F_0 = \frac{3}{2}\pi w R$$

where a_{equiv} is the equivalent contact radius, w is the adhesion work of the two materials, F_z is the applied load, R is the equivalent radius of the two solids and E^* is the equivalent modulus of elasticity of the two solids including the effect of the silica substrate for the rubber. Here, R is equal to $R = \sqrt{R_{ice}R_{disc}} \approx 10.7$ mm. The two adjustable parameters are E^* and w.

The apparent rubber-ice contact size S_a was measured instead of the semi major and minor axes a and b. In order to perform fit with the JKR theory, the following approximation was performed:

$$S_a \approx \pi\left[A_0\left(F_z + 2F_0 + 2\sqrt{F_0(F_z + F_0)}\right)\right]^{2/3} \tag{2.6}$$

The fit performed via the equation 2.6 allowed to get an elastic modulus E^* of almost 400 MPa which is two order of magnitude larger than the expected rubber elastic modulus, approximately 4 MPa. This non-consistency is explained by the effect of the silica substrate. Therefore the modulus of elasticity measured here is not the equivalent modulus of elasticity E^* but an effective modulus $\widetilde{E}$[32, 94].

This effective modulus arises from the impossibility of thin soft non-compressible film to deform in the direction normal to the applied load direction, the only direction of possible deformation is along the axis of compression. The expression of the effective

modulus is given by the equation:

$$\widetilde{E} = E\frac{1-\nu}{(1+\nu)(1-2\nu)}$$

where $\widetilde{E}$ is the effective modulus, E is the Young modulus and ν is the Poisson's ratio.

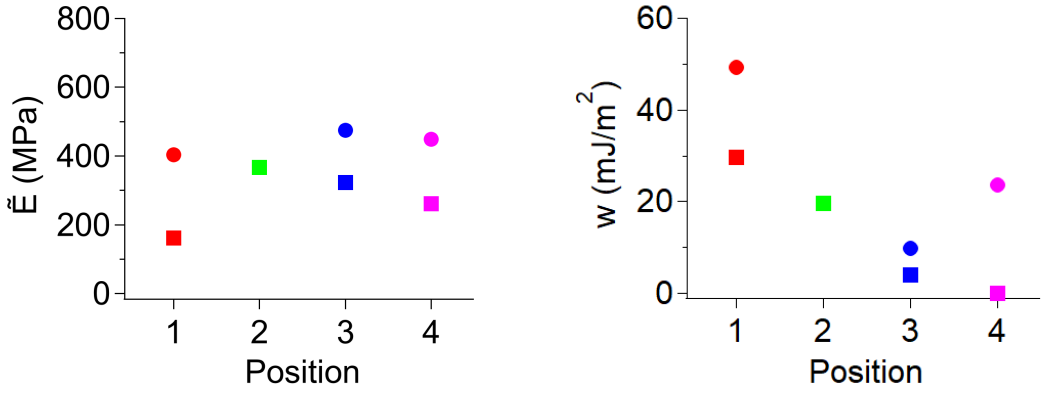

(a) Local effective modulus $\widetilde{E}$.

(b) Local adhesion work w.

Figure 2.12.: Estimate of the effective modulus $\widetilde{E}$ and the adhesion work w for several rubber-ice positions. Squares represent first iterations, and circles represent second iterations. For all fits, the value $R = \sqrt{R_{ice}R_{rubber\ disc}} = 10.7$ mm was used ($R_{ice} = 7$ mm and $R_{rubber\ disc} = 20$ mm).

An example of fit through the JKR equation is given in the figure 2.11b and the values of the fitting parameters - $\widetilde{E}$ instead of E^* and w - are reported in the figure 2.12.

The figure 2.12 highlights several phenomena. The effective modulus and adhesion work values of second load iterations - for all positions investigated - are higher than those obtained after the first iterations. This can be attributed to the existence of a transfer of material between the two surfaces as shown in figure 2.7. The variability of the elasticity from one position to another is not surprising in the case of elastomers because:

- The Poisson's ratio is close to 0.5 (condition of incompressibility).
- The thickness of the rubber is in the range of [10; 60 μm].

Thus, for small variations in the coefficient of incompressibility of the rubber, a very large difference in the apparent elasticity of the rubber can be expected:

- For $E = 3$ MPa and $\nu = 0.49$, $\widetilde{E} \approx 51$ MPa;
- For $E = 3$ MPa and $\nu = 0.499$, $\widetilde{E} \approx 500$ MPa;
- For $E = 3$ MPa and $\nu = 0.4999$, $\widetilde{E} \approx 5000$ MPa;

Another observation is the high volatility of the adhesion work of the ice-rubber en-

semble between the different positions which tends to indicate an heterogeneity of the rubber or/and ice surfaces.

The water used for ice manufacturing was distilled water. Therefore, the heterogeneity cannot arise from ice composition. As described in paragraph 1.3.6.a , the ice was grown from a seed - here the hydrophilic mica mold - with a favored C-axis normal to the mold. Therefore, a possible heterogeneity of the polycrystalline ice at the surface could result in heterogeneous orientation of the axes a and b.

Rubbers - even without additives such as the 'pure' rubber - are composite materials composed of various vulcanized elastomers. Thus, the local variability is not so surprising especially for low applied loads and small contact area - approximately 160 μm wide - more sensitive to local surface properties.

For larger contact areas, figure 2.11a shows that contact area on the different positions and iterations does not always converge to the same value. However, for the range of applied load investigated, the contact size grows with a similar ratio, in concordance with the elasticity $\widetilde{E}$ - which is approximately independent of the position investigated.

2.2.3. 'Tire' rubber case: results and discussion

The evolution of the contact area of 'tire' rubber 7 was also investigated. The figure 2.13 shows that this rubber behaves very differently from 'pure' rubber (see figure 2.11). Two different steps, for all the positions, can be highlighted during loading:

- The first step, in which the contact size increases slowly - up to 5 mN for P3, 28 mN for P2 and 11 mN for P1. This period corresponds to the bumps compression. These bumps could be due to the presence of filler agglomerates at the rubber surfaces as shown by Petitet [7].
- The second step exhibits faster growth of the contact size, which is more consistent with the mechanical behavior of a standard adhesive contact. In this period the contact area versus applied load curve can be fitted via the JKR theory.

The load axis of each plot of figure 2.13 - was re-scaled in order to take into account the contribution of the bump compression by considering that the load origin corresponds to where the contact starts increasing steeply. With this re-scaling, all curves collapse during the second phase which means that the contact behavior is independent of the position on the surfaces. The values of the adjustable parameters, $\widetilde{E}$ and w, obtained from this re-scaling are presented in table 2.2 and are consistent with the observations for the 'pure' rubber in figure 2.12. Therefore it can be assumed that once the compression of the bumps finished, the contact behaves as for a 'pure' rubber.

$\widetilde{E}$ (MPa)	w (mJ.m^{-2})
243	31.7

Table 2.2.: JKR fit parameters used in figure 2.13b with $R = \sqrt{R_{ice} R_{rubber\ disc}} = 10.7$ mm ($R_{ice} = 7$ mm and $R_{rubber\ disc} = 20$ mm).

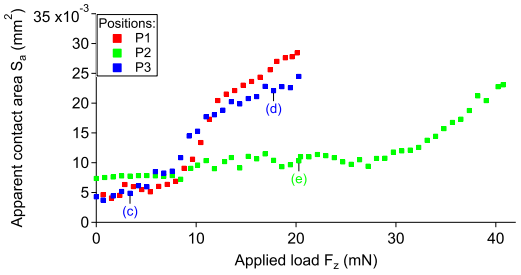

(a) Evolution of the contact area S_a as a function of the applied load F_z.

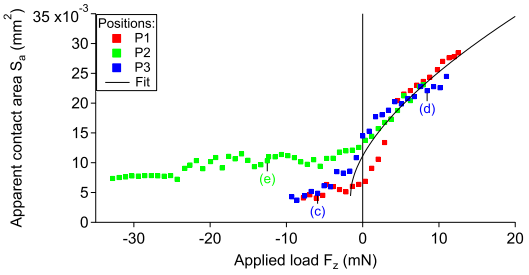

(b) Contact area S_a shifted versus the rescalled to the applied load F_z.

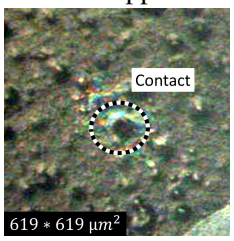

(c) Position P3

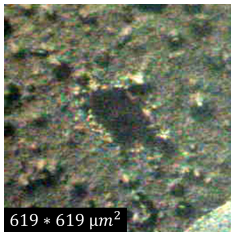

(d) Position P3

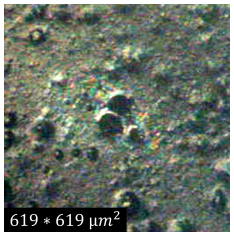

(e) Position P2

Figure 2.13.: 'Tire' rubber-ice contact measurement with associated contact images. Each color represents a rubber-ice position and JKR fits are represented in black. These measurements were performed with a rubber with a thickness of 22 μm and a normal displacement ramp at 1 μm.s^{-1} - i.e a continuous loading ramp of 169 μN.s^{-1}. In the images, the contact area is black - the contact is highlighted in the image (c) - and the asperities of the rubber can be distinguished all around.

The contact images in figure 2.13c, figure 2.13d and figure 2.13e highlight the influence of the morphology on the growth of the contact area during loading. It is easily seen that the black contact area in the figure.2.13d is irregular, unlike the contact in the case of 'pure' rubber shown in the figure 2.9b. This effect was observed for all 'tire' rubber cases.

It was also observed that during the first loading step, the apparent contact area S_a increases much slowly compared to the second step. This corresponds to a decrease of the local modulus of elasticity during the increase of the applied load. The size of the apparent contact area measured for this first step corresponds to bump diameters of 30 to 40 μm. This implies that the high rigidity initially measured is mostly due to the bump of the rubber surface.

From these observations it can be deduced that:

- The contact between the rubber and the ice is initiated at the asperity top. This is correlated with larger scale observations performed by Kriston, Tuononen, Fülöp

and Isitman [83, 84, 85].
- The initial rubber contact area is composed of asperities with an elasticity modulus higher than the rubber matrix surrounding it. This result is consistent with the estimate of the Young modulus of the filler aggregates composing the agglomerates described in section 1.2.2.
- The local morphology of the rubber surface drives the evolution of the contact area.

2.3. Viscoelastic properties of the interface

To investigate the viscoelastic properties of the rubber interfaces, Resonance Shear Measurements were used and the 'pure', 'no filler', and 'tire' rubbers 1, 3 and 7 were tested.

The RSM - detailed in paragraph 2.1.2.b - consists in generating a forced displacement - via a piezotube - within a mechanical oscillator containing a rubber sample. Therefore, the viscoelastic properties of the rubber sample influence the response to the imposed oscillation and can be measured as a function of applied load.

From this description, the RSM is similar to Dynamic Mechanical Analysis - so called DMA - except that:
- DMA measures the 'global' mechanical properties of the rubber;
- RSM measures the local mechanical properties of small rubber surfaces - i.e smaller than 0.1 mm^2.

According to previous JKR measurements, a strong influence of the agglomerates of fillers was expected on the local viscoelastic properties of the rubber.

2.3.1. Description of Resonance Shear Measurement results

The figure 2.14 presents an example of a RSM result obtained with a rubber. The resonance peaks can be divided into three categories depending on the nature of the interface:
- the Air Separation peak (AS) - described in paragraph 2.1.3.e . This resonance peak corresponds to an extreme case where there is no contact between the upper and lower units. The resonance peak is due to the contribution of the mechanical properties of the upper unit such as mass, spring stiffness *etc*
- the Solid Contact peak (SC) - described in paragraph 2.1.3.e . This resonance peak corresponds to another extreme case where there is no sliding at the interface between the disc of the upper unit and the disc of the lower unit. The resonance peak is due to the contribution of the viscoelasticity of the interface in addition to that of the mechanical impedance of both upper and lower units.

- the Rubber contact. These resonance peaks correspond to the frequency behavior as well as the contact mechanics of a thin rubber layer as a function of the applied load. The resonance peaks contain - in addition to information on the mechanical properties of the upper and lower units - information on the viscoelasticity of the rubber layer.

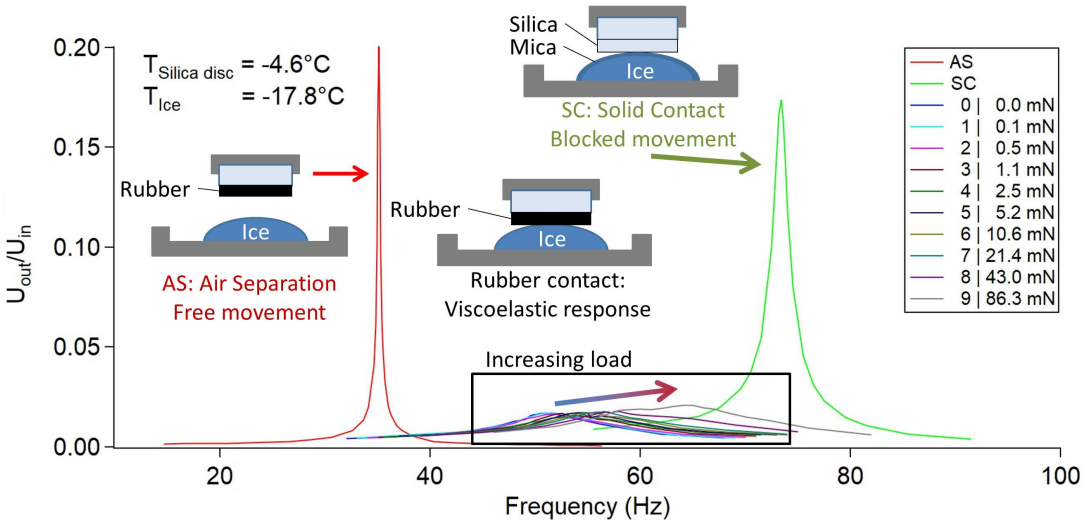

Figure 2.14.: Example of RSM performed with 'pure' rubber on ice. The lowest frequency peak - in red - represents the air separation case which corresponds to a free movement of the rubber surface. The highest frequency peak - in green - represents the solid contact which corresponds to a uniform displacement of the upper silica disc and the lower ice surface - covered with a mica sheet - together.

The existence of the two singularities - i.e the AS and SC cases - makes it difficult to directly interpret the results of the rubber contact results. Indeed, the viscoelastic response of the rubber is mixed with the frequency response of the upper and lower units which can vary from one setting to another.

Therefore, the identification and isolation of the specific rubber response requires a mechanical modeling to identify the system response via the AS and SC measurements.

2.3.2. Mechanical modeling of the RSM measurements

Rubbers are viscoelastic materials which mechanical response presents a strong dependence on:

- the amplitude of the applied deformation;
- the applied stress frequency;
- the temperature.

These characteristics must be taken into account when interpreting the RSM results such as those presented in figure 2.14.

Therefore, a new mechanical oscillator model was proposed based on the previous description of the SFA by Mizukami and Kurihara [96] to analyze the global response of the device and of the interface to the applied sinusoidal signal accounting for the frequency dependence of the rubber viscoelasticity.

The amplitude and temperature dependencies may be neglected because the displacements within the SFA-RSM are small - in the order of a few µm - and then generate a negligible amount of heat.

The global description performed by Mizukami and Kurihara [96] gives a good representation of the different functions of the SFA-RSM. The system is composed - from top to bottom - of:

- The capacitance probe, which provides an output voltage u_{out} to monitor the horizontal displacement of the upper unit;
- An upper unit fixed to the frame by two leaf springs;
- The upper disc - where the rubber surface is located - which is fixed to the upper unit via a piezo-tube. The bending of the piezo-tube is controlled by an applied harmonic voltage u_{in};
- The lower disc - the ice surface - which is directly clamped into the lower unit.
- The lower unit which is fixed to the frame via two leaf springs.

In order to build a mathematical representation of the SFA-RSM, several hypotheses were made:

- The leaf springs were mainly elastic. A small viscous component was also associated to the leaf springs to represent their damping;
- The displacement of the mechanical oscillator was sufficiently small to be considered as only horizontal;
- The piezo-tube worked as a motor producing a bending displacement controlled by a voltage and a frequency. It is the only source of incoming energy;
- The sample investigated - located between the upper and lower surfaces - was a viscoelastic system.

In addition, the following simplifications were made:

- The upper unit and lower unit were considered as point masses m_{1_1} and m_2;
- The piezo-tube was considered to be fixed on one side to the upper unit, and the other side is considered fixed to the sample. The ability of the piezo-tube to deform imposed a difference in position between the two sides. The piezo-tube had its own mass which is here divided between the upper unit - within m_1 and the mass of the 'tip' of the piezo-tube m_{1_2}.
- The viscoelastic sample was considered to be fixed to the lower unit and to the bottom side of the piezo-tube.

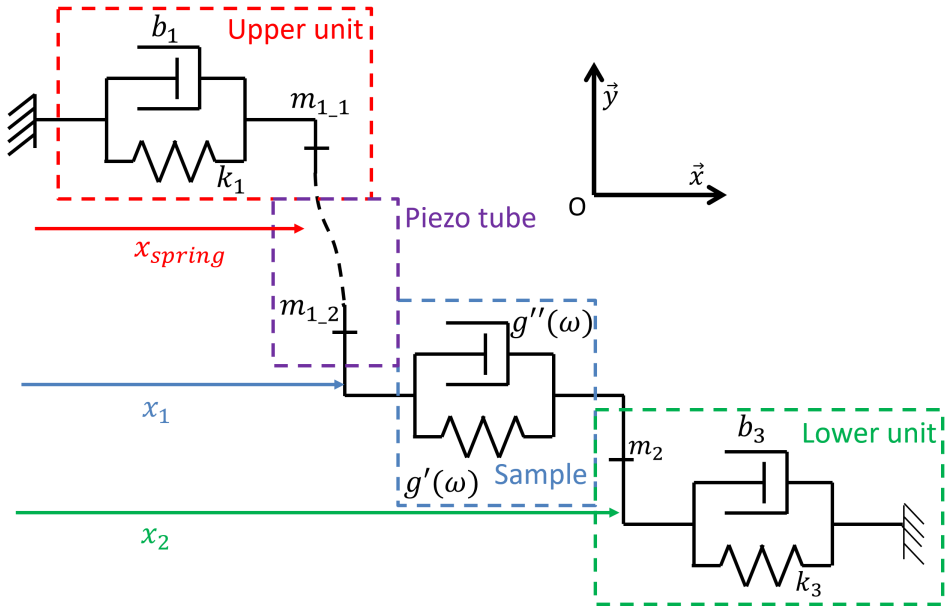

Figure 2.15.: Mechanical model of the SFA-RSM. The upper unit is connected to the frame by two leaf springs as well as the lower unit. The sample is considered as a viscoelastic system. The piezo-tube imposes the displacement between the sample and the upper unit.

From the previous hypotheses, a representation of the system is given in figure 2.15 and the different mechanical equations of the system can be written as:

- The gravitational acceleration of the ground is not considered here thanks to the hypothesis of 'only horizontal displacement';
- The isolated upper unit - numbered as <1> - of mass m_{1_1} at the position x_{spring} is subject to:
  - The contact force of the frame via the spring leafs: $\overrightarrow{F_{frame/1}} = -(k_1 x_{spring}(t) + b_1 \dot{x}_{spring}(t)).\vec{x}$
  - The contact force of the piezo-tube: $\overrightarrow{F_{piezo/1}}$
- The isolated piezo-tube with a mass splitted between m_{1_1} and m_{1_2} is submitted to:
  - The contact force of the upper unit: $\overrightarrow{F_{1/piezo}}$
  - The contact force of the sample: $\overrightarrow{F_{2/piezo}}$
- The isolated sample - numbered as <2> - with zero mass at the position x_1 is submitted to:
  - The contact force of the piezo-tube: $\overrightarrow{F_{piezo/2}}$
  - The contact force of the lower unit: $\overrightarrow{F_{3/2}} = -g(x_1(t) - x_2(t)).\vec{x}$
- The isolated lower unit - numbered as <3> - with a mass m_2 at the position x_2 is

submitted to:

- The contact force of the sample: $\overrightarrow{F_{2/3}} = -g(x_2(t) - x_1(t)).\overrightarrow{x}$
- The contact force of the frame via the spring leafs: $\overrightarrow{F_{frame/3}} = -(k_3 x_2(t) + b_3 \dot{x}_3(t)).\overrightarrow{x}$

where $g(\epsilon(t))$ is the viscoelastic model used for the rubber sample - see page section 1.2.1 - $\overrightarrow{x}$ is the vector of the movement of the mechanical oscillator, k_i is the stiffness of the element i and b_i is the dissipative stiffness (or damping stiffness) of the element i.

The Newtonian fundamental principle of dynamics - with an orthogonal projection on $\overrightarrow{x}$ - is then applied to:

- The upper unit: $m_{1\_1}\ddot{x}_{spring} = -k_1 x_{spring}(t) - b_1 \dot{x}_{spring}(t) + \overrightarrow{F_{piezo/1}}.\overrightarrow{x}$
- The piezo-tube: $\overrightarrow{0} = \overrightarrow{F_{1/piezo}} + \overrightarrow{F_{2/piezo}}$
- To the bottom side of the piezo-tube: $m_{1\_2}\ddot{x}_1(t) = -g(x_1(t) - x_2(t)) + \overrightarrow{F_{piezo/2}}.\overrightarrow{x}$
- To the lower unit: $m_2\ddot{x}_2 = -k_3 x_2(t) - b_3 \dot{x}_2(t) - g(x_2(t) - x_1(t))$

The combination of these equations gives two equations to which are added two other equations that model the piezo-tube bending and the measurement of the capacitance probe. This system of four equations 2.7 determines the resonance shear measurements.

$$\begin{cases} m_{1\_1}\ddot{x}_{spring}(t) + m_{1\_2}\ddot{x}_1(t) + m_2\ddot{x}_2(t) + k_1 x_{spring}(t) + b_1\dot{x}_{spring}(t) + k_3 x_2(t) + b_3\dot{x}_2(t) = 0 \\ \\ m_2\ddot{x}_2(t) + k_3 x_2(t) + b_3\dot{x}_2(t) + g(x_2(t) - x_1(t)) = 0 \\ \\ x_1(t) - x_{spring}(t) = C_{in}u_{in}(t) \\ \\ x_{spring}(t) = C_{out}u_{out}(t) \end{cases} \tag{2.7}$$

The use of Fourier transform on the equations 2.7 - which is developed in the appendix B - allows to obtain the relationship between the complex harmonic signals: $\underline{U_{in}}(\omega, t) = U_{in}(\omega)e^{j\omega t}$ and $\underline{U_{out}}(\omega, t) = U_{out}(\omega)e^{j\omega t + j\phi(\omega)}$.

The final result gives the relationship between the two measured signals $\underline{U_{out}}/\underline{U_{in}}(\omega)$:

- as a function of the different properties of the system;
- as a function of the stress frequency applied by the piezo-tube
- independently of the instantaneous temporal coordinate.

$$\frac{\underline{U_{out}}}{\underline{U_{in}}}(\omega) = \underline{H}(\omega) = -\frac{C_{in}}{C_{out}} \frac{m_{1\_2}(j\omega)^2(m_2(j\omega)^2 + b_3 j\omega + k_3) + \underline{g}(\omega)((m_{1\_2} + m_2)(j\omega)^2 + b_3 j\omega + k_3)}{((m_{1\_1} + m_{1\_2})(j\omega)^2 + b_1 j\omega + k_1)(m_2(j\omega)^2 + b_3 j\omega + k_1) + \underline{g}(\omega)((m_{1\_1} + m_{1\_2} + m_2)(j\omega)^2 + (b_1 + b_3)j\omega + k_1 + k_3)} \tag{2.8}$$

where $\underline{g}$ is a viscoelastic model used for the rubber sample and $\omega = 2\pi f$ is the pulsation with f the frequency.

Two extreme cases can be identified in this model:

- The air separation (AS) case - where $\underline{g} = 0$ - corresponds to a free movement of the upper unit:

$$\frac{\underline{U_{out}}}{\underline{U_{in}}}(\omega) \underset{\underline{g}\to 0}{\longrightarrow} \underline{H}_1(\omega) = -\frac{C_{in}}{C_{out}} \frac{m_{1\_2}(j\omega)^2}{(m_{1\_1} + m_{1\_2})(j\omega)^2 + b_1 j\omega + k_1} \tag{2.9}$$

- The solid contact (SC) case - where $\underline{g} \to \infty$ - corresponds to a direct link between the piezo-tube 'tip' and the lower unit - so when $x_1 = x_2$:

$$\frac{\underline{U_{out}}}{\underline{U_{in}}}(\omega) \underset{\underline{g}\to\infty}{\longrightarrow} \underline{H}_3(\omega) = -\frac{C_{in}}{C_{out}} \frac{(m_{1\_2} + m_2)(j\omega)^2 + b_3 j\omega + k_3}{(m_{1\_1} + m_{1\_2} + m_2)(j\omega)^2 + (b_1 + b_3)j\omega + k_1 + k_3} \tag{2.10}$$

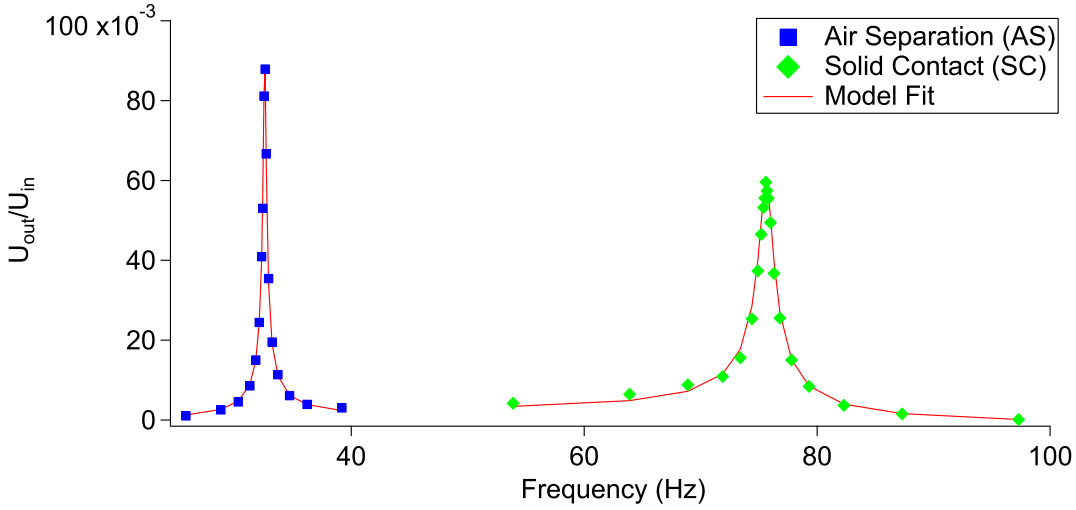

Figure 2.16.: Fitting of the measured signal $U_{out}/U_{in} = \left\|\underline{U_{out}}/\underline{U_{in}}\right\|$ measured with the model. Parameters obtained are: $m_{1\_2} = 8.3$ g, $k_1 = 1275$ N.m^{-1}, $b_1 = 50.6$ mN.s.m^{-1}, $k_3 = 8983$ N.m^{-1}, $b_3 = 312$ mN.s.m^{-1}, $C_{in}/C_{out} = 2.73 * 10^{-3}$ with m_{1_1} fixed at 22.2 g and m_2 fixed at 15 g.

The prediction ability of a model is one of the main criteria of quality. In order to extract values of the parameters m_{1_1}, m_{1_2}, *etc*, two extreme cases, AS and SC measurements, were used.

In addition, to validate the mechanical model, previous measurement of Prof. Mizukami of the displacement of the bottom side of the piezotube, x_1, and of the displacement of the bottom side of the lower unit, x_{spring}, were considered and are presented in figure 2.16. Equations 2.7 were rewritten to give the theoretical evolutions of the displacement ratio $x_1/x_{spring}(\omega)$:

- In the case of the air separation:

$$\frac{\underline{x_1}}{\underline{x_{spring}}}(\omega) \underset{\underline{g}\to 0}{\longrightarrow} -\frac{m_{1\_1}(j\omega)^2 + b_1 j\omega + k_1}{m_{1\_2}(j\omega)^2}$$

and

$$\left\| \frac{\underline{x_1}}{\underline{x_{spring}}} \right\| (\omega) \underset{\underline{g}\to 0}{\longrightarrow} \frac{\sqrt{(k_1 - m_1\omega^2)^2 + (b_1\omega)^2}}{m_{1\_2}\omega^2}$$

- In the case of the solid contact:

$$\frac{\underline{x_1}}{\underline{x_{spring}}}(\omega) \underset{\underline{g}\to \infty}{\longrightarrow} -\frac{m_{1\_1}(j\omega)^2 + b_1 j\omega + k_1}{(m_{1\_2} + m_2)(j\omega)^2 + b_3 j\omega + k_3}$$

and

$$\left\| \frac{\underline{x_1}}{\underline{x_{spring}}} \right\| (\omega) \underset{\underline{g}\to \infty}{\longrightarrow} \sqrt{\frac{(k_1 - m_{1\_1}\omega^2)^2 + (b_1\omega)^2}{(k_3 - (m_{1\_2} + m_2)\omega^2)^2 + (b_3\omega)^2}}$$

These equations were plotted in figure 2.17 and compared to experimental measurements. The very good agreement confirms the validation of the mechanical model.

2.3.3. Viscoelastic response of materials

Resonance shear measurements were performed for all available types of rubber: 'pure', 'no filler', 'tire 1', 'tire 3' and 'tire 7' during loading and unloading.

From these measurements and thanks to the mechanical model described above, the viscoelastic response of the rubber layers in contact with the ice were extracted. The mechanical model considers that the rubber in contact with ice is in a state of total adherence. No sliding was therefore considered at the rubber-ice interface in this model.

Thus, the elastic stiffness $g'(\omega)$ - which is the real part of $\underline{g}(\omega)$ - and the dissipative stiffness $g''(\omega)$ - which is the imaginary part of $\underline{g}(\omega)$ - both in N.m^{-1} - can be obtained from equation 2.8 as a function of the applied load F_z as well as the applied mechanical shear frequency f.

In the following section, the frequency of 30 Hz and the Zener representation of the rubber were considered in order to compare the results obtained for the rubber thin

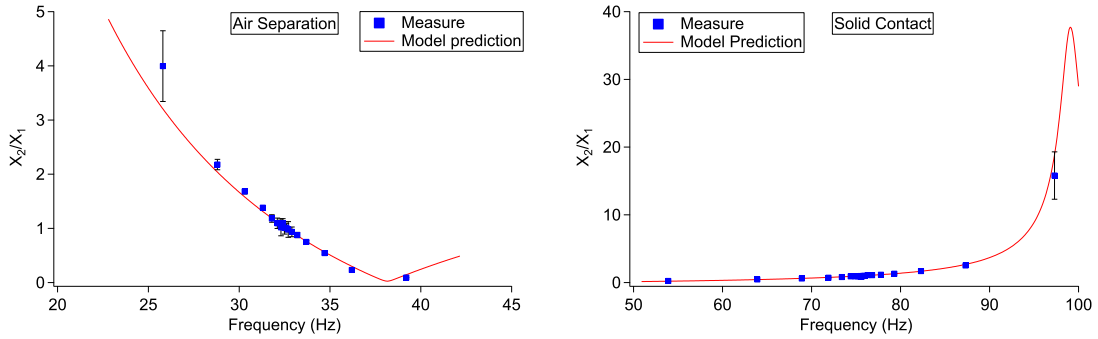

(a) Prediction of the displacement of the SFA during an Air Separation measurement.

(b) Prediction of the displacement of the SFA during a Solid Contact measurement.

Figure 2.17.: Prediction of the SFA displacements by the model based on the parameters obtained from the fit in figure 2.16. The reliability of the mechanical model was good because it made possible the prediction of the measured displacement, especially for frequencies close to the resonance peak of the signal U_{out}/U_{in}.

layers with the available Dynamic Mechanical Analysis (DMA) data measured for 'tire' rubbers.

2.3.3.a . Influence of the rubber composition

The figure 2.18 presents the evolution of the average elastic and dissipative stiffness of the rubber layer as a function of its composition. The average was performed on the few positions probed and the variance is presented in the form of a standard deviation (1σ).

The results presented in the figure 2.18 show a large standard deviation which indicates a variance of the viscoelastic response, position by position and make difficult the comparison of the properties $g'(\omega)$ and $g''(\omega)$ between the different samples.

In addition, viscoelastic properties depend on the temperature. Temperatures of the ice and the silica disc - almost constant during measurements - are presented in the table 2.3. These temperatures give the boundaries of the temperature of the rubber sample.

A clear difference in viscoelastic properties is observed between the loading and the unloading phases. This hysteresis tends to indicate a dependence or a correlation of the viscoelastic stiffness response with the contact area.

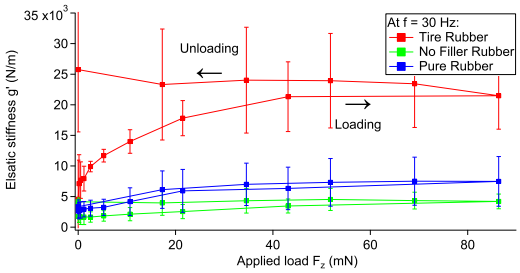

(a) Elastic stiffness $g'(\omega)$ as a function of the applied load.

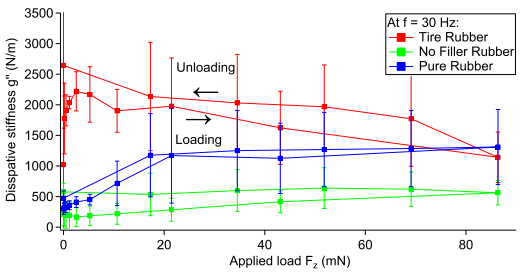

(b) Dissipative stiffness $g''(\omega)$ as a function of the applied load.

Figure 2.18.: Viscoelastic stiffness measured via the mechanical modeling for 'pure' rubber, 'no filler' rubber and 'tire' rubber 7. The average was performed on several positions and error bars represent one standard deviation (1σ).

'Pure' rubber	'No Filler' rubber	'Tire' rubber 7
$T_{disc} \approx -4.6°C$	$T_{disc} \approx -1.3°C$	$T_{disc} \approx -2.0°C$
$T_{ice} \approx -17.8°C$	$T_{ice} \approx -12.9°C$	$T_{ice} \approx -18°C$

Table 2.3.: Average temperature of measurements with 'pure', 'no filler' and 'tire' 7 rubbers. T_{ice} is the temperature of the probe inside the ice, T_{disc} is the temperature of the probe located inside the upper silica disc where was the rubber sample. The temperature variation during RSM experiment was negligible, limited in a range of $\pm 0.5°C$.

To verify this correlation and/or the dependence of the local stiffness on the contact area, the calculation of the viscoelastic shear properties G^* and $\tan\delta$ was performed from the measurements of the complex stiffness on the basis of the classical definition of the shear modulus.

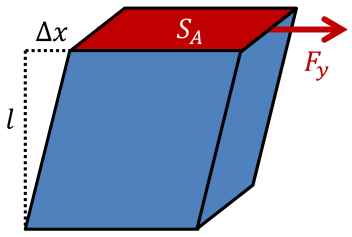

Figure 2.19.: Schematic of shearing principle.

By considering the shearing of a block as presented in figure 2.19, the shear modulus can be written as:

$$G^* \triangleq \frac{F_y/S_a}{\Delta x/l} \tag{2.11}$$

$$G^* = \frac{l}{S_a} g^* \text{ and } G^* = \sqrt{G'(\omega)^2 + G''(\omega)^2} \tag{2.12}$$

and the dissipative factor as:

$$\tan\delta = G''(\omega)/G'(\omega) \tag{2.13}$$

where F_y is the tangential shear force, S_a is the contact area on which is applied the shear force F_y, Δx is the shear deformation, l is the thickness, G^* is the shear modulus, G' is the elastic shear modulus, G'' is the dissipative shear modulus and δ is the loss angle. The evolution of the shear modulus G^* and the dissipative factor deduced from equations 2.12 and 2.13 are plotted in figure 2.20.

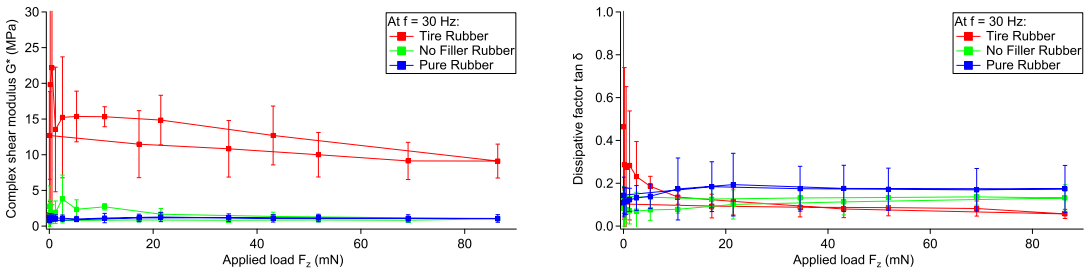

(a) Complex shear modulus as a function of the applied load.

(b) Dissipative factor as a function of the applied load.

Figure 2.20.: Viscoelastic properties of the 'pure' rubber, 'no filler' rubber and 'tire' rubber 7 calculated from the figure 2.18, the apparent contact area measured during JKR measurements and the rubber sample thickness. The average was performed on several positions and the error bars represent one standard deviation (1σ).

Several observations can be made from the comparison of the figure 2.20 with the figure 2.18:

- Materials properties can be now compared because the standard deviation was decreased. It confirms that the variance previously observed was induced by the contact area and rubber sample thickness;
- The hysteresis observed on figure 2.18 is also no more present on figure 2.20, implying a clear dependence on the contact area.

From the comparison of the 'pure', 'no filler' and 'tire' rubbers in figure 2.18 it can be observed that:

1. The shear modulus G^* for the 'tire' rubber is higher than those of 'no filler ' and 'pure' rubbers;

2. The shear modulus G^* shows no standard deviation for the 'pure' and the 'no filler' rubber compared to the 'tire' rubber;
3. The viscoelastic properties of the 'pure' and 'no filler' rubber are similar with respect to the applied load and the local position;
4. Large standard deviations appear for the 'tire' rubber for low applied loads, especially for applied loads lower than 10 mN. This point is discussed further in the next section.

From these different observations, it can be assumed that the 'pure' and 'no filler' rubber present little heterogeneities from a viscoelastic point of view - i.e $G'(\omega)$ and $G''(\omega)$ compared to what is observed for the 'tire' rubber. It implies that the differences observed in the evolution of the contact area in figure 2.11 were caused by heterogeneities of adhesion work, rather than Young modulus. It also correlates with the observation of a large standard deviation of the dissipative factor position by position. The comparison also suggests the presence of fillers is responsible for increase of the viscoelastic variance as well as an increase of the local shear modulus.

For the 'no filler' and 'pure' rubbers, the latter shows no differences implying that addition of plasticizers and oils may not affect the local rigidity of the rubber. This last observation must be tempered by the fact that the temperature between the measurement with the 'pure' and 'no filler' rubbers may be significantly different as shown in the table 2.3.

2.3.3.b . Influence of the material on the mechanical properties

Resonance shear measurements were performed for the three 'tire' rubber samples: 'tire 1', 'tire 3' and 'tire 7' (see figure 2.21).

Ice and silica disc temperatures - which are almost constant during measurements - are presented in the table 2.4. These temperatures give the boundaries of the temperature of the rubber sample.

'Tire' rubber 1	'Tire' rubber 3	'Tire' rubber 7
$T_{disc} \approx -4.0°\text{C}$	$T_{disc} \approx -2.0°\text{C}$	$T_{disc} \approx -2.0°\text{C}$
$T_{ice} \approx -17.5°\text{C}$	$T_{ice} \approx -16°\text{C}$	$T_{ice} \approx -18°\text{C}$

Table 2.4.: Average temperature of measurements with 'tire' rubbers. T_{ice} is the temperature of the probe inside the ice, T_{disc} is the temperature of the probe located inside the upper silica disc on which was the rubber sample. The temperature variation during RSM experiment was negligible, limited in a range of $\pm 0.5°\text{C}$.

The influence of the material on the shear modulus G^* and the dissipative factor is visible on figure 2.21a and figure 2.21c. The applied load also plays a role on the value

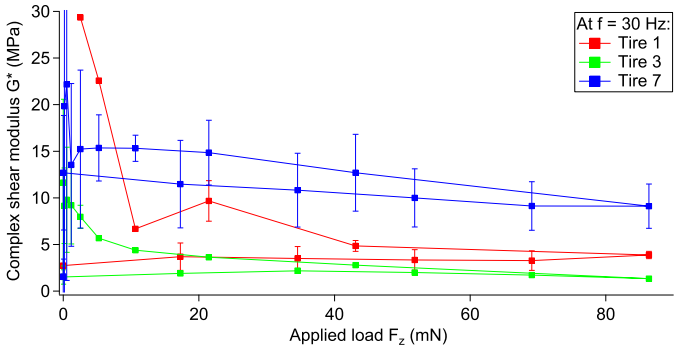

(a) Local average complex shear modulus measured by RSM.

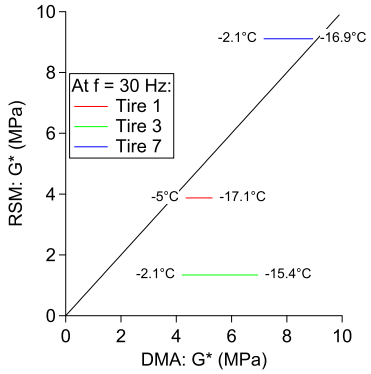

(b) Comparison of G^* measured by DMA and RSM.

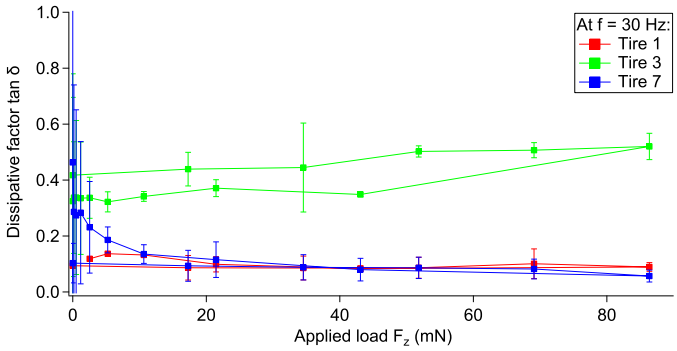

(c) Local average dissipative factor measured by RSM at 30 Hz.

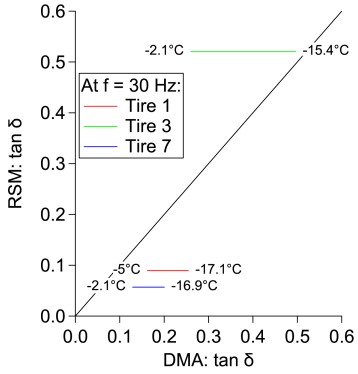

(d) Comparison of $\tan\delta$ measured by DMA and RSM at 30 Hz.

Figure 2.21.: Comparison of the shear modulus G^* and the dissipative factors $\tan\delta$ for 'tire' rubbers. The average was performed on several positions and the error bars represent one standard deviation (1σ). Figure (b) presents the comparison of the G^* values measured at 86 mN on figure (a) to the DMA value for the interval of temperature presented in table 2.4. Figure (d) presents the comparison of the $\tan\delta$ value measured at 86 mN on figure (c) to the DMA value for the interval of temperature presented in table 2.4.

of G^* and $\tan\delta$.

The shear modulus and dissipative factor by RSM can be compared to the one measured by DMA. The contact between the rubber and ice hemi-cylinder is equivalent to the indentation of a rubber plane by a spherical ice, therefore the deformation can be

estimated [7]:

$$\epsilon = \frac{a}{4R} \approx 0.23\% \tag{2.14}$$

with the radius of the contact being $a \approx 120$ μm and the equivalent radius of the two solids $R = \sqrt{R_{ice}R_{disc}} \approx 10.7$ mm.

The shear modulus measured by RSM at 86 mN was therefore compared to the one measured by DMA for low shear strain (0.2%) in figure 2.21b and showed similar ranking of 'tire' rubbers. The shear modulus values measured by RSM and DMA are quantitatively close to each other for high load. The differences may arise from different factors:

- The influence of the temperature on the viscoelastic properties is clearly highlighted in figure 2.21b. For example the viscoelastic properties of 'tire' rubber 3 varies on wide range with temperature, which makes difficult the ranking.
- RSM is performed on small volumes of rubber which behavior is dominated by the presence of filler agglomerates - that can induce a bias such as the Payne effect increasing the local rigidity G'.
- The quality of the fit can also be questioned. The measurements performed to obtain the viscoelastic properties of the rubber were made at a higher frequency than that used in DMA for the comparison. The figure 2.17 shows that the precision of the fits can decrease far from the peaks of frequency presented in figure 2.16.

For low applied loads - up to 10 mN - there is a large variety of shear modulus measured from RSM with values which diverge from those obtained with the DMA. Different hypotheses can be considered:

1. A first one could be the appearance of predominant mechanical behavior at low load such as:
    - A partial or complete sliding of the interface not modeled by the mechanical model. Low applied load favors a larger partial sliding contact area according to Mindlin theory [32, 97, 98]. This sliding may cause additional energy dissipation due to friction.
    - Low initial adhesion due to oils or any other types of materials that can be easily detachable from the surface - as shown in figure 2.7.
2. A second one could be the Payne effect - described in section 1.2.2 - which limits the deformation response due to the oscillation imposed by the piezo-tube. It is known from the JKR measurements on 'tire' rubber, that the ice touches first the asperities made by the agglomerates present on the rubber-surface. Then, when the load is high enough, the contact area increases and the ice comes into contact also with the rubber matrix. This could explain why the values of shear modulus measured by RSM converge to those measured by DMA at high loads.

Two observations can be made from the figure 2.21c:

- The 'tire 7' presents a high dissipative factor for the low load phase.
- The 'tire 3' presents a larger dissipative factor than expected from the DMA for all the applied loads.

The same mechanisms that for the shear modulus - i.e 'carbon black hysteresis' and the Mullins effect - can explain the variability of the dissipative factor.

The comparison of the dissipative factor measured by RSM at 86 mN and DMA presented in figure 2.21d also shows an equivalence in ranking of the 'tire' rubbers. The values of dissipative factors measured by RSM and DMA are close to each other, especially for high load and unloading phases.

The agreement between DMA and RSM (see figure 2.21b and 2.21d) as well as the prediction in the figure 2.17 - validates the mechanical model used to obtain the viscoelastic response of rubbers in contact with the ice.

The non-agreement between DMA and RSM for low applied load - lower than 10 mN - also highlights that the effect of the agglomerates of fillers which decrease the influence of the viscoelasticity of the rubber matrix.

2.4. Conclusion

The study of the rubber-ice contact in SFA with various families of rubber samples: 'pure', 'no filler' and 'tire' - and variations of plasticizers for the last one - allowed us to identify key-mechanisms in their adhesion and viscoelastic properties.

'Pure' rubber is characterized by wide variations of its interfacial energy with ice. These variations are correlated to a large variance of the dissipative factor from one position to another. This could be explained by the local heterogeneities of the rubber-ice interface that may arise from:

- the vulcanized elastomer which is a composite material;
- the non-homogeneous orientation of the a and b axis of the polycristaline ice.

Young modulus of rubber surface and interfacial energy also highlights a possible variation of the interface properties for a contact made of fresh ice or on parts of the surface that have already been squeezed.

The 'no filler' rubber with the 'pure' rubber present similar shear modulus and dissipative factor, which implies that plasticizers and oils may have little effect on these parameters. This observation should be tempered by the fact that the testing temperatures can be different for these two rubbers. It can be worth noticing that the addition of these compounds also resulted in an increase of the average surface roughness.

The 'tire' rubbers exhibit different behaviors due to the addition of fillers such as silica and carbon black. The fillers increased the average surface roughness of the rubbers as they form bumps overall the surfaces. The morphology of rubber surface controlled by these fillers and their organization on the form of bumps influence the evolution of the contact area. The bumps favored the contact with ice on their summit during the initial stage of the loading. Indeed, at low loads, the contact area was small and was mainly due to surface fillers agglomerates. These bumps showed a rigidity higher than that of the surrounding rubber matrix and were responsible for a large variance in shear modulus. They also influence the apparent viscoelastic properties, especially for applied loads lower than 10 mN because of Payne or Mullins effects.

For all the rubber investigated, it was shown that the response of local viscoelastic stiffness was clearly - and not surprisingly - driven by the contact area between the ice and rubber.

The effect of the temperature was not directly studied here, but according to the observations - such as the correlation between DMA and SFA measurements - it is highly likely that the viscoelastic response has a temperature dependence.

Chapter 3

Friction of the rubber-ice sliding interface and real-time contact evolution

---

This chapter presents an investigation of the sliding of the rubber-ice contact, for contact size of few mm in diameter and applied load of 10 N, in terms of contact mechanics and friction.

The Kōri tribometer developed and used for this study is first described. This tribometer allows us to measure the frictional forces and to visualize the rubber-ice interface simultaneously for controlled contact kinematics in a negative temperature environment. The protocols associated to the preparation and characterization of the surfaces as well as the protocols used for the different measurements were detailed.

Static rubber-ice contacts were investigated for several applied loads showing an evolution classically associated to weakly adhesive contacts. Rubber-ice contacts were also observed during sliding at -2.5°C and -10°C. At -2.5°C, the contact remains mainly elliptical while at -10°C, the shape of the contact deforms in the range of velocity [1; 100 mm.s^{-1}]. Ploughing of the ice surface was also observed, the width of the scratches corresponding to the size of the rubber surface asperities.

The effect of the sliding velocity and the temperature was investigated on rubbers with various mechanical properties. The rubber-ice friction as a function of the sliding velocity formed a bell-shaped curve classically observed for rubber friction. The higher the temperature, the lower the friction coefficient.

Several mechanisms are expected to govern the rubber-ice friction response. These mechanisms are ice surface melting due to friction heating [60, 61, 65], adhesion of polymer chains to the ice substrate [44, 80], viscoelastic dissipation within the rubber [46, 49], ice creep due to preferential orientation of the ice structure [56, 70] and the so-called quasi-liquid layer on ice surfaces [56, 57, 66].

In order to deepen the understanding of the ice-rubber friction and to isolate and observe phenomena which may arise from the mechanisms described above, an experimental strategy was proposed, based on the design of a tribometer realizing a contact between ice and rubber under controlled contact kinematics in a cold environment.

Several low temperature tribometers already exist [62, 79, 99, 83, 86, 100, 101] and allow to fulfill at least one of the following requirements:

- to perform a large range of controlled sample-track sliding velocity;
- to measure accurately the contact forces (normal and tangential);
- to reach temperatures 'near' and 'far' below the melting point of ice and maintain this temperature stable over the long-term;
- to control the ice track surface state;
- to observe the contact between the rubber sample and the ice track in real time and simultaneously with the force measurement under a controlled contact kinematics.

However, it is much less common to obtain all of them on the same apparatus. In particular, the simultaneous real-time visualization of the rubber-ice contact represents the unique solution to the lack of information from the buried rubber-ice interface. As a consequence, the Kōri[1] tribometer combining real-time rubber-ice contact visualization, force measurement and a compact controlled environment system was developed. The influence on friction and contact evolution of various parameters such as the sliding velocity, the temperature T, the mechanical properties of the rubber and the surface state of rubber and/or ice was investigated. The discussion about mechanisms responsible for the phenomena exhibited in this chapter is presented in the next chapter.

3.1. Low temperature tribometer

The low temperature tribometer Kōri was designed on the basis of the modular and upgradable tribometer, referred to as LUG tribometer, designed in the Laboratoire de Tribologie et Dynamique des Systemes (LTDS) at Ecole Centrale de Lyon [102].

Several challenges were taken up. The first technical challenge was the ability to cool down the environment of the experiment until negative Celsius temperature for long-term use, independently of outside temperature and humidity conditions. Thus, an

[1]The word Kōri corresponds to the Japanese character 氷(Koori) meaning ice. This character is traditionally used in Japan to indicate places where ice and ice creams are sold.

insufficient thermal insulation increases the dependence of the system on the outside temperature. Humidity, for negative temperature, can easily cause the formation of ice on the fins of heat exchangers, and therefore it can decrease the cooling performance by reducing air circulation. In the litterature, most of the ice-rubber contacts were studied using a cold chamber, where a linear tribometer [83, 99] or a rotating tribometer [79, 100, 62] is located. On the one hand, this approach offers the possibility to reach low temperatures - at least -25°C - readily with a commercial cold chamber. On the other hand, it implies that the tribometer can only be devoted for negative working temperatures and that its electrical, mechanical and optical components have to be adapted to a cold environment. This solution has two major consequences:

- It requires to continuously run the chamber in order to avoid defrosting problems such as:
  - electrical short-circuit caused by melted ice;
  - optical obstruction caused by moisture on lens;
- It requires to keep stable the monitoring parameters of the tribometer, in order to avoid problems such as thermal expansion.

The second technical challenge was the quality and reproducibility of the ice surface, and therefore the ice track preparation. Indeed, surface manufacturing has a strong influence on contact behavior and friction results [80, 77] as it affects the whole tribological response of contacts involving ice.

The third technical challenge, much less addressed in the literature, is the ability to visualize the ice-rubber contact in real time. If previous attempts were successful in tracking the evolution of the ice surface before, during and after the friction tests [79, 86, 83, 84, 85], hardly any of them addressed the question of real-time contact evolution in terms of contact area, etc. This is also due to the quality of transparency of the ice and to its micrometric to millimetric thickness that make classical interferometry techniques less adapted.

Considering these elements, a compact system that offers real-time contact visualization simultaneously to force measurements (from 0 to 30 N for the tangential force F_y and from 0 to 50 N for the normal applied force F_z) under controlled contact kinematics (from 50 μm.s^{-1} to 3 m.s^{-1}) and cold controlled environment (until -20°C), was developed. Particular attention was paid to the visualization of the contact between a transparent ice and a rubber sample, using the adequate light source, camera and controlling the ice quality, both bulk and surface. A dedicated image processing was also developed.

3.1.1. The LUG tribometer

The basic principle of the LUG tribometer is to realize a point contact between two rotating solids, a disc and a sphere, which velocities were controlled independently and

simultaneously, while measuring the contact forces and visualizing the contact area - as shown in figure 3.1. The LUG tribometer usually works at ambient temperature. In this study, it will be combined with a modified visualization unit and an environmental temperature control system.

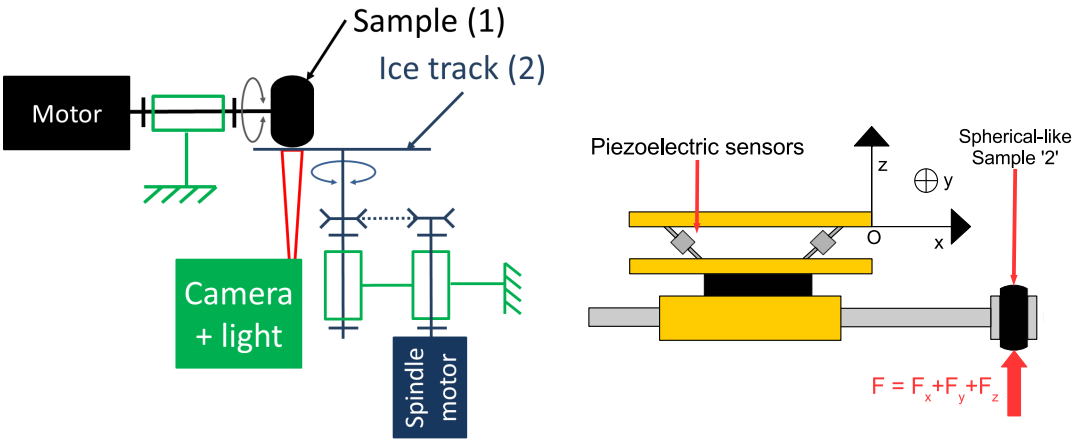

(a) Schematic of the modified LUG tribometer kinematic. The glass disc is replaced here by an ice disc.

(b) Lateral view schematic of the force measurement system.

Figure 3.1.: Figure (a) presents the rubber sample (1) and the ice track (2) kinematics. Rotations can be controlled independently and simultaneously by two synchronous motors. A camera is used for real-time observation of the sample-track contact through ice track. Figure (b) presents the force measurements system. Contact forces, between the sphere and the disc, applied at the tip of the axis are measured with off-centered force sensors.

3.1.1.a . The tribometer

The LUG tribometer itself was detailed elsewhere [102]. The tribometer is composed of an aluminium plate on a hollow concrete bloc. At the center of the aluminium plate is located a vertical high precision spindle driven in rotation, by a brushless servomotor (Kollmorgen, AKM64L-ANCNR-00), from 0.001 to 3500 rpm with a maximum torque of 21 N.m. Speed and angular position of the spindle are measured at high frequency (almost 1650 Hz) with a high resolution encoder from Renishaw, with a resolution of 0.001°. The disc sample holder is fixed to the spindle. The disc diameter is 90 mm. The second solid in contact, here the rubber barrel, is fixed to the motorized axis of the force measurement module, by means of a ER collet system. The rubber barrel is obtained by compressing a rubber cylinder with a diameter of 30 mm, between two steel surfaces,

until the largest diameter of the barrel reaches 31.1 mm. It results in a rubber sample with two radii of curvature.

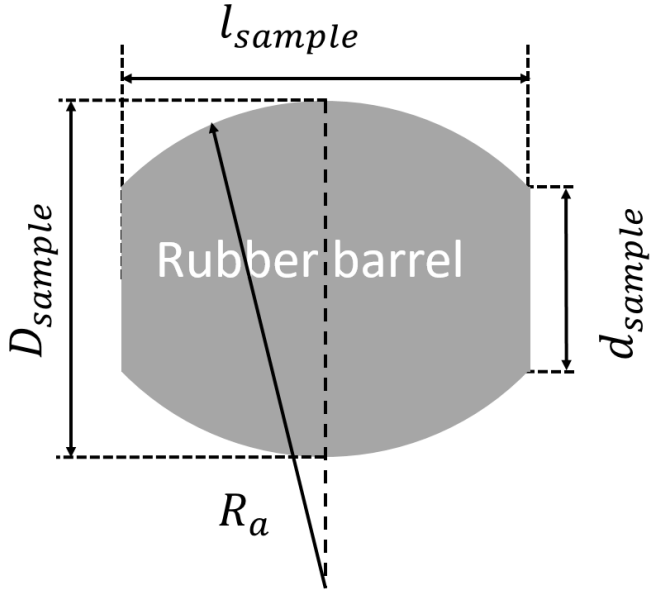

Figure 3.2.: Scheme of the circular rubber barrel.

The first one is calculated from the measurement of the largest diameter D_{sample} of the rubber sample:

$$R_b = \frac{D_{sample}}{2} \tag{3.1}$$

The second one is calculated from the measurement of the largest diameter D_{sample}, the smallest diameter d_{sample} and the width l_{sample} of the rubber sample and by using the equation of curvature of circular barrel (see figure 3.2):

$$R_a = \frac{(D_{sample} - d_{sample})^2 + l_{sample}^2}{4(D_{sample} - d_{sample})} \tag{3.2}$$

All the rubber samples used in this study had the same dimensions $D_{sample} \approx 31.1$ mm, $d_{sample} \approx 30$ mm and $l_{sample} \approx 11.9$ mm, leading to $R_a \approx 32.5$ mm and $R_b \approx 15.5$ mm. The rubber barrel curvature radii and the ice disc are presented in figure 3.3b. The rubber sample is fixed to an axis which can be driven in rotation by a brushless servomotor (Kollmorgen, AKM22E-ANBNR-00) from 0 to 8000 rpm. Kinematic of the tribometer is shown in figure 3.1a. This allows us to perform a large variety of contact kinematics from pure rolling, rolling-sliding to pure sliding.

3.1.1.b . The contact visualization unit

The contact visualization part consists of a motorized optical macroscope from Leica located under the flat transparent ice disc inside the concrete bloc. The position of the macroscope can be adjusted vertically and horizontally by means of micrometer screws. A high pressure Mercury lamp, emitting a white light, was used with magnification from x10 to x80 in order to observe the contact between the transparent ice disc and the rubber ball. The camera, Jai GO-5000C-USB, offers a resolution of 5x5 μm^2 with pictures of 2560x2048 pixels in size. The use of an ice disc implied a specific development, detailed later in this chapter (paragraph 3.2.2.b).

3.1.1.c . The force measurement system

A load is applied between the disc and the sphere thanks to the vertical displacement of the sphere holder and the resulting forces, up to 30 N for the tangential force and 50 N for the normal force, are measured simultaneously. These measurements are obtained through 6 strain gauges (FB101, Technologie et Equipement Industriel TEI) runways in a triangular layout (see figure 3.1b). The main advantage of this system is its ability to measure the contact forces and torques, far away from the contact itself (few cm away), as shown in figure 3.1b. This allows one to maintain the force sensors at room temperature, even if the contact itself is located in the cold chamber, avoiding any temperature drift. The use of an ice disc generated a specific development, detailed later in the paragraph 3.2.2.b .

3.1.2. The environmental temperature control system

To design a compact cooling system capable of reaching negative temperature in a fast and reproducible manner, several constraints were taken into account. Among them, the three main ones are listed below:

- The system had to reach low temperatures, down to -20°C, despite seasonal temperature variations, from 15°C to 38°C, and potentially high humidity rate;
- During air cooling operations, the system had to be opened to set ice in position, change tools or rubber samples and then the temperature had to quickly return to its operating value;
- The geometry of the tribometer lead to various thermal and air leakage.

3.1.2.a . The cold environment generation

To optimize environmental stability, the cooling system was structured in two chambers, the so-called 'generating' chamber and the 'test' chamber. The former corresponds to the chamber where the cold air is produced and stored. This chamber with the largest

volume of almost 15 dm^3 is never opened during cooling operations. The latter, where the friction tests are performed has the smallest volume.

The two chambers which are presented in figure 3.3 are connected by a lateral hole, in which a commercial PC fan was placed to force air circulation from the 'generating' chamber to the 'test' chamber. The fan velocity can be adjusted or switched off to avoid air transfer when the 'test' chamber is opened to handle ice disc or tool-sample.

The cold air is produced in the 'generating' chamber by an air-oil heat exchanger (6120G1SB, Lytron). Two additional metallic fans (Kona fan, Lytron) placed on the heat exchanger were used to perform forced convection. The cold oil is produced by a refrigeration bath circulator (Huber CC-505, Huber). During the operation of the tribometer, the 'generating' chamber produced cold and dry air, the humidity of the environment is accumulated in the fins of the heat exchanger in the form of ice, drying the air.

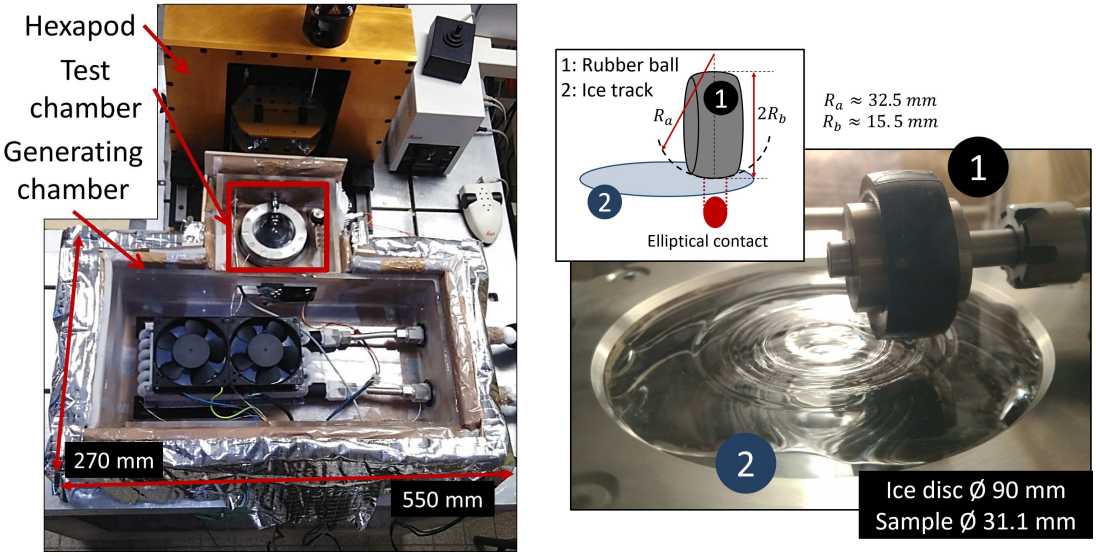

(a) Global view of the cooling system.

(b) Rubber and ice samples in test conditions.

Figure 3.3.: Kōri tribometer. Figure (a) presents the different parts of the tribometer with from bottom to top: the largest 'generating' chamber, the smallest 'test' chamber and the force measurement system. Figure (b) presents a zoom of the test chamber where the rubber sample is in contact with the transparent ice. The schematic illustrates the contact between the rubber sample and the ice track and the two main curvature radii R_a and R_b of the rubber barrel.

3.1.2.b . The thermal insulation

To reach low temperature in both chambers, independently of the outside temperature, a high level of thermal insulation was compulsory. For this purpose, different types of common thermal insulation materials were chosen regarding to their conductive properties: multi-layer insulation, expanded polystyrene, 'static' air and silica aerogel (Spaceloft, Isolproducts). A combination of these materials was used to cover the acrylic walls, bottom and top sides of the chambers. A 20 mm thick sheet of silica aerogel held by a wooden frame was added on the acrylic walls. A multi-layer insulation sheet was installed on the exterior of the wooden frame to trap a 'static' air layer within a 20 mm space between both. A 20 mm thick sheet of silica aerogel was placed under the bottom side of the 'generating' chamber. A 10 mm thick sheet of expanded polystyrene was placed under the 'test' chamber, silica aerogel was not used because potential damages could occur from the rotation of the tribometer. 20 mm of expanded polystyrene and a multi-layer sheet were used on the top, for user comfort reasons. Another multi-layer sheet cover was also added on the entire 'generating' chamber to reduce the effect of remaining existent thermal/air leakage in the thermal insulation described previously.

To operate the system with an optimal control of temperature over a long period of time (few hours), it was necessary to minimize air exchange between the inside and the outside of the system. Depending on outside conditions, these exchanges introduce humidity within the system. The latter tends to freeze on the various cooling parts, and therefore induces a decrease in performance.

To allow friction measurement, an access hole for the sample holder was opened in one of the walls of the 'test' chamber. This hole brings a thermal and air breach. To reduce this air leakage and compensate the thermal loss, a polymer membrane was added between the box and the sample holder. Another thermal breach was created by an access hole within the spindle to be able to perform contact visualization. To do so without any air leakage and to be able to visualize the contact, a 1 mm thick glass disc was installed on the microscope optical path under the ice disc.

3.1.2.c . The temperature control and monitoring

In order to control and monitor temperatures in the system, five temperature probes were used.

- The control temperature probe, provided with the cooling bath circulator Huber CC-505, was placed in the 'test' chamber at the same height as the ice disc. It was used to automatically drive the cooling bath circulator during the normal operating mode (i.e. when both chambers were closed).

- Two monitoring temperature probes (K-type thermocouple with a temperature range from -75°C to +250°C, TC Direct) were placed in the 'generating' chamber, one near the top of the heat exchanger output and the second one near the oil pipe entry pass in the 'generating' chamber wall (Figure 3.4a). These probes monitor the performance of the air cooling of the system.

- The two last temperature probes, also K-type thermocouple with a temperature range from -75°C to +250°C, TC Direct, were located in the 'test' chamber, one near the transfer hole between the two chambers and the other one near the access hole for the sample holder. These probes monitor the homogeneity of the 'test' chamber temperature. Figure 3.4a presents the location of the monitoring temperature probes in both chambers.

3.1.3. Validation of the cooling system

In order to validate the temperature performance of the cooling system and its different compounds (thermal insulation, thermal exchanger and ventilation systems), a cooling test was performed. The room temperature was 23°C. This test consists in four steps and temperatures were continuously monitored at different spots inside the chambers - see Figure 3.4.

- During the first 1h-step, the cooling bath circulator was set to its lowest temperature - -40°C - and both chambers, 'generating' and 'test', were carefully closed. Only the two exchanger fans were switched on. Temperature probes show that temperature in the 'generating' chamber (T_1 and T_2) were homogeneous and rapidly decrease to negative values. In the 'test' chamber, where the temperature is higher, the temperature was slightly heterogeneous (see that $T_3 < T_4$). In order to simulate the real operating process, the 'test' chamber was also shortly opened during this step, leading to an instantaneous increase/decrease in temperature in the 'generating' chamber.
- During the second step, the exchanger fans were switched off and the transfer fan was switched on. This operation was instantaneously associated with an increase in temperature in the 'generating' chamber and a temperature decrease in the 'test' chamber. In addition, the temperature in the 'generating' chamber became heterogeneous with a lower temperature near the thermal exchanger (T_1).
- During the third step, all the fans were switched on and the temperature inside the 'generating' chamber became homogeneous. In the 'test' chamber, the temperature was still heterogeneous, but the difference between T_3 and T_4 decreased with $T_3 > T_4$.
- During the last step, the rotation speed of the transfer fan was increased, leading to an homogeneous temperature inside the 'test' chamber and allowing to reach temperature below -20°C after 6 hours of cooling.

These different steps highlighted the interest and capabilities of the different fans as well as thermal insulation to cool down and homogenize the environmental temperature of the 'test' chamber where tribological experiments will be performed.

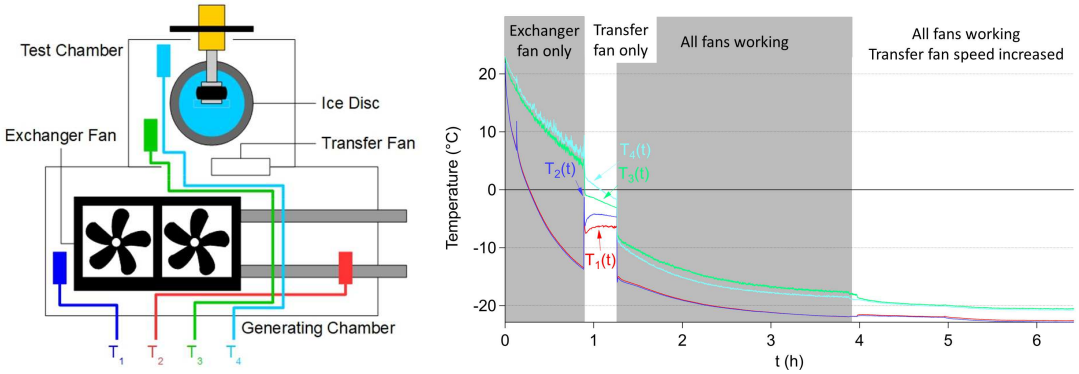

(a) Localization of the monitoring temperature probe.

(b) Temperature during the cooling test.

Figure 3.4.: The position of the temperature probes and of the convective fans are indicated in top view of the environmental chambers (a). Evolution of temperature with time during the cooling test is presented (b).

3.2. The surfaces

3.2.1. The 'tire' rubber surfaces

Rubber-ice friction experiments were carried out with 'tire' rubbers 1, 3 and 7 having the same mechanical properties as those used in the chapter 2. Figure 3.5 presents an image of the 'tire' rubber 1 surface obtained via optical microscopy before friction experiment. The rubber surface presents heterogeneities which correspond to agglomerates of filler aggregates as described in the paragraph 2.1.3.a . Similar images were obtained for 'tire' rubbers 3 and 7. The average size and the density of these agglomerates were characterized via interferometrical images for the three 'tire' rubbers and are presented in table 3.1. Similar sizes and density were obtained for the three 'tire' rubber samples.

The average diameter of these agglomerates is almost 30 μm with a density of approximately 40 agglomerates.mm^{-2} which corresponds:

- to the diameters observed for the 'tire' rubber layer used with the SFA-RSM shown in paragraph 2.1.3.a ;
- to the observations of Kriston, Tuononen, Fülöp and Isitman [83, 84, 85] described in paragraph 1.7.3.b ;

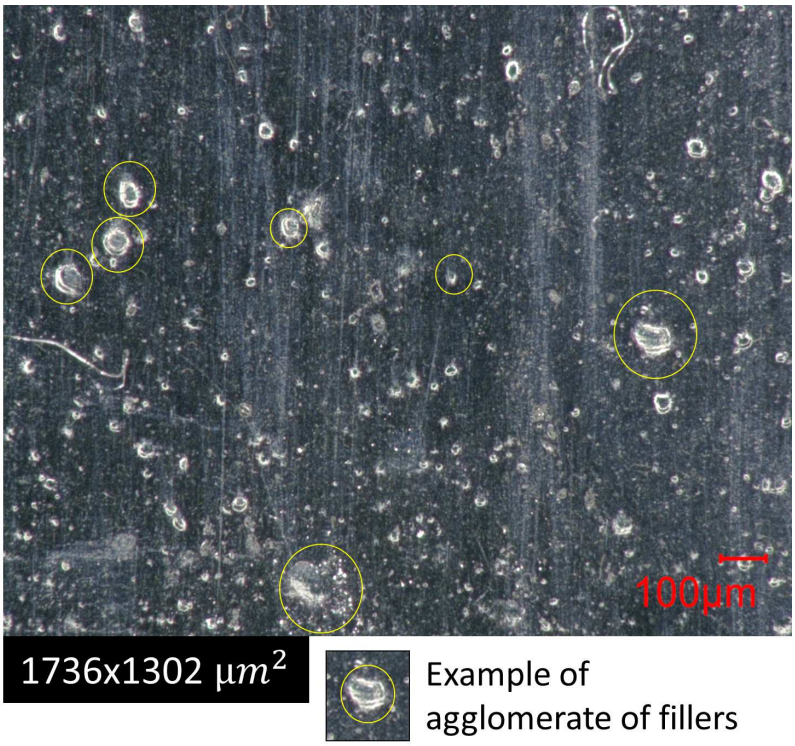

Figure 3.5.: Fresh 'tire' rubber 1 surface images visualized with an optical microscope. The presence of agglomerates of filler aggregates was observed on the rubber surface and examples are highlighted in yellow circles.

'Tire' rubber	1	3	7
Average diameter D_{agg} (µm)	26.3 ± 10.8	33.5 ± 16.4	27 ± 16.9
Average height h_{agg} (µm)	2.85 ± 1.25	3.03 ± 1.59	3.2 ± 1.5
Surface density $\psi_{s\ agg}$ ($agglomerates.mm^{-2}$)	38.9	38.9	44.5
Linear density $\psi_{l\ agg}$ ($agglomerates.mm^{-1}$)	6.2	6.2	6.7

Table 3.1.: Average dimensions of 'tire' rubber 1, 3 and 7 surface agglomerates of filler aggregates measured for one image via interferometrical images of fresh 'tire' rubber surfaces. The average diameter and height are given with one standard deviation. The linear density of agglomerates is given by: $\psi_{l\ agg} = \sqrt{\psi_{s\ agg}}$.

- to the order of magnitude of the size measured by Petitet [7] who got an average size of 25 μm with a distribution of 60 agglomerates.mm^{-2}.

According to the section 2.2.3, the contact at low load between the rubber and the ice surface is favored on the top of these agglomerates and their elastic modulus is larger

than the surrounding rubber matrix, 500 MPa for the aggregates of fillers composing the agglomerates and approximately 3 MPa for the elastomer matrix [7]. Therefore, the agglomerates on the rubber surface may influence the evolution of the sliding rubber-ice interface.

3.2.2. The ice surfaces

The ice used in these experiments was deposited on a 90 mm-diameter non-coated glass disc. Two criteria of quality had to be respected:

- The ice had to be homogeneous and transparent, without bubbles nor cracks. This criterion ensures good conditions of the rubber-ice contact visualization;
- The ice needed to be flat in order to avoid load variations and possible contact loss during one friction cycle.

These two aspects are detailed in the following parts.

3.2.2.a . Transparent ice manufacturing

The natural growth of ice - described in paragraph 1.3.6.a for lake and river case [17, 23] - tends to create bubbles and cracks which are likely to interfere with contact visualization. Bubbles are due to the presence of dissolved gases, within the water, which were not able to reach the surface during ice expansion. Cracks are caused by the trapping of liquid water within the solid phase during the ice growth as schematically shown in figure 3.6a. In addition to the increase in specific volume during the solidification, the trapping of liquid water increases stress within the ice, which can lead to crack formation too.

One solution consists in controlling the velocity and direction of ice growth during the manufacturing process. In our case, we chose to make ice grow from bottom to top: freezing water was directly in contact with air, dissolved gases could easily reach the ice front and water could expand freely in volume. This solution is presented in figure 3.6b.

For this purpose, a dedicated device was designed to create a temperature gradient which controls the velocity and direction of the ice growth. Its principle is presented in figure 3.7.

This device is composed of two elements: a cold source with a Peltier cell, and a heat source with thermal resistances. Both sources were placed in a negative temperature environment, that is to say, a commercial freezer. The heat produced by the Peltier cell was dissipated by means of a heat sink and a fan.

The environment temperature was set at -15°C and the heater was preheated. Thus the silica disc, on which the ice grows, was placed on the cold Peltier cell and almost

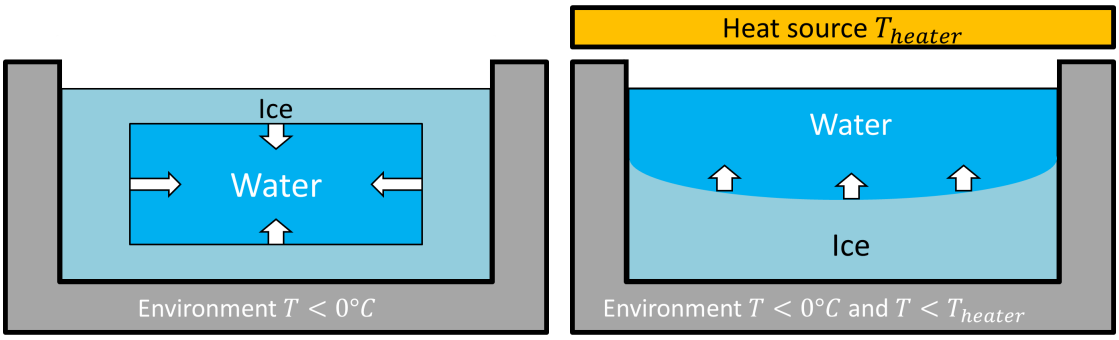

(a) Typical natural ice, growing from outside to inside.

(b) Controlled ice growth, growing with a temperature gradient from bottom to top.

Figure 3.6.: Schematic of ice growing process (a) for typical natural ice and (b) with a temperature gradient. Ice growth preferential direction is indicated with white arrows.

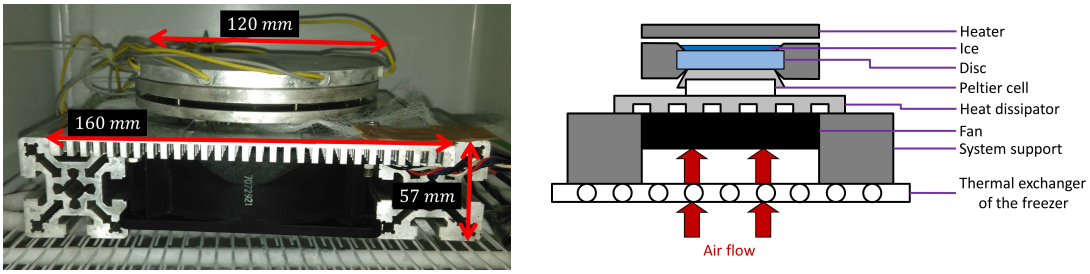

(a) Ice growing device.

(b) Principle of the ice growing device.

Figure 3.7.: The temperature gradient was obtained by means of a heat radiator, located on top, and a cold Peltier cell below. The whole system was placed inside a freezer at -15°C. The electrical voltages, fan speed, etc, were controlled and monitored from outside.

3 ml of distilled water was added on the silica substrate, until full coverage of the surface. Then the heat source was held above the top of the ice - almost 1 mm above - to keep an air circulation and avoid direct contact between the heater and the ice at the end of the freezing process.

Finally the Peltier cell was switched on and 30 min later a homogeneous and transparent ice with neither bubbles nor cracks was obtained in a fast and reproducible manner - as shown in Figure 3.8a.

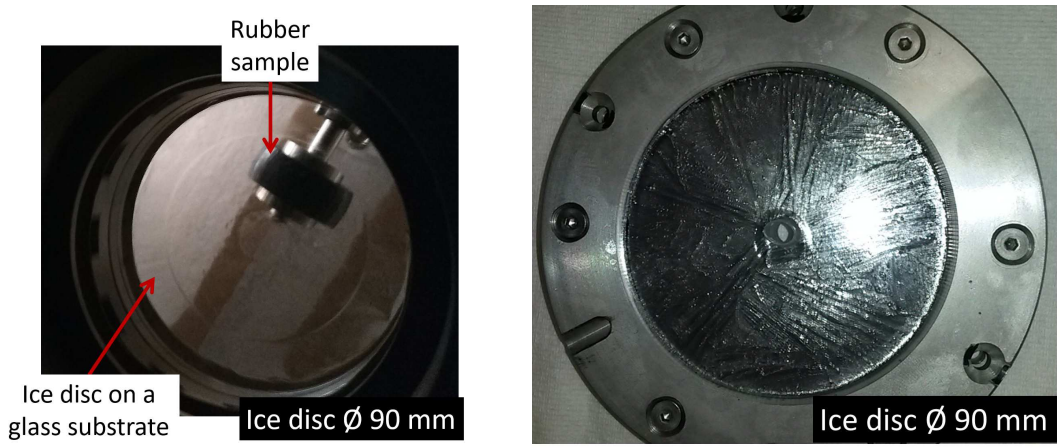

(a) Bottom view of the transparent machined ice from the point of view of the camera.

(b) Top view of a 'naturally' grown ice.

Figure 3.8.: Illustration of ice manufacturing success in (a) and fail in (b). In (a), the rubber sample can be observed through the transparent ice. Figure (b) presents unsuccessful manufactured ice. The crystallization of the ice was not controlled and lead to an opaque surface.

3.2.2.b . Flat ice preparation

Manufactured ice presented a variation of thickness all over the disc surface. This relative variation, of the order of 0.1 mm, could lead to a variation of loading, or even to contact loss during sliding. Ice was then tooled to obtain a flatness that limits the load variation in the range [-0.1 N; 0.1 N] during measurements.

Surface machining of the ice was performed with a commercial chambering tool fixed in place of the rubber sample directly on the tribometer in the cold 'test' chamber. Then, the ice disc was set to rotate at a velocity of 5 rpm at a stable temperature of -5°C. Figure 3.9 presents this tooling process of the ice disc. This setting allowed us to obtain a flat ice track, flattened relatively to the rubber sample during a test, mitigating the possible geometrical defects, in the alignment of the tribometer and to ensure a uniform surface.

3.2.3. Contact preparation

Prior to any rubber-ice friction experiment, the following protocol of preparation was used:

1. Ice was grown on a silica disc and at the same time the 'test' chamber was cooled down to -5°C;
2. Thereafter, the ice was transferred to the 'test' chamber and machined. At the

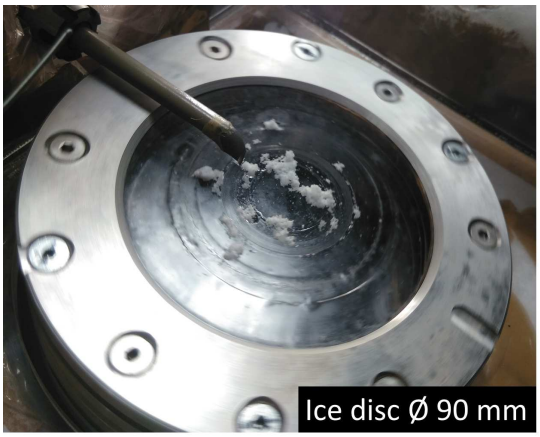

(a) Ice tooling process.

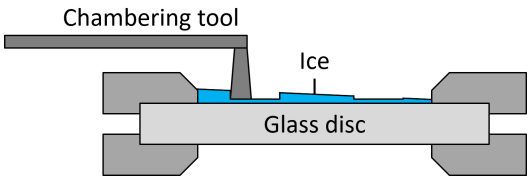

(b) Schematic illustrating the machining.

(c) The chambering tool.

Figure 3.9.: Machining of the plane surface track within the ice at 5 rpm at -5°C.

same time, the rubber barrel-shaped sample was transferred from the storage area at -15°C to the 'test' chamber at -5°C;

3. After the end of the machining phase, the tool was removed and the rubber sample was installed. The temperature set point was changed in order to reach the tested temperature.
4. The rubber was thereafter set in position in the tribometer for one hour and half to ensure the stability of the bulk rubber temperature. A thermocouple was used to measure the bulk temperature of the rubber sample and showed that rubber samples reached the temperature of the 'test' chamber in less than 30 min after being at outside temperature during almost 20 min.

During the transfer of the rubber sample from the freezer to the 'test' chamber, frost may appear on the surface of the rubber. This frost disappeared during the temperature stabilization period due to sublimation in the dry air of the 'test' chamber.

3.3. Static rubber-ice contact

3.3.1. Validation of the contact visualization procedure

Figure 3.10 presents an example of initial images of ice surface and rubber-ice contact as well as the corresponding post-processed image of rubber-ice contact.

As shown in figure 3.10a, the ice surface was optically heterogeneous. Once the rubber was in contact, a darker shape appeared (as highlighted with a continuous line in figure 3.10b). In order to exhibit the rubber-ice contact, a post-processing of the contact image was performed according to the calculations of the two parameters $I_{x,y\ compared}$

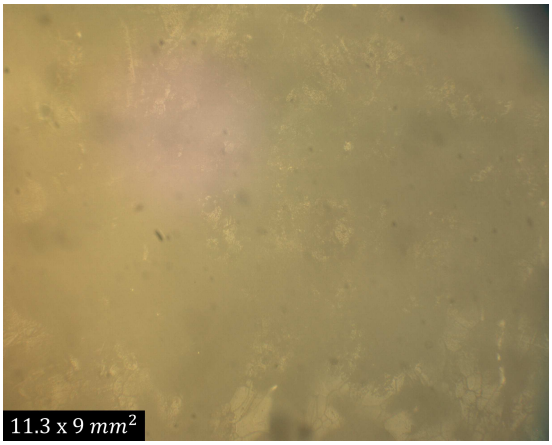

(a) Ice surface without contact with the rubber.

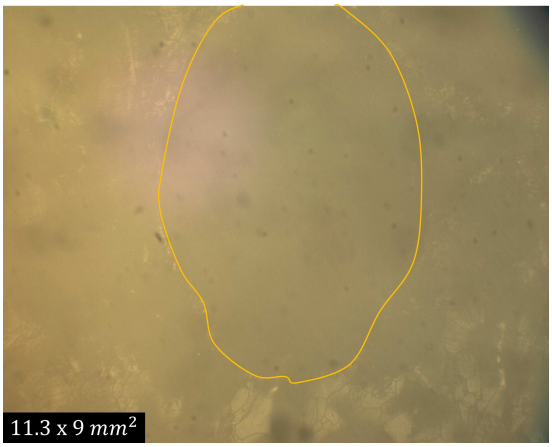

(b) Ice surface with contact with the rubber.

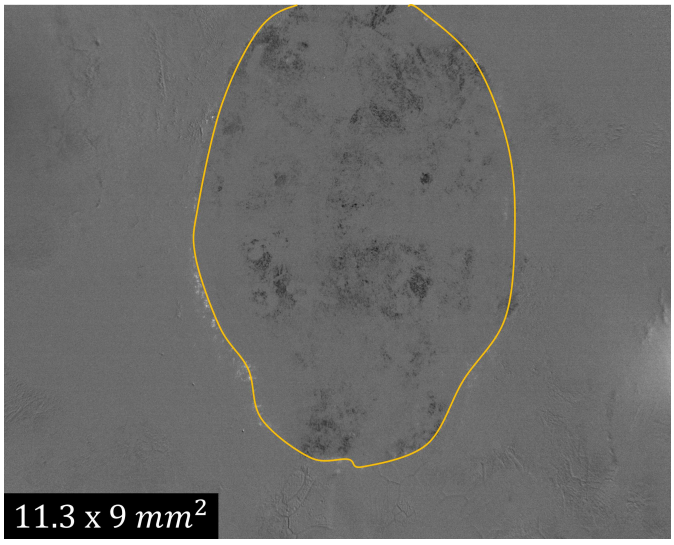

(c) Post-processed image.

Figure 3.10.: Ice surface image without contact (a) and in contact with the 'tire' rubber sample 1 (b) at -10°C after the machining and the thermalization of the ice. The image in figure (a) was taken before the image in figure (b). The figure (c) presents the post-processed image with an improved visibility of the 'tire' rubber 1-ice contact.

and $I_{x,y\ normalized}$ in equation 3.3 and 3.4.

$$I_{x,y\ compared} = \frac{Y_{x,y\ loaded} - Y_{x,y\ unloaded}}{Y_{x,y\ unloaded}} \tag{3.3}$$

$$I_{x,y\ normalized} = \frac{I_{x,y\ compared} - \min\limits_{\forall x,y} I_{x,y\ compared}}{\max\limits_{\forall x,y} I_{x,y\ compared} - \min\limits_{\forall x,y} I_{x,y\ compared}} \tag{3.4}$$

where $Y_{x,y\ unloaded}$ is the greyscale (see equation 2.2) of the pixel at the coordinate {x,y} of the image of the ice surface before contact, $Y_{x,y\ loaded}$ is the greyscale of the pixel at the coordinate {x,y} of the image of the rubber-ice contact, $I_{x,y\ compared}$ is the result and $I_{x,y\ normalized}$ is the normalized pixel of the image resulting from the post-processing.

In equation 3.3, the subtraction exhibits the difference between the two images that may correspond to the rubber-ice contact and the division removes the light heterogeneities from the image. Finally the constrast of the image is increased thanks to the calculation in equation 3.4.

An illustration of post-processed contact image is presented in figure 3.10c. From this image, the number of pixels belonging to the zone identified as the apparent contact area was calculated, leading to a measured value of an apparent contact area. For instance, under 10 N at -10°C, the elliptical apparent contact area measured from figure 3.10c for tire rubber 1 was: $S_a = 34 \pm 1$ mm^2. The apparent contact area was obtained by measuring the circumscribed and the inscribed ellipse of the contact and was calculated as the average of the area of both ellipses.

3.3.2. Analysis of the static contact mechanics

3.3.2.a . Experimental measurements

In order to investigate the adhesive properties of the rubber-ice interface, the contact area was measured as a function of the load for two different positions on ice. In addition, two ice surface states were tested: before sliding (once the ice surface machining and thermalization were achieved) and after a series of 14 sliding steps. The normal load was varied from 0 to 10 N and the temperature was either -2.5°C, near the melting temperature, or -10°C.

Figure 3.11 presents the evolution of the contact size as a function of the applied normal load F_z for 'tire' rubber 1, 3 and 7 before sliding. The contact area increases similarly with the applied normal load, regardless of the temperature. The apparent contact areas were similar for 'tire' rubbers 1 and 3 and larger than for 'tire' rubber 7, consistently with the mechanical properties measured by DMA (see annex A). Very little or no adhesion was detected during the loading phase. During unloading, hysteresis appeared, regardless of the rubber in contact because of a significant increase in adhesion during unloading for the three 'tire' rubbers.

After sliding, a very similar behavior was observed. The hysteresis was larger during

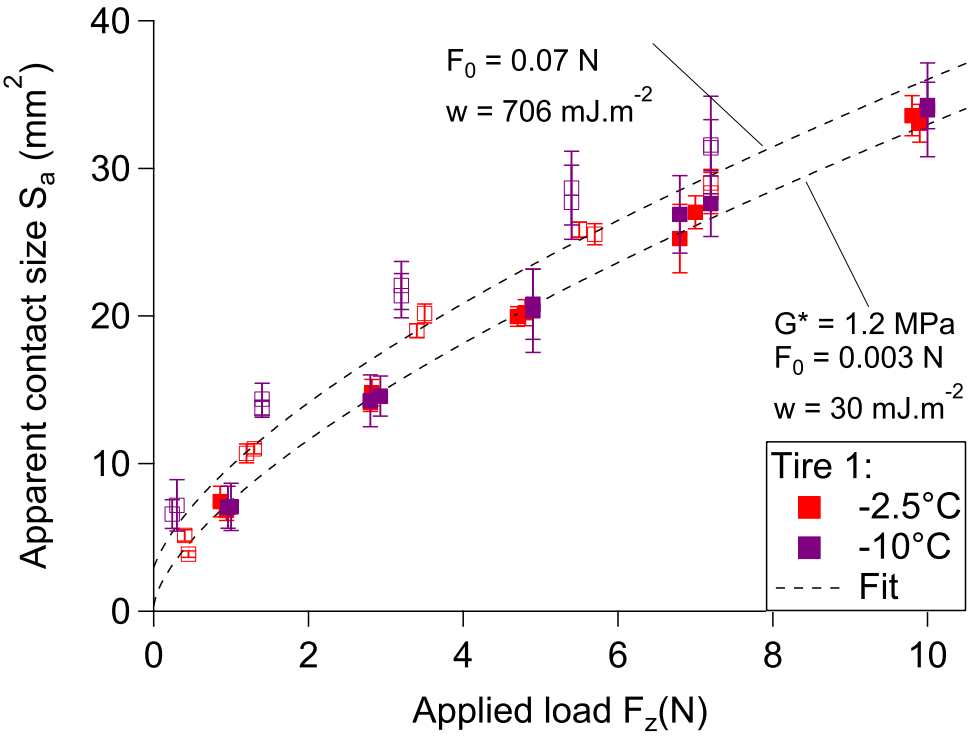

(a) 'Tire' rubber 1.

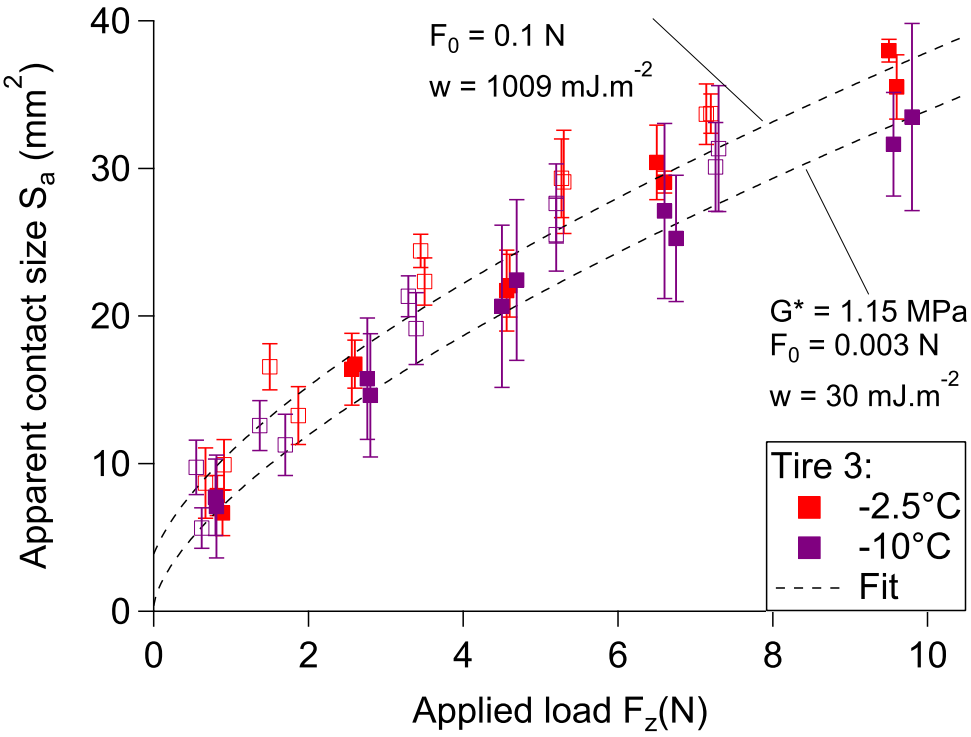

(b) 'Tire' rubber 3.

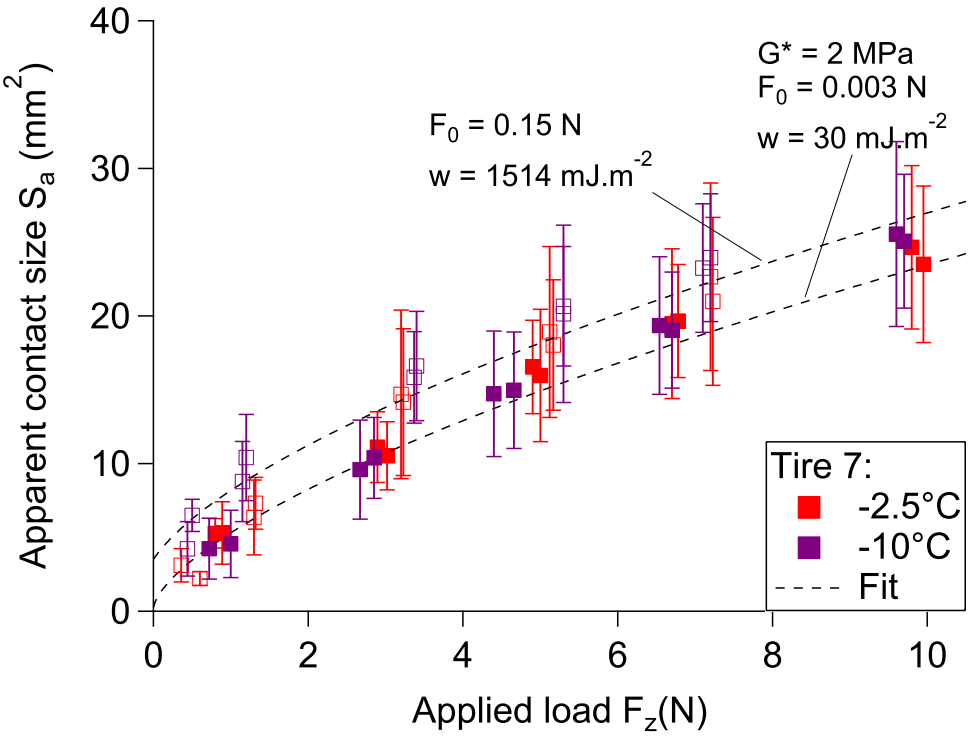

(c) 'Tire' rubber 7.

Figure 3.11.: Contact versus load measurement performed for 'tire' rubbers 1, 3 and 7 for a fresh rubber-ice interface (before sliding) at -2.5 and -10°C. Contact size during the loading phase are indicated with filled squares and during the unloading phase with empty squares. The dotted line represents the JKR fits calculated with the adhesion force F_0, the adhesion work w and the shear modulus G^* indicated in the graphs. The standard deviation represents the uncertainty on the value of the apparent contact area.

unloading as shown in figure 3.12, especially for 'tire' rubbers 1 and 3. After sliding, the uncertainty of the measurement was higher, due to a difficult post-processing of the contact images. This point is illustrated by the diverging sets of data during unloading at -10°C for 'tire' rubbers 1 and 3.

The geometry of the rubber sample was complex, because of its barrel-shape, and presented two radii of curvature, $R_a \approx 32.5$ mm and $R_b \approx 15.5$ mm (see paragraph 3.1.1.a). This leads to an elliptical apparent contact area. For non-adhesive elliptical contacts, one can calculate the semi-major radii [103] from the Hertz theory:

$$a = a_1 \left(\frac{3F_z R'}{2E^*}\right)^{1/3} \qquad \text{and} \qquad b = b_1 \left(\frac{3F_z R'}{2E^*}\right)^{1/3} \tag{3.5}$$

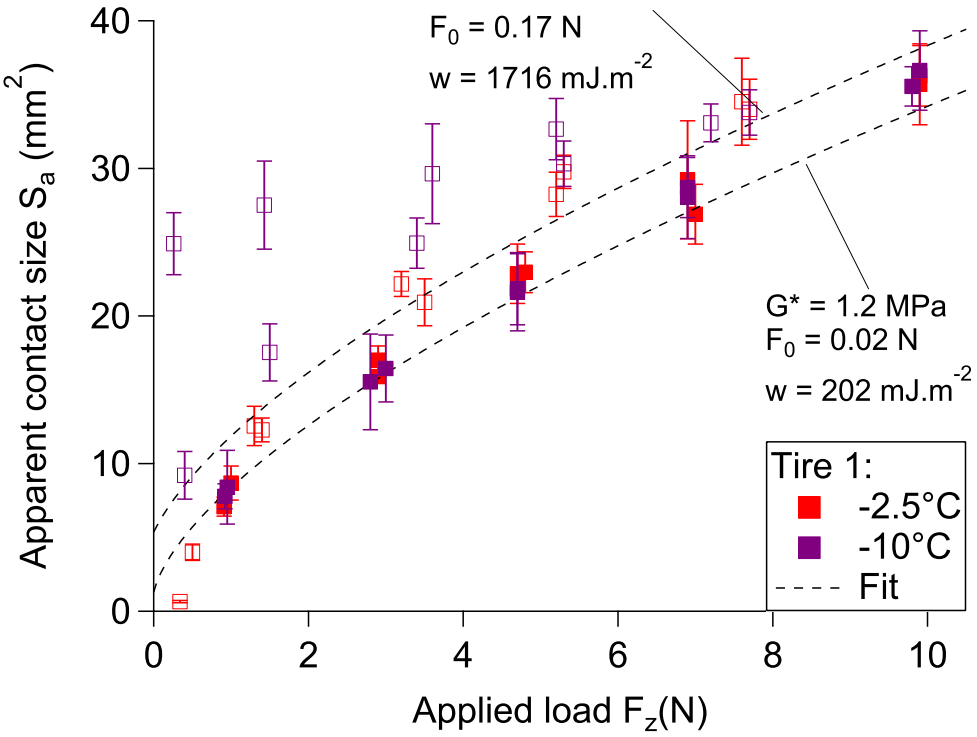

(a) 'Tire' rubber 1.

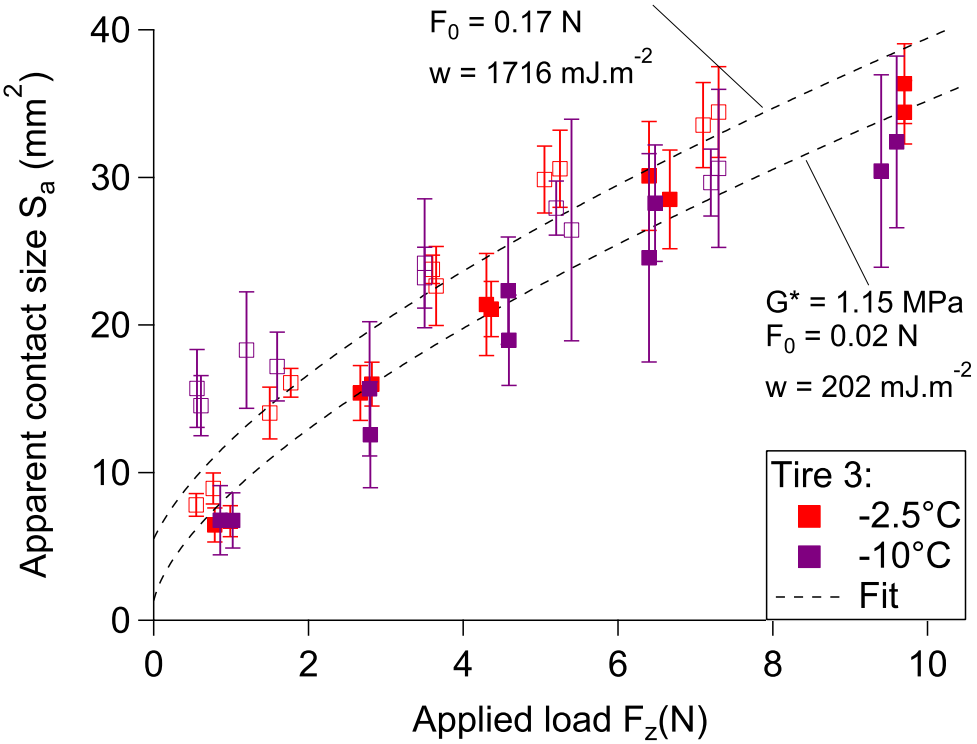

(b) 'Tire' rubber 3.

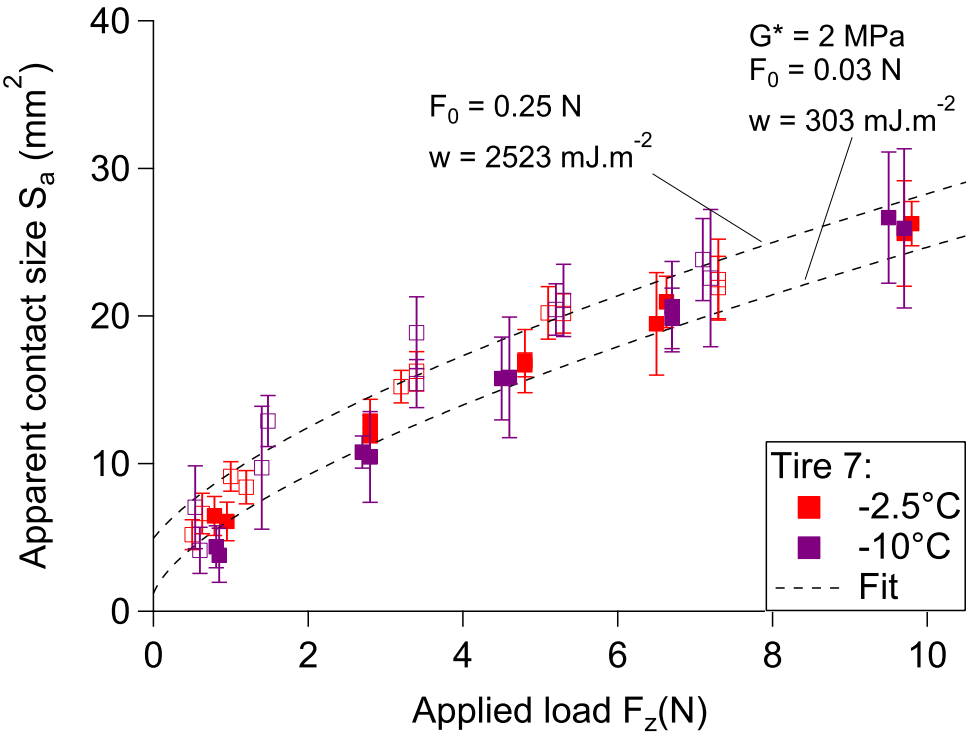

(c) 'Tire' rubber 7.

Figure 3.12.: Contact versus load measurement performed for 'tire' rubbers 1, 3 and 7 for a run-in rubber-ice interface (after sliding) at -2.5 and -10°C. Contact size during the loading phase are indicated with filled squares and during the unloading phase with empty squares. The dotted line represents the JKR fits calculated with the adhesion force F_0, the adhesion work w and the shear modulus G^* indicated in the graphs. The standard deviation represents the uncertainty on the value of the apparent contact area.

where F_z is the applied load, R' is the reduced radius of curvature of the two solids, E^* is the equivalent Young modulus of the two solids.

The reduced radius of curvature of the two solids (including a flat) can be calculated [103], as:

$$R' = \left(\frac{1}{R_a} + \frac{1}{R_b} \right)^{-1} \tag{3.6}$$

The coefficients a_1 and b_1 depend on an ellipticity prameter, $k_{ellipticity}$ that is given by [103]:

$$k_{ellipticity} = \frac{\sqrt{\left(\frac{1}{R_a} - \frac{1}{R_b}\right)^2}}{\left(\frac{1}{R_a} + \frac{1}{R_b}\right)}$$

where R_a is the major radius of the rubber sample and R_b is the minor radius of the rubber sample.

$k_{ellipticity}$ is about 0.35, resulting in $a_1 = 1.25$ and $b_1 = 0.8$ [103]. The relative difference in contact area, between the elliptical case and the circular case, for this value of ellipticity, is less than 3%. This small relative difference between the elliptical and circular case was demonstrated by Johnson and Greenwood [95] for mildly elliptical contact ($R_a/R_b < 5$). In our case $R_a/R_b \approx 2.10$, that is why in the following, we will use the theories applied to circular contact cases with a reduced radius R' of 10.5 mm.

3.3.2.b . Modeling of the contact mechanics

The investigation of the 'tire' rubber-ice surface interactions in chapter 2 provided an estimation of the adhesion work of 30 mJ.m^{-2} in agreement with the work of Roberts and Richardson [80]. This corresponds to an adhesive pull-off force of 0.003 N in this geometry, below the resolution of the measurement at macroscale.

The plot of the JKR apparent contact area (see equation 1.3) as a function of the load was presented in figure 3.11 and 3.12 with $G^*_{tire\ 1} \approx 1.2$ MPa, $G^*_{tire\ 3} \approx 1.15$ MPa and $G^*_{tire\ 7} = 2$ MPa and $F_0 = 0.003$ N for 'tire' rubber 1, 3 and 7 during loading. These shear modulus values correspond to the DMA measurement for a stress frequency of 0.01 Hz for large shear strain deformation (10%) presented in annex A. In our case, the rubber deformation was static and the deformation value was of the same order of magnitude [7]:

$$\epsilon = \frac{a}{4R} \approx 4.3\% \tag{3.7}$$

with the radius of the contact being approximately $a \approx 3.9$ mm and the equivalent radius of the two solids $R = \sqrt{R_a R_b} \approx 22.4$ mm.

This predicts pretty well the experimental evolution of the contact area during the loading phases before sliding for the three 'tire' rubbers. Larger values of pull-off force, $F_0 = 0.07$ N for 'tire' rubber 1, $F_0 = 0.1$ N for 'tire' rubber 3 and $F_0 = 0.15$ N for 'tire' rubber 7 were required to describe the evolution of the contact area during unloading before sliding.

After sliding, larger values of pull-off force than before sliding, $F_0 = 0.02$ N for 'tire' rubber 1, $F_0 = 0.02$ N for 'tire' rubber 3 and $F_0 = 0.03$ N for 'tire' rubber 7 were required to describe the evolution of the contact area during loading. The pull-off force measured was enhanced after sliding experiments for the three 'tire' rubbers with $F_0 = 0.17$ N for 'tire' rubber 1 and 3 and $F_0 = 0.25$ N for 'tire' rubber 7. It was

attributed to the transfer of rubber and oil over the ice surface, as shown in chapter 2, and/or to ice surface modification during sliding.

Before sliding, the adhesion works measured (almost 30 $mJ.m^{-2}$) were consistent with the observations from the section 2.2.2 and the litterature [80]. During unloading the adhesion works required to pull off the rubber was much larger (from 700 $mJ.m^{-2}$ to 1500 $mJ.m^{-2}$) than during loading. It implies that it is energetically favorable for the rubber and the ice to be in contact than to be separated by air. Therefore, this mechanism might induce an adhesive friction force. After sliding, the work of adhesion during the loading (from 200 $mJ.m^{-2}$ to 300 $mJ.m^{-2}$) and unloading (from 1700 $mJ.m^{-2}$ to 2500 $mJ.m^{-2}$) were clearly enhanced. As above mentioned, it may be due to modifications of the rubber-ice interface via ice surface wear (see later in paragraph 3.3.3.c). It may imply a larger adhesion friction force for a run-in rubber-ice interface than for a fresh one.

3.3.3. Sliding contact: in situ visualization and its evolution with the sliding velocity and the temperature

The observation of the evolution of the shape and size of the contact as a function of the sliding velocity and temperature can improve our understanding of the frictional behavior of the rubber-ice contact and could be used to detect the occurrence of melting during sliding.

However, as shown in figure 3.10, the images need post-processing to be interpreted. The post-processing used in the previous section cannot be used when the ice moves. This is why two solutions were proposed to investigate the phenomena appearing during rubber-ice sliding:

- To analyze the contact image-by-image. This solution limits the observation to local and transient phenomena.
- To rebuild the image of the contact. This solution requires the development of the adequate post-processing. It limits the observation to stationary phenomena.

3.3.3.a . Sliding contact imaging analysis

The solution adopted to rebuild the contact area from the images is the use of a newly developed algorithm, so called here 'Phantom imaging', as it makes it possible to build an image of the contact that partially appear on several images such as a phantom. This algorithm benefits from the optical properties of the rubber-ice contact as shown in figure 3.13.

- The lightest zone corresponds to an area in which the light is reflected by the ice surface. This means that this zone is non-contact area;
- The darkest zone corresponds to an area in which the light is not reflected by the ice surface. This can indicate the presence of a contact spot or the non-reflectivity

of the ice surface.

The 'Phantom imaging' allows to rebuild in one image, the non-contact area from a set of hundred of images of the contact during the steady-state friction regime (loading and initial shear phases were ignored). More precisely, the algorithm identifies the brightest RGB levels pixel by pixel - which are parts of non-contact area - regardless of the image. From the knowledge of the non-contact area , the apparent contact area can be extracted.

In more details, the algorithm browses all the images of the sliding rubber-ice contact. Two new images were then computed: the so-called phantom image $I_{phantom}$ and the 'average' image $I_{average}$. Each pixel of the phantom image - presented in figure 3.13b - corresponds to the maximum of the levels of red, blue and green of each pixel of the series of images.

$$I_{phantom} = \begin{cases} R_{x,y\ phantom} &= \max\limits_{\forall k} R^k_{x,y} \\ G_{x,y\ phantom} &= \max\limits_{\forall k} G^k_{x,y} \\ B_{x,y\ phantom} &= \max\limits_{\forall k} B^k_{x,y} \end{cases} \quad \text{with} \quad I^k = \begin{cases} R^k_{x,y} \\ G^k_{x,y} \\ B^k_{x,y} \end{cases} \tag{3.8}$$

where $I_{phantom}$ is the phantom image, I^k is the k^{th} image measured and $R_{x,y}$, $G_{x,y}$ and $B_{x,y}$ are the red, green and blue level of the pixel at the position (x, y).

The average image corresponds to the average of the levels of red, blue and green for each pixel position.

$$I_{average} = \begin{cases} R_{x,y\ average} &= \frac{1}{N_{images}} \sum\limits_{k=1}^{N_{images}} R^k_{x,y} \\ G_{x,y\ average} &= \frac{1}{N_{images}} \sum\limits_{k=1}^{N_{images}} G^k_{x,y} \\ B_{x,y\ average} &= \frac{1}{N_{images}} \sum\limits_{k=1}^{N_{images}} B^k_{x,y} \end{cases} \quad \text{with} \quad I^k = \begin{cases} R^k_{x,y} \\ G^k_{x,y} \\ B^k_{x,y} \end{cases} \tag{3.9}$$

where $I_{average}$ is the 'average' image and N_{images} the number of images processed.

The final step was the building of the 'normalized' phantom image - shown in figure 3.13c - based on the phantom image and the 'average' image. First, a temporary image corresponding to an homogenization of the light was built:

$$I_{phantom\ homogeneized} = I_{phantom} - I_{average}$$

therefore the image was normalized:

$$I_{phantom\ normalized} = \frac{I_{phantom\ homogeneized} - \min\limits_{\forall x,y,color} I_{phantom\ homogeneized}}{\max\limits_{\forall x,y,color} I_{phantom\ homogeneized} - \min\limits_{\forall x,y,color} I_{phantom\ homogeneized}} \tag{3.10}$$

where $I_{phantom\ normalized}$ is the 'normalized' phantom image, $I_{phantom\ homogeneized}$ is the phantom image with an homogeneous light, (x, y) is the position of the pixel and $color$ the color index which can be R (red), B (blue) or G (green).

The example of figure 3.13 shows the efficiency and the reliability of this algorithm and how it allows to measure the surface of the apparent contact.

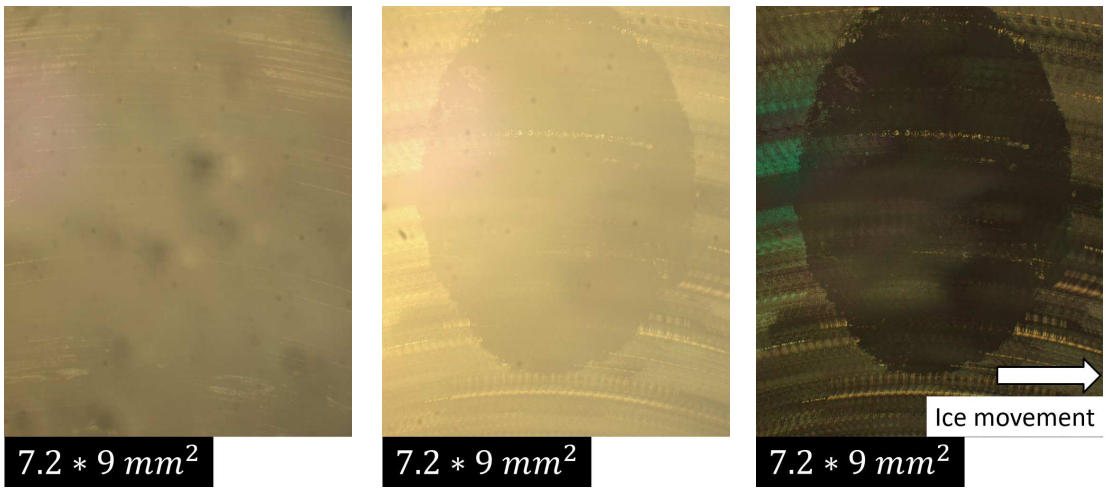

(a) One of the original images. **(b)** Phantom image. **(c)** Normalized phantom image.

Figure 3.13.: Example of the image analysis applied to a sliding contact between 'tire' rubber 1 and ice at 0.213 mm.s^{-1} at -10°C in order to observe and measure the apparent contact area. The steps of the process are presented in order from figure (a) to figure (c). Figure (a) presents one of the hundred images used to compute the phantom image. Figure (b) presents the phantom image and figure (c) the normalized version. The figure (c) makes it possible to identify the apparent rubber-ice contact which corresponds to the dark elliptical area. The sliding direction of the ice disc is indicated by the arrow on figure (c).

Nevertheless, the phantom imaging algorithm presents some limitations such as:

- The non-preservation of short-duration phenomena. Phenomena such as contact

instabilities may not be observed, especially if the frame-rate and/or the total duration of the video measurement is large (almost a thousand images acquired at 25 Hz for example).
- An overestimation of the non-contact area. The algorithm identifies only the brightest pixels. This means that the existence of a non-contact pixel in one image is enough to transform the corresponding pixel into a non-contact pixel in the final phantom image. This is confirmed by the comparison of the contact size measured during sliding to the static contact area. The latter are lower in size than the former in average.

3.3.3.b . Evolution of the contact area as a function of the sliding velocity and temperature

The following protocol was used at two temperatures, -2.5°C and -10°C, to estimate the evolution of the contact area versus the sliding velocity for the three 'tire' rubbers 1, 3 and 7:

- For each temperature, a fresh ice was manufactured;
- Each measurement was made for an initial load of 10 N;
- Then sliding of the rubber on the ice disc was performed for 30 s, with a constant sliding velocity by keeping the rubber sample rotation blocked;
- At the end of the 30 s period, the rubber sample was unloaded while the ice disc continued to rotate.
- Between unloading and loading, a waiting time of 30 s allowed ice and rubber to come back to thermal equilibrium with the 'test' chamber air;
- Each measurement was performed once for each sliding velocity;
- The sliding velocity was raised from 50 μm.s^{-1} to 1 m.s^{-1} using a logarithmic ramp.

It must be noticed that the sliding distance varies with the sliding velocity (30 mm at 1 mm.s^{-1} and 30 m at 1 m.s^{-1} for example) and may induce bias in the results. Indeed, for sliding velocities below 0.21 mm.s^{-1}, the sliding distance is smaller than the average width of the elliptical contact (approximately 5.6 mm).

The evolution of the rubber-ice contact area during sliding was observed thanks to the rebuild images algorithm described previously for 'tire' rubber 1, 3 and 7 at -2.5°C and -10°C and is presented in figure 3.14 and figure 3.15.

Several observations can be made:

- the values of the contact area depend on the rubber: the stiffer the rubber, the smaller the contact area.
- the values of the contact are lower than that of a static contact mechanic at the same conditions except for 'tire' rubber 3 at -2.5°C. The values of the contact area close to that of the static one for low velocities (around 0.2 mm.s^{-1}) and for the largest velocity (1 m.s^{-1}).

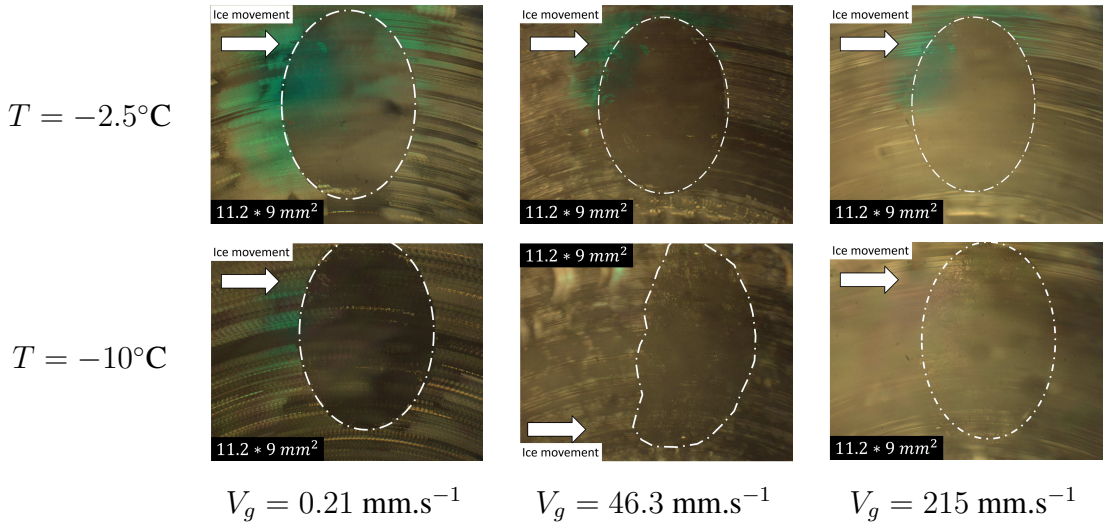

Figure 3.14.: Rebuilt images of the rubber-ice contact for the case of tire' 1 at -2.5°C and -10°C for 0.21, 46.3 and 215 mm.s^{-1}.

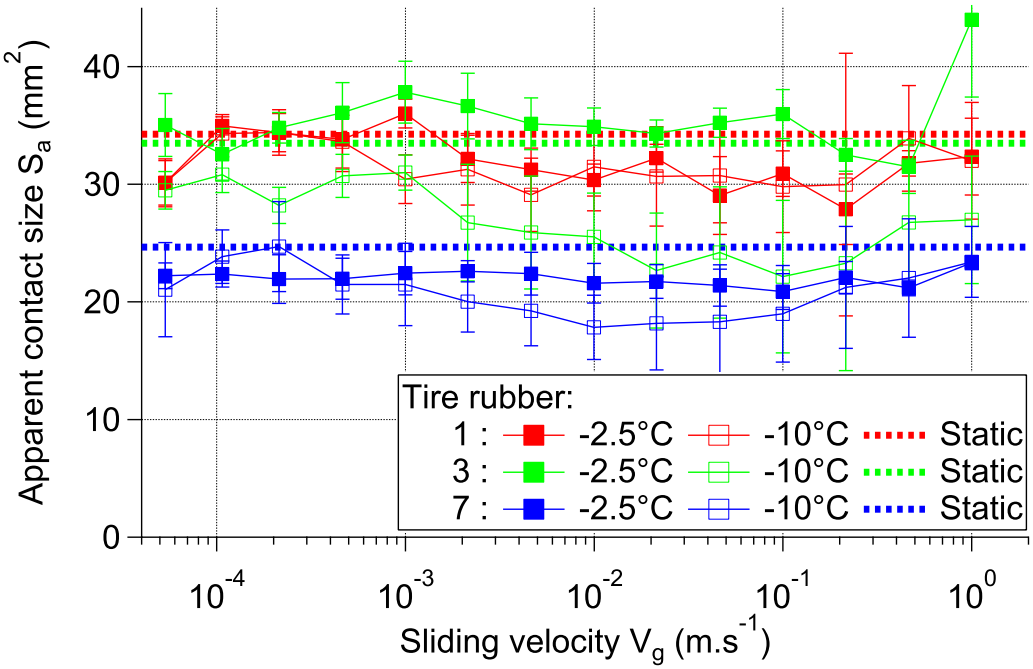

Figure 3.15.: Evolution of the rubber-ice apparent contact size for the 'tire' rubber 1, 3 and 7 at -2.5 and -10°C as a function the sliding velocity measured using rebuilt images of the rubber-ice contact (figure 3.14). The standard deviation represents the uncertainty on the value of the apparent contact size. The static apparent contact sizes measured via JKR measurement (see figure 3.11) under an applied load of 10 N for fresh-rubber interface are represented with discontinuous line.

- at -2.5°C, the contact shape remained elliptical and the apparent contact remained almost constant independently of the sliding velocity.
- at -10°C, a modification of the shape was observed as a function of the sliding velocity, regardless of the rubber:
  - below 1 mm.s^{-1}, the contact shape remained elliptical;
  - from 1 mm.s^{-1} to 100 mm.s^{-1}, the contact shape became semi-elliptical;
  - above 100 mm.s^{-1}, the contact shape recovered the elliptical form.

  This change in the shape of the contact was correlated with a decrease of the apparent contact size.

The change of shape observed for all 'tire' rubbers at -10°C could be due to contact oscillations, observed on the recorded video, such as a stick-slip phenomena or detachment waves [52] caused by rubber adhesion on the ice surface. Another possibility is the influence of the shear stress increasing within the contact that leads to a decrease of the contact area [104] as the macroscale consequence of the shrinking of individual microjunctions between the rubber surface and the counter face [105]. Such phenomena were not observed at -2.5°C, near the melting temperature, nor for sliding velocities faster than 100 mm.s^{-1} at -10°C. This might indicate a change in the nature of the ice surface such as the appearance of a 'quasi-liquid' layer and/or melting due to frictional heating within the contact.

3.3.3.c . Ice surface state during and after sliding

Image-by-image investigations allowed us to analyze modifications of the ice surface during sliding. The appearance of dark strips, at the entrance and the exit of the contact, was observed independently of the temperature, the sliding velocity and the rubber as shown in figure 3.16. The strips have a difference of reflection from the fresh ice, so the darker color could be either due to the presence of water or to the deformation of the ice. According to figures 3.16a and 3.16b, the source of the strips was located on the rubber surface and according to the figure 3.16c, the width of the strips, in the range [8 μm; 230 μm] covered the diameter range of the rubber surface agglomerates. This suggests that the agglomerates of the rubber surface plough the ice surface.

After six consecutive sliding experiments made on the same ice track, the ice surface presented a scratched wear scar as presented in figure 3.17. The wear scar size observed was is in agreement with the contact size measured after sliding (see figure 3.12c) rather than the contact size before sliding (see figure 3.11c). This correlation was observed regardless of the rubber and the temperature. The scratches width (almost 0.1 mm) are in agreement with the range measured in figure 3.16. This tends to confirm the appearance of a ploughing mechanism of the ice by rubber surface agglomerates.

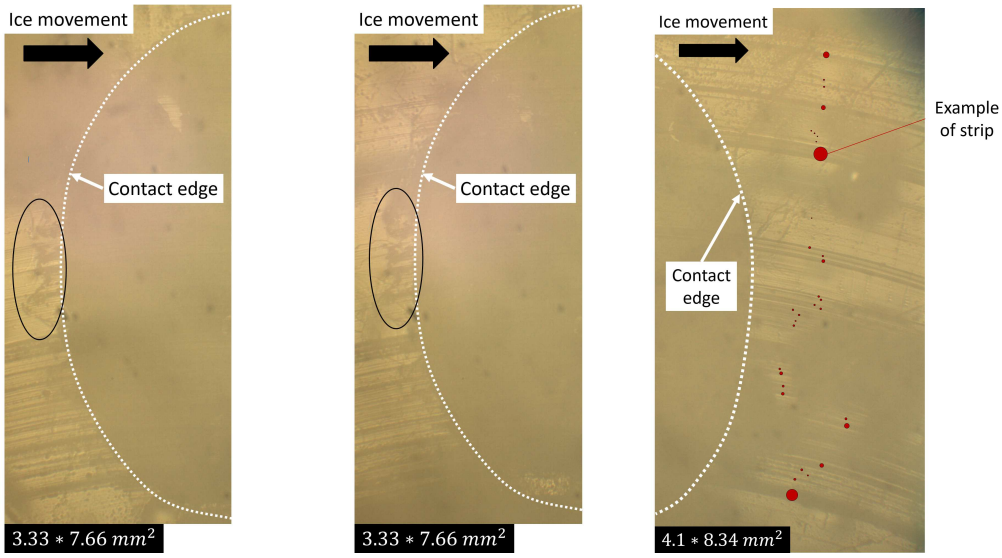

(a) Ice at $V_g = 4.6$ mm.s^{-1}. **(b)** Ice 0.98 s after the figure (a) ($V_g = 4.6$ mm.s^{-1}). **(c)** Wear scratches on ice. $V_g = 1$ mm.s^{-1}.

Figure 3.16.: 'Tire' rubber 1 contact at -2.5°C. Figure (a) presents the initiation of some strips on ice at the entrance of the contact at 4.6 mm.s^{-1}. Figure (b) highlights the persistence of this phenomenon during the sliding. Figure (c) presents several examples of these strips highlighted by red dots at 1 mm.s^{-1}.

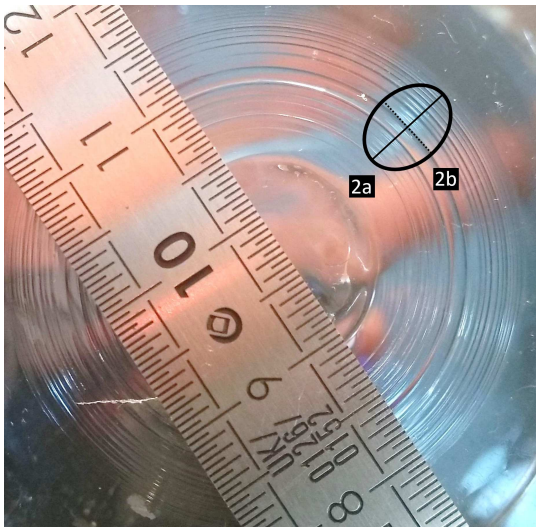

Figure 3.17.: Top view of the ice surface after six sliding experiments with 'tire' rubber 7 at -2.5°C. The apparent contact area of the rubber sample in contact with ice is indicated by the black ellipse (almost 26.7 mm^2) - semi major axis $a \approx 3.4$ mm and semi minor axis $b \approx 2.5$ mm. The size of wear track is similar to the length of the major axis of the apparent contact area. Graduation unit of steel ruler (between two black marks) is 0.5 mm.grad^{-1}.

3.4. Rubber-ice friction results

The influence of the sliding velocity, environmental temperature as well as the rubber mechanical properties on friction is detailed from the analysis of tribological experiments performed according to the protocols described in previous section 3.3.3.b .

3.4.1. Typical friction results

Results were presented on the form of a tangential friction force F_y and applied normal load F_z as a function of time, sliding velocity, temperature and rubber. The friction coefficient was calculated:

$$\mu(t) = \frac{F_y(t)}{F_z(t)} \tag{3.11}$$

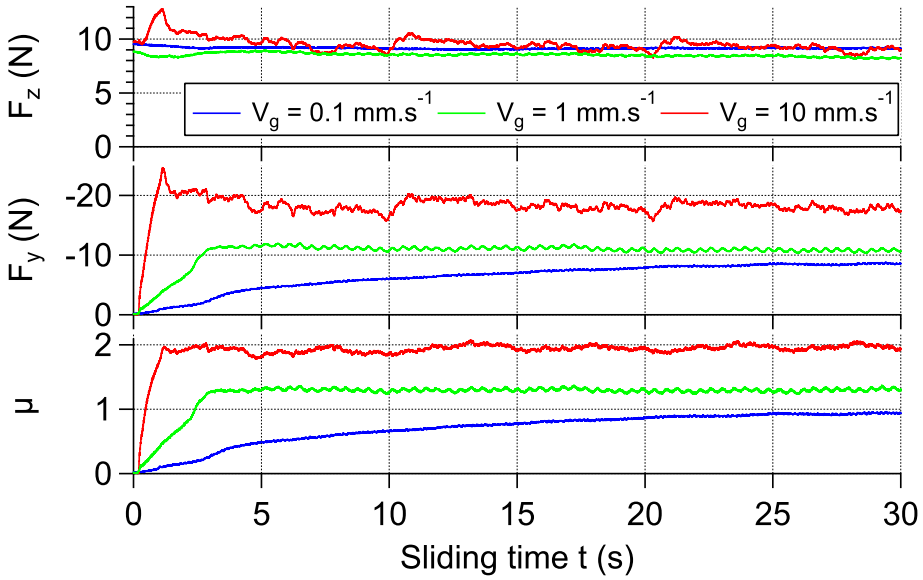

Figure 3.18.: Example of rubber-ice friction measurement as a function of sliding time t at 0.1 mm.s^{-1}, 1 mm.s^{-1} and 10 mm.s^{-1} at -10°C with 'tire' rubber 1. The ice disc was rotating while the rubber sample was blocked. The applied load was 10 N.

Examples of the temporal evolution of applied normal force, tangential friction force and friction coefficient, are presented in figure 3.18 at 0.1 mm.s^{-1}, 1 mm.s^{-1} and 10 mm.s^{-1}. Sliding distances at 1 mm.s^{-1} (30 mm) and at 10 mm.s^{-1} (300 mm) are larger than the contact size (approximately 5.6 mm). Sliding distances are smaller than the contact size below 0.21 mm.s^{-1}.

Several observations can be made for sliding velocity above 0.21 mm.s^{-1}:

- a transient regime was observed during the first 1.1 s (11 mm) of sliding at 10 mm.s^{-1} and during the first 3.2 s (3.2 mm) of sliding at 1 mm.s^{-1};
- the applied normal force remained constant during the whole measurement;
- some oscillations were observed on F_z, F_y and μ.

Below 0.21 mm.s^{-1}, the transient phase seems to occur during the 30 s of sliding.

The transient regime observed initially during sliding is associated to an initial shear phase. It implies that below 0.21 mm.s^{-1}, the rubber-ice interface did not slide and that force measured are not representative of the kinetic friction.

The almost constant applied normal load validates the capability of the ice manufacturing protocol to obtain a flat ice surface.

3.4.2. Analysis of the friction signals

In order to compare friction experiments, representative friction values for each rubber, sliding velocity, temperature and sliding set were chosen as the kinetic steady-state friction defined from the following relation:

$$\mu_{steady\ state} = \frac{1}{t_{95\%} - t_{80\%}} \int_{t_{80\%}}^{t_{95\%}} \mu(t)\,\mathrm{d}t \tag{3.12}$$

where $\mu(t)$ is the instantaneous coefficient of friction, t is the time coordinate and $t_{80\%} = 24$ s and $t_{95\%} = 28.5$ s are arbitrary boundaries of the kinetic steady-state friction. These boundaries were chosen to avoid the transient regime that may occur during the initiation of the sliding above 0.21 mm.s^{-1}. The standard deviation during the friction versus time measurement between $t_{80\%} = 24$ s and $t_{95\%} = 28.5$ s is calculated from the following relation:

$$\sigma_{error\ measurement} = \sqrt{\frac{1}{t_{95\%} - t_{80\%}} \int_{t_{80\%}}^{t_{95\%}} (\mu_{steady\ state} - \mu(t))^2\,\mathrm{d}t} \tag{3.13}$$

3.4.3. Influence of the sliding velocity

The figure 3.19 presents an example of the evolution of the kinetic steady-state friction (equation 3.12) as a function of the sliding velocity at -10°C and -2.5°C for 'tire' rubber 1.

Several observations can be made:

- Friction curves have a bell shape as a function of the sliding velocity regardless the temperature;
- The friction reaches a maximum value at almost 21.3 mm.s^{-1} ($\mu \approx 2$ at -10°C and $\mu \approx 0.3$ at -2.5°C) regardless of the temperature of the 'test' chamber;

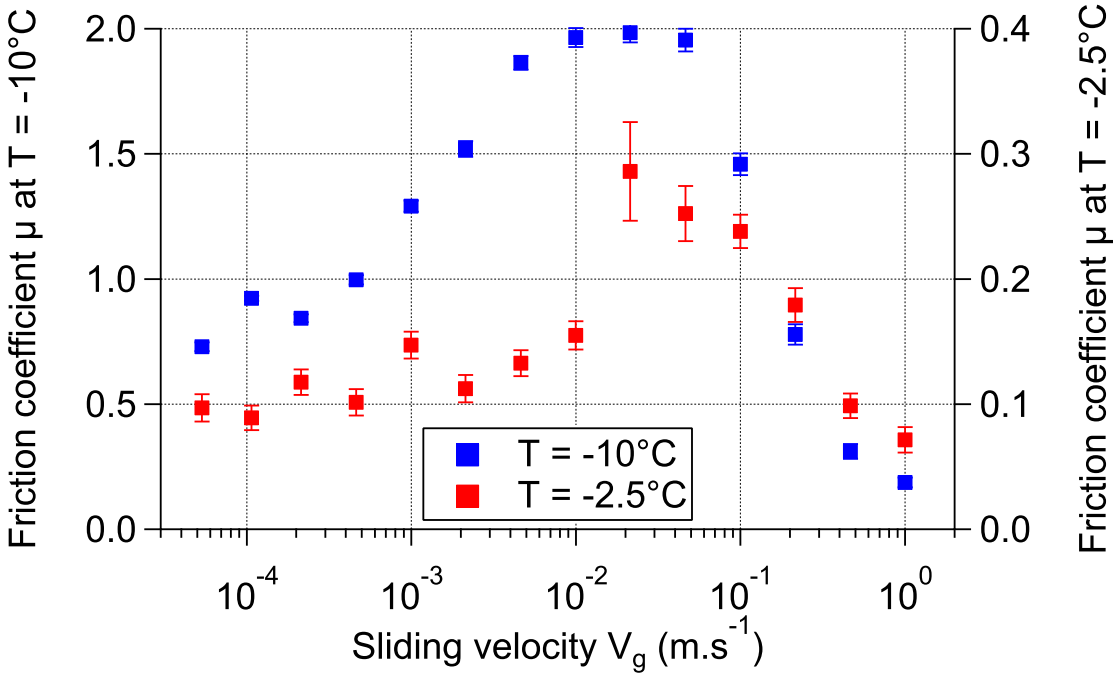

Figure 3.19.: Evolution of the average steady-state kinetic friction of the rubber-ice contact as a function of the sliding velocity at -10°C and -2.5°C for 'tire' rubber 1. The applied load was 10 N. The ice disc was rotating while the rubber sample was blocked. Left ordinate axis corresponds to the friction measurement at -10°C marked with blue squares and the right ordinate axis corresponds to the friction measurement at -2.5°C marked with red squares.

- The kinetic steady state friction drastically decreases above 46.1 mm.s^{-1} regardless of the temperature.

These observations can be extended to the 'tire' rubber 3 and 7 with the exception of the 'tire' rubber 7 at -2.5°C.

The bell shape of the friction curve is classically observed for rubbers sliding on different materials such as polished glass or ice. It is governed by the viscoelastic properties of the rubber [49, 77]. In their experiments on ice, Grosch [49] and Roberts and Richardson [80] obtained friction values ranging from 0.3 to 3.5 highly dependent on the material, velocity, temperature and pressure conditions. These values have the same order of magnitude as those measured in the present study (see figure 3.19). These observations about the bell-shaped curve and the maximum of friction are made at all temperatures, rubbers and sliding sets. However, the level of friction and the value of the friction peak vary. At high sliding velocity, the level of friction was very low suggesting

two possibilities:

- the rubber reached its glassy state;
- the existence of a liquid layer within the rubber-ice contact.

3.4.4. Correlation between friction force and contact area

Figure 3.20 and figure 3.21 present the evolution of the apparent contact area S_a, the friction coefficient and the average shear stress σ in the contact as a function of the sliding velocity at -2.5 and -10°C for 'tire' rubber 1, 3 and 7 for a fresh rubber-ice interface according to the protocol described in paragraph 3.3.3.b . The average shear stress σ within the contact was calculated according to the relation:

$$\sigma = \frac{1}{S_a} F_{y\ steady\ state} \tag{3.14}$$

where $F_{y\ steady-state}$ is the kinetic steady-state friction force:

$$F_{y\ steady\ state} = \frac{1}{t_{95\%} - t_{80\%}} \int_{t_{80\%}}^{t_{95\%}} F_y(t)\,\mathrm{d}t \tag{3.15}$$

The error on the calculation of the average shear stress is calculated via the propagation of uncertainty:

$$\sigma_{error\ \sigma} \approx \sigma \sqrt{\left(\frac{\sigma_{error\ S_a}}{S_a}\right)^2 + \left(\frac{\sigma_{error\ F_y}}{F_{y\ steady\ state}}\right)^2} \tag{3.16}$$

where $\sigma_{error\ S_a}$ is the uncertainty on the measurement of the apparent contact size using rebuilt images of rubber-ice contacts and $\sigma_{error\ F_y}$ is the error of measurement on F_y:

$$\sigma_{error\ F_y} = \sqrt{\frac{1}{t_{95\%} - t_{80\%}} \int_{t_{80\%}}^{t_{95\%}} (F_{y\ steady\ state} - F_y(t))^2\,\mathrm{d}t} \tag{3.17}$$

Several general remarks can be made, on the average level of friction and the average shear stress:

- The shear stress and friction coefficient is much lower at -2.5°C than at -10°C regardless of the rubber and the sliding velocity.
- At -10°C, a contact size drop correlated at intermediate velocities to the contact deformation was also correlated to an increase of friction force leading to shear stress (above 0.2). This drop of the contact area leads to the bell shaped curve observed for shear stress and friction values.
- At -2.5°C, no distinct contact size drop or contact deformation was observed and

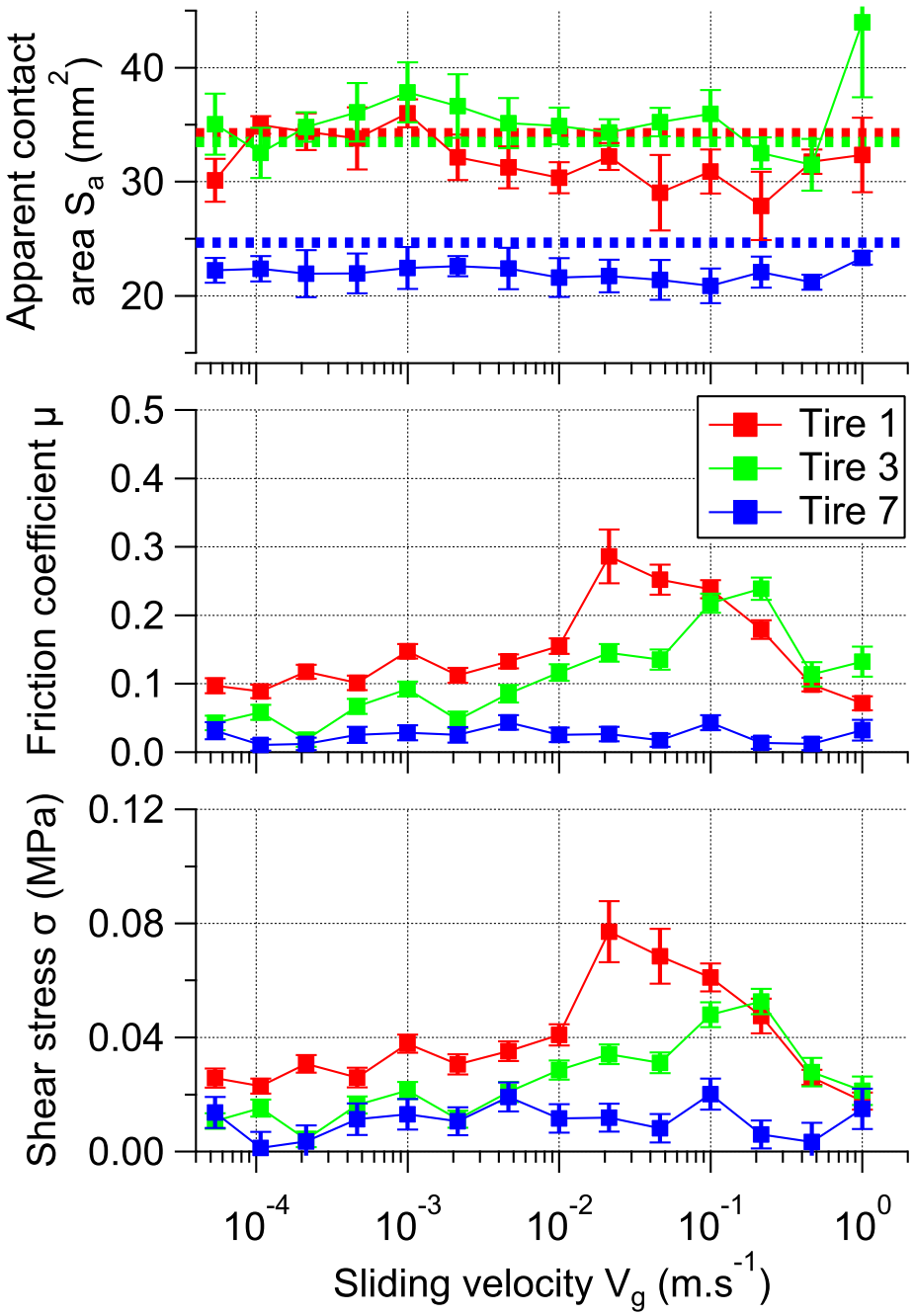

Figure 3.20.: Evolution of the apparent contact area, the average steady-state kinetic friction coefficient and the shear stress of the rubber-ice contact versus sliding velocity for 'tire' rubber 1, 3 and 7 at -2.5°C with an initial applied load of 10 N. The apparent contact area was measured by using the image processing methodology described in paragraph 3.3.3.a . The static apparent contact size measured via JKR measurement (see figure 3.11) under an applied load of 10 N for fresh-rubber interface are represented with discontinuous line.

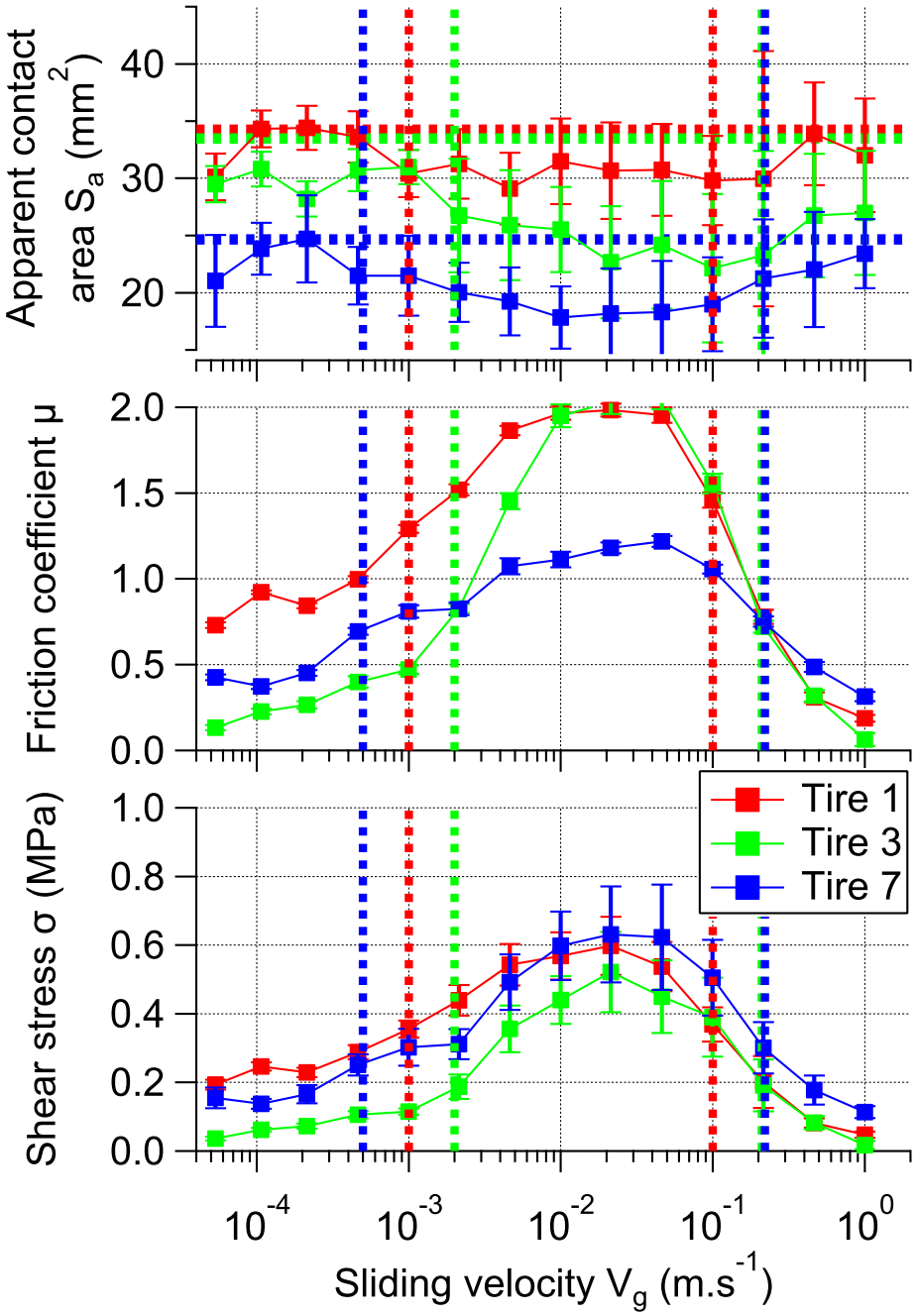

Figure 3.21.: Evolution of the apparent contact area, the average steady-state kinetic friction coefficient and the shear stress of the rubber-ice contact versus sliding velocity for 'tire' rubber 1, 3 and 7 at -10°C with an initial applied load of 10 N. The apparent contact area was measured by using the image processing methodology described in paragraph 3.3.3.a . The static apparent contact size measured via JKR measurement (see figure 3.11) under an applied load of 10 N for fresh-rubber interface are represented with discontinuous line.

the contact is not dependent on the sliding velocity regardless of the 'tire' rubber.

The analysis of the shear stress brings new insights into the mechanisms.

The large difference of behaviors exhibited at -2.5°C and -10°C for all rubbers suggests a strong influence of the temperature, independently of the sliding velocity. This is in agreement with the observations of Jellinek [57] and the hypothesis of the formation of a 'quasi' liquid layer on ice for temperatures close to the melting one, that could influence the friction response.

However, an effect of the material was detected at -2.5°C: the highest shear stress was measured for 'tire' rubber 1 and the lowest one for 'tire' rubber 7. Below 5 mm.s^{-1}, 'tire' rubber 3 and 7 presented a similar shear stress. Above 100 mm.s^{-1}, the shear stress measured for 'tire' rubber 3 was about the same as the one of tire rubber 1. At -10°C, the influence of the material differs: below 46 mm.s^{-1}, 'tire' rubbers 1 and 7 present similar shear stress. However the shear stress of the 'tire' rubber 7 remaining slightly lower than 'tire' rubber 1. For this range of velocities, 'tire' rubber 3 presented a lower shear stress. Above 46 mm.s^{-1}, 'tire' rubber 7 had the maximum shear stress and 'tire' rubbers 1 and 3 shear stress could be superimposed.

These observations suggest a complex coupling between the temperature, the sliding velocities and the viscoelastic properties of the rubber. With these measurements, at -2.5°C, it seems that the stiffer the rubber, the lower the shear stress, especially at high velocities. However, the level of shear stress remains very low for all the samples and it it is hard to conclude. At -10°C, the levels are higher and the lower the T_g, the higher the shear stress at low velocities although the stiffness may become preponderant at high velocities.

These observations tend to exhibit two sliding velocity regimes:

- At low' sliding velocity, below 100 mm.s^{-1}, where the shear stress correlates with the difference of viscoelastic properties of the rubbers, due to the difference in T_g;
- At 'high' sliding velocity, above 100 mm.s^{-1}, where the shear stress seems less correlated to the variation of T_g of the rubber but more to the modulus of elasticity.

3.5. Conclusion

The results presented in this chapter make it possible to draw several conclusions.

A compact system to control the environmental temperature of a tribometer was designed and used. This system allows a small confined volume to be cooled down from 0°C to -20°C while simultaneously performing friction measurements and visualizing the rubber-ice contact. An ice manufacturing protocol was also developed to obtain a transparent flat reflective ice surface without any cracks nor bubbles.

The contact visualization associated to post-processing provided new information on

the behavior, size and shape of the rubber-ice contact during the friction measurements.

Static contact versus load measurement highlighted that rubber-ice contact is adhesive. An adhesion hysteresis between loading and unloading was observed. During loading, the work of adhesion estimated for a fresh rubber-ice interface (before any sliding) via the JKR theory was almost 30 mJ.m^{-2} in accordance with results of the previous chapter and the literature [80]. However during unloading, the work of adhesion was one order of magnitude larger than during loading (from 700 mJ.m^{-2} to 1500 mJ.m^{-2}). This results implies that rubber-ice interface is energetically more favorable than a separated one, thereby favoring an adhesive contribution to the friction force. The adhesion works measured during loading (from 200 mJ.m^{-2} to 300 mJ.m^{-2}) and unloading (from 1700 mJ.m^{-2} to 2500 mJ.m^{-2}) for a run-in rubber-ice interface (after a set of sliding experiments) were drastically enhanced. This was associated with modifications of the ice interface due to sliding against the rubber.

Ploughing of the ice surface by the rubber surface agglomerates was also observed. Similar observations were performed by Kriston, Tuononen, Fülöp and Isitman [83, 84, 85]. These authors associate the presence of surface agglomerates to an increase of friction that potentially favor ice melting.

The closer the ice temperature to the melting temperature, the lower the friction and the shear stress. Clear differences appear in the evolution of the shape of the rubber-ice contact as a function of the sliding velocity and the temperature. At -2.5°C, the contact shape remained elliptical and its size was roughly independent of the sliding velocity, whereas at -10°C, the contact shape and size changed at intermediate velocity. The low shear stress at -2.5°C correlated with the absence of contact deformation suggest a same cause. The hypothesis of the formation of a 'quasi' liquid layer on ice for temperatures close to the melting one [57] may be suggested. However, a strong coupling between temperature, sliding velocity and rubber viscoelastic properties was observed.

The dependence of the shear stress and the contact deformation on sliding velocity suggest two sliding velocity ranges:

- a 'low' sliding velocity range, below 100 mm.s^{-1}, where the shear stress seems to be correlated to viscoelastic properties of the rubbers (through the glassy temperature T_g);
- a 'high' sliding velocity range, above 100 mm.s^{-1}, where the shear stress seems to be correlated to the modulus of elasticity.

The transition may be caused by frictional heating of the ice surface classically hypothesized in the literature [60, 61, 64]. The different mechanisms at stake will be discussed in more details in the next chapter.

Chapter 4

Rubber-ice friction mechanisms

This chapter presents an attempt to better understand and decouple the role of the rubber viscoelasticity, the ice temperature, the sliding velocity, the presence of rubber surface agglomerates and the ice surface properties on rubber-ice friction.

Friction forces measured as a function of the sliding velocity for similar temperature and rubber sample but different manufactured ice surfaces were compared. In agreement with previous results, two behaviors were identified: at 'low' sliding velocity range below 100 mm.s^{-1} large differences of friction were observed and attributed to the ice, and at 'high' velocity range above 100 mm.s^{-1}, the friction was repeatable regardless of the ice.

Consistency of the rubber-ice friction with the WLF theory was also investigated. In this framework, using a reference temperature as defined by Grosch, the velocity friction curves can be superimposed for 'low' sliding velocities which suggests a frictional behavior dominated by the viscoleastic properties of the rubber.

The modeling of the contact temperature T_c from the friction measurements shows that the ice melting is initiated at a critical velocity of 100 mm.s^{-1} regardless the environmental temperature T_0 and the rubber. This effect controlled the transition of the friction regime from 'low' to 'high' sliding velocity regime. Moreover the ratio $(T_c - T_0)/(T_m - T_0)$, where T_m is the the melting temperature of the ice collapse on a same master-curve for all environmental temperatures and rubbers. The existence itself of this master-curve implies that the interfacial shear stress within the contact can be analytically predicted as a function of the sliding velocity, temperature and viscoelastic properties of the rubber.

The chapters 2 and 3 have highlighted that the rubber-ice friction could be potentially influenced by:

- the viscoelasticity;
- the temperature and the sliding velocity;
- the presence of rubber surface agglomerates.

In this chapter, an attempt to better understand the role of these parameters was made.

4.1. Effect of the surface on the friction measurement repeatability

Southern and Walker [77] and Roberts and Richardson [80] showed the existence of a large rubber-ice friction variation day-to-day for freshly prepared ice surfaces under the same conditions. Such variations may be expected for measurements performed according to the protocol described in paragraph 3.3.3.b where contact visualization and friction measurements were performed simultaneously. To obtain reproducible measurements, Southern *et al* and Roberts *et al* conditioned ice via multiple sliding experiments. For this reason, the previous protocol (see paragraph 3.3.3.b) was modified to investigate this phenomenon.

4.1.1. Modified protocol

The protocol detailed in paragraph 3.3.3.b was modified:

- Each sliding experiment - so called here an iteration - was performed three times consecutively for each sliding velocity on a different initial position on ice.
- The set of 14 sliding velocity steps with three iterations - referred to as a sliding set - was performed six times on a same manufactured ice.
- The rubber-ice contact visualization was not performed considering that the multiple iterations of friction measurement quickly damage the ice surface (see paragraph 3.3.3.c) that alter the quality of the contact images.

In order to limit any potential external influence, the experiments were performed in the same winter season from November 2017 to February 2018 in Ecully in France. The season in this city is characterized by a low atmospheric temperature and a low dew point - from 1 to 4°C. Measurements with different 'tire' rubbers were performed within the shortest feasible time interval in order to keep the same environment conditions (temperature, dew point, humidity, *etc*) as possible. A new manufactured ice was used for each 'tire' rubber and for each temperature.

4.1.2. Quantification of the average steady state kinetic friction

With this modified protocol, three kinetic steady-state coefficients were obtained for each sliding velocity, temperature, rubber and sliding set. Therefore, an average kinetic steady-state friction coefficient was calculated for the three iterations:

$$\overline{\mu}_{steady\ state} = \frac{1}{N_{it}} \sum_{k}^{N_{it}} \mu_{steady\ state_k} \tag{4.1}$$

where N_{it} is the number of iterations and k is the iteration index.

The error due to the differences between the three iterations was calculated:

$$\sigma_{error\ iteration} = \sqrt{\frac{1}{N_{it}} \sum_{k}^{N_{it}} \left(\mu_{steady\ state_k} - \overline{\mu}_{steady\ state}\right)^2} \tag{4.2}$$

The error of measurement for the three iterations was calculated via the method of the pooled variances, which gives:

$$\overline{\sigma}_{error\ measurement} = \sqrt{\frac{1}{N_{it}} \sum_{k}^{N_{it}} \left(\sigma_{error\ measurement_k}\right)^2} \tag{4.3}$$

4.1.3. Comparison of friction for fresh ice

The figure 4.1 compares the kinetic steady-state friction measurement presented in figure 3.19 to the average steady-state kinetic friction measured with three iterations at -2.5°C and -10°C. In both cases, friction measurements were performed with 'tire' rubber 1 for a fresh rubber-ice interface. Two parameters affect the results: the number of iterations (3 in the 'average' case) and the ice ('ice' 1 for the single iteration and 'ice' 2 for the 'average' case). However, both ices were fresh.

Several remarks emerge from the comparison of the friction experiments for each temperature:

- the bell shape curve is still observed regardless of the ice and the temperature;
- the influence of the ice is preponderant: there is a difference of friction level ice-to-ice for sliding velocity below 100 mm.s^{-1}. This difference is even more significant at -2.5°C, casting doubt upon the values of friction measured with 'ice 1' (single iteration, summer 2018). Above 100 mm.s^{-1}, friction levels were similar for each temperature regardless of the ice. However, the velocity range at which, the friction coefficient reachs its maximum is the same regardless the ice and the sliding iteration.
- the errors of iteration and measurement measured via the modified protocol were

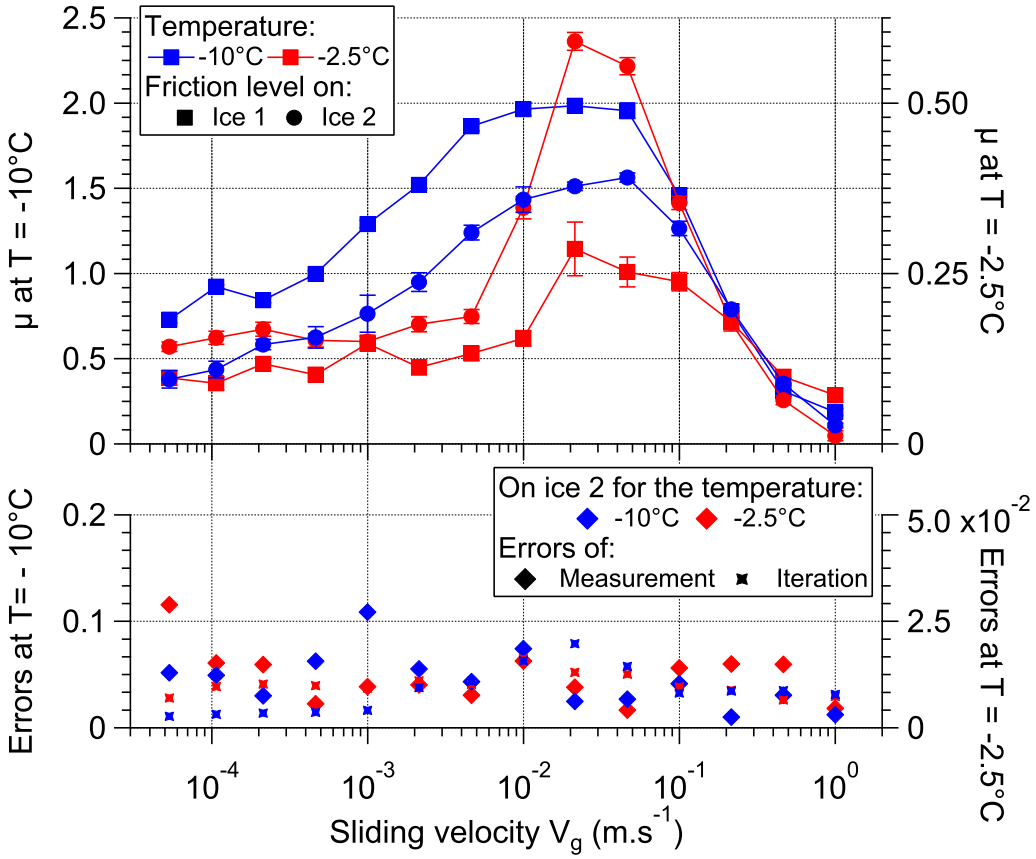

Figure 4.1.: Comparison of steady state kinetic friction, referred to as 'ice 1', to the average steady-state kinetic friction, referred to as 'ice 2' for the 'tire' rubber 1 at -2.5°C and -10°C. For 'ice 1', the kinetic steady-state friction was measured with one sliding iteration for each sliding velocity (see paragraph 3.3.3.c). For 'ice 2', the average kinetic steady-state friction was obtained via three sliding iterations. For each 'ice' and temperature, a new ice was manufactured. The applied load was 10 N. The ice disc was rotating while the rubber sample was blocked. Left ordinate axis corresponds to the friction measurement at -10°C in blue and the right ordinate axis corresponds to the friction measurement at -2.5°C in red. Errors of measurement and iteration for the 'ice 2' at -2.5°C and -10°C are presented in the bottom graph.

similar. Theses errors were also small compared to the friction level indicating that there was no variability of friction from one position to another on the same ice.

These remarks for 'tire' rubber 1 can be extended to 'tire' rubber 3 at -2.5 and -10°C,

and 7 at -10°C. These observations suggest the existence of friction variability from one manufactured ice to another for sliding velocities below 100 mm.s^{-1}. However, this variability disappeared above 100 mm.s^{-1}. Thermal effects, above a sliding velocity of 100 mm.s^{-1}, may explain the repeatability of the friction measurements in this range of velocity. At lower velocities, a contribution of the rubber viscoelasticity, coupled to an effect induced by the ice surface state (fresh, run-in or worn) can be expected on the kinetic friction coefficient. In the remainder of this manuscript, the results issued from this modified protocol (3 iterations and ice manufactured during winter) will be used.

4.2. Consistency of friction response with the WLF theory

The existence of a friction master-curve is expected when one of the sliding material is viscoelastic according to the William-Landel-Ferry theory [5, 48]. However, according to Southern and Walker [77], the friction measurements performed for fresh rubber-ice interfaces cannot be shifted to form such a friction master-curve. Master-curve building was only possible for ice conditioned via multiple sliding. For that reason, the superimposition of friction measurements via the use of the WLF theory should indicate the end of the ice surface run-in step.

4.2.1. Validity and coefficient of the WLF theory

The study carried out in chapter 2 confirmed the existence of a viscoelastic response of the rubber in contact with ice surfaces for temperature of approximately -10°C.

The figure 4.2 presents the viscoelastic properties for large deformations (10%, which is consistent with the contact deformation) of the 'tire' rubber 1 measured at -2.5°C and -10°C shifted via the WLF transform (see equation 1.2). According to William *et al* [5], the reference temperature may be chosen arbitrary for each rubber as long as it is above the temperature of glassy transition T_g. In this case, $T_{ref} = 0$°C was chosen because this temperature is almost 50°C above the glassy temperature transition T_g of the rubber sample and corresponds to the melting temperature of the ice.

The dissipative factor $\tan\delta$ and shear modulus G^* curves of 'tire' rubber 1, 3 and 7 measured at -2.5°C and -10°C superimposed at the reference temperature of 0°C with the parameters $C_1 = 8.86$ and $C_2 = 140\ K$ (see annex A for 'tire' rubber 3 and 7). These two parameters are close to the one commonly used for rubbers ($C_1 = 8.86$ and $C_2 = 101.5\ K$). These results validate that the rubber sample viscoelastic properties obey to the WLF theory for the temperature range corresponding to their rubbery-state above their T_g.

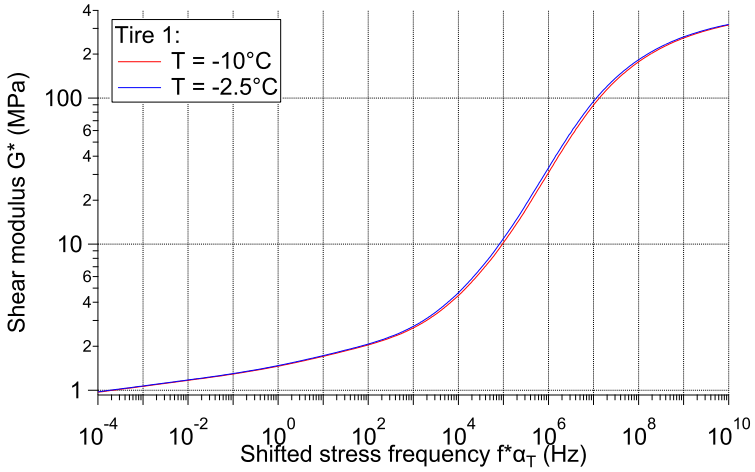

(a) 'Tire' rubber 1 shear modulus G^*

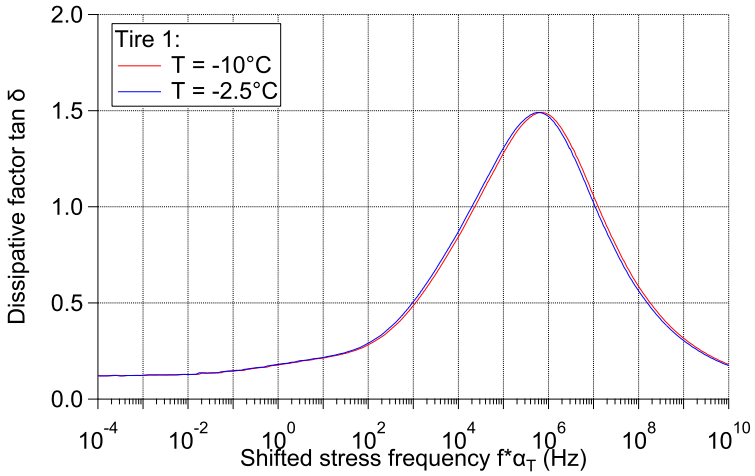

(b) 'Tire' rubber 1 loss factor $\tan\delta$

Figure 4.2.: Shear modulus G^* and loss factor $\tan\delta$ measured via DMA for large deformations (10%) shifted according to the WLF theory to the reference temperature $T_{ref} = 0°\text{C}$ for 'tire' rubber 1 with the coefficient $C_1 = 8.86$ and $C_2 = 140\ K$.

4.2.2. Consistency of the friction measurement

A velocity shift of rubber-ice friction curve, according to the WLF theory, was succesfully performed by Gnörich and Grosch [78] and Southern and Walker [76, 77]. This approach allowed to obtain a friction master-curve. Following the same methodology, an attempt of sliding velocity shift was performed for rubber-ice friction curve measured at -15°C, -10°C, -7.5°C and -2.5°C based on the following hypotheses:

- the validity of the temperature-frequency equivalence. Viscoelastic properties of the three rubber samples obeyed the WLF theory for the temperature range corresponding to their rubbery state (see figure 4.2).
- the temperature-sliding velocity range where the rubber friction was measured is compatible with the temperature-sliding velocity range where the rubber is in its 'rubbery' state - i.e where a master curve can be built;

These hypotheses make it possible to rewrite, as made by Grosh [48], the term α_T:

$$\alpha_T = \frac{V_{g_{ref}}}{V_{g_T}}$$

where $V_{g_{ref}}$ is the sliding velocity of reference at the temperature T_{ref} and V_{g_T} the sliding velocity at the temperature T.

It gives the following relation:

$$V_{g_{ref}} = V_{g_T} 10^{-\frac{C_1(T-T_{ref})}{C_2+T-T_{ref}}} \tag{4.4}$$

In the cases presented thereafter the reference temperature was set at 0°C for the reasons detailed in the previous paragraph.

The figure 4.3 presents the shifted friction curve according to the WLF theory for the case of the 'tire' rubber 1. Different sliding sets were performed consecutively. Several observations can be made:

- the friction curve measured at -2.5°C can never be superimposed with those measured at other temperatures;
- a superimposition of data was observed for the sliding set 1 from 2 mm.s^{-1} to 40 mm.s^{-1} at -7 and -15°C;
- a superimposition was observed for sliding sets 2 to 4 from 2 mm.s^{-1} to 200 mm.s^{-1};
- the superimposition became less clear and dispersed for sliding sets 5 to 6;
- the friction clearly differed for 'high' sliding velocities;
- each friction curve present a maximum at 'low' velocities. The sliding velocity of the maximum of friction is different for each curve after the velocity shift: the lower the environment temperature, the higher the velocity of the maximum.

These remarks for 'tire' rubber 1 can be extended to 'tire' rubber 3 and 7.

Some preliminary interpretations of those observations can be made by considering the influence of the history of sliding of the rubber-ice interface. On the first sliding set, partial superimposition was observed below 100 mm.s^{-1}, however the second sliding set exhibits a clearer superimposition. The partial superimposition observed on the first sliding set may be associated to the effect of fresh ice surface on the repeatability of the rubber-ice friction observed in previous section. These observations suggest that the dispersion observed on the first sliding set resulted from a run-in phenomenon

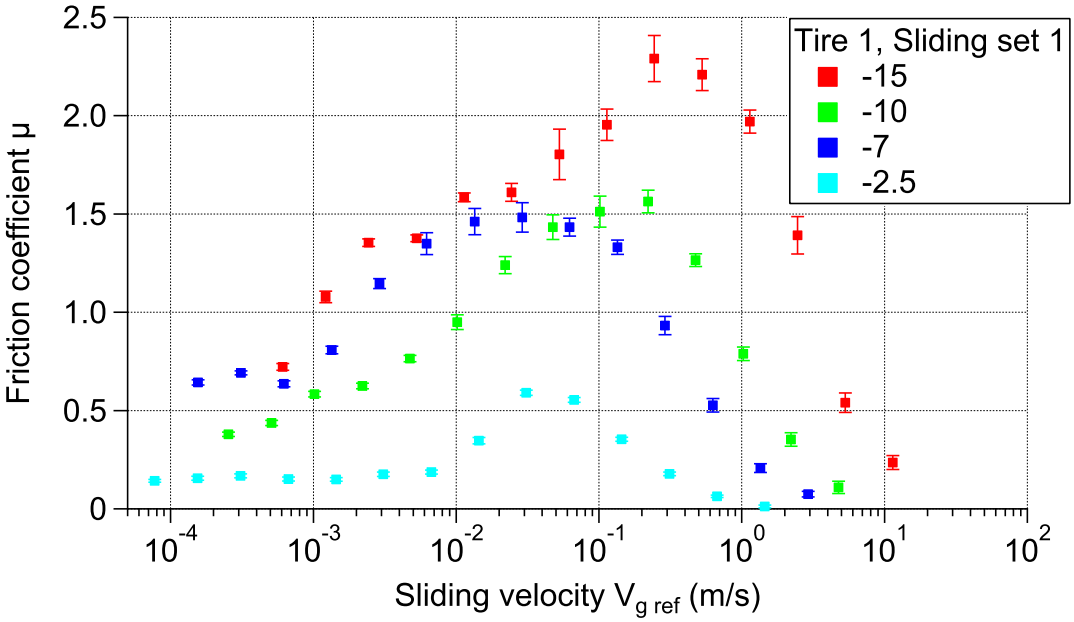

(a) Sliding set 1 corresponding to a fresh rubber-ice interface.

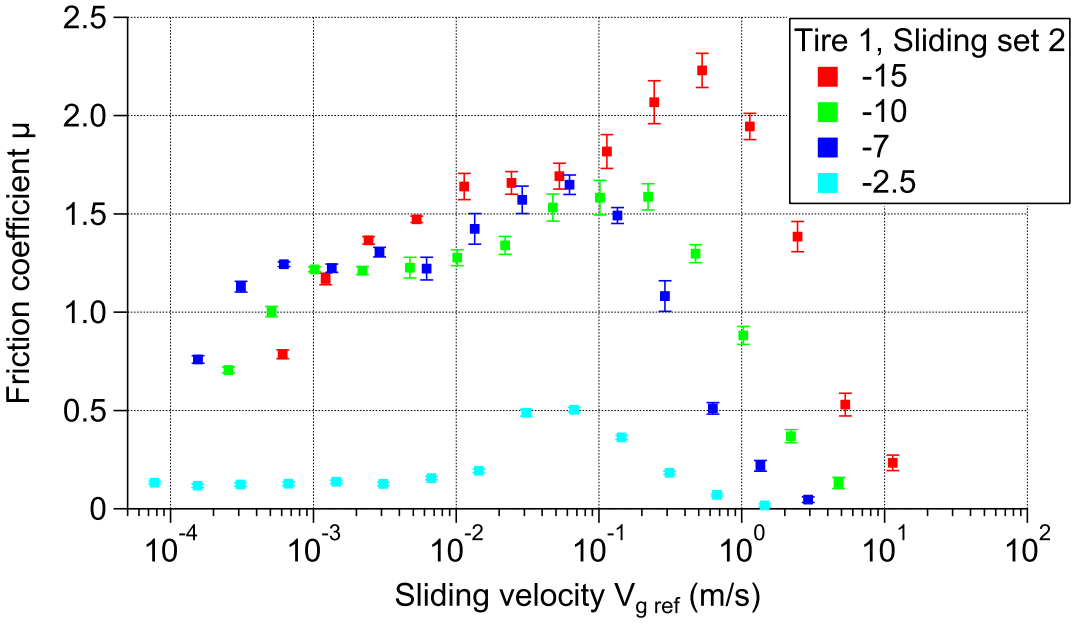

(b) Sliding set 2 corresponding to a slightly run-in rubber-ice interface.

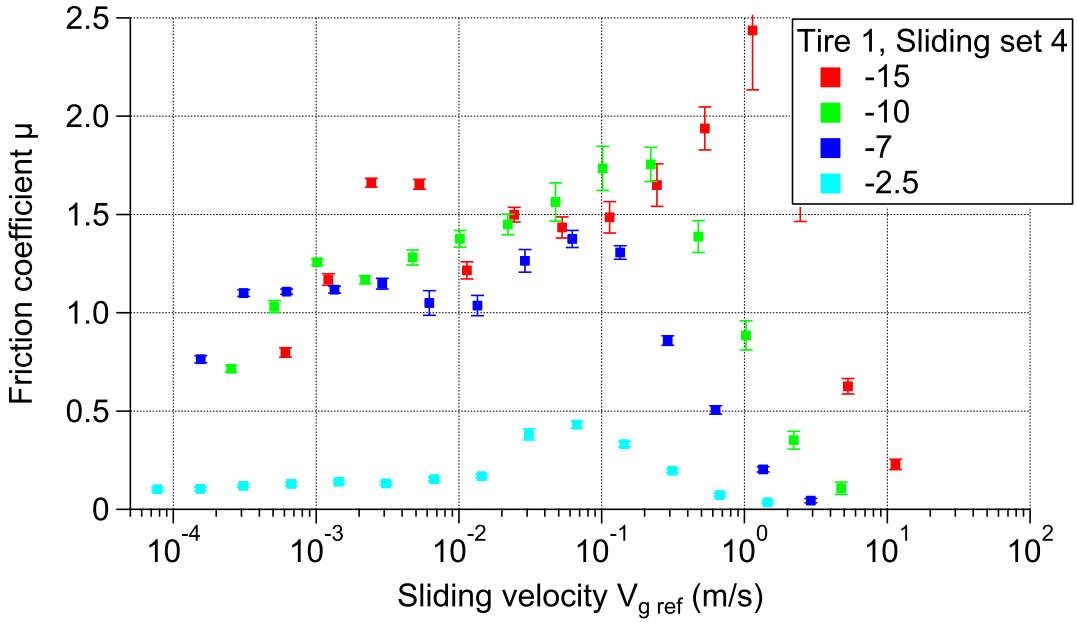

(c) Sliding set 4 corresponding to a worn rubber-ice interface.

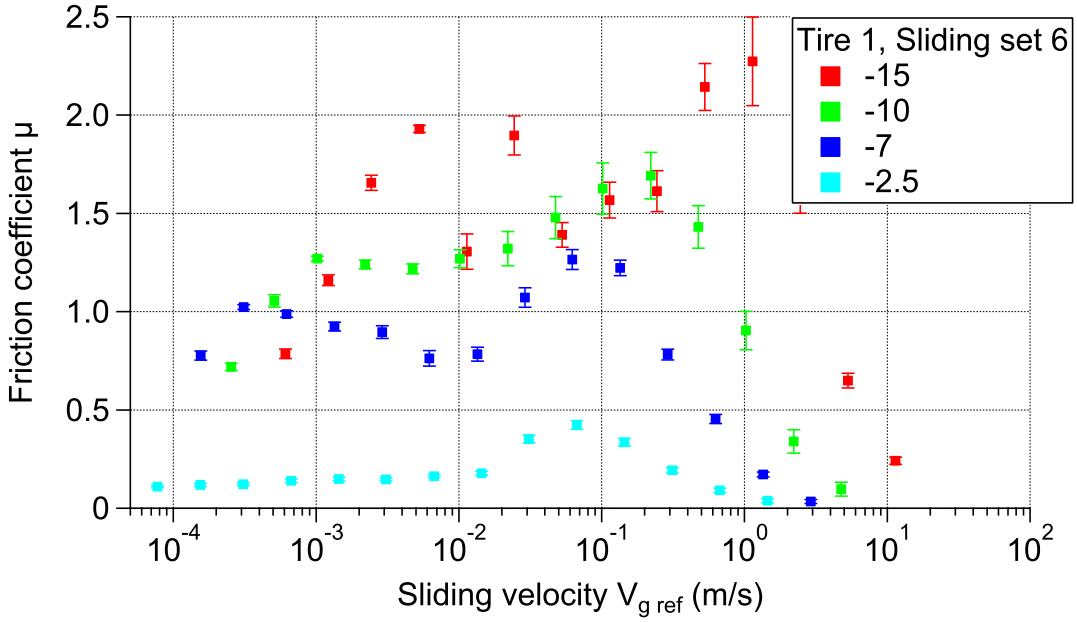

(d) Sliding set 6 corresponding to a worn rubber-ice interface.

Figure 4.3.: Rubber-ice friction shifted as a function of the temperature for the 'tire' rubber 1 for $T_{ref} = 0$°C according to the WLF theory with $C_1 = 8.86$ and $C_2 = 140\ K$. Several sliding sets are presented, (a) corresponds to a fresh rubber-ice interface, (b) corresponds to a run-in rubber-ice interface, (c) and (d) correspond to a worn rubber-ice interface. For sliding velocities slower than 200 mm.s^{-1}, a superimposition appeared for sliding set 2 (b) to 4 (c) at -7, -10 and -15°C.

of the rubber-ice interface. From the fifth sliding set, any superimposition was hardly observed, highlighting the possible role of ice surface ploughing by tire rubber agglomerates, as shown in section 3.3.3.c .

A transition seems to occur as a function of the sliding velocity. Below 100 mm.s^{-1}, a superimposition of the rubber-ice friction data was visible at -7°C, -10°C and -15°C, indicating the preponderant role of the rubber viscoelasticity for this sliding velocity range for sliding sets 1 and 2. Above 100 mm.s^{-1}, friction measured at -7°C, -10°C and -15°C never superimposed. For this 'high' velocity case, at least a partial melting of the ice surface may be expected, preventing the stress of the rubber surface by the ice surface.

The friction measurements performed at -2.5°C never superimposed with friction measurements performed at -7°C, -10°C and -15°C regardless of the sliding velocity and the sliding set. Mechanisms such as the apparition of a 'quasi' liquid layer on the ice surface may be probably considered.

In the remainder of the text, only data issued fom sliding sets 1 and 2 will be considered to discuss the friction mechanisms.

4.3. Rubber-ice friction and thermal effects

To investigate in more detail these possible thermal effects, a simple modeling of the contact temperature was proposed.

4.3.1. Modeling of the contact temperature

The modeling of the temperature inside the contact between two solids was first performed by Jaeger [106, 107] by solving the heat equation:

$$\rho_{ice} c_{ice} \frac{\partial T}{\partial t} - \vec{\nabla}\left(k_{ice}\vec{\nabla}T\right) = p_v \tag{4.5}$$

where ρ_{ice} is the ice density, c_{ice} is the ice specific heat, k_{ice} is the ice thermal conductivity, T is the temperature at the coordinate (x, y, z, t) and $\vec{\nabla}$ describes the gradient operator.

The variable p_v translates the volumetric heat power generated in W.m^{-3} that may arise from material phase transition or chemical reactions for example.

This model considers two semi-infinite solids with a relative motion at the sliding velocity V_g: a rubber slider and an ice plane, both represented in figure 4.4. The frictional force F_y arises within the contact and creates a surface heat flux q_{heat} that is partitioned between the two solids [108] without loss. The transient regime is not taken into account, the heat flux in each solid is considered as completely established and no

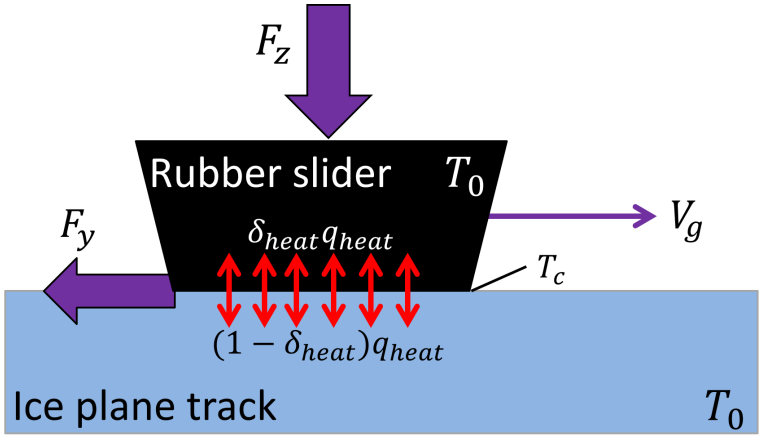

Figure 4.4.: Illustration of a rubber block sliding on a ice plane track under a load F_z. The heat produced q_{heat} within the contact is partitioned with the factor δ_{heat} between the slider and the plane and increases the temperature within the contact T_c. The heat is generated from the resultant friction force F_y within the contact.

volumetric power is generated inside the ice plane (no phase transition) or inside the slider, then:

$$\frac{\partial T}{\partial t} = 0 \qquad \text{and} \qquad p_v = 0$$

It is supposed that the temperature at the slider surface T_{slider} (respectively at the ice surface, T_{track}) is homogeneous all over the rubber-ice interface. The temperature T_{slider} (respectively T_{track}) is calculated by assuming that for the slider (respectively for the ice) the heat source is immobile (respectively mobile for the ice). For an elliptical contact with a semi-ellipsoidal distribution of the heat [107], T_{slider} and T_{track} are given by:

$$T_{slider} - T_0 = \frac{3\pi}{8} \frac{\delta_{heat} \overline{q}_{heat} b}{k_{slider} \sqrt{S_e}} \tag{4.6}$$

$$T_{track} - T_0 = 2.32 \frac{(1-\delta_{heat}) \overline{q}_{heat} b}{k_{ice} \sqrt{\pi (1.234 S_e + P_e)}} \tag{4.7}$$

where T_0 is the temperature far from the contact that corresponds in this case to the environment temperature, S_e is the function characteristic from elliptical heat sources, δ_{heat} is the partitioning coefficient expressing the ratio of heat flux entering the rubber slider ($1 - \delta_{heat}$ express the ratio of heat flux entering the ice), $\overline{q}_{heat}$ is the average flux created within the contact and P_e is the Peclet number.

The function describing elliptical heat sources is defined as:

$$S_e = \frac{16\left(\frac{a}{b}\right)^{1.75}}{(3+\left(\frac{a}{b}\right)^{0.75})(1+3\left(\frac{a}{b}\right)^{0.75})} \tag{4.8}$$

where a is the semi major axis and b the semi minor axis of the elliptical contact.

The Peclet number is defined as:

$$P_e = \frac{V_g b}{2\alpha_{ice}} \tag{4.9}$$

As in the contact, $T_{slider} = T_{track} = T_c$ (T_c is the mean contact temperature), the partitioning factor δ_{heat} can be written as:

$$\delta_{heat} = \frac{18.56 k_{slider}\sqrt{S_e}}{18.56 k_{slider}\sqrt{S_e} + 3\pi k_{ice}\sqrt{\pi(1.234 S_e + P_e)}} \tag{4.10}$$

Assuming that the contact temperature increase is only due to the friction dissipation, it comes:

$$\overline{q}_{heat} = \frac{\mu F_z}{\pi a b} V_g \tag{4.11}$$

where μ is the friction coefficient, F_z the applied normal load and V_g is the sliding velocity.

Therefore by combining equations 4.6, 4.10 and 4.11, the maximum temperature increase within the contact can be deduced:

$$T_c - T_0 = 18.56\frac{3\pi}{8}\frac{\mu\frac{F_z}{\pi a b} b V_g}{18.56 k_{slider}\sqrt{S_e} + 3\pi k_{ice}\sqrt{\pi(1.234 S_e + P_e)}} \tag{4.12}$$

Or,

$$T_c - T_0 = 18.56\frac{3\pi}{4}\alpha_{ice}\frac{\overline{\sigma} P_e}{18.56 k_{slider}\sqrt{S_e} + 3\pi k_{ice}\sqrt{\pi(1.234 S_e + P_e)}} \tag{4.13}$$

where $\overline{\sigma} = \mu\frac{F_z}{\pi a b}$ is the average interfacial shear stress in the rubber-ice contact.

4.3.2. Contact temperature evolution

The contact temperature was deduced using the friction evolution presented in figure 4.3 and the values of contact area and thermal properties reported in table 4.1. An example of contact temperature calculated for tire rubber 1 is illustrated in figure 4.5

as a function of the sliding velocity for the two first sliding sets. The evolution is very similar for both of them: the contact temperature increases with the sliding velocity up to 100 mm.s^{-1}, until it reaches positive values, regardless of the environment temperature. This confirms the initiation of ice surface melting at 100 mm.s^{-1}. Above this critical sliding velocity, the contact temperature decreases: this may be attributed to the appearance of water in the contact. Indeed the equation 4.13 is based on the hypotheses that there is only a rubber-ice contact and that the heat source is distributed on a semi-ellipsoidal form within the contact. The semi-ellipsoidal heat distribution was chosen on the assumption that it follows the pressure distribution within the contact which should be close to Hertzian distribution according to the contact mechanics measurements presented in figure 3.11. The apparition of water within the contact should make invalid these two hypotheses. Even though the thermal properties of the interface could be modified by the existence of a water layer, we supposed that most of the dissipation will occur in the ice and the rubber. At low velocity, the contact temperature is higher as the environment gets hotter. This behavior may explain the peculiar friction response at -2.5°C.

Experimental conditions		
Tire 1	a	3.88 mm
	b	2.87 mm
Tire 3	a	3.47 mm
	b	2.90 mm
Tire 7	a	3.40 mm
	b	2.53 mm
	Fz	10 N

Thermal properties	
k_{ice}	2.21 W.m^{-1}.K^{-1} [24]
α_{ice}	$1.14 * 10^{-6}$ m^2.s^{-1}
k_{slider}	0.216 W.m^{-1}.K^{-1} [109]

Table 4.1.: Experimental contact sizes and thermal parameters used as input data in the equation 4.15 corresponding to the 'tire' rubbers 1, 3 and 7. The semi major and minor axis a and b were measured via phantom images at -10°C at 0.1 mm.s^{-1}. These values ares slightly dependent on the temperature according to the chapter 3.

The evolution of the contact temperature also allows us to calculate and plot the dimensionless temperature increase $(T_c - T_0)/(T_m - T_0)$. Indeed, divided by $T_m - T_0$, equation 4.13 can be made dimensionless:

$$\frac{T_c - T_0}{T_m - T_0} = \frac{3\pi}{4}\alpha_{ice}\frac{\mu\frac{F_z}{\pi ab}}{T_m - T_0}\frac{18.56P_e}{18.56k_{slider}\sqrt{S_e} + 3\pi k_{ice}\sqrt{\pi(1.234S_e + P_e)}} \tag{4.14}$$

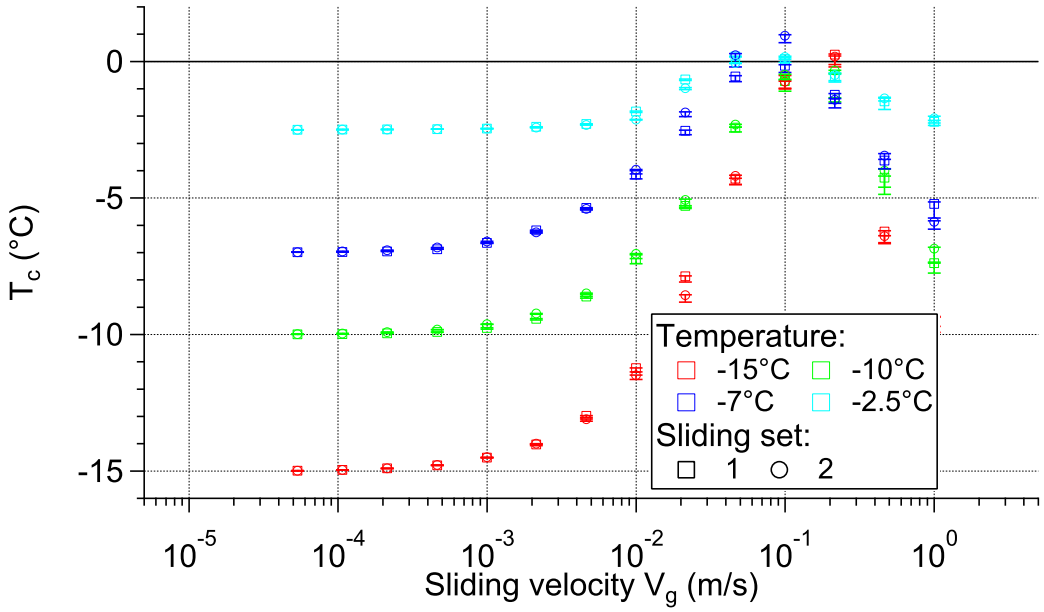

Figure 4.5.: Estimate of the contact temperature within the rubber-ice contact from friction measured at -2.5, -7, -10 and -15°C for 'tire' rubber 1 for a fresh (sliding set 1) and slightly run-in (sliding set 2) interface.

Putting $\lambda_k = \frac{k_{slider}}{k_{ice}}$ and knowing that $\alpha_{ice} = \frac{k_{ice}}{\rho_{ice} c_{ice}}$, this leads to:

$$\boxed{\frac{T_c - T_0}{T_m - T_0} = \frac{3\pi}{4} \frac{\overline{\sigma}}{\rho_{ice} c_{ice} (T_m - T_0)} \frac{18.56 P_e}{18.56 \lambda_k \sqrt{S_e} + 3\pi \sqrt{\pi (1.234 S_e + P_e)}}} \tag{4.15}$$

Thanks to equation 4.15, it is also possible to estimate the evolution of the ratio $(T_c - T_0)/(T_m - T_0)$ as a function of the sliding velocity for each 'tire' rubber and temperature according to the contact and thermal parameters in table 4.1. According to the figure 3.15, the contact area during sliding is close to the static one, for that reason the contact area measured at 0.1 mm.s^{-1} at -10°C was used for the calculations. The figure 4.6 shows that, for 'tire' rubber 1, this dimensionless temperature collapse on the same curve, regardless of the environmental temperature. This trend was also observed for 'tire' rubbers 3 and 7.

The values of $(T_c - T_0)/(T_m - T_0)$ was averaged for different environment temperature T_0 at a given velocity for 'tire' rubber 1, 3 and 7. The evolution of the obtained average value is plotted in figure 4.7 as a function of the sliding velocity. Surprisingly, the points collapse once again on a single curve regardless of the 'tire' rubber, at least in the short range of T_g and G^*, covered by the three rubber samples. Moreover, the maximum of the two master curves of figure 4.6 and 4.7 is reached at the sliding velocity of 100 mm.s^{-1}

which corresponds to the ice surface melting initiation. It can be deduced from the ratio $(T_c - T_0)/(T_m - T_0)$ a function $\kappa(V_g)$, independent of T_0, T_g and G^*, accounting for the viscoelastic and adhesion properties of the rubber-ice interface contribution as well as these of the ice ploughing on the interfacial shear stress.

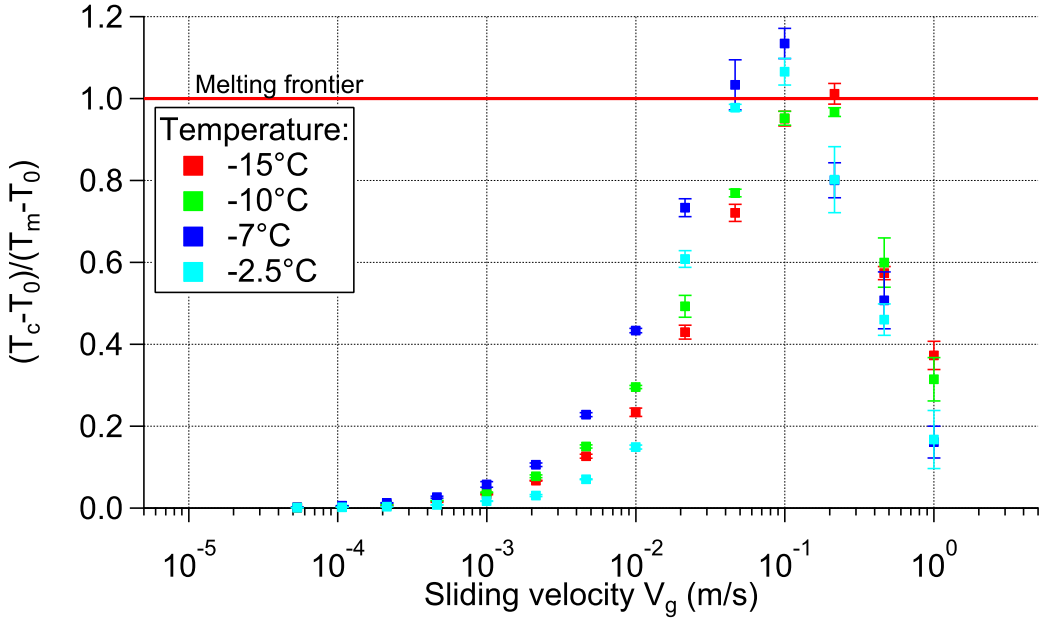

Figure 4.6.: Estimate of the dimensionless temperature increase $(T_c - T_0)/(T_m - T_0)$ within the rubber-ice contact from friction measured at -2.5, -7, -10 and -15°C for 'tire' rubber 1 for a slighly run-in rubber-ice interface.

4.3.3. Estimate of the interfacial average shear stress

According to equation 4.15 and considering that the average interfacial shear stress within the rubber-ice contact is $\overline{\sigma} = \mu \frac{F_z}{\pi ab}$, the collapsing of $(T_c - T_0)/(T_m - T_0)$ means that:

$$\boxed{\overline{\sigma} = \rho_{ice} c_{ice} (T_m - T_0) \left(\frac{4}{3\pi} \frac{\sqrt{S_e}}{P_e} \lambda_k + \frac{1}{4.64} \frac{\sqrt{\pi(1.234 S_e + P_e)}}{P_e} \right) \kappa(V_g)} \qquad (4.16)$$

where κ is the dimensionless function characteristic of the master-curve and which only depends on the sliding velocity. In other words, the interfacial average shear stress only depends on the sliding velocity V_g, the environmental temperature T_0, on the ice melting temperature T_m and on the viscoelastic properties of the rubber at that temperature.

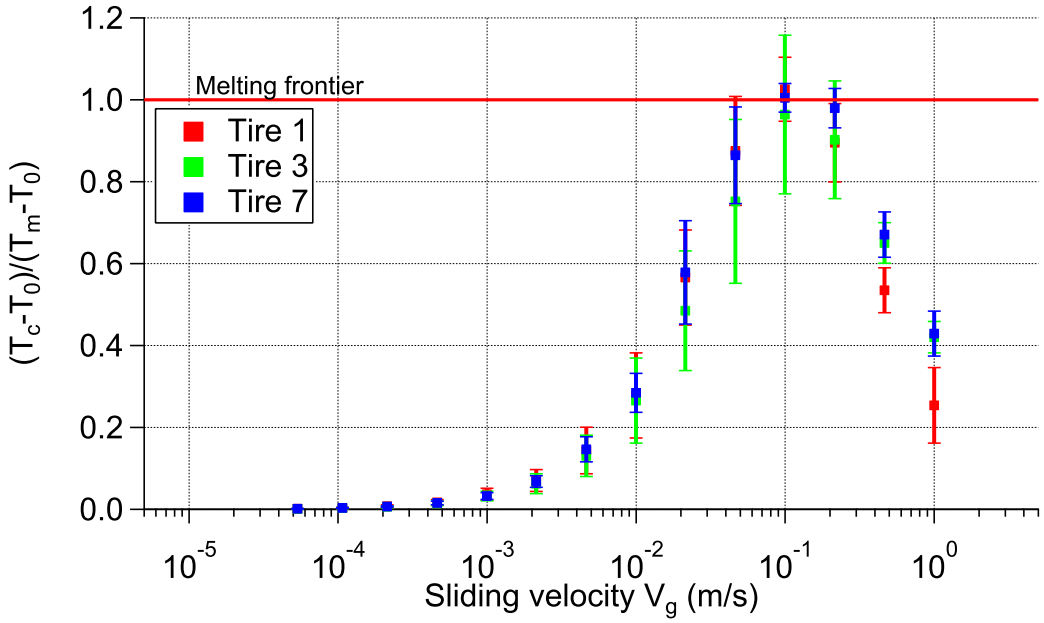

Figure 4.7.: Average estimate of the dimensionless temperature increase $(T_c - T_0)/(T_m - T_0)$ within the rubber-ice contact for 'tire' rubber 1, 3 and 7 for a run-in rubber-ice interface.

According to the equation 4.16, the difference of average interfacial shear stress between the 'tire' rubber 1, 3 and 7 arise principally from the contact size and the thermal conductivity of the rubber regardless of the environment temperature. Moreover, the interfacial shear stress captures all the physics of the friction of the rubber-ice contact, by decoupling the thermal phenomena induced by frictional heating and the role of the viscoelastic properties.

From the determination of the function κ as a function of the sliding velocity V_g and the measurements of the contact size (see table 4.1), it is then possible to predict and estimate the interfacial average shear stress such as presented in figure 4.8 at -10°C.

First, it can be observed that the velocity at which the shear stress is maximum does not coincide with the velocity at which the κ function is maximum. Second, for sliding velocity above the latter, the evolution of the shear stress with the sliding velocity is the same for each 'tire' rubber. This confirms the dominant contribution of thermal effect and ice melting on the frictional behavior of the rubber.

An average effect of the different 'tire' rubbers may be observed below 46 mm.s^{-1}, 'tire' rubbers 1 and 7, with a same T_g, presented a similar interfacial shear stress, that of 'tire' rubber 7 is slightly lower than 'tire' rubber 1. The 'tire' rubber 3, with a higher T_g than 'tire' rubbers 1 and 7, had a lower interfacial shear stress than the two other rubbers. These observations are similar to those made previously on the measurement

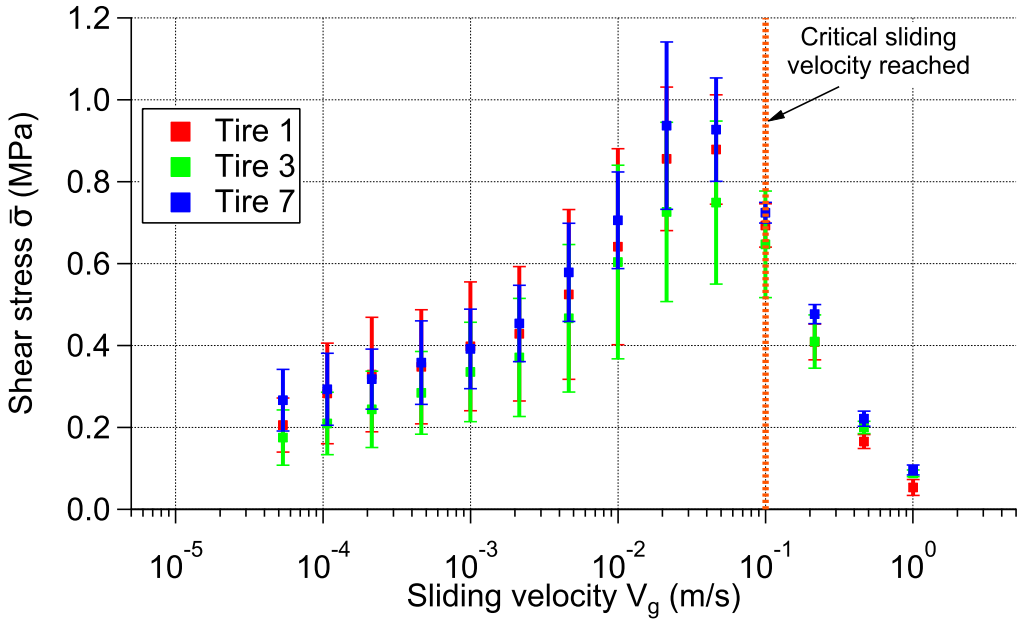

Figure 4.8.: Estimate of the average interfacial shear stress within the rubber-ice contact for 'tire' rubber 1, 3 and 7 at -10°C for a fresh rubber-ice interface. According to the figure 4.7, melting point of the ice is reached at 100 mm.s^{-1}.

presented in figure 3.21 as well as the shear stress level. This result emphasizes the effect of the material properties on the average shear stress despite the effect of the ice variability: the lower the T_g, the higher the shear stress at 'low' velocity. This was also observed by Ahagon *et al* [81].

The average interfacial shear stress $\overline{\sigma}$ can be estimated at several temperatures and were shifted according to the WLF theory such as presented in figure 4.9 for 'tire' rubber 1 with a run-in rubber-ice interface. Almost the same observations can be performed from figure 4.9 as from figure 4.3:

- the shear stress estimated at -2.5°C do not superimposed with the one estimated for other temperatures;
- the shear stress superimposed within the deviation for sliding velocities below 100 mm.s^{-1} at -7°C, -10°C and -15°C;
- the shear stress clearly diverged for 'high' sliding velocities at -7°C, -10°C and -15°C;
- each estimated interfacial shear stress curve present a maximum at 'low' velocities. The sliding velocity of the maximum of shear stress is different for each curve after the velocity shift: the lower the environment temperature, the higher the velocity of the maximum.

Once again, these observations can be extended to 'tire' rubbers 3 and 7. They con-

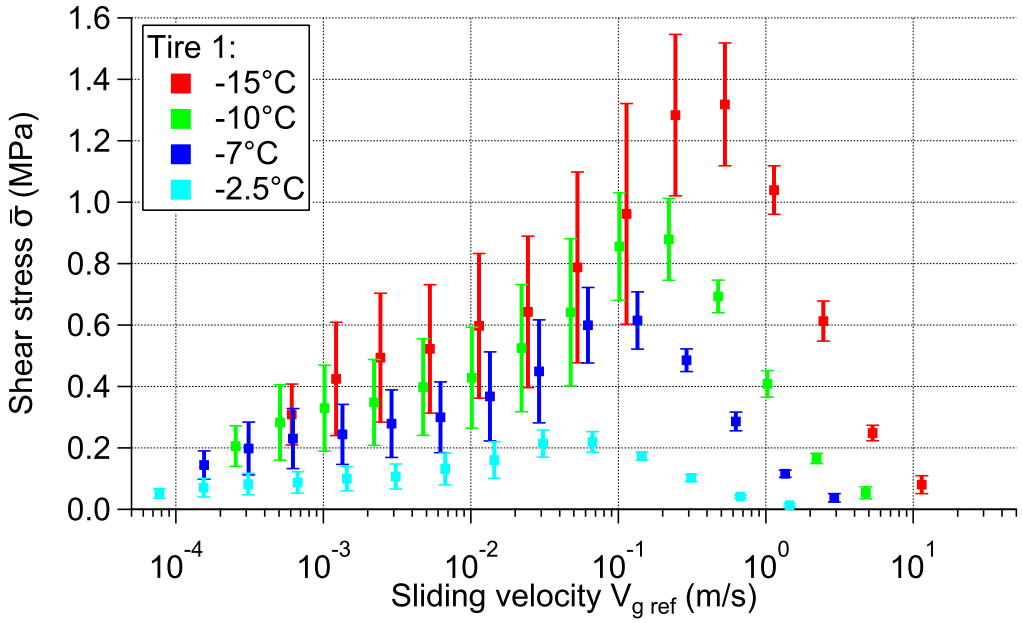

Figure 4.9.: Estimate of the average interfacial shear stress within the rubber-ice contact for 'tire' rubber 1 with a run-in rubber-ice interface shifted according to the WLF theory to the reference temperature $T_{ref} = 0°\text{C}$.

firm the compatibility of the WLF theory for a rubber-ice interface with the existence of the dimensionless temperature curve at least 'far' below the melting temperature and for the 'low' sliding velocity regime.

Dimensionless temperature and shear stress curves were obtained from the master-curve and the contact visualization protocol that give a direct measurement of the contact area. Thus they were compared for the 'tire' rubber 1 for a fresh rubber-ice interface such as in figure 4.10. The dimensionless temperature curves in figure 4.10a showed almost no differences between the master-curve and the temperature in the contact during contact visualization (1 iteration). However, the average interfacial shear stress comparison in figure 4.10b showed large differences from 10 mm.s^{-1}. Both observations can be extended to 'tire' rubbers 3 and 7. The similarity of the figure 4.10a suggests that even large variations of interfacial shear stress due to ice variability such as observed for fresh-rubber ice interface (see figure 4.1) have little influence on the ice surface melting initiation. The divergence of both curves in figure 4.10b shows that the accurate estimation of the interfacial shear stress requires the knowledge of the evolution of the contact area as a function of the sliding velocity.

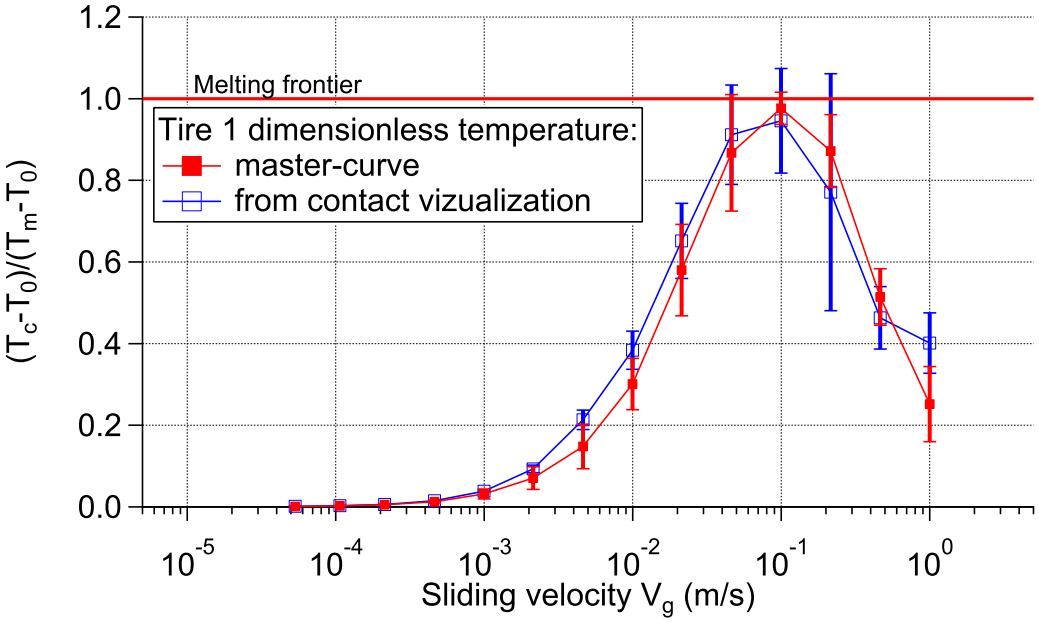

(a) Dimensionless temperature within the rubber-ice contact

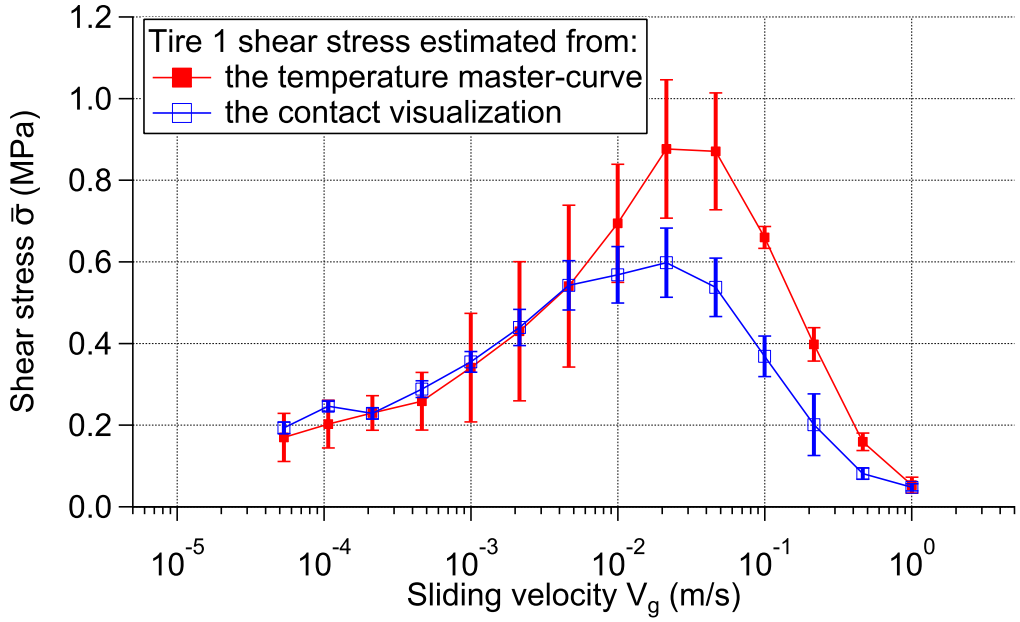

(b) Estimate of the average interfacial shear stress within the rubber-ice contact.

Figure 4.10.: Comparison of the dimensionless temperature and interfacial shear stress obtained via the master-curve (in red, three iterations in average) and the contact visualization (in blue, single iteration) for 'tire' rubber 1 for a fresh rubber-ice interface.

4.4. Conclusion

Several conclusions can be drawn on the role of the viscoelasticty, the temperature, the sliding velocity, the presence of rubber surface agglomerates and the manufactured ice surface on the rubber-ice friction.

Two sliding velocity regimes were identified regardless of the environmental temperature, the ice manufactured and the sliding history of the rubber-ice interface. The transition occurs at a velocity that initiates the ice melting within the rubber-ice interface. It depends on the rubber and ice thermal properties, the contact geometry and the average interfacial shear stress within the contact.

At 'low' sliding velocity, below 100 mm.s^{-1}, where the ice surface is solid and the maximum temperature within the contact is below the melting temperature of the ice. In this regime, the main contribution on friction arises from the viscoelastic dissipation of the bulk rubber. However the friction level is also influenced by the manufactured ice surface and the ploughing of the ice surface by rubber surface agglomerates. The friction curves can be shifted thanks to the application of the WLF theory when the ice surface has been accommodated by the sliding. At 'high' sliding velocity, above 100 mm.s^{-1}, where ice surface melting occur, friction measurements are repeatable. Their variation with the sliding velocity is the same for all rubber type and ice temperature.

According to these observations, the interfacial shear stress only depends on the sliding velocity, the ice melting and the environment temperatures and on the viscoelastic properties of the rubber via the contact size. Effects of the difference of viscoelastic properties seem to be observed on the interfacial shear stress: at 'low' sliding velocity, in average the higher the T_g, the lower the shear stress.

General conclusion

Rubber-ice interaction were performed via two approaches: the study of the rubber-ice friction and the interactions of the rubber-ice interface. Rubber-ice interface was studied via the use of a Surface Force Apparatus (SFA) designed in Kurihara Laboratory. Contact mechanics measurements and Resonance Shear Measurements (RSM) were performed for several variation of rubbers (filled and unfilled) with various viscoelastic properties. Rubber-ice friction was studied via a Kōri tribometer designed in LTDS. This system allowed to cool down a small confined environment while performing friction measurements and simultaneously visualizing the rubber-ice contact. The contact visualization was made possible thanks to an ice manufacturing protocol, that allowed to obtain a flat transparent ice surface, and the image post-processing, that provided completely new information on the behavior, the size and the shape of the rubber-ice contact during friction measurements.

Contact mechanics measurements were performed via an SFA for rubber with fillers (carbon black, silica, *etc*) and without any additional compound (pure vulcanized styrene-butadienne rubber). Both presented consistency with the JKR theory and an adhesion work of almost 30 $mJ.m^{-2}$. On a larger scale, contact mechanics measurements were also performed via the the Kōri tribometer with filled rubber and were consistent with the JKR theory. Adhesion works measured with the SFA were consistent with the value measured at larger scale. However, the adhesion work was enhanced after sliding experiments performed with the rubber-ice interface. In any case, these results imply that the rubber-ice contact is energetically more favorable than their separation by air causing an adhesion friction force.

Contact mechanics measurements performed with filled rubber via the SFA exhibited the influence of the agglomerates of fillers on the rubber surface. These agglomerates present a larger rigidity than the surrounding rubber matrix and the contact with the ice is favored on their top. During sliding, the rubber surface agglomerates modified the ice surface by ploughing it.

Maximum contact temperature was modeled and evidenced initiation of ice surface melting from 100 $mm.s^{-1}$ regardless of the environment temperature. It highlights two sliding velocity regimes. Below 100 $mm.s^{-1}$, the ice surface temperature was below the melting temperature and variation of friction exists from one ice to another one. For this regime, friction measurements were consistent with the WLF theory and Resonance Shear Measurements confirmed that the rubber-ice interface viscoelasticity on solid ice was consistent with bulk rubber viscoelastic properties. At 100 $mm.s^{-1}$, melting tem-

perature was reached within the rubber-ice contact, for that reason, at least partial melting of the ice surface is expected above 100 mm.s^{-1}. For this 'high' velocity regime, friction measurement were repeatable regardless of the ice surface.

The maximum contact temperature calculated for each environment temperature and made dimensionless, by dividing by the difference of temperature between melting and environment temperatures, collapsed on a same master-curve. It implied that the interfacial shear stress within the rubber-ice contact depends:

- on thermal properties of the rubber and ice;
- on the geometry of the contact;
- on the sliding velocity;
- on a function κ, corresponding to the master-curve, depending of the viscoelastic properties of the rubber and the sliding velocity;
- linearly on the difference between the melting temperature and the environment temperature.

In addition, it was observed that large interfacial shear stress within the contact (larger than 0.2 to 0.3 MPa) leads to a deformation of the rubber-ice contact.

Interfacial shear stress was estimated via two different approaches:

- via the measure of the friction force simultaneously with the contact visualization;
- via the estimate of the master-curve κ.

Both methods exhibited an agreement in average of 'tire' rubber ranking despite the variability ice-by-ice. Below 100 mm.s^{-1}, the higher the T_g, the lower the shear stress.

Appendix A

Mechanical properties of 'tire' rubber samples

In this annex are presented the mechanical properties G^* and $\tan\delta$ of the 'tire' rubbers investigated. Firstly, DMA measurements - i.e Dynamic Mechanical Analysis - are presented for two cases:

- for small shear strain deformation (0.2%) at the stress frequency $f = 1$ Hz and $f = 30$ Hz as a function of the temperature T;
- for large shear strain deformation (10%) at the temperature $T = -2.5°\text{C}$ and $T = -10°\text{C}$ as a function of the stress frequency f.

Secondly, the G^* and $\tan\delta$ shifted via the use of the WLF theory described in section 1.2.1 are presented.

A.1. Dynamic mechanical analysis

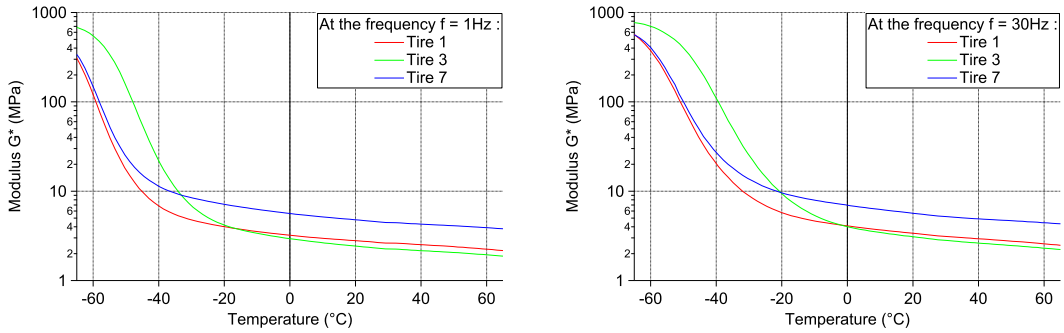

(a) Shear modulus G^* at $f = 1$ Hz. **(b)** Shear modulus G^* at $f = 30$ Hz.

Figure A.1.: Shear modulus G^* measured by DMA for 'tire' rubber 1, 3 and 7 for small shear strain (0.2%).

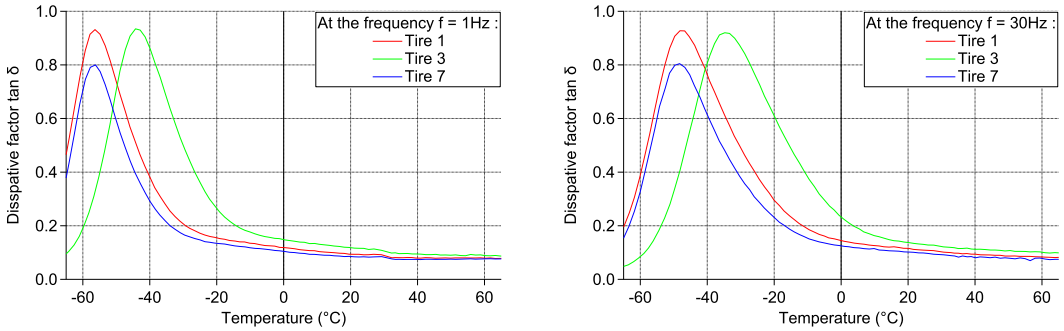

(a) Loss factor $\tan\delta$ at $f = 1$ Hz. **(b)** Loss factor $\tan\delta$ at $f = 30$ Hz.

Figure A.2.: Loss factor $\tan\delta$ measured by DMA for 'tire' rubber 1, 3 and 7 for small shear strain (0.2%).

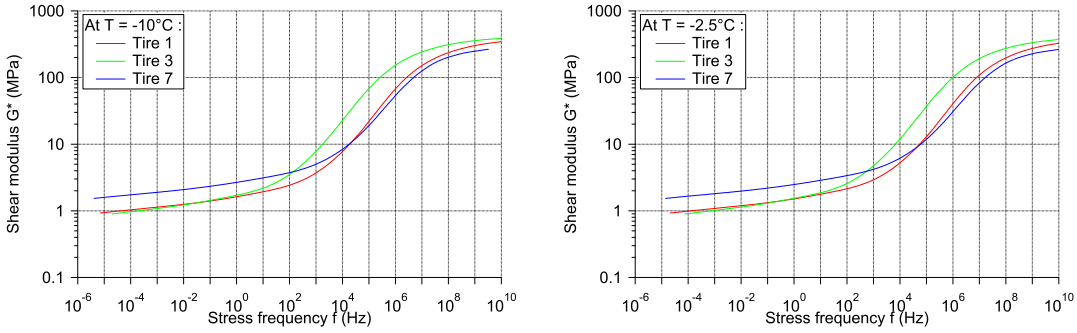

(a) Shear modulus G^* at $T = -10°$C. **(b)** Shear modulus G^* at $T = -2.5°$C.

Figure A.3.: Shear modulus G^* measured by DMA for 'tire' rubber 1, 3 and 7 for large shear strain (10%).

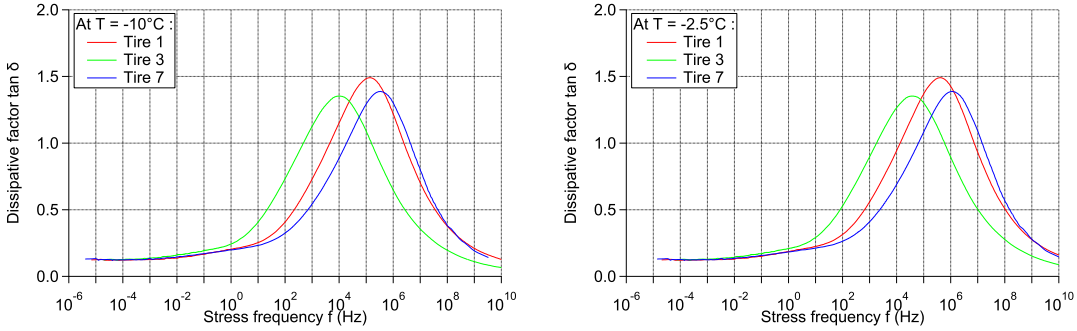

(a) Loss factor $\tan\delta$ at $T = -10°$C. **(b)** Loss factor $\tan\delta$ at $T = -2.5°$C.

Figure A.4.: Shear modulus G^* and loss factor $\tan\delta$ measured by DMA for 'tire' rubber 1, 3 and 7.

A.2. WLF transform

This section presents the mechanical properties - i.e G^* and $\tan\delta$ - measured for large deformations (10%) shifted in temperature using the WLF transform with the coefficient $C_1 = 8.86$ and $C_2 = 140\ K$ to the reference temperature of 0°C. The frequency shift shows that rubber properties measured at -2.5°C and -10°C well superimposed.

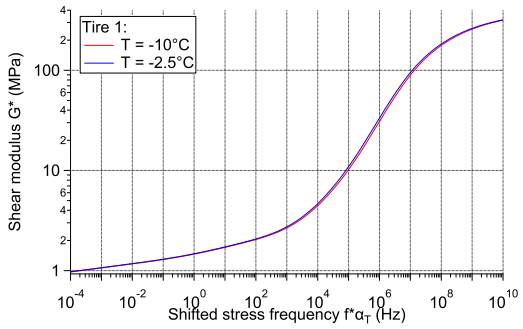

(a) 'Tire' rubber 1 shear modulus G^*

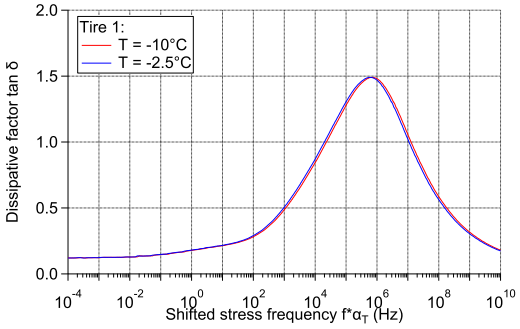

(b) 'Tire' rubber 1 loss factor $\tan\delta$

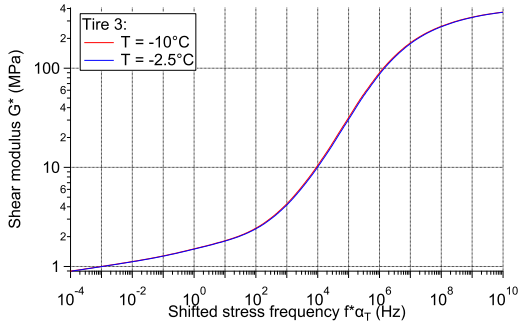

(c) 'Tire' rubber 3 shear modulus G^*

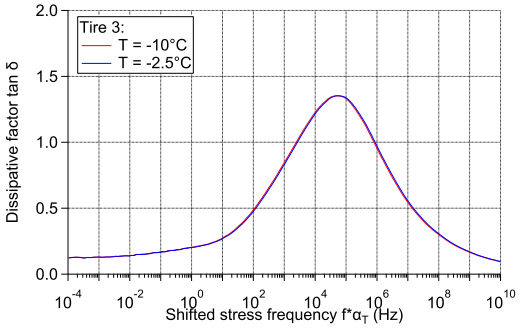

(d) 'Tire' rubber 3 loss factor $\tan\delta$

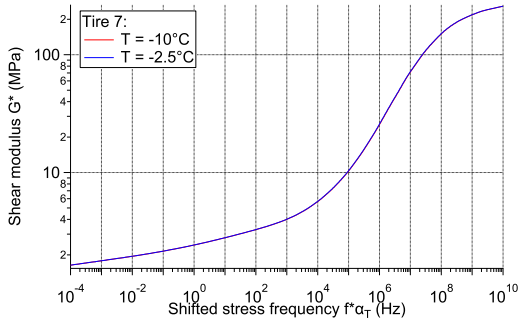

(e) 'Tire' rubber 7 shear modulus G^*

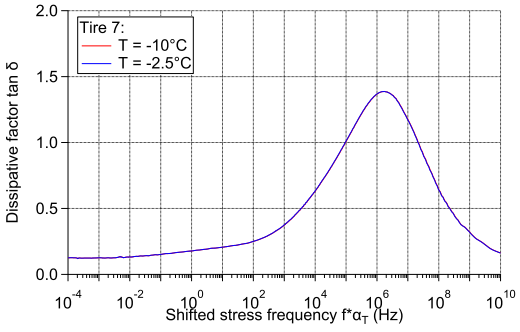

(f) 'Tire' rubber 7 loss factor $\tan\delta$

Figure A.5.: Shear modulus G^* and loss factor $\tan\delta$ measured for large deformations (10%) shifted in temperature to the temperature 0°C for 'tire' rubber 1, 3 and 7.

Appendix B

SFA mechanical model

In this annex are detailed several points of the model that were not presented in the manuscript on page 78:

- The Fourier transform and the development of the calculation between the equations 2.7 and the equation 2.8;
- The shear deformation applied on the sample;
- The shear force applied on the sample;
- The nondimensionalization of the equations 2.9 and 2.10 in order to ease the fitting of resonance peaks such as presented in figure 2.14.

B.1. Calculation development

The equations 2.7 can be rewritten in the frequency domain in the following form:

$$m_{1\_1}(j\omega)^2\underline{x_{spring}}(\omega)+m_{1\_2}(j\omega)^2\underline{x_1}(\omega)+m_2(j\omega)^2\underline{x_2}(\omega) = -k_1\underline{x_{spring}}(\omega)-b_1j\omega\underline{x_{spring}}(\omega)-k_3\underline{x_2}(\omega)-b_3j\omega\underline{x_2}$$

$$m_2(j\omega)^2\underline{x_2}(\omega) = -k_3\underline{x_2}(\omega) - b_3j\omega\underline{x_2}(\omega) - \underline{g}(\omega)(\underline{x_2}(\omega) - \underline{x_1}(\omega))$$

$$\underline{x_1}(\omega) - \underline{x_{spring}}(\omega) = C_{in}\underline{U_{in}}(\omega)$$

$$\underline{x_{spring}}(\omega) = C_{out}\underline{U_{out}}(\omega)$$

where the the model $g(x_2(t) - x_1(t))$ verifies the following condition on its Fourier transform: $\mathcal{F}(g(x_2(t) - x_1(t)) = \underline{g}(\omega)(\underline{x_2}(\omega) - \underline{x_1}(\omega))$.

Therefore:

$$(m_{1\_1}(j\omega)^2+b_1j\omega+k_1)\underline{x_{spring}}(\omega)+m_{1\_2}(j\omega)^2\underline{x_1}(\omega)+(m_2(j\omega)^2+b_3j\omega+k_3)\underline{x_2}(\omega) = 0$$

$$\underline{x_2}(\omega) = \frac{\underline{g}(\omega)}{m_2(j\omega)^2 + b_3j\omega + k_3 + \underline{g}(\omega)}\underline{x_1}(\omega)$$

$$\underline{x_1}(\omega) - \underline{x_{spring}}(\omega) = C_{in}\underline{U_{in}}(\omega)$$
$$\underline{x_{spring}}(\omega) = C_{out}\underline{U_{out}}(\omega)$$

Therefore replacing $\underline{x_2}(\omega)$:

$$(m_{1\_1}(j\omega)^2 + b_1 j\omega + k_1)\underline{x_{spring}}(\omega) + \left(m_{1\_2}(j\omega)^2 + \frac{\underline{g}(\omega)[m_2(j\omega)^2 + b_3 j\omega + k_3]}{m_2(j\omega)^2 + b_3 j\omega + k_3 + \underline{g}(\omega)}\right)\underline{x_1}(\omega) = 0$$

Therefore replacing $\underline{x_{spring}}(\omega)$ and $\underline{x_1}(\omega)$:

$$\left(m_{1\_2}(j\omega)^2 + \frac{\underline{g}(\omega)(m_2(j\omega)^2 + b_3 j\omega + k_3)}{m_2(j\omega)^2 + b_3 j\omega + k_3 + \underline{g}(\omega)}\right)(C_{out}\underline{U_{out}}(\omega) + C_{in}\underline{U_{in}}(\omega))$$
$$+(m_{1\_1}(j\omega)^2 + b_1 j\omega + k_1)C_{out}\underline{U_{out}}(\omega) = 0$$

Therefore grouping $\underline{U_{in}}(\omega)$ and $\underline{U_{out}}(\omega)$:

$$\left(m_{1\_2}(j\omega)^2 + \frac{\underline{g}(\omega)(m_2(j\omega)^2 + b_3 j\omega + k_3)}{m_2(j\omega)^2 + b_3 j\omega + k_3 + \underline{g}(\omega)} + m_{1\_1}(j\omega)^2 + b_1 j\omega + k_1\right)C_{out}\underline{U_{out}}(\omega)$$
$$+\left(m_{1\_2}(j\omega)^2 + \frac{\underline{g}(\omega)(m_2(j\omega)^2 + b_3 j\omega + k_3)}{m_2(j\omega)^2 + b_3 j\omega + k_3 + \underline{g}(\omega)}\right)C_{in}\underline{U_{in}}(\omega) = 0$$

Therefore:

$$\frac{\underline{U_{out}}}{\underline{U_{in}}}(\omega) = -\frac{C_{in}}{C_{out}}\frac{m_{1\_2}(j\omega)^2 + \frac{\underline{g}(\omega)(m_2(j\omega)^2 + b_3 j\omega + k_3)}{m_2(j\omega)^2 + b_3 j\omega + k_3 + \underline{g}(\omega)}}{m_{1\_2}(j\omega)^2 + \frac{\underline{g}(\omega)(m_2(j\omega)^2 + b_3 j\omega + k_3)}{m_2(j\omega)^2 + b_3 j\omega + k_3 + \underline{g}(\omega)} + m_{1\_1}(j\omega)^2 + b_1 j\omega + k_1}$$

Therefore:

$$\frac{\underline{U_{out}}}{\underline{U_{in}}}(\omega) = -\frac{C_{in}}{C_{out}}\frac{m_{1\_2}(j\omega)^2[m_2(j\omega)^2 + b_3 j\omega + k_3 + \underline{g}(\omega)] + \underline{g}(\omega)(m_2(j\omega)^2 + b_3 j\omega + k_3)}{((m_{1\_2} + m_{1\_1})(j\omega)^2 + b_1 j\omega + k_1)(m_2(j\omega)^2 + b_3 j\omega + k_3 + \underline{g}(\omega))}$$
$$+\underline{g}(\omega)(m_2(j\omega)^2 + b_3 j\omega + k_3)$$

Therefore grouping $\underline{g}(\omega)$ in the denominator, the final transfer equation linking $\underline{U_{in}}(\omega)$ and $\underline{U_{out}}(\omega)$ is obtained:

$$\frac{\underline{U_{out}}}{\underline{U_{in}}}(\omega) = -\frac{C_{in}}{C_{out}} \frac{m_{1\_2}(j\omega)^2(m_2(j\omega)^2 + b_3 j\omega + k_3) + \underline{g}(\omega)((m_{1\_2} + m_2)(j\omega)^2 + b_3 j\omega + k_3)}{((m_{1\_1} + m_{1\_2})(j\omega)^2 + b_1 j\omega + k_1)(m_2(j\omega)^2 + b_3 j\omega + k_3) + \underline{g}(\omega)((m_{1\_1} + m_{1\_2} + m_2)(j\omega)^2 + (b_1 + b_3)j\omega + (k_1 + k_3))}$$

B.2. Shear deformation

Shear deformation can be easily established from equations 2.7. This results gives an idea of the shear deformation of the rubber sample.

$$\frac{\underline{x_2}}{\underline{x_1}}(\omega) = \frac{\underline{g}(\omega)}{m_2(j\omega)^2 + b_3 j\omega + k_3 + \underline{g}(\omega)}$$

The module and phase of displacement are as follows:

$$\left\| \frac{\underline{x_2}}{\underline{x_1}} \right\| (\omega) = \frac{\left\| \underline{g}(\omega) \right\|}{\sqrt{\left(Re(\underline{g}(\omega)) + k_3 - m_2(\omega)^2 \right)^2 + \left(Im(\underline{g}(\omega)) + b_3\omega \right)^2}}$$

$$\begin{aligned} arg\left(\frac{\underline{x_2}}{\underline{x_1}}(\omega)\right) &= arg\left(\frac{\underline{g}(\omega)}{m_2(j\omega)^2 + b_3 j\omega + k_3 + \underline{g}(\omega)}\right) \\ &= arctan\left(\frac{Im(\underline{g}(\omega))}{Re(\underline{g}(\omega))}\right) - arctan\left(\frac{Im(\underline{g}(\omega)) + b_3\omega}{Re(\underline{g}(\omega)) + k_3 - m_2\omega^2}\right) \end{aligned}$$

B.3. Shear force

Shear deformation can be easily established from equations 2.7 by defining the shear force as:

$$\|F_{shear}\| = \left\| \overrightarrow{F_{3/2}} \right\| = |-g(x_1(t) - x_2(t))|$$

Therefore in the frequency domain:

$$\underline{F_{shear}}(\omega) = -\underline{g}(\omega)\left(\underline{x_1}(\omega) - \underline{x_2}(\omega)\right)$$

We know that:

$$\frac{\underline{x_2}}{\underline{x_1}}(\omega) = \frac{\underline{g}(\omega)}{m_2(j\omega)^2 + b_3 j\omega + k_3 + \underline{g}(\omega)}$$

And the relationship between $\underline{x_1}(\omega)$ and $\underline{x_{spring}}(\omega)$:

$$(m_{1\_1}(j\omega)^2 + b_1 j\omega + k_1)\underline{x_{spring}}(\omega) + \left(m_{1\_2}(j\omega)^2 + \frac{\underline{g}(\omega)(m_2(j\omega)^2 + b_3 j\omega + k_3)}{m_2(j\omega)^2 + b_3 j\omega + k_3 + \underline{g}(\omega)}\right)\underline{x_1}(\omega) = 0$$

$$\underline{x_1}(\omega) = -\frac{(m_{1\_1}(j\omega)^2 + b_1 j\omega + k_1)(m_2(j\omega)^2 + b_3 j\omega + k_3 + \underline{g}(\omega))}{m_{1\_2}(j\omega)^2(m_2(j\omega)^2 + b_3 j\omega + k_3 + \underline{g}(\omega)) + \underline{g}(\omega)(m_2(j\omega)^2 + b_3 j\omega + k_3)}\underline{x_{spring}}(\omega)$$

Therefore the relationship between the shear fore $\underline{F_{shear}}(\omega)$ and $\underline{x_{spring}}(\omega)$ is the following:

$$\underline{F_{shear}}(\omega) = -\underline{g}(\omega)\left(1 - \frac{\underline{g}(\omega)}{m_2(j\omega)^2 + b_3 j\omega + k_3 + \underline{g}(\omega)}\right)\underline{x_1}(\omega)$$

$$\underline{F_{shear}}(\omega) = \underline{g}(\omega)\left(1 - \frac{\underline{g}(\omega)}{m_2(j\omega)^2 + b_3 j\omega + k_3 + \underline{g}(\omega)}\right)$$
$$\frac{(m_{1\_1}(j\omega)^2 + b_1 j\omega + k_1)(m_2(j\omega)^2 + b_3 j\omega + k_3 + \underline{g}(\omega))}{m_{1\_2}(j\omega)^2(m_2(j\omega)^2 + b_3 j\omega + k_3 + \underline{g}(\omega)) + \underline{g}(\omega)(m_2(j\omega)^2 + b_3 j\omega + k_3)}\underline{x_{spring}}(\omega)$$

Therefore:

$$\underline{F_{shear}}(\omega) = \underline{g}(\omega)\frac{m_2(j\omega)^2 + b_3 j\omega + k_3}{m_2(j\omega)^2 + b_3 j\omega + k_3 + \underline{g}(\omega)}$$
$$\frac{(m_{1\_1}(j\omega)^2 + b_1 j\omega + k_1)(m_2(j\omega)^2 + b_3 j\omega + k_3 + \underline{g}(\omega))}{m_{1\_2}(j\omega)^2[m_2(j\omega)^2 + b_3 j\omega + k_3 + \underline{g}(\omega)] + \underline{g}(\omega)(m_2(j\omega)^2 + b_3 j\omega + k_3)}\underline{x_{spring}}(\omega)$$

Therefore by replacing $\underline{x_{spring}}(\omega)$ by $C_{out}\underline{U_{out}}(\omega)$:

$$\underline{F_{shear}}(\omega) = \frac{\underline{g}(\omega)(m_2(j\omega)^2 + b_3 j\omega + k_3)}{m_2(j\omega)^2 + b_3 j\omega + k_3 + \underline{g}(\omega)}$$
$$\frac{(m_{1\_1}(j\omega)^2 + b_1 j\omega + k_1)(m_2(j\omega)^2 + b_3 j\omega + k_3 + \underline{g}(\omega))}{m_{1\_2}(j\omega)^2(m_2(j\omega)^2 + b_3 j\omega + k_3 + \underline{g}(\omega)) + \underline{g}(\omega)(m_2(j\omega)^2 + b_3 j\omega + k_3)}C_{out}\underline{U_{out}}(\omega) \tag{B.1}$$

B.4. Nondimensionalization

In order to ease the fitting of resonance peaks - such as shown in Figure.2.16 - a nondimensionalization of the AS and SC frequency equation was performed.

The air separation frequency equation $\underline{H}_1(\omega)$ can be rewritten as follows:

$$\underline{H}_1(\omega) = -\frac{C_{in}}{C_{out}} \frac{m_{1\_2}(j\omega)^2}{(m_{1\_1}+m_{1\_2})(j\omega)^2 + b_1 j\omega + k_1} = H_1 \frac{\left(j\frac{\omega}{\omega_{01}}\right)^2}{\left(j\frac{\omega}{\omega_{01}}\right)^2 + j2\zeta_1\frac{\omega}{\omega_{01}} + 1}$$

where the canonical parameters are:

$$H_1 = -\frac{C_{in}}{C_{out}} \frac{m_{1\_2}}{m_{1\_1}+m_{1\_2}} \quad \text{and} \quad \omega_{01}^2 = \frac{k_1}{m_{1\_1}+m_{1\_2}} \quad \text{and} \quad \zeta_1 = \frac{1}{2}\frac{b_1}{k_1}\omega_{01}$$

The solid contact frequency equation $\underline{H}_3(\omega)$ can be rewritten as follows:

$$\underline{H}_3(\omega) = -\frac{C_{in}}{C_{out}} \frac{(m_{1\_2}+m_2)(j\omega)^2 + b_3 j\omega + k_3}{(m_{1\_1}+m_{1\_2}+m_2)(j\omega)^2 + (b_1+b_3)j\omega + k_1 + k_3} = H_3 \frac{\left(j\frac{\omega}{\omega_3}\right)^2 + j2\zeta_{33}\frac{\omega}{\omega_3} + 1}{\left(j\frac{\omega}{\omega_{03}}\right)^2 + j2\zeta_3\frac{\omega}{\omega_{03}} + 1}$$

where the canonical parameters are:

$$H_3 = -\frac{C_{in}}{C_{out}} \frac{k_3}{k_1+k_3} \quad \text{and} \quad \omega_{03}^2 = \frac{k_1+k_3}{m_{1\_1}+m_{1\_2}+m_2} \quad \text{and} \quad \zeta_3 = \frac{1}{2}\frac{b_1+b_3}{k_1+k_3}\omega_{03}$$

$$\text{and} \quad \omega_3 = \frac{k_3}{m_{1\_2}+m_2} \quad \text{and} \quad \zeta_{33} = \frac{1}{2}\frac{b_3}{k_3}\omega_3$$

This nondimensionalization gives useful parameters such as:

- The static gains, H_1 and H_3, which influence the the resonance peak height and the zero frequency value;
- The attenuation factors, ζ_1 and ζ_3, which influence the height of the peak and tend to shift the resonance peak in frequency;
- The natural pulsation ω_{01} and ω_{03} that can be expressed as a function of the natural frequency - also called eigenfrequency - $f_{01} = \frac{\omega_{01}}{2\pi}$ and $f_{03} = \frac{\omega_{03}}{2\pi}$ which are good approximations of the frequency of the resonance peak - when attenuation factors are low;
- The parameter ω_3 influences the high frequency gain;
- The ζ_{33} remains difficult to interpret.

These eight canonical parameters give eight equations that may be solved to obtain

the eight parameters of the system: m_{1_1}, m_{1_2}, m_2, k_1, k_3, b_1, b_3 and $C = C_{in}/C_{out}$.

Unfortunately, one of the equations corresponds to a combination of the others, implying that only relationships between system parameters can be found.

Therefore, at least one parameter of the system must be fixed. Here, it was decided to fix two parameters: m_{1_1} and m_2 which are easily measurable and to not use the the parameter ζ_{33} - which is the most difficult to interpret - to perform the fits.

Thus solving of the canonical parameters gave the following relationships:

$$\left|\frac{C_{in}}{C_{out}}\right| = H_1 \frac{m_{1\_1} + m_{1\_2}}{m_{1\_2}}$$

$$k_1 = \omega_{01}^2 (m_{1\_1} + m_{1\_2})$$

$$b_1 = 2\zeta_1 \omega_{01} (m_{1\_1} + m_{1\_2})$$

$$k_3 = \omega_{03}^2 (m_{1\_1} + m_{1\_2} + m_2) - k_1$$

$$b_3 = 2\zeta_3 \omega_{03} (m_{1\_1} + m_{1\_2} + m_2) - b_1$$

$$\zeta_{33} = \frac{1}{2}\frac{b_3}{k_3}\omega_3$$

$$m_{1\_2} = -\frac{(2H_1\omega_{03}^2 - 2H_1\omega_{01}^2 - H_3\omega_{03}^2)m_{1\_1} + (H_1 - H_3)\omega_{03}^2 m_2}{2(H_1\omega_{03}^2 - H_1\omega_{01}^2 - H_3\omega_0 3^2)}$$
$$\left(1 \pm \sqrt{1 - 4\frac{(H_1\omega_{03}^2 - H_1\omega_{01}^2 - H_3\omega_{03}^2)\left((H_1\omega_{03}^2 - H_1\omega_{01}^2)m_{1\_1} + H_1\omega_{03}^2 m_2\right) m_{1\_1}}{\left((2H_1\omega_{03}^2 - 2H_1\omega_{01}^2 - H_3\omega_{03}^2)m_{1\_1} + (H_1 - H_3)\omega_{03}^2 m_2\right)^2}}\right)$$

Bibliography

[1] F. P. Bowden and D. Tabor. *The friction and lubrication of solids: Part II*. Oxford: Clarendon Press, 1964. ISBN: 978-0-198-51238-7. 1

[2] Manufacture Française des Pneumatiques Michelin. The tire digest, 2018. URL: thetiredigest.michelin.com. 4

[3] G. Petitet and M. Barquins. *Matériaux caoutchouteux*. Presses Polytechniques et Universitaires romandes, 2008. ISBN: 978-2-88074-744-2. 4, 6, 7, 14

[4] A. Mark. *Polymer Science Dictionary*. Springer, 1989. ISBN: 185-1-66220-0. doi:10.1007/978-94-024-0893-5. 6, 13

[5] M. L. Williams, R. F. Landel, and J. D. Ferry. The temperature dependence of relaxation mechanisms in amorphous polymers and other glass-forming liquids. *Journal of American Chemical Society*, 77(14), 1955. doi:10.1021/ja01619a008. 9, 133

[6] A. K. Doolittle. The dependence of the viscosity of liquids on freespace. *American Institute of Physics*, 22(12), 1951. doi:10.1063/1.1699894. 9

[7] G. Petitet. *Contribution à la compréhension des mécanismes élémentaires d'usure douce des élastomères chargés réticulés*. PhD thesis, 2003. 12, 13, 47, 73, 87, 101, 102, 112

[8] K. Kendall. Agglomerate strength. *Powder Metallurgy*, 31(1), 1988. doi:10.1179/pom.1988.31.1.1. 12

[9] K. Kendall, N. M. Alford, W. J. Clegg, and J. D. Birchall. Flocculation clustering and weakness of ceramics. *Nature*, 339, 1989. doi:10.1038/339130a0. 12

[10] J. L. Leblanc. Rubber-filler interactions and rheological properties in filled compounds. *Progress in Polymer Science*, 27(4), 2002. doi:10.1016/S0079-6700(01)00040-5. 12

[11] E. M. Danneberg. The effects of surface chemical interactions on the properties of filler-reinforced rubbers. *Rubber Chemistry and Technology*, 48(3), 1975. doi:10.5254/1.3547460. 13, 14

[12] A. Einstein. Eine neue bestimmung der moleküldimensionen. *Annalen der Physik*, 324(2), 1906. doi:10.1002/andp.19063240204. 13

[13] M-J. Wang. The role of filler networking in dynamic properties of filled rubber. *American Chemical Society*, 72(2), 1998. doi:10.5254/1.3538812. 14

[14] E. R. Pounder. *The Physics Of Ice*. Pergamon Press, 1965. ISBN: 978-1-48322-696-5. doi:10.1016/C2013-0-08278-3. 15

[15] M. Truffler. *Ice Physics*. University of Alaska, Fairbanks, 2013. URL: https://glaciers.gi.alaska.edu/sites/default/files/icephysics.pdf. 16, 20, 21, 24

[16] M. Chaplin. Water structure and science, 2018. URL: www1.lsbu.ac.uk/water. 16, 17, 18, 19

[17] V. F. Petrenko and R. W. Whitworth. *Physics Of Ice*. Oxford University Press, 2002. ISBN: 978-0-19851-894-5. doi:10.1093/acprof:oso/9780198518945.001.0001. 16, 18, 21, 24, 25, 102

[18] J. D. Bernal and R. H. Fowler. A theory of water and ionic solution, with particular reference to hydrogen and hydroxyl ions. *The Journal of Chemical Physics*, 1(8), 1933. doi:10.1063/1.1749327. 18

[19] L. E. Bove, S. Klotz, A. Paciaroni, and F. Sacchetti. Anomalous proton dynamics in ice at low temperatures. *Physical Review Letters*, 103(16), 2009. doi:10.1103/PhysRevLett.103.165901. 18

[20] M. I. Ryzhkin, A. V. Klyuev, V. V. Sinitsyn, and I. A. Ryzhkin. Liquid state of hydrogen bond network in ice. *JETP Letters*, 104(4), 2016. doi:10.1134/S0021364016160013. 18

[21] J. G. Dash, H. Fut, and J. S. Wettlaufert. The premelting of ice and its environmental consequences. *Reports on Progress in Physics*, 58(1), 1995. doi:10.1088/0034-4885/58/1/003. 20

[22] J. G. Dash, A. W. Rempel, and J. S. Wettlaufer. The physics of premelted ice and its geophysical consequences. *Review of Moder Physics*, 78(3), 2006. doi:10.1103/RevModPhys.78.695. 20

[23] B. Michel and R. O. Ramseier. Classification of river and lake ice. *Canadian Geotechnical Journal*, 8(1), 1971. doi:10.1139/t71-004. 21, 102

[24] Å. Melinder. Properties and other aspects of aqueous solutions used for single phase and ice slurry applications. *Internationnal Journal of Refrigeration*, 33(8), 2010. doi:10.1016/j.ijrefrig.2010.07.014. 22, 23, 141

[25] P. H. Gammon, H. Kiefte, M. J. Clouter, and W. W. Denner. Elastic constants of artificial and natural ice by Brillouin spectroscopy. *Journal of Glaciology*, 29(103), 1983. doi:10.3189/S0022143000030355. 24

[26] H. Hertz. Ueber die berührung fester elastischer körper (On the contact of elastic solids). *Journal fur die Reine und Angewandte Mathematik*, 1882. For english translation see *Hertz's miscellaneous papers* by H. Hertz, Eds. D. E. Jones and G. A. Schott, Macmillan, 1896. URL: https://archive.org/details/cu31924012500306. 25

[27] H. Hertz. Üeber die berührung fester elastischer körper und üeber die harte (On the contact of elastic solids and on hardness). *Verhandlungen des Vereins zur Beförderung des Gewerbefleisses*, 1882. For english translation see *Hertz's miscellaneous papers* by H. Hertz, Eds. D. E. Jones and G. A. Schott, Macmillan, 1896. URL: https://archive.org/details/cu31924012500306. 25

[28] K. L. Johnson. *Contact mechanics*. Cambridge University Press, 1987. ISBN: 978-1-13917-173-1. doi:10.1017/CBO9781139171731. 25

[29] K. L. Johnson and J. A. Greenwood. An adhesion map for the contact of elastic spheres. *Journal of Colloid and Interface Science*, 192(2), 1997. doi:10.1006/jcis.1997.4984. 27

[30] R. S. Bradley. The cohesive force between solid surfaces and the surface energy of solids. *The London, Edinburgh, and Dublin Philosophical Magazine and Journal of Science*, 13(86), 1932. doi:10.1080/14786449209461990. 26

[31] K. L. Johnson, K. Kendall, and A. D. Roberts. Surface energy and the contact of elastic solids. *Proceedings of the Royal Society*, 324(1558), 1971. doi:10.1098/rspa.1971.0141. 26

[32] V. L. Popov. *Contact mechanics and friction: Physical principles and applications*. Springer-Verlag Berlin Heidelberg, 2010. doi:10.1007/978-3-642-10803-7. 26, 69, 71, 87

[33] B. V. Derjaguin, V. M. Muller, and Y. P. Toporov. Effect of contact deformations on the adhesion of particles. *Journal of Colloid and Interface Science*, 53(2), 1975. doi:10.1016/0021-9797(75)90018-1. 28

[34] V. M. Muller, B. V. Derjaguin, and Y. P. Toporov. On two methods of calculation of the force of sticking of an elastic sphere to a rigid plane. *Colloids and Surfaces*, 7(3), 1983. doi:10.1016/0166-6622(83)80051-1. 28

[35] D. Tabor. Surface forces and surface interractions. *Journal of Colloid and Interface Science*, 58(1), 1976. doi:10.1016/0021-9797(77)90366-6. 29

[36] D. Maugis. Adhesion of spheres: The JKR-DMT transition using a Dugdale model. *Journal of Colloid and Interface Science*, 150(1), 1991. doi:10.1016/0021-9797(92)90285-T. 29

[37] R. W. Carpick, D. F. Ogletree, and M. Salmeron. A general equation from fitting contact area and friction vs load measurement. *Journal of Colloid and Interface Science*, 211(2), 1998. doi:10.1006/jcis.1998.6027. 30

[38] H. W. Kummer. *Unified theory of rubber and tire friction*. Pennsylvania State University, College of Engineering, 1966. 30, 31, 32, 35

[39] A. D. Roberts. A guide to estimating the friction of rubber. *Rubber Chemistry and Technology*, 65(3), 1992. doi:10.5254/1.3538633. 30

[40] A. D. Roberts. Rubber contact phenomena. *Rubber Chemistry and Technology*, 87(3), 2014. doi:10.5254/rct.14.85982. 30, 31, 35, 46, 50

[41] R. H. Smith. *Analyzing friction in the design of rubber products and their paired surfaces*. CRC Press, 2008. ISBN: 978-0-849-38136-2. 31, 32, 35

[42] W. O. Yandell. A new theory of hysteretic sliding friction. *Wear*, 17(4), 1970. doi:10.1016/0043-1648(71)90027-5. 31, 32

[43] J. M. Golden. Hysteresis and lubricated rubber friction. *Wear*, 65(1), 1980. doi:10.1016/0043-1648(80)90010-1. 31, 32

[44] A. Schallamach. Recent advances in knowledge of rubber friction and tire wear. *Rubber Chemistry and Technology*, 41(1), 1968. doi:10.5254/1.3539171. 31, 32, 35, 92

[45] J. Yu, S. Chary, S. Das, J. Tamelier, K. L. Turner, and J. N. Israelachvili. Friction and adhesion of gecko-inspired PDMS flaps on rough surfaces. *Langmuir*, 28(31), 2012. doi:10.1021/la301783q. 32

[46] D. Tabor. The mechanism of rolling friction II. The elastic range. *Proceeding of the Royal Scociety A*, 229(1177), 1955. doi:10.1098/rspa.1955.0082. 32, 92

[47] A. R. Savkoor. On the friction of rubber. *Wear*, 8(3), 1965. doi:10.1016/0043-1648(65)90161-4. 32, 35

[48] K. A. Grosch. Relation between the friction and visco-elastic properties of rubber. *Nature*, 274(1356), 1963. doi:10.1098/rspa.1963.0112. 32, 33, 45, 50, 133, 135

[49] K. A. Grosch. Rubber friction and its relation to tire traction. *Rubber Chemistry and Technology*, 80(3), 2007. doi:10.5254/1.3548172. 34, 37, 38, 47, 92, 122

[50] A. Schallamach. Friction and frictional rise of wedge sliders on rubber. *Wear*, 13(1), 1969. doi:10.1016/0043-1648(69)90428-1. 34

[51] F. L. Roth, R. L. Driscoll, and W. L. Holt. Frictional properties of rubber. *Journal of the Franklin Institute*, 16(1), 1942. doi:10.5254/1.3540095. 34

[52] A. Schallamach. How does rubber slide? *Wear*, 17(4), 1971. doi:10.1016/0043-1648(71)90033-0. 35, 118

[53] Y. Wang and Q. J. Wang. Stribeck curves. In Q. J. Wang and Y. Chung, editors, *Encyclopedia of Tribology*. Springer US, 2013. ISBN: 978-0-387-92896-8. 36

[54] B. N. J. Persson, U. Tartaglino, O. Albohr, and E. Tosatti. Rubber friction on wet and dry road surfaces: The sealing effect. *Physical Review B*, 71(3), 2005. doi:10.1103/PhysRevB.71.035428. 37

[55] M. Faraday. Ueber die regelation. *Annalen der Physik*, 187(12), 1860. doi:10.1002/andp.18601871217. 38

[56] D. Tabor and J. C. F. Walker. Creep and friction of ice. *Nature*, 228, 1970. doi:10.1038/228137a0. 38, 39, 41, 92

[57] H. H. G. Jellinek. Adhesive properties of ice. *Journal of colloid science*, 14(3), 1959. doi:10.1016/0095-8522(59)90051-0. 38, 41, 50, 92, 126, 127

[58] J. R. Blackford, G. Skouvaklis, M. Purser, and V. Koutsos. Friction on ice: Stick and slip. *Faraday Discussions*, 156, 2012. doi:10.1039/C2FD00128D. 38

[59] S. J. Jones, H. Kitagawa, K. Izumiyama, and H. Shimoda. Friction of melting ice. *Annals of Glaciology*, 19, 1994. doi:10.3189/1994AoG19-1-7-12. 38, 42

[60] P. Oksanen and J. Keinonen. The mechanism of friction of ice. *Wear*, 78(3), 1982. doi:10.1016/0043-1648(82)90242-3. 38, 43, 92, 127

[61] O. E. Pushkarev. Sliding of a body over a melting surface at high velocity. *Journal of Engineering Physics*, 60(6), 1991. doi:10.1007/BF00871513. 38, 44, 92, 127

[62] L. Bäurle, D. Szabó, M. Fauve, H. Rhyner, and N. D. Spencer. Sliding friction of polyethylene on ice: Tribometer measurements. *Tribology Letters*, 24(1), 2006. doi:10.1007/s11249-006-9147-z. 38, 92, 93

[63] I. I. Kozlov and A. A. Shugai. Experimental study of high-speed. *Fluid Dynamics*, 26(1), 1991. doi:10.1007/BF01050128. 38, 44

[64] N. Maeno, M. Arakawa, A. Yasutome, N. Mizukami, and S. Kanazawa. Ice-ice friction measurements, and water lubrication and adhesion shear mechanisms. *Canadian Journal of Physics*, 251(4), 2003. doi:10.1139/p03-023. 38, 39, 127

[65] A. J. Fowler and A. Bejan. Contact melting during sliding on ice. *International Journal of Heat and Mass Transfer*, 36(5), 1993. doi:10.1016/S0017-9310(05)80087-0. 39, 44, 92

[66] C. D. Niven. A proposed mechanism for ice friction. *Canadian Journal of Physics*, 37(3), 1959. doi:10.1139/p59-029. 39, 42, 92

[67] D. Tabor. Junction growth in metallic friction: The role of combined stresses and surface contamination. *Proceedings of the Royal Society A*, 251(1266), 1959. doi:10.1098/rspa.1959.0114. 39

[68] L. Makkonen. Application of a new friction theory to ice and snow. *Annals of Glaciology*, 19, 1994. doi:10.3189/1994AoG19-1-155-157. 40

[69] A.-M. Kietzig, S. G. Hatzikiriakos, and P. Englezos. Ice friction: The effects of surface roughness, structure, and hydrophobicity. *Journal of Applied Physics*, 106(2), 2009. doi:10.1063/1.3173346. 40, 43

[70] J. Perez, C. Mai, J. Tatibouët, and R. Vasoille. Internal friction and microplasticity of ice Ih. *Società Italiana di Fisica*, 33(1), 1976. doi:10.1007/BF027224. 42, 92

[71] F. P. Bowden and T. P. Hughes. The mechanism of sliding on ice and snow. *Proceedings of the Royal Society*, 172(949), 1939. doi:10.1098/rspa.1939.0104. 42

[72] S.-K. Cho, S.-Y. Jeong, J.-S. Ha, and K.-J. Kang. Study on friction characteristics between ice and various rough plates. In *Proceedings of the International Conference on Offshore Mechanics and Arctic Engineering - OMAE*, 2015. doi:10.1115/OMAE2015-41023. 43

[73] A-M. Kietzig, S. G. Hatzikiriakos, and P. Englezos. Ice friction: The effect of thermal conductivity. *Journal of Glaciology*, 56(197), 2010. doi:10.3189/002214310792447752. 43

[74] D. Slotfeldt-Ellingsen and L. Torgersen. Water on ice: Influence on friction. *Journal Physics D: Aplied Physics*, 16(9), 1983. doi:10.1088/0022-3727/16/9/017. 44, 48, 50

[75] H. Strausky, J. R. Krenn, A. Leitner, and F. R. Aussenegg. Sliding plastics on ice: fluorescence spectroscopic studies on interfacial water layers in the μm thickness regime. *Aplied Physics B: Laser and Optics*, 66(5), 1997. doi:10.1007/s003400050442. 44, 48, 50

[76] E. Southern and R. W. Walker. Friction of rubber on ice. *Nature*, 237, 1972. doi:10.1038/physci237142a0. 45, 134

[77] E. Southern and R. W. Walker. A laboratory study of the friction of rubber on ice. *Advances in Polymer Friction and Wear, Polymer Science and Technology*, 5, 1974. doi:10.1007/978-1-4613-9942-1_13. 45, 47, 48, 93, 122, 130, 133, 134

[78] W. Gnörich and K. A. Grosch. The friction of polymers on ice. *Rubber Chemistry and Technology*, 48(4), 1975. doi:10.5254/1.3539657. 45, 46, 48, 50, 134

[79] D. D. Higgins, B. A. Marmo, and J. R. Blackford C. E. Jeffree, V. Koutsos. Morphology of ice wear from rubber-ice friction tests and its dependence on temperature and sliding velocity. *Wear*, 265(5-6), 2008. doi:10.1016/j.wear.2007.12.015. 45, 48, 92, 93

[80] A. D. Roberts and J. C. Richardson. Interface study of rubber-ice friction. *Wear*, 67(1), 1981. doi:10.1016/0043-1648(81)90075-2. 45, 48, 49, 50, 92, 93, 112, 113, 122, 127, 130

[81] A. Ahagon, T. Kobayashi, and M. Misawa. Friction on ice. *Rubber Chemistry and Technology*, 61(1), 1988. doi:10.5254/1.3536173. 46, 48, 145

[82] S. Venkatesh. Laboratory studies of the friction of rubber on ice. *Tribology International*, 8(2), 1975. doi:10.1016/0301-679X(75)90052-3. 47, 48

[83] A. Kriston, N. A. Isitman, T. Fülöp, and A. J. Tuononen. Structural evolution and wear of ice surface during rubber-ice contact. *Tribology International*, 93(A), 2015. doi:10.1016/j.triboint.2015.09.020. 47, 62, 75, 92, 93, 100, 127

[84] A. J. Tuononen, A. Kriston, and B. Persson. Multiscale physics of rubber-ice friction. *Journal of Chemical Physics*, 145(11), 2016. doi:10.1063/1.4962576. 47, 62, 75, 93, 100, 127

[85] N. A. Isitman, A. Kriston, , and T. Fülöp. Role of rubber stiffness and surface roughness in the tribological performance on ice. *Tribology Transactions*, 61(2), 2018. doi:10.1080/10402004.2017.1319002. 47, 62, 75, 93, 100, 127

[86] A. Klein-Paste and N. K.Sinha. Microstructural investigation of ice surfaces after rubber-ice and sand-ice sliding friction tests. *Tribology International*, 43, 2010. doi:10.1016/j.triboint.2009.12.036. 47, 48, 50, 92, 93

[87] E. Sokolovskij. Automobile braking and traction characteristics on the different road surfaces. *Transport*, 22(4), 2007. doi:10.1080/16484142.2007.9638141. 49

[88] A. K. Bhoopalam, C. Sandu, and S. Taheri. Experimental investigation of pneumatic tire performance on ice: Part 1 - Indoor study. *Journal of Terramechanics*, 60, 2015. doi:10.1016/j.jterra.2015.02.006. 49, 51

[89] A. K. Bhoopalam, C. Sandu, and S. Taheri. Experimental investigation of pneumatic tire performance on ice: Part 2 - Outdoor study. *Journal of Terramechanics*, 60, 2015. doi:10.1016/j.jterra.2015.03.001. 49, 51

[90] S. Yamazaki, M. Yamaguchi, E. Hiroki, and T. Suzuki. Effects of the number of siping edges in a tire tread block on friction property and contact with an icy road. *Tire Science and Technology*, 28(1), 2000. doi:10.2346/1.2135992. 50

[91] D. Tabor and R. H. S. Winterton. Surface forces: Direct measurement of normal and retarded van der Waals forces. *Nature*, 219, 1968. doi:10.1038/2191120a0. 56

[92] C. D. Dushkin and K. Kurihara. Nanotribology of thin liquid-crystal films studied by the shear force resonance method. *Colloids and Surfaces A: Physicochemical and Engineering Aspects*, 129-130(30), 1997. doi:10.1016/S0927-7757(97)00031-9. 57

[93] F. Lecadre, M. Kasuya, A. Harano, Y. Kanno, and K. Kurihara. Low-temperature surface forces apparatus to determine the interactions between ice and silica surfaces. *Langmuir*, 34(38), 2018. doi:10.1021/acs.langmuir.8b01902. 57

[94] E. Gacoin, C. Fretigny, A. Chateauminois, A. Perriot, and E. Barthel. Measurement of the mechanical properties of thin films mechanically confined within contacts. *Tribology Letters*, 21(3), 2006. doi:10.1007/s11249-006-9030-y. 69, 71

[95] K. L. Johnson and J. A. Greenwood. An approximate JKR theory for elliptical contacts. *Journal of physics D: Applied Physics*, 38(7), 2005. doi:10.1088/0022-3727/38/7/012. 69, 112

[96] M. Mizukami and K. Kurihara. A new physical model for resonance shear measurement of confined liquids between solid surfaces. *Review of Scientific Instruments*, 79(11), 2008. doi:10.1063/1.3012811. 77

[97] R. D. Mindlin. Compliance of elastic bodies in contact. *Journal of Applied Mechanics*, 16, 1949. 87

[98] D. Mazuyer. *La force de frottement limite*. PhD thesis, 1989. 87

[99] G. Skouvaklis, J. R. Blackford, and V. Koutsos. Friction of rubber on ice: A new machine, influence of rubber properties and sliding parameters. *Tribology International*, 49, 2012. doi:10.1016/j.triboint.2011.12.01. 92, 93

[100] C. McCarthy, H. M. Savage, T. Koczynski, and M. A. Nielson. An apparatus to measure frictional, anelastic, and viscous behavior in ice at temperate and planetary conditions. *Review of Scientific Instruments*, 87(5), 2016. doi:10.1063/1.4950782. 92, 93

[101] Y. Lyu, E. Bergseth, and U. Olofsson. The effect of subzero temperature and snow on the tribology of wheel-rail contact. *Civil-Comp Proceedings*, 110, 2016. 92

[102] J. Le Rouzic, A. Le Bot, J. Perret-Liaudet, M. Guibert, A. Rusanov, L. Douminge, F. Bretagnol, and D. Mazuyer. Friction-induced vibration by Stribeck's law: Application to wiper blade squeal noise. *Tribology Letters*, 49(3), 2013. doi:10.1007/s11249-012-0100-z. 92, 94

[103] A. W. Batchelor G. W. Stachowiak. *Engineering Tribology*. Butterworth-Heinemann, 2001. ISBN: 978-0-750-67304-4. 109, 111, 112

[104] A. R. Savkoor and G. A. D. Briggs. The effect of tangential force on the contact of elastic solids in adhesion. *Proceedings of the Royal Society A*, 356(1684), 1977. doi:10.1098/rspa.1977.0123. 118

[105] R. Sahli, G. Pallares, C. Ducottet, I. E. Ben Ali, S. Al Akhrass, M. Guibert, and J. Scheibert. Evolution of real contact area under shear and the value of static friction of soft materials. *Proceedings of the National Academy of Sciences of the United of America*, 115(3), 2018. doi:10.1073/pnas.1706434115. 118

[106] J. C. Jaeger. Moving source of heat and the temperature at sliding contacts. *Proceedings of the Royal Society of NSW*, 76, 1942. 138

[107] F. E. Kennedy. Frictional heating and contact temperatures. In B. Bhushan, editor, *Modern Tribology Handbook*. CRC Press, 2000. ISBN: 978-0-849-38403-5. 138, 139

[108] J.-M. Georges. *Frottement, usure et lubrification*. Eyrolles, CNRS Editions, 2000. ISBN: 978-2-271-05668-9. 138

[109] J. Steen, W. J. Aben, and K. E. D. Wapenaar. Optimization of the vulcanization process of rubber products. *Polymer Engineering and Science*, 33(3), 1993. doi:10.1002/pen.760330309. 141